Novel Phosphors for Solid State Lighting

This dissertation is submitted for
the degree of

Doctor of Philosophy

in

Materials Science and Metallurgy

at

Robinson College
University of Cambridge

by

Joshua D. Furman

Supervisor
Professor Anthony K. Cheetham

Tuesday 19th October, 2010

UNIVERSITY OF
CAMBRIDGE

Novel Phosphors for Solid State Lighting

ABSTRACT

Novel Phosphors for Solid State Lighting

by

Joshua D. Furman

Solid state white light emitting diode lighting devices outperform conventional light sources in terms of lifetime, durability, and lumens per watt. However, the capital contribution is still to high to encourage widespread adoption. Furthermore, the colour from today's devices is unsuitable for general room illumination and thus new phosphor materials are needed. This dissertation will examine the synthesis of inorganic nanoparticles and the possibility of using hybrid inorganic-organic frameworks in the search for new lighting phosphors. Nanoparticles of the oxide compound yttrium aluminium garnet were synthesized using an emulsion technique, though it was found that the high temperature processing needed for good optical properties was not compatible with maintaining nano-sized particles. In terms of hybrid framework phosphors, several aspects of this new area have been explored. The mechanical and optical properties of a dense cerium oxalate formate hybrid framework compound have been investigated. Its strength was found to be nearly as great as some classical ceramic compounds, and clearly robust enough for device applications. While the photoluminescence of the cerium oxalate formate was not suitable for solid state lighting, the impressive mechanical properties evaluated are expected to be valid for a wide range of dense inorganic-organic frameworks. A novel approach to solid state lighting phosphors was introduced by using ligand-based photoluminescence in hybrid frameworks. Novel frameworks were prepared using 9,10-anthraquinone-2,3-dicarboxylic acid in combination with calcium, manganese, nickel, and zinc. These compounds show excellent photoluminescent emission for use in solid state lighting applications, although the luminescence is quenched at room temperature due to dynamic effects. The excitation, while reaching the blue part of the spectrum, falls just short of what is needed for use today's devices. To address these issues, a second class of novel framework compounds was prepared using 9-fluorenone-2,7-dicarboxylic acid in combination with calcium, strontium, barium, cadmium, and manganese. They are more rigid structures and show good luminescence at room temperature with a photoluminescent excitation spectrum extending further into the blue than the anthraquinones. Additionally, quantum yield in the calcium fluorenone is nearly double that of its parent ligand, suggesting that there is an enhancement in luminescent properties as a result its inclusion in a framework structure. An explanation for the differences in efficiency between seemingly similar compounds are drawn from their compositions, crystal structures, photoluminescence, and specific heat properties. Finally, some structural and chemical targets for future hybrid phosphor development are identified based on the relationships identified in this work.

PREFACE

Tuesday 19th October, 2010

The work described in this dissertation is all original and has been carried out solely by the author or in collaboration with others as detailed below.

The research on yttrium aluminium garnet nanoparticles in Chapter 3 was was carried out in collaboration with Katherine Page, who was responsible for the PDF refinements, Gautam Gundiah, who assisted with the synthesis and microscopy, and Nancy Pizzaro, who performed many of the luminescence measurements. This work was published in Chemical Physics Letters as: J. D. Furman, K. Page, N. Pizzaro, G. Gundiah, and A. K. Cheetham. "Local structure and time resolved luminescence of emulsion prepared YAG nanoparticles." *Chem. Phys. Lett.*, **465**, 67 (2008). [DOI: 10.1016/j.cplett.2008.09.045].

The oxalate-formate study described in Chapter 4 was carried out in collaboration with Jin Chong-Tan who performed the mechanical testing and analysis. This work was published in the Journal of the American Chemical Society as: J. C. Tan and J. D. Furman and A. K. Cheetham. "Relating Mechanical Properties and Chemical Bonding in an Inorganic-Organic Framework Material: A Single-Crystal Nanoindentation Study." *J. Am. Chem. Soc.*, **131**, 14252 (2009). [DOI: 10.1021/ja9060307].

The research on anthraquinone compounds described in Chapter 5 was carried out in collaboration with my intern Min Tang who assisted with the synthesis, and Alexander Mikhailovsky who performed some of the optical characterization.

The research on fluorenone compounds in Chapter 6 was carried out in collaboration with Brent Melot, who performed the heat capacity measurements, Simon Teat who assisted with the crystallography, Alexander Mikhailovsky who

performed many of the optical measurements, and Alina Warner who assisted with some of the synthesis. This was published in Chemistry of Materials as: J. D. Furman, A. Y. Warner, S. J. Teat, A. A. Mikhailovsky and A. K. Cheetham. "Tunable, ligand-based emission from inorganic-organic frameworks: A new approach to phosphors for solid state lighting and other applications." *Chem. Mater.*, **22**, 2255-2260 (2010). [DOI: 10.1021/cm9030733]. A second manuscript was published in Physical Chemistry Chemical Physics as: J. D. Furman, B. C. Melot, S. J. Teat, A. A. Mikhailovsky and A. K. Cheetham. "Towards enhanced ligand-centered photoluminescence in inorganic-organic frameworks for solid state lighting." *Phys. Chem. Chem. Phys.*, 2010, [In Press].

The majority of this work was made possible through the generous support of Mitsubishi Chemical Center for Advanced Materials. Some of the facilities at the University of Cambridge were supported by a European Research Council Advanced Investigator Award. The EPSRC United Kingdom National Crystallography Service and Dr. James Orton were responsible for some of the single crystal X-ray diffraction experiments. Laboratory facilities at University of California Santa Barbara (UCSB) were supported by NSF DMR05-20415. The Advanced Light Source is supported by the Director, Office of Science, Office of Basic Energy Sciences, of the U.S. Department of Energy under Contract No. DE-AC02-05CH11231. Use of the Advanced Photon Source was supported by the U.S. Department of Energy, Office of Science, Office of Basic Energy Sciences, under Contract No. DE-AC02-06CH11357.

ACKNOWLEDGEMENTS

None of this work would have been possible without the support and guidance of my supervisor Anthony K. Cheetham. His knowledge and enthusiasm are limitless and his willingness to guide with a gentle hand gave me the freedom to shift projects and change approaches while keeping the overall goal in focus. The support and advice of Mitsubishi Chemical Center for Advanced Materials have been invaluable, and many discussions with Kijima-san, Shimomura-san, and Jeff Gerbec have given my work real-world relevance. Great thanks are also owed to Professor Ram Seshadri, who provided endless chemical insight, suggestions, prodding, advice, focus, and otherwise along the way.

As always, no good science is carried out behind closed doors and so I owe many thanks to my collaborators along the way. Peter Davies his student David Stein at the University of Pennsylvania who offered me my first chance to work in a laboratory during my undergraduate years. Starting my career in research by hand grinding oxides for solid solutions gave me a grounding in solid state chemistry that no one should be without. Gautam Gundiah, Brent Melot, Katherine Page, Nancy Pizzaro, Jin-Chong Tan, Zeric Hulvey, Alexander Mikhailovsky, Guang Wu, and Simon Teat have been key in developing my skills, knowledge, and in building the impact of these projects. Countless discussions and support also came from all of the other members of the Cheetham groups: Russell Feller, Kinson Kam, Eduardo Falcao, Crystal Merrill, Leah Appelhans, Efrain Rodriguez, Isabelle Etchart, Ryan Burwood, Thiru Alagarsamy, Wei Li, and Ali Kalaji. Dan Shoemaker, Josh Kurzman, and Joe Doyle at UCSB also deserve a special mention. Many interns helped with these projects along the way and without the enthusiasm, committment, and creativity of Alina Warner, Alison Morrison and Min Tang, some of this work would not have been possible.

To my family, for their support and encouragement.

And to Becca, who has been there through it all.

Contents

List of Figures

List of Tables

Aims of research

The goal of this thesis was the development of new phosphor materials for solid state lighting. More specifically, to develop new compounds which could be used to efficiently convert the blue light available from GaN-based light emitting diodes into lower energy wavelengths of the visible spectrum, resulting in white light output. Applicability was considered both in terms of phosphor brightness and device-level implications.

Chapter 1 describes the history of phosphors and luminescent materials, and gives some examples of oxide phosphor materials and the mechanisms of excitation and emission. This is followed by an introduction to inorganic-organic hybrid framework materials, a class of materials distinctly different from oxides that will be used to develop the luminescent materials described later in Chapters 5 and 6. Finally, some precedent for trying to make hybrid materials is described at the end of Chapter 1.

Chapter 2 outlines the experimental techniques that were used repeatedly throughout this research. For instance, hydrothermal reactions, which are used to synthesize the hybrid materials, and single crystal X-ray diffraction, which has been used to solve the crystal structure of novel compounds. Throughout the chapters that follow, more specific methods are described for individual experiments.

Chapter 3 concerns the use of nanoparticles made from a well known inorganic phosphor system, cerium-doped yttrium aluminum garnet. There have been conflicting reports about the benefits and difficulties of using nanoscale particles of phosphor materials in light emitting diodes (LEDs), as opposed to the more common 1-50 μm size used commercially today. It is thought that they might reduce light scattering and increase the total efficiency of a device. Small particles were synthesized by an emulsion route and characterized by temperature dependent luminescence measurements and synchrotron pair distribution function, a real-space local-structure analysis.

The work described in Chapter 4 began as an attempt to make phosphors from hybrid materials of rare earth metals and oxalic acid. While it was found that they were not particularly impressive as luminescent materials, they made an ideal case for studying the nearly unexplored mechanical properties of inorganic-organic frameworks. If these materials are to be used in commercial devices, their strength and hardness becomes important for processing and product lifetime.

Chapter 5 introduces four novel inorganic-organic hybrid framework compounds. The were prepared hydrothermally from filled shelled metals and the ligand 9,10-anthraquinone-2,3-dicarboxylic acid. The luminescence of these compounds at low temperature, while not useful for device applications, is important in explaining some of the behavior seen for the framework compounds.

The final experimental section, Chapter 6, describes what is probably the most interesting set of materials in this thesis. The crystal structure and luminescent properties of five novel framework compounds containing 9-fluorenone-2,7-dicarboxylic acid in combination with calcium, strontium, barium, and cadmium are presented. An attempt is made to explain the differences between the light-emitting properties of each of each compound using crystallographic, chemical,

and specific heat measurements.

Seventy years of development in oxide phosphors has only given some limited design criteria in identifying high efficiency phosphor materials from simply their crystal structure and chemical composition. At the end of this work, some initial design targets for developing new frameworks using inorganic-organic framework phosphor materials are proposed, describing which chemical and structural parameters most critical and which are less important.

Chapter 1

Introduction

1.1 Materials for light conversion

Solid state lighting in the form of white light emitting diodes (LEDs) is poised to replace incandescent and mercury-containing fluorescent lighting in the near future [1, 2]. Incandescent lights are already facing bans in many countries. Today's commercial solid state devices use a GaN-based emitter in combination with a yellow-emitting phosphor, typically Ce^{3+}-doped yttrium aluminium garnet (YAG:Ce) [3–5]. Figure 1.1 shows a typical cross-section of a phosphor-based LED device. The reflective cup, which directs the light out of the device, is filled with a polymer encapsulant to contain the phosphor particles. This combination of blue and yellow light is relatively inexpensive and efficient but shows poor colour-rendering properties. Consequently, there has been an extensive search in the past decade for new phosphor materials with broad emission spectra in the the green, yellow, and red [6]. The vast majority of these newly reported compounds have been rare-earth doped oxides [7–11] and nitrides [12, 13]. Ideally, a solid state lighting phosphor will be excited in the blue or near-UV and emit in the

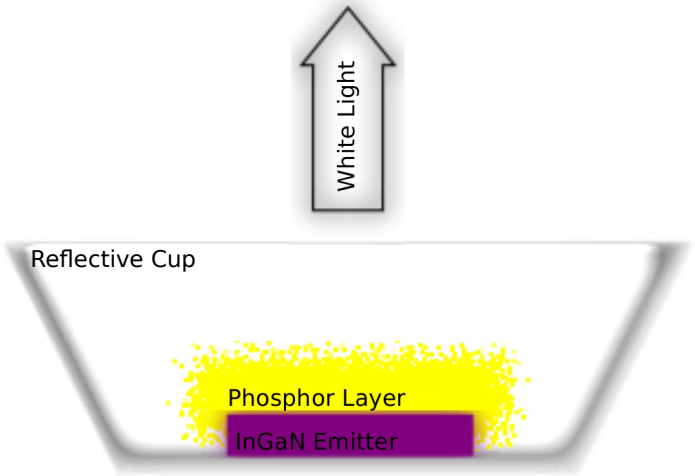

Figure 1.1: Schematic of a phosphor-converted white LED device. A GaN-based emitter (purple) is surrounded by phosphor particles (yellow) and placed in a reflective cup to focus the light output.

green-to-red regions to create a broad spectrum white light similar to blackbody radiation [14]. The thermal stability of colour and intensity are also critical as the temperatures at the emitter can reach over 100°C [15].

Quantifying the quality of a light source in terms of colour can be difficult as many factors need to be taken into account. The colour itself is often described by a point on a chromaticity diagram like the one in Figure 1.2. However, simply identifying the emitted colour does not fully describe how a light source will perform in practice, since the specific mixing of colours that leads to that final emission colour is also important. The colour rendering index, or CRI, is a scale from 0 to 100 that quantifies how well colours are represented when the incident light reflects from an object's surface. It is formally defined as the *"effect of an illuminant on the colour appearance of objects by conscious or subconscious comparison with their colour under a reference illuminant"* [16]. Sunlight, which comes

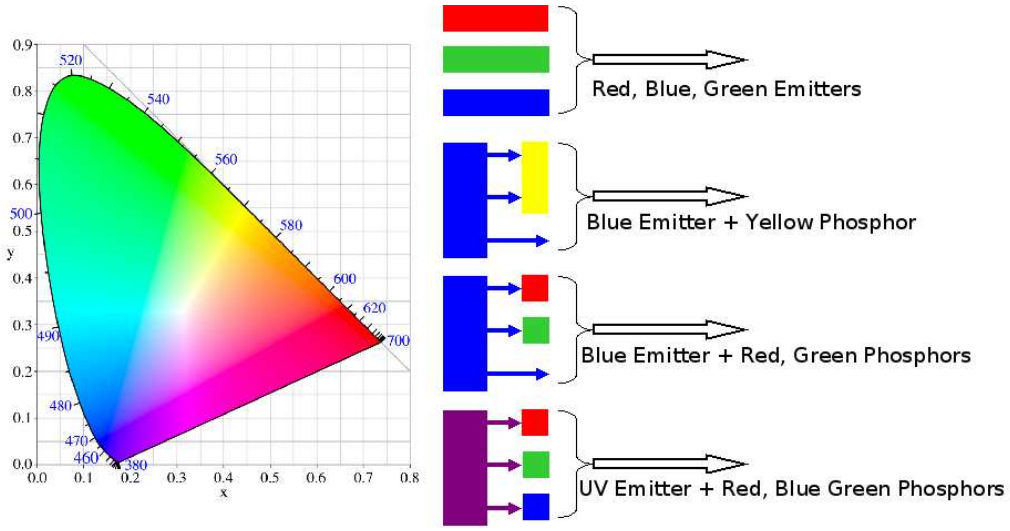

Figure 1.2: LEFT: Chromaticity diagram used to describe the colour of light by the x and y coordinates. RIGHT: Methods to produce white light employed in phosphor-converted white LEDs.

from a very high temperature black-body radiation source with a colour temperature around 6000 K, is taken as a reference light source and given the value 100. Blackbody radiation is given by Planck's law such that the spectral radiance I at wavelength ν and temperature T is:

$$I\left(T,\nu\right)=\frac{2h\nu^{3}}{c^{2}}\frac{1}{e^{\frac{h\nu}{kT}}-1} \tag{1.1}$$

The temperature of a blackbody radiation source defines its colour temperature. A light source is then characterized by comparing its accuracy in colour representation to a blackbody source of the same colour temperature. Incandescent lamps achieve a CRI of 100 by definition, while traditional fluorescent tubes are between 60 and 80, and the yellowish sodium vapour street lights can be as low as 20 [17]. Today's common commercially available white LEDs have a CRI around 70 [18], which is generally unsuitable for general room lighting. This system of charac-

terization obviously has some shortcomings, particularly in that normalizing for colour temperature belies its importance in real world performance. For instance, a 60 watt incandescent lamp and sunlight both have a CRI of 100 but significantly different colour temperatures, whereas a fluorescent and an incandescent might have the same colour temperature but significantly different colour rendering characteristics. Nevertheless, the CRI is the current standard and is useful as a means of comparison between different types of largely similar light sources, especially when it is reported along with colour temperature [19]. Although the CRI's of the compounds described herein have not been measured, the complexity in defining so-called "white" light is indicative of the difficulty in creating it from non-blackbody sources.

The light from LEDs is nearly monochromatic, typically centred at 465 nm or shorter for a GaN-based emitter. The emission spectra from YAG:Ce is centred at 550 nm, resulting in a blue-tinged white light from devices. The total output spectra from a white LED device, along with a fluorescent tube lamp and sunlight are shown in Figure 1.3. The next generation of white LEDs is expected to use a blue emitter in combination with red and green phosphors or a near-UV emitter in combination with red, green, and blue phosphors. The use of multiple phosphors allows the colour temperature of the white light to be tuned and thus the colour rendering to be increased [14, 20]. The possibility of improved colour rendering by the use of red and green phosphors in place of a yellow phosphor has already been well demonstrated at the lab scale [12]. However, this approach introduces its own problems, particularly in that the behaviour of each individual phosphor material must be invariant with temperature and time.

Increasing the total light output requires optimization of the emitter, device geometry, packaging materials, and phosphor efficiency. The brightness of a phos-

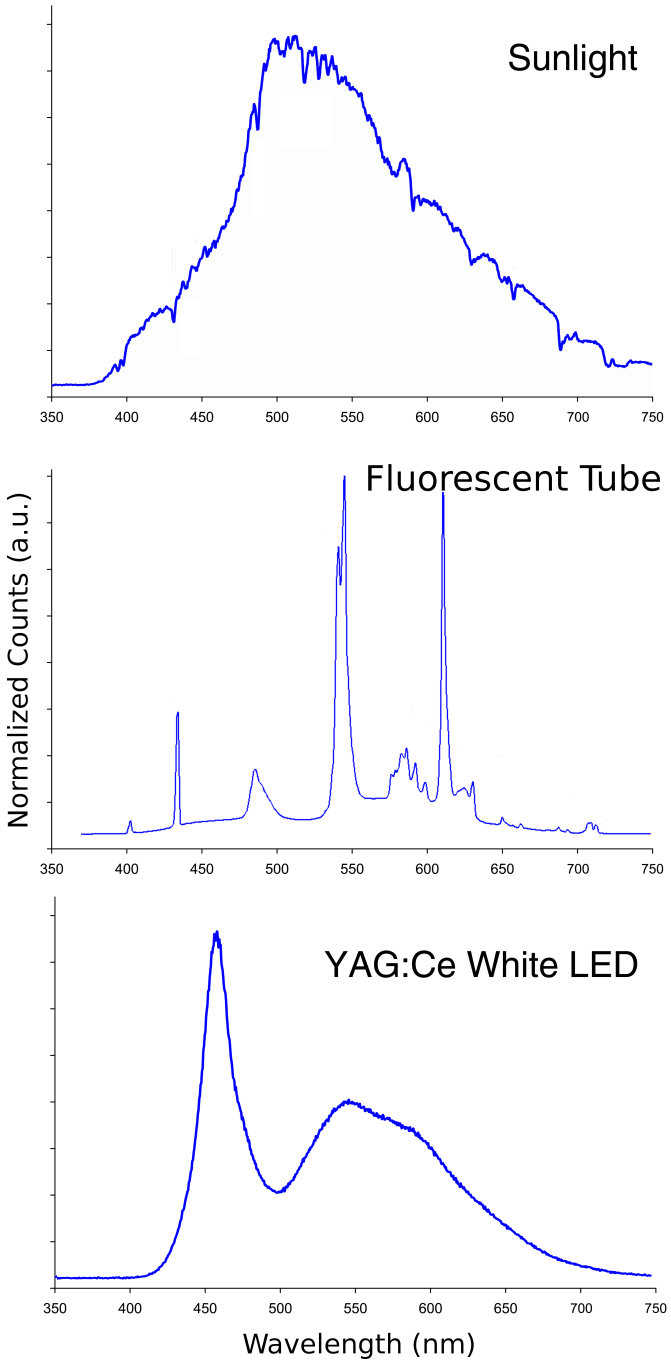

Figure 1.3: TOP: Emission spectra of daylight sun showing broad emission. MIDDLE: A fluorescent tube showing multiple sharp emission peaks. BOTTOM: YAG:Ce converted white LED, showing a 465 nm blue emission peak from the emitter and a broad yellow emission from the phosphor layer. Both the fluorescent and LED lights have been designed to try and fill the space indicated by the sunlight spectra as well as possible [21].

phor is best characterized by the quantum yield (QY), which is the ratio of absorbed to emitted photons. The temperature-dependent quantum yield is difficult to measure directly but can be extracted from emission spectra taken at a range of temperatures, scaled to a measurement of QY at room temperature. The temperature-dependent QY is very important for device considerations as the operating temperature of phosphor materials can reach 100°C and thermal quenching of photoluminescence at these temperatures can be significant.

1.2 Luminescence

Luminescence is the process of light emission as an excited atom returns to its ground state. In 1600, Vincenzo Cascariolo reportedly discovered a deposit of the mineral Baryte ($BaSO_4$) in the hills outside Bologna. An amateur alchemist, he managed to purify it into a phosphorescent powder which glowed long after being exposed to light and he called it *lapis solaris*, meaning stone of the sun, or Bologna Stone [22]. Cascariolo's Bologna stone is generally thought to be the first phosphor prepared in Europe, though reports many centuries older from Japan make reference to glowing inks prepared from seashells and sulfurous volcanic rocks, which likely would have contained calcium and magnesium sulfates [23]. Luminescent processes are generally divided into fluorescence and phosphorescence. Fluorescence describes a spin-allowed transition and thus occurs relatively rapidly, with decay times typically on the order of nanoseconds [24]. It was first formally described in George Stokes' optical investigations on the mineral fluorspar (CaF_2), from which fluorescence draws its name. Phosphorescence, taking its name from the element phosphorus, describes a typically slower, spin-forbidden transitions with decay times typically on the order of milliseconds, though occasionally up to

minutes or hours. Generally speaking, the faster fluorescent emissions are more efficient because the short lifetimes of the excited states provide less opportunity non-radiative deactivation.

The method of excitation is also important in defining luminescence. If the excited states are created by incident photons, as is used in white LED devices, it is referred to as photoluminescence. Electroluminescence is the process through which semiconductor LED devices generate their light. Typically, charge is directly injected into a junction of hole-doped and electron-doped materials. Conduction band electrons enter the junction from the electron doped region and valence band holes enter from the hole-doped region. The subsequent recombination of these electron-hole pairs results in the emission of a photon with a wavelength equal to that of the semiconductor bandgap. GaN-based blue LEDs, which are used as the basis for photoluminescent phosphor converted white LEDs, undergo electroluminescence. Chemoluminescence occurs on the recombination of excited states formed by chemical reactions and is known for its use in glo-sticks. The closely related bioluminescence refers to chemical reactions in living organisms such as algae, fireflies, and deep-sea fishes.

In the phosphors used for solid state lighting, electron–hole pairs are excited by an incident photon from the highest occupied molecular orbital (HOMO), or the top of the valence band in an extended solid. The electron moves to the bottom of the lowest unoccupied molecular orbital (LUMO), or bottom of the conduction band, by a non-radiative process known as internal conversion, and then returns to the ground state by emitting a photon. This often results in a wide range of excitation wavelengths above a threshold energy, but a well-defined emission peak. A Jablonski diagram, named after the polish physicist Aleksander Jabłoński, is used in spectroscopy to draw simplified transitions between accessible energy levels.

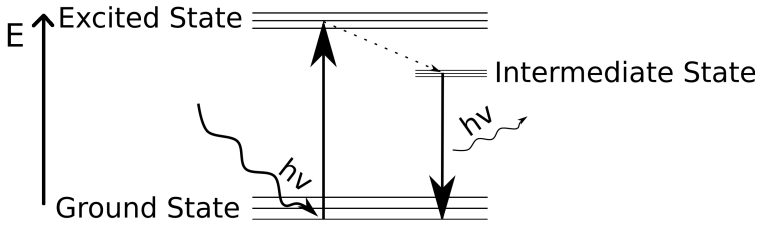

Figure 1.4: Jablonski diagram of photoexcitation and radiative emission from an intermediate state. Solid lines represent radiative processes and dotted lines represent non-radiative.

Figure 1.4 shows a simplified Jablonski diagram for photoexcitation, followed by non-radiative decay to an intermediate state, and then emission of a lower energy photon as the electron returns to the ground state. The change in colour is referred to as the Stoke's shift, named after physicist George G. Stokes. It arises from a difference in the transition energy between an excitation up from the lowest ground state and a recombination down from the lowest excited state when momentum is held constant, as explained by the Franck-Condon principle and is illustrated in Figure 1.5. The figure shows the ground state energy levels E_0 and an excited state E_1 in a simple system, plotted as energy versus q, labelled nuclear coordinates or configuration coordinates. The parameter q for a simple 2-body system indicates the interatomic separation.

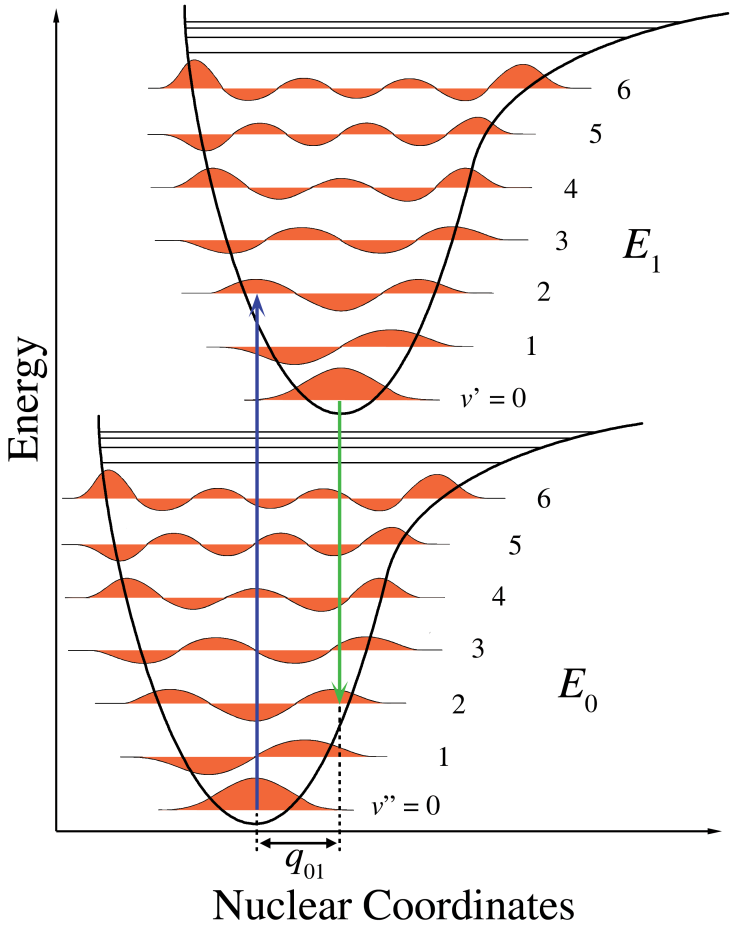

Figure 1.5: The Franck-Condon principle explains the Stoke's shift (q_{01}) between excitation (blue) and emission (green) wavelengths. Plotted as Energy versus nuclear or configurational coordinates q

1.2.1 Inorganic phosphors

The development of inorganic phosphor materials for devices began along with lighting technology, dating as far back as 1856 in combination with a mercury discharge tube [23]. Edison patented a calcium tungstate phosphor based fluorescent tube light in 1896, only 17 years after he filed his first carbon filament lamp patent (although it was 94 years after Davy's first report of an incandes-

cent lamp) [25]. These also quickly found use in cathode ray tubes for oscilloscopes, radar screens, and black and white televisions. As technology advanced forward, phosphors with sharp, well-defined emission spectra that were excitable by cathode ray were needed for colour televisions. Simultaneously, broadly emitting phosphors that could be excited by mercury discharge tubes at 254 nm were developed for fluorescent tube lighting. When blue-emitting GaN LEDs went into production in 1993, there was a resurgence in phosphor development, searching for broad emitting phosphors that were excited near 430 nm. With solid state light available at the highest energy of the visible spectrum, phosphors could then be used to create white light from an LED.

Fluorescence in inorganic materials can be achieved in several ways. The simplest arrangement is where luminescent impurities are doped into a host lattice. These *activator* ions intrinsically contain all of the required energy levels for radiative processes and the host lattice serves to isolate the activator ions [26]. As optically active ions are brought together, cross-relaxation between excitons leads to non-radiative decay and a decrease of luminescence in what is known as concentration quenching [27]. For example, the Eu^{3+} ion is well known to emit red light and can be excited directly in the UV, but Eu(III) oxide does not show any luminescence. Re-absorption of emitted light by the activators can also occur and reduce efficiency when the excitation and emission spectra display significant overlap. Often, luminescent intensity is observed to increase to a maximum with a doping doping between 1% and 10% in an oxide lattice, beyond which further doping leads to a decrease in intensity.

The emission colour from activator ions depends on their electronic structure. For most of the rare earth ions, where the $f \rightarrow f$ transitions responsible for luminescence are not involved in chemical bonding, the emission peaks are sharp and

generally do not change based on the host lattice. This is the case for red emitting Eu^{3+} and green emitting Tb^{3+}, which makes them useful for display applications. Figure 1.6 shows the energy levels available to the trivalent lanthanides with many of the visible transitions marked with coloured arrows [28].

When $f \rightarrow d$ transitions are involved, such as for Ce^{3+} and Eu^{2+}, the transitions become dependent on the crystal field of the activator ion and the peaks are generally broader, which makes them useful for lighting applications where blackbody radiation is being approximated [29, 30]. Figure 1.7 shows the crystal field splitting for cubic trivalent cerium. The emission colour from the $5d^1 \rightarrow 4f^1$ transition is dependent upon the field strength Δ and other factors, and the band is broadened by the Russell-Saunders splitting of the ^2F ground state [31]. By changing the coordination arrangement and distances around the cerium ions, the emission colour can be tuned from the UV down to the red. The compound used in most commercial white LEDs is based on yttrium aluminium garnet doped with trivalent cerium (YAG:Ce), which produces an efficient yellow emission in this way. Both the absorption and emission processes occur on the cerium ion and the lattice serves to dilute the cerium ions, preventing concentration quenching. The crystal field around the cerium ions is such that the emission is shifted to a 530 nm maximum. Photoluminescent excitation and emission spectra are shown in Figure 1.8. The luminescent behaviour of YAG:Ce and nanoparticles of the same compound will be described in detail in Chapter 3.

Another rare earth ion that shows the broad emission spectra that is desirable for lighting applications is divalent europium. Although none of the compounds described in this thesis use this emission mechanism, it is an important approach for solid state lighting. Figure 1.9 shows a simplified diagram of the crystal field splitting for Eu^{2+}. A UV-emitting $f \rightarrow f$ transition indicated by the purple line, and

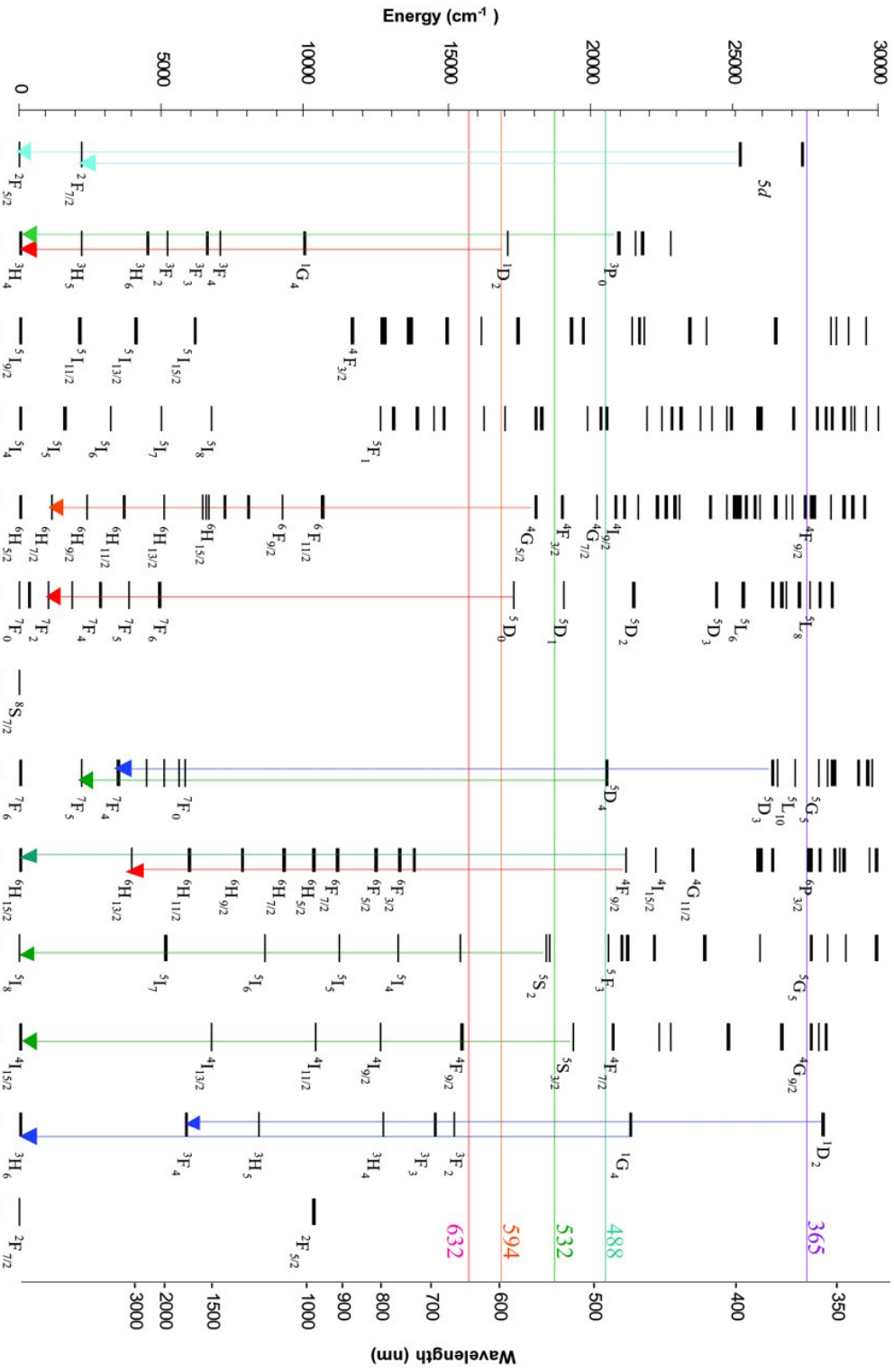

Figure 1.6: Energy level diagram for the trivalent lanthanide ions [28].

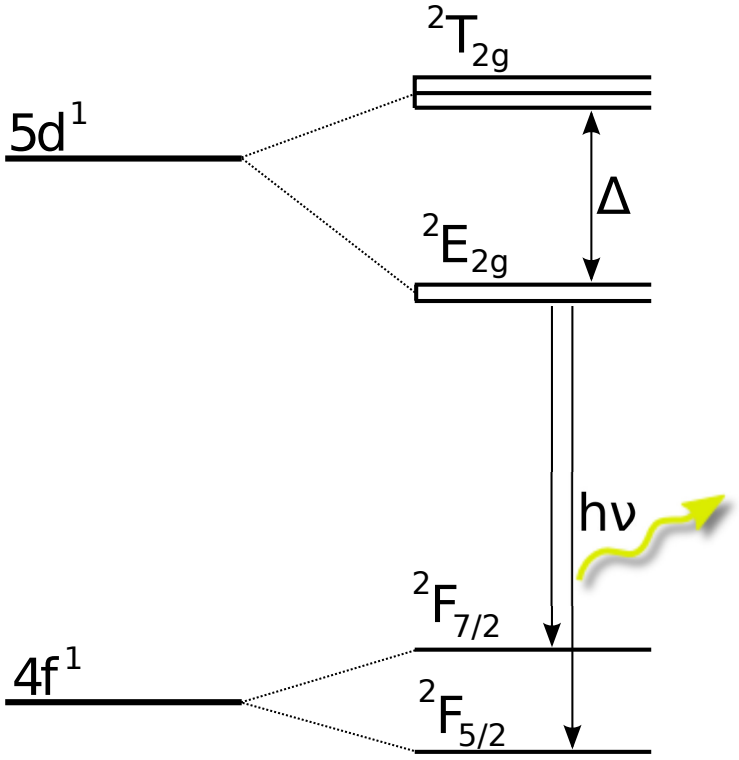

Figure 1.7: Crystal field splitting in Ce^{+3} is indicated by Δ, which allows for tuning of of the optical emission wavelength. Adapted from Gundiah et al [29].

the coloured emissions with decreasing transition energy are selectively present depending on the ligand field strength. Ligand field splitting, which accounts for the broad emission bands, is not shown. A blue emitting phosphor used in many fluorescent light applications, $BaMgAl_{10}O_{17}:Eu^{2+}$ (BAM:Eu), uses the spin-allowed $4f \rightarrow 5d$ transition of divalent europium to both absorb and emit light.

For some activator ions, the emission may be intense and of the desired colour but the incident photon absorption is either too weak or occurs at the wrong wavelength. In this case, a *sensitizer* ion may be co-doped along with the activator ions. The incident photons are then absorbed by the sensitizer and the energy is transferred to the activators, either by exciton migration or charge trans-

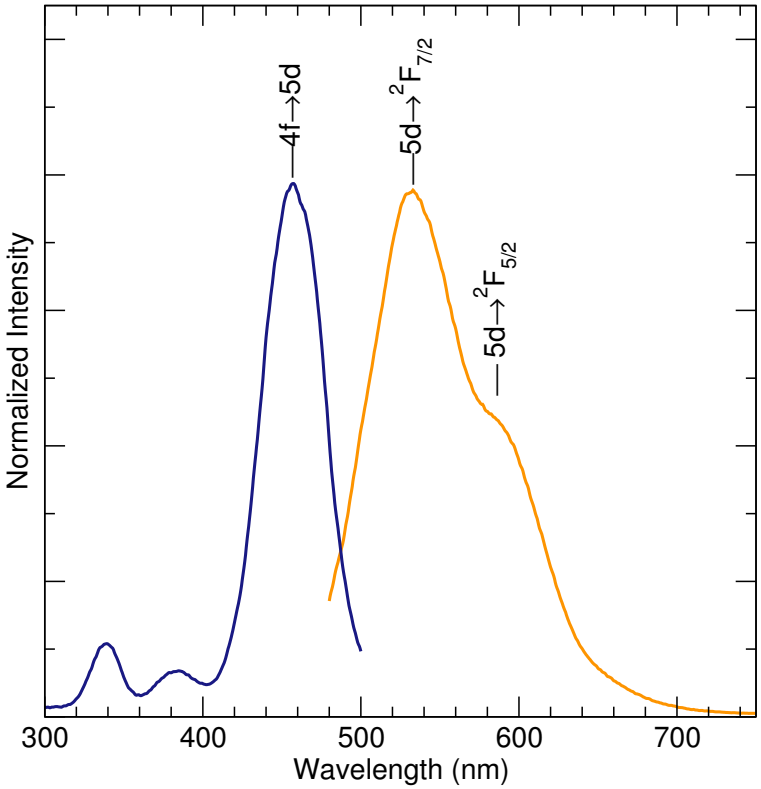

Figure 1.8: Photoluminescent excitation and emission spectra for YAG:Ce. λ_{ex}=460 nm, λ_{em}=530 nm. The 4f ground state is split into a double of ${}^2F_{\frac{5}{2}}$ and ${}^2F_{\frac{7}{2}}$, the transitions to which are both labelled in the emission spectra. Excitations peaks are transitions from the 4f ground state to various 5d levels, the most intense, labelled peak indicates the lowest 5d level.

fer bands, where a lower energy photon is then emitted. When BAM is co-doped with Eu^{2+} and Mn^{2+} (BAM:Eu,Mn), nearly all of the energy absorbed by the sensitizing europium is transferred to the manganese activator ions. High spin divalent manganese generally produces a broad green emission from its $d \rightarrow d$ transition. While BAM:Eu can be excited by wavelengths as long as 425 nm, BAM:Mn is only excited much further into the UV. The co-doping allows for blue excitation of the green manganese luminescence. Figure 1.10 shows the photoluminescent excitation and emission of BAM:Eu,Mn with europium fixed at 15% and x amount of

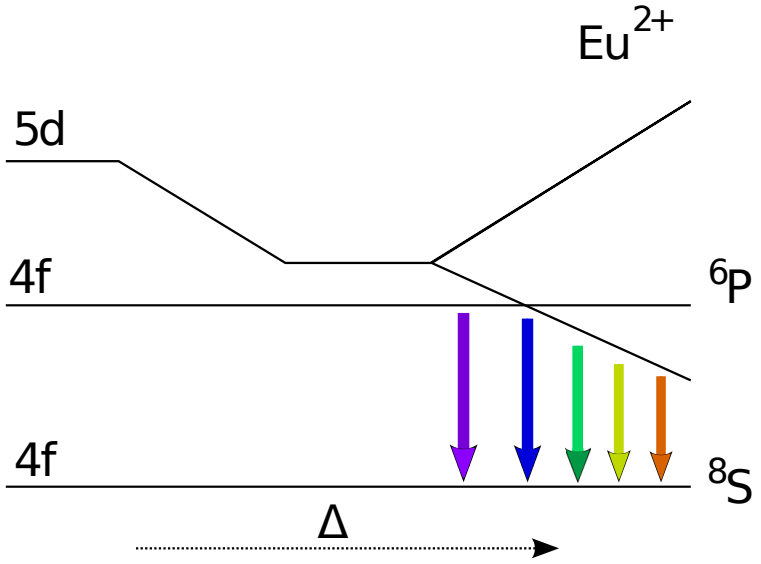

Figure 1.9: Simplified Eu^{2+} energy diagram showing how the crystal field dependent $5d$ bands impact the emission colour from $5d \rightarrow 4f$ transitions. Adopted from [26].

manganese [32].

The host lattice itself can be a sensitizer, absorbing the incident photons and transfer the energy to the activator ions. This process is commonly found in molybdate, vanadate [33], and tungstate phosphors [7]. For example, in the red-emitted europium-doped yttrium vanadate YVO_4:Eu^{3+}, the vanadate groups of the lattice act as sensitizers and the energy is transferred to the europium activator ions. Figure 1.11 from Gundiah et al. shows the photoluminescent excitation and emission behaviour of YVO_4:Eu^{3+} that has been co-sensitized with Bi^{3+} [33].

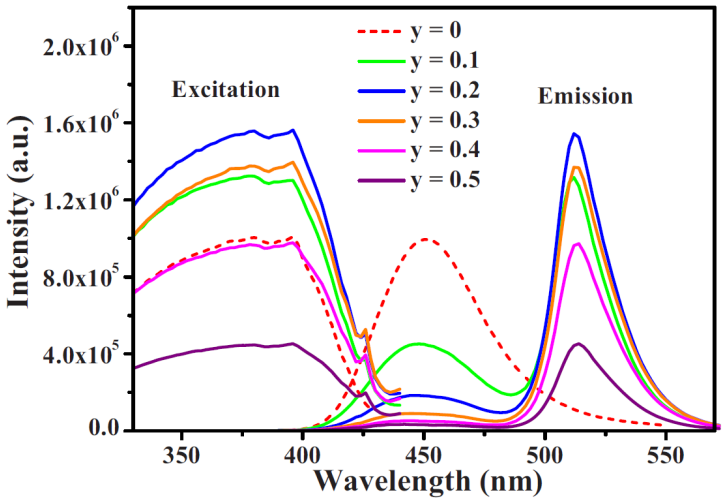

Figure 1.10: Photoluminescent excitation and emission spectra of BAM:15% Eu, x% Mn. As the manganese content increases, the energy absorbed by the sensitizing europium ions in transferred to the activating manganese ions, resulting in a near-UV excited green emission. λ_{ex}=370 nm, λ_{em}=514 nm. From Ke et al. [32].

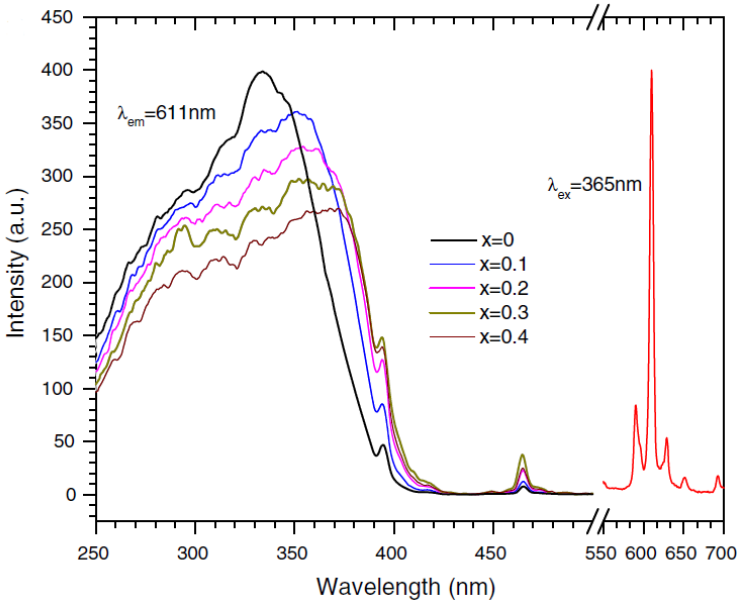

Figure 1.11: Photoluminescent excitation and emission of YVO_4:Eu^{3+} at various levels of bismuth co-doping (x). λ_{ex}=365 nm. λ_{em}=611 nm. From Gundiah et al. [33].

1.2.2 Fluorescence and phosphorescence

In the most general terms, luminescence is the process in which an electron returns from an excited state to a ground state and emits a photon. If that process is spin-allowed, such that the spin quantum number of the electron does not need to change after it reaches the ground state to avoid violating the Pauli exclusion principle, then the process is known as fluorescence. If the process is spin-forbidden, the recombination occurs at a slower rate and this is known as phosphorescence. It is important to note that while spin-forbidden, the process does still occur. Figure 1.12 shows a simplified example of singlet and triplet states for a two-electron system. In the ground state S_0, both electrons sit in the same orbital with opposite spins, thus a total spin equal to 0. Some incident energy promotes one of those electrons into an excited state, which is labelled S_1, or the first excited singlet state. If this electron then returned to the ground state by emitting a photon, that process would be labelled fluorescence. Photons of higher energy can also be absorbed into the system, promoting an electron into a higher excited state, i.e. S_2, S_3. This will typically return by the non-radiative process known as internal conversion to the lowest excited state before (potentially) emitting a photon on the transition from excited to ground state. Alternatively, while in S_1, a non-radiative process called spin-orbit coupling can change the spin of one of those excited state electrons. This intersystem crossing, where an electron spin is changed, takes place by coupling with phonon lattice energy. In the excited triplet state T_1, the total spin is equal to 1. To return from the triplet excited state T_1 to the ground state is a slower process than $S_1 \rightarrow S_0$ because it involves another intersystem crossing to return to an antiparallel spin state with total spin equal to 0. Generally, the T_1 state is of lower energy than S_0, resulting in red-shifted luminescence. This lower energy is, in part, due to the increased separation between the

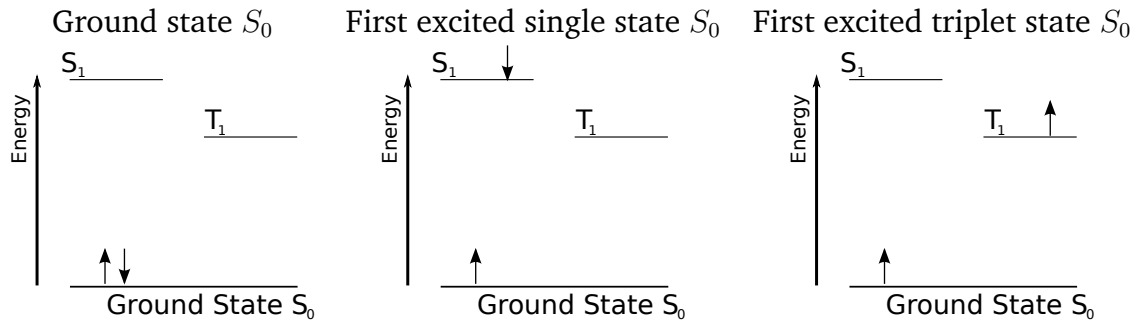

Figure 1.12: Two-electron system showing the LEFT: ground state S_0, where both electrons exist in the same orbital with spins +1/2 and -1/2, MIDDLE: Singlet excited state S_0, where incident energy has promoted one of the ground state electrons into a higher energy orbital, without an change in spin, and RIGHT: the triplet excited state T_1, where spin-orbit coupling has changed the spin of one of the excited states, moving it into a lower energy triplet state.

spins of the same orientation and thus decreased Coulomb interaction. The direct excitation into the triplet state from the ground state $S_0 \rightarrow T_1$, however, is statistically unfavourable such that it is only observed under very special experimental conditions.

In the accessible energy levels of an molecule is a highest energy orbital occupied by electrons in the ground state, called the HOMO (highest occupied molecular orbital) and a lowest unoccupied level, known as the LUMO. The energy of the so-called HOMO–LUMO gap is lowest energy by which a photon will be absorbed into the system, such that as described above the position of the LUMO generally corresponds to the energy of the first excited state, such that: This is in a way comparable to the band-gap in extended network solids.

$$\Delta E = E_{HOMO} - E_{LUMO} \tag{1.2}$$

wherein if

$$h\nu_{absorbed} > \Delta \tag{1.3}$$

then

$$S_0 \rightarrow S_1 \tag{1.4}$$

Because triplet state phosphorescence is a slower process than fluorescence, and requires phonon energy for the intersystem crossings, the two types of luminescence can be separated experimentally by using either ultrafast laser excitations, or by measuring at low temperatures. Additionally, while for inorganic compounds the phosphorescent lifetimes are often reported as being on the order of milliseconds up to minutes and hours, organic phosphorescence can easily be in the same nanosecond range as fluorescence because the phonon energies required to move in and out of the triplet states are reduced.

1.2.3 Coordination compound phosphors

In coordination compound phosphors, where an organic ligand is bound to an optically active metal ion, several mechanisms can apply. A first route, called Ligand to Metal Charge Transfer (LMCT), is where the ligand is excited by incident light and then transfers energy to an emitting metal ion. LMCT photoluminescence is often referred to as the *antenna effect* since the strongly absorbing ligand acts as a receiving antenna for the bound metal ion, as illustrated in Figure 1.13 [34]. A second route, Metal to Ligand Charge Transfer (MLCT), is where the metal ion acts as an absorber and the organic is luminescent. For instance, tris(2,2-bipyridyl)ruthenium(II) (RuBPY), shown in Figure 1.14, uses the ruthenium ion to harvest light and transfer it to the light emitting emitting 2,2'-bipyridyl. Derivatives of RuBPY are used in some organic LEDs. A third way of introducing lu-

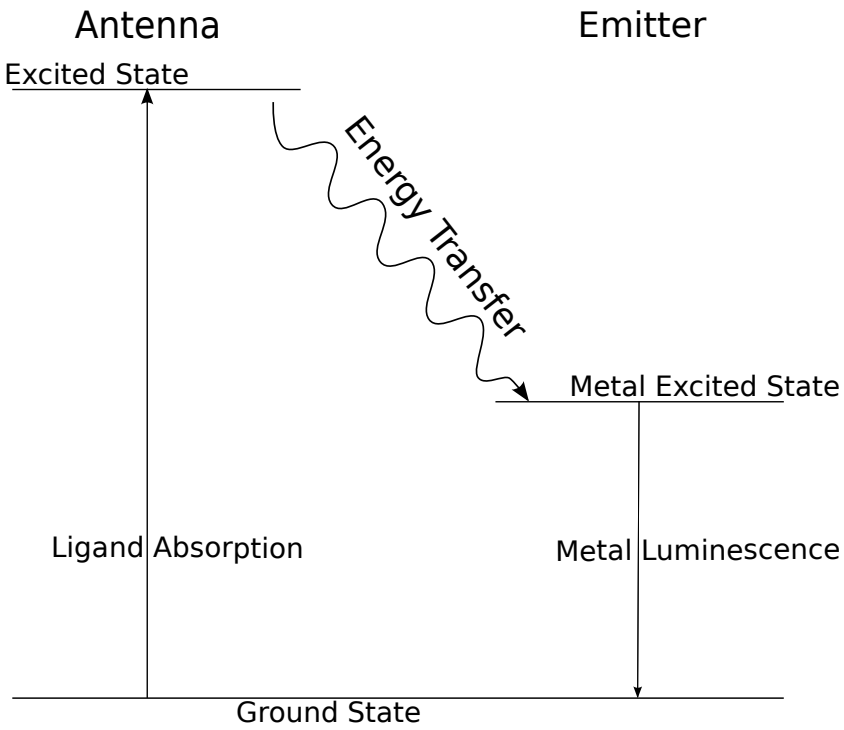

Figure 1.13: Jablonski diagram of the antenna effect in ligand to metal charge transfer (LMCT). Adopted from Sabbatini et al. [34].

minescent elements to a hybrid compound is by including luminescent organic species. These compounds show visible luminescence as a result of their intrinsic HOMO–LUMO gap, rather than any donor/acceptor states introduced by dopants. While the luminescence is intrinsic to the organic materials, the specific nature of the emission and excitation are sensitive to the presence of metals and other, non-luminescent, organic species.

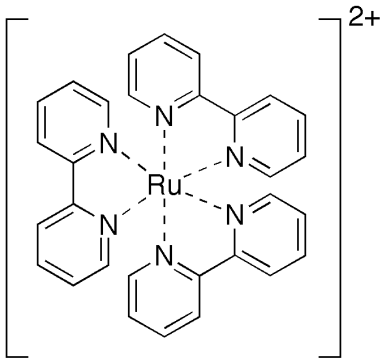

Figure 1.14: MLCT compound tris(2,2-bipyridyl)ruthenium(II) (RuBPY)

1.3 Inorganic-organic hybrid frameworks

The field of hybrid framework research has grown rapidly in the past two decades, resulting in the discovery of materials that exhibit a wide range of structural diversity [35] and physical phenomena [36–39]. They are known alternatively as metal organic frameworks (MOFs), coordination polymers, and inorganic-organic hybrids, but all refer to the same general structure type. The class of materials is most generally defined as displaying bonding between metal atoms by organic ligands with infinite connectivity in at least one dimension. They are, in a way, a partly organic extension of the purely inorganic zeolite structure type [40–42]. Nearly all of these compounds are prepared hydrothermally or solvothermally from mixtures of organic acids and metal salts, which results in an enormous array of topologies and chemical compositions. Hydrothermal synthesis has the additional benefit of often yielding crystal products suitable for structure determination by single crystal X-ray diffraction.

The most studied and well known inorganic-organic framework, MOF-5 [43], is a cubic arrangement of zinc octahedra connected by 1,4-benzene dicarboxylate

ligands. Figure 1.15 shows the cubic topology of the structure and the atomic structure. Extensive explorations for porous framework materials to be used in gas storage and catalysis like MOF-5 [38, 44] have been carried out, but for this thesis the properties of dense framework structures are more applicable. These non-porous compounds tend to show greater thermal and chemical stability than their porous counterparts. Since density and connectivity tend to increase with the synthesis temperature, dense structures also tend to be less hydrated or anhydrous, which contributes to their thermal stability. The work of Forster et al. on cobalt succinates showed that five unique phases could be formed from the same starting mixture simply by varying the temperature of the reaction [45]. When a mixture of cobalt hydroxide and succinic acid in water was heated at 60°C, a 1-dimensional chain structure formed with 4 water molecules per metal atom. Heating to 250°C lead to a 3-dimensional anhydrous structure. That phase shows stability in air up to 320°C [46]. These structures, along with a two dimensional phase formed at 150°C are shown in Figure 1.16.

Framework structures show a remarkable range of structural diversity. The work of Kam et al. on magnesium tartrates described 9 novel structures formed from magnesium and the DL-, D-, and *meso-* forms of tartaric acid [47]. Figure 1.17 shows two examples from that work, a 3-dimensional anhydrous structure synthesized at 200°C, and a 1-dimensional chain structure with three water molecules per magnesium that was synthesized at 125°C. The structures reported follow the same general trend of higher dimensionality, higher density, and lower hydration as the synthesis temperature was increased.

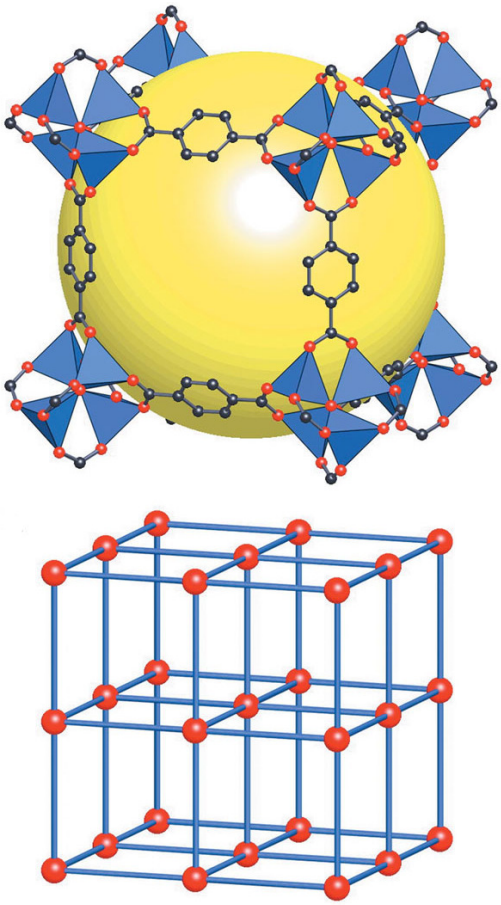

Figure 1.15: TOP: Atomic structure of zinc benzenedicarboxylate (MOF-5) with zinc tetrahedra in blue, oxygen in red, carbon in black, and the pore space represented by the yellow sphere. BOTTOM: Topological cubic network of MOF-5. From [38]

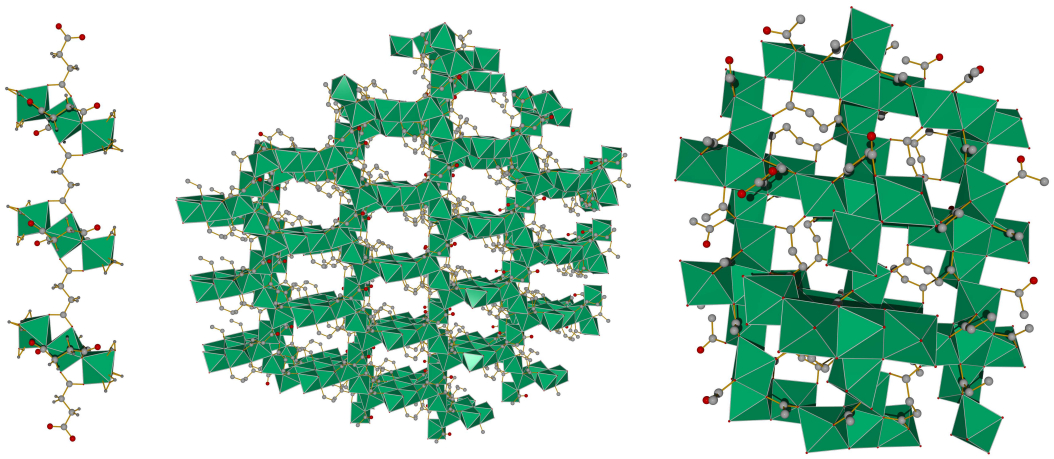

Figure 1.16: LEFT: 1-dimensional chain structure of cobalt succinate formed at 60°C. CENTRE: 2-dimensional structure of cobalt succinate formed hydrothermally at 150°C from the same starting mixture. RIGHT: 3-dimensional dense anhydrous structure formed at 250°C. From [45].

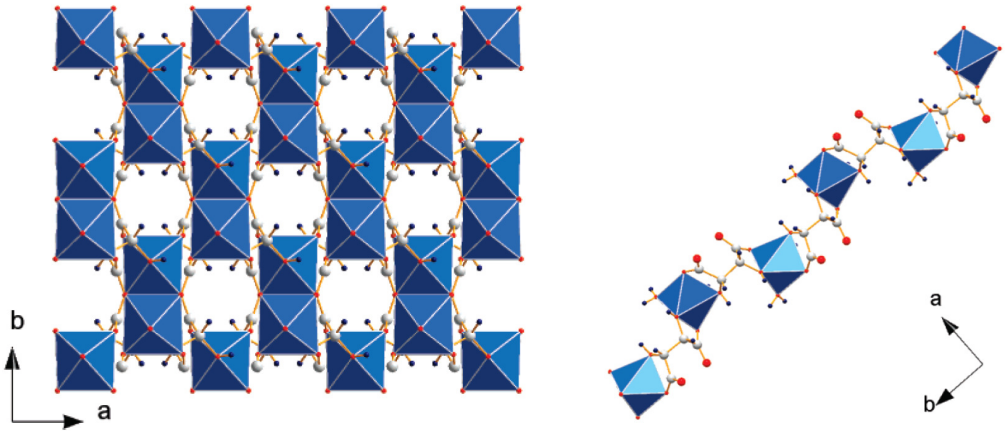

Figure 1.17:]

LEFT: 3-dimensional anhydrous framework structure Mg(*meso*-tartrate). RIGHT: 1-dimensional structure Mg(*meso*-tartrate)$(H_2O)_2 \cdot H_2O$. From [47].

1.4 Hybrid frameworks as phosphors

Much research has been carried out on purely organic luminescent materials for use in organic LEDs (OLEDs) and other applications, but they tend to be highly sensitive to moisture and temperature. Inorganic phosphor materials can show high quantum yields, but also often require high temperature processing and expensive starting materials. Presented here is an intermediate approach to phosphors for solid state lighting, combining some of the properties of both inorganic and organic systems in a single structure. These hybrid frameworks are typically more temperature and moisture stable than organic materials and may have certain advantages over purely inorganic systems. It is thought that hybrids may be more compatible with the polymer encapsulants used in LED device packaging because of their organic content. Also, because hybrids are formed hydrothermally, they can be synthesized at significantly lower temperatures than inorganic phosphors, which avoids the environmentally unfriendly solvents used in organic synthesis and may make nanoparticles more accessible. Small particles should increase device efficiency by reducing light scattering and more evenly covering the emitter chip. Circularly polarized luminescence has also been reported from framework structures containing chiral ligands [48]. Finally, highly luminescent phosphor materials can be made without the use of rare earth or other exotic and expensive metals. The compounds that will be described in Chapters 5 and 6 contain only carbon, oxygen, hydrogen, and common metals like calcium and zinc.

A review by Allendorf et al. profiled hybrid structures for luminescence, listing potential applications as sensors, scintillators, and non-linear optical materials [49]. Solid state lighting was not discussed as a potential application, probably

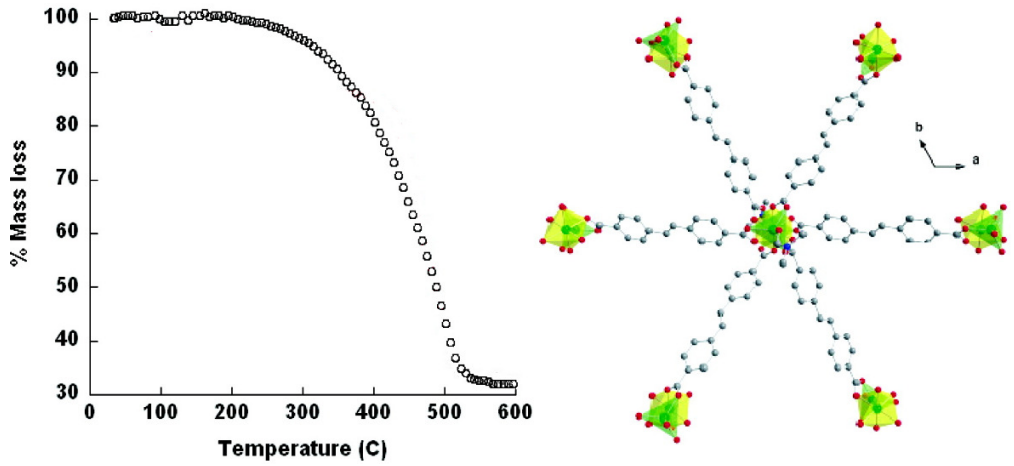

Figure 1.18: Zinc-stilbene dicarboxylic acid luminescent framework. RIGHT: Crystal structure. LEFT: Thermogravimetric analysis, showing stability in air up to approximately 250°C. From [50].

because very few luminescent inorganic-organic papers give details of the excitation and quantum yield data that is a critical parameter for lighting efficiency. From the same research group, a zinc-stilbene framework was reported in 2007 by Bauer et al. [50]. Shown in Figure 1.18, the compound is a 2-dimensional network of tri-nuclear zinc units linked by *trans*-stilbene dicarboxylic acid. Because the system is anhydrous, it is stable in air up to around 250°C. This would make it a good system for lighting applications, but the photoluminescent emission from the compound is centred near 440 nm, almost the same as the light colour available in from GaN LEDs.

The luminescent processes outlined in Section 1.2 were first described for 0-dimensional coordination compounds. These can be thought of as the molecular analogues of extended inorganic-organic frameworks, or alternatively, coordination compounds are the monomers that form extended coordination polymers. Coordination compounds have been studied for decades and find uses in biological

systems, organic LEDs, and sensors [51]. It is expected that the LMCT, MLCT, and direct excitation processes known in molecular coordination complexes should occur similarly in multidimensional hybrids.

Ligand-based emission, where closed-shell metals act to stabilize an intrinsically luminescent organic, is less commonly reported. This is the process occurring in the zinc-stilbene system mentioned above. A few hybrid structures showing this type of ligand-centred luminescence have been described in the literature [52–60], but all of them report excitation wavelengths in the far UV and emission wavelengths in the near UV and blue. Since a large portion of the emission lies out of the visible range, such materials are clearly not suitable for solid state lighting applications. It is expected that placing organic chromophores in a covalently bonded and highly ordered extended framework structure will give rigidity to the organic molecules. This should lead to higher luminescent efficiencies than those found for a hydrogen bonded crystal or cross-linked polymer of the same chromophore.

Chapter 2

Experimental Methods

Specific synthesis procedures will be discussed in subsequent chapters, but some common techniques and general procedures that occur throughout are outlined here.

2.1 Hydrothermal Synthesis

The inorganic-organic framework compounds described in this thesis are prepared under hydrothermal conditions. Stainless steel 23 mL autoclaves with a polytetrafluoroethylene (PTFE) liner are used, as shown in Figure 2.1. They are closed systems of fixed volume inside of which an aqueous mixture or slurry is heated. This allows for aqueous mixtures to be heated above 100°C as the autogenous pressure increases the boiling point of the water. The reaction space is thus extended beyond what would otherwise be the upper limit for reactions at ambient pressure. At these elevated temperatures, many organic species become water soluble and the water itself becomes more reactive. Because it is a solvent based reaction, single crystals suitable for X-ray diffraction are often produced. The

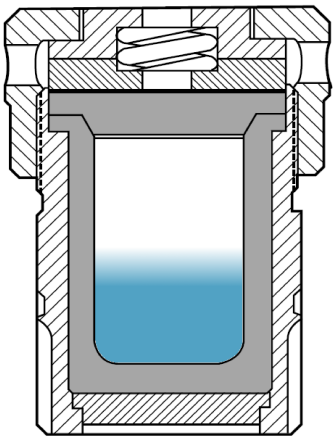

Figure 2.1: Sketch of Parr Acid Digestion Bomb, showing the PTFE liner in gray and the stainless steel pressure enclosure in hatched lines. Image from www.parrinst.com.

maximum reaction temperature is limited by the PTFE liners used to 250°C, above which significant creep occurs, and a maximum pressure limit of 122 atm. An autoclave half full with 6M HCl at 250° produces only 62 atm, only half the limit, but chemical reactions which release vapour can also contribute. A pressure release rupture value allows for relatively safe over-limit protection. In practice for hybrid framework synthesis, reaction temperatures usually limited by the decomposition temperatures of the organic reagents.

In this work, a typical hydrothermal reaction mixture includes 1 mmol of a metal salt and 1 charge balancing equivalent of an organic acid in 5 mL of water, heated for 2 days at a temperature between 100°C and 250°C. Other additions to the reaction mixture included acids and bases to adjust pH, and co-solvents such as dimethyl formamide and isopropanol. The main variables in the reaction include metal source, time, temperature, pH, fill volume, reactant stoichiometry and total concentration. Solid products were recovered by vacuum filtration and washed

with water and acetone to remove any excess reagents. In the case of very small particles, products were recovered by centrifuge. Some exploratory reactions were also carried out by microwave rather than conventional heating.

2.2 Diffraction in periodic structures

Diffraction of light can occur in periodic structures due to constructive and destructive interference. Bragg's law defines the scattering angles where constructive interference of monochromatic light will occur after interacting with a crystal lattice such that:

$$n\lambda = 2dsin\theta \tag{2.1}$$

where n is a positive integer, λ is the wavelength of the incident light, d is the periodic interval between lattice planes, and θ is the angle between the incident light and the lattice plane. To probe the structure of crystalline materials, X-ray light is often used, as its wavelength is on the order of the inter-atomic spacings.

The basic repeating unit of a periodic crystal is the unit cell, typically defined by lattice vectors **a,b,c**, or as a solid with edge lengths a, b, and c, and angles α, β, and γ. Planes in a periodic crystal are defined in terms of their miller indices hkl, which are independent of Cartesian coordinates and instead dependent upon the unit cell dimensions. For the simple case of a cubic structure, where $a = b = c$ and $\alpha = \beta = \gamma = 90°$, the spacing d for between adjacent planes with the indices hkl is equal to:

$$d_{hkl} = \frac{a}{\sqrt{h^2 + k^2 + l^2}} \tag{2.2}$$

and more generally:

$$\left(\frac{h}{a}\right)^2 d_{hkl}^2 + \left(\frac{k}{b}\right)^2 d_{hkl}^2 + \left(\frac{l}{c}\right)^2 d_{hkl}^2 = 1 \tag{2.3}$$

This allows the conversion from the Cartesian a, b, c parameters to internal coordinates.

The lattice is also often described in reciprocal space, which is defined as a transform of the real space lattice. New lattice vectors $\mathbf{a}^*$, $\mathbf{b}^*$, and $\mathbf{c}^*$ are defined by cross-products of the scattering vectors such that:

$$\mathbf{a}^* = \frac{b \times c}{a \cdot (b \times c)} \tag{2.4}$$

$$\mathbf{b}^* = \frac{c \times a}{a \cdot (b \times c)} \tag{2.5}$$

$$\mathbf{c}^* = \frac{a \times b}{a \cdot (b \times c)} \tag{2.6}$$

This construction is useful because the positions of the diffracted intensity are defined most directly in reciprocal space.

The constructive interference in Bragg diffraction occurs because of the path length travelled by the incident light to multiple planes with the same hkl value is equal to some integer multiple of its plane spacing d. Thus knowing the basic repeating unit cell of a structure allows one to calculate all of the incident light angles at which constructive interference should occur by calculating the d spacings for all possible hkl planes. This only predicts the position of the Bragg peaks in a scattering experiment, however. The intensity of the scattering is determined by the contents of the unit cell. For X-ray scattering, where the interaction with the material occurs in the electron shells, the number of electrons on an atom de-

termines how strongly the incident light will be diffracted. For instance, lead and bismuth will scatter many more X-rays than carbon and nitrogen. Thus if the hkl plane contains mostly light atoms, its diffracted intensity will be less than that of a plane containing heavy atoms. This scattering factor of an atom is defined as f_j The structure factor F, which determines the scattering intensity from a plane, is defined as the sum of the products of the scattering factor and their phase factors:

$$F = \sum_j (f_j \times phasefactor) \tag{2.7}$$

$$F_{hkl} = |F|e^{i\phi} = \sum f_j e^{2\pi i(hx+ky+jz)} \tag{2.8}$$

where ϕ is the phase of the scattered intensity and xyz are defined in Cartesian coordinates. It can be seen from this relationship that intensity decreases as hkl increases, and that it is linearly dependent upon the scattering factors f_j. Intensity can further be reduced by symmetry within the unit cell, which results in partial or total destructive interference where there should otherwise be Bragg scattering. This is known as a systematic absence and can be used to determine crystal symmetry in an unknown system. Finally, the observed intensity is subject to a number of instrumental and thermal corrections. This is summarized by the equation:

$$I_{hkl} = sLpF_{hkl}^2 \tag{2.9}$$

where for a reflection hkl, its intensity given by I is the product of a scale factor s, a geometrical correction L, a polarization correction p, and its structure factor F_{hkl}.

2.3 Single crystal X-ray diffraction

The atomic structures of novel compounds were determined by single crystal X-ray diffraction. This is a technique in which a single crystal, typically with a size between 0.1 mm and 1 mm, is exposed to a focused, monochromatic X-rays. The beam interacts with the electron shells of the constituent atoms and a small amount of it is diffracted in a predictable, well defined direction as described above. Figure 2.3 shows a representative diffraction image with well defined spots. The position of each spot reflects the plane spacing d as defined by its hkl value. For powder diffraction, these spots would be extended into rings, retaining d-spacing information but losing specific hkl identity. This diffracted intensity, is collected on a 2-dimensional charge-coupled device (CCD) mounted on a goniometer that rotates through ω. Multiple data sets are collected by rotating the crystal in ϕ and then moving the CCD through the same ω range. A typical single crystal instrument is shown in Figure 2.2, with the X-ray source at right, crystal at centre and detector at left.

A unit cell is determined computationally using SAINT [61] using peaks that are identified in the CCD exposure. The reciprocal lattice vectors are computed relating to each peak, differences vectors are generated from those lattice vectors. The most frequently occurring difference vectors are assumed to be the lattice basis vectors, and this is used to define an orientation matrix that translates between the physical position of the crystal on the instrument and the crystallographic axes. Based on these values, the positions of expected hkl peaks can be calculated and improved by iterative least squares refinement. Once a suitable unit cell is determined, the intensities measured by the CCD exposures are assigned to hkl reflections. This is performed by constructing a box in reciprocal space where a peak in

Figure 2.2: Photograph of a typical single crystal diffraction instrument, with the source shown at right and the detector left. The position of the detector is rotated around the goiniometer to collect a hemisphere of data.

scattering intensity should exist based on the unit cell and integrating the counts from the ccd over that area, subtracting out for background intensity. These intensities are adjusted empirically for absorption effects using SADABS [62], which corrects for the path length differences through a non-spherical crystal. This step is performed by calculating what the expected intensities should be for each peak and then comparing them to the range that is observed. Trends in the error of observed intensity are correlated to the position of the crystal on the instrument, resulting in a list of corrected hkl and intensity values. A space group, which describes the symmetry of the unit cell contents is then determined by identifying systematic absences in those hkl intensities.

The so called “phase problem” in diffraction arises because that transformation requires knowledge of both the amplitude and phase of the scattered wave. In the scattering factor (Equation 2.8), the scattering includes an amplitude and a phase

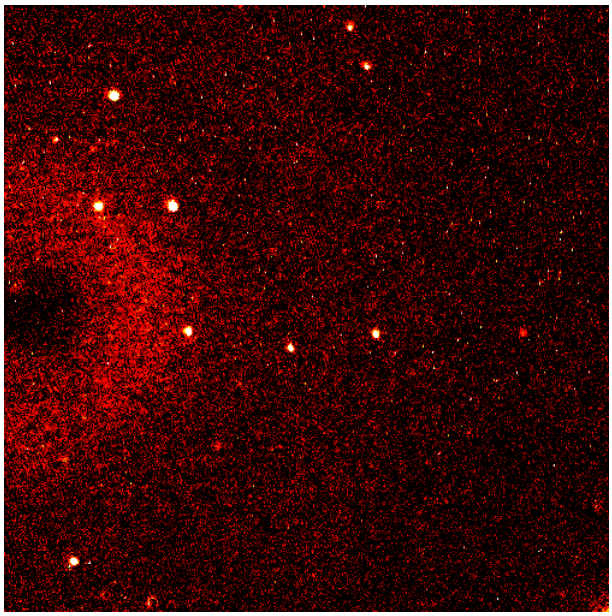

Figure 2.3: A single ccd frame of single crystal diffraction shows bright spots (white) on a diffuse background (red). d-spacing is measured radially from a point at the centre of the left edge

component. The CCD cannot measure this phase angle, however, and instead the data collected is related to the structure factor squared, where no phase information is retained. In these systems, the phase problem is overcome by a largely brute force computational method. Using "direct methods," as implemented by SHELX [63], random phases are assigned to each intensity value and a reciprocal space map of points is calculated by Fourier transform. Direct methods works well where most of the atoms are of similar scattering factor and are relatively evenly distributed throughout the unit cell [64]. The measured values of $|F_{hkl}|^2$ are normalized by the scattering power of the atoms f to form normalized factors E_{hkl}:

$$|E_{hkl}|^2 = \frac{|F_{hkl}|^2}{\epsilon \sum_n f_n^2} \tag{2.10}$$

where ϵ is a normalization factor dependent upon the laue group symmetry of the structure. The Sayer probability relationship is used where S(hkl) is the sign of E_{hkl}:

$$S(hkl) \approx S(h', k', l') \cdot S(h - h', k - k', l - l') \tag{2.11}$$

using $\approx$ to mean "probably equal" to the product of the sign of some normalized factor $E_{h'k'l'}$ and the sign of those indicides subtracted from hkl. This "probably equal" goes as:

$$P = \frac{1}{2} + \frac{1}{2} tanh \left(\frac{1}{N} E_{hkl} \cdot E_{h'k'l'} \cdot E_{h-h',k-k',l-l'} \right) \tag{2.12}$$

Thus the signs of the first few strong reflections are randomly assigned and then the signs of the rest of the peaks are assigned according to these rules. The random sets are repeated and evaluated based on self-consistency of the subsequent assignments.

The initial structure solution is then refined by a least squares method. The Fourier transform is generated of the atomic model to create a reciprocal space map. This map is subtracted from the observed data, resulting in a difference map. Large residual peaks can be assigned to atoms based on chemical knowledge of the system, and the position of all of the atoms is refined iteratively using small steps to reduce the any residual differences between the observed and calculated. An atomic displacement parameter U is also refined for each value, modelling the spread in peak shape from the theoretical delta function due to thermal and other atomic motion. U is defined as the mean-squared displacement in Å. For high resolution data, the atomic displacement can be defined anisotropically as 6 tensors U_{ij} where i and j = 1,2,3.

The quality of the refinement is determined by the residual error that is de-

scribed as R1:

$$R1 = \frac{\sum ||F_o| - |F_c||}{\sum |F_o|} \tag{2.13}$$

where F_o are the observed structure factors and F_c are the calculated. In practice, a weighted parameter based on F^2 is used, wR_2:

$$wR_2 = sqrt \sum [w(F_o^2 - F_c^2)^2] / \sum [w(F_o^2)^2] \tag{2.14}$$

where w is a weighting parameter. The goodness of fit (GooF) is also calculated as:

$$GooF = \sqrt{\frac{\sum [w(F_o^2 - F_c^2)^2]}{n - p}} \tag{2.15}$$

where n is the number of hkl reflections and p is the number of refined parameters in the model and ideally approaches 1 when the error becomes small.

The model for least squares refinement contains position and atomic displacement parameters for each atom. However, restraints are sometimes added to the least squares refinement to keep some of the atoms in chemically relevant positions if they are not in statistically stable positions. For instance, hydrogen atoms, which diffract very weakly and cannot always be located in the residual diffraction data, are often restrained by setting a fixed distance and/or angle from a neighbouring atom.

2.4 Powder X-ray diffraction and Rietveld analysis

X-ray diffraction experiments can also be performed on finely ground powders. While this typically does not provide enough information to determine an unknown crystal structure, it tends to outperform single crystal experiments in terms

of impurity phase identification, refinement of lattice parameters, and atomic positions. This is in large part because the resolution of peak positions can be improved over that shown in Figure 2.3, the statistical error resulting from identifying the orientation of a single crystal is removed, and absorption effects from differing path lengths through the crystal are eliminated. The spots that would be collected for a single crystal instead become rings, and a trace in d space along those rings lead to a intensity/d-space powder diffractogram. In practice, intensity/2θ is typically plotted. In a sample of finely ground powder, it is assumed that if there is a set of Bragg planes that could be oriented to diffract at that incident angle of light, then some sample of crystallites will be correctly oriented. As before, the peak positions are determined by the unit cell dimensions and the peak heights are determined by crystallographic symmetry and atomic scattering factors. The peak shape profiles for powder diffraction data can be carefully measured and used to reveal chemical information about the sample. Theoretically, Bragg scattering at 0 K should result in delta function peaks. These peaks are broadened by thermal motion, instrumental parameters, lattice defects, lattice strain, and crystallite size.

Rietveld refinement is a total pattern matching means of evaluating and improving a crystal model to powder diffraction data. A peak position, height, and shape is calculated for each hkl reflection given the starting unit cell, atomic position data, crystal symmetry, and a peak shape function. An intensity correction parameter K_{ph} is used such that:

$$K_{ph} = \frac{E_{ph} A_h O_{ph} M_p L}{V_p} \tag{2.16}$$

where E_{ph} is an extinction correction which takes into account how deeply the incident light penetrates the sample, A_h is an absorption correction, taking into account absorption of X-rays by the sample, O_{ph} is preferred orientation which

corrects for any systematic ordering of the crystallites, M_p is the reflection multiplicity and L is an angle dependent intensity correction that is dependent upon the light source, and V_p is the unit cell volume. The peak shape profile in this work is modelled empirically as the sum of a Gaussian and a Lorentzian with both angle-dependent and angle-independent parameters, known as a pseudo-Voigt function. The intensity at a given angle 2θ around an hkl peak with intensity I_{hkl} will be:

$$I(2\theta) = I_{hkl} \cdot [\eta L(2\theta - 2\theta_o) + (1 - \eta)G(2\theta - 2\theta_o)] \tag{2.17}$$

where $2\theta_o$ is the position of the expected hkl peak, and L and G are Lorentzian and Gaussian functions.

The peak shapes for all of the hkl values and a background function are thus calculated and refined in a least squares manner, as described above, to the measured intensity values. Individual parameters in the model are alternatively allowed to refine or are fixed until some convergence is reached. The least squares refinement proceeds based on a minimization function M, based on the difference between observed and expected intensities and residual error is reported as χ^2 where:

$$M = \sum w(I_o - I_c)^2 \tag{2.18}$$

$$\chi^2 = \frac{M}{N_{obs} - N_{var}} \tag{2.19}$$

where I_o is the observed intensity, I_c is the calculated intensity, w is a weighting parameter, N_{obs} is the total number of observations, or data points, N_{var} is the number of parameters being refined in the model, and M is the minimization function. For a powder diffraction Rietveld experiments where χ^2 is defined in this way, the values approach 1 from above and anything below 5 is considered to be a very good fit.

2.5 Synchrotron single crystal diffraction

Typical lab sources for single crystal diffraction are X-ray tubes with copper or molybdenum targets. The molybdenum Kα_1 and Kα_2 lines together provide 0.7107 Å X-rays which are generally preferred to the longer wavelength CuKα for large unit cells as it moves the spots closer together. However, the X-ray flux from these lab sources is limited and thus long counting times and high quality crystals must be used. Beamline 11.3.1 on the Advanced Light Source at Lawrence Berkeley National Laboratory provides high brightness X-rays for single crystal diffraction. The endstation of the beamline is a commercial goiniometer and CCD detector, much the same as a lab source diffractometer, but the X-ray tube is replaced with a synchrotron ring. The beamline provides a flux of 1×10^{11} photons/s/0.01%BW at 10 keV, at a wavelength of 0.77490 Å, about five orders of magnitude brighter than a typical lab X-ray source. Figure 2.4 shows the average spectral brightness of lab and synchrotron sources with the lab source marked with a blue dot and the synchrotron marked with a red dot. Light comes off the ring and is passed through a Si(111) monochromator, then focused using a toroidal mirror, passed through a beryllium window and through a final set of focusing slits before reaching the sample. These high brightness, highly monochromatic X-rays allow for samples with an edge lengths as short as 10μm to be analysed where a standard lab source would require crystal edge lengths longer than 100μm. The very sharp X-ray spectra also allows for structures to be more successfully determined from crystals with imperfections or twinning since the split peaks can be resolved.

2.6 Synchrotron X-ray powder diffraction

Powder diffraction data to confirm bulk phase homogeneity was collected for some samples at the Argonne National Laboratory Advanced Photon Source beamline 11-BM and on a Bruker D8 advance with a copper source. The synchrotron beamline uses a bending magnet operating at 7 GeV and the final incident energy is between 15 and 35 keV, corresponding to a wavelength of 1.0 to 0.34 Å. Each run is calibrated using a cerium standard to determine wavelength and peak shape profiles. The beam is passed through a Si(111) monochromator and two focusing mirrors before reaching the sample. Detection of diffracted intensity is performed by 12 Si(111) analyser crystals with $LaCl_3$ scintillation detectors, enabling high speed collection of data without loss of resolution or quality. This high peak resolving power makes small impurity phases visible that might otherwise be hidden underneath overlapping peaks or mistaken for mis-assigned intensity.

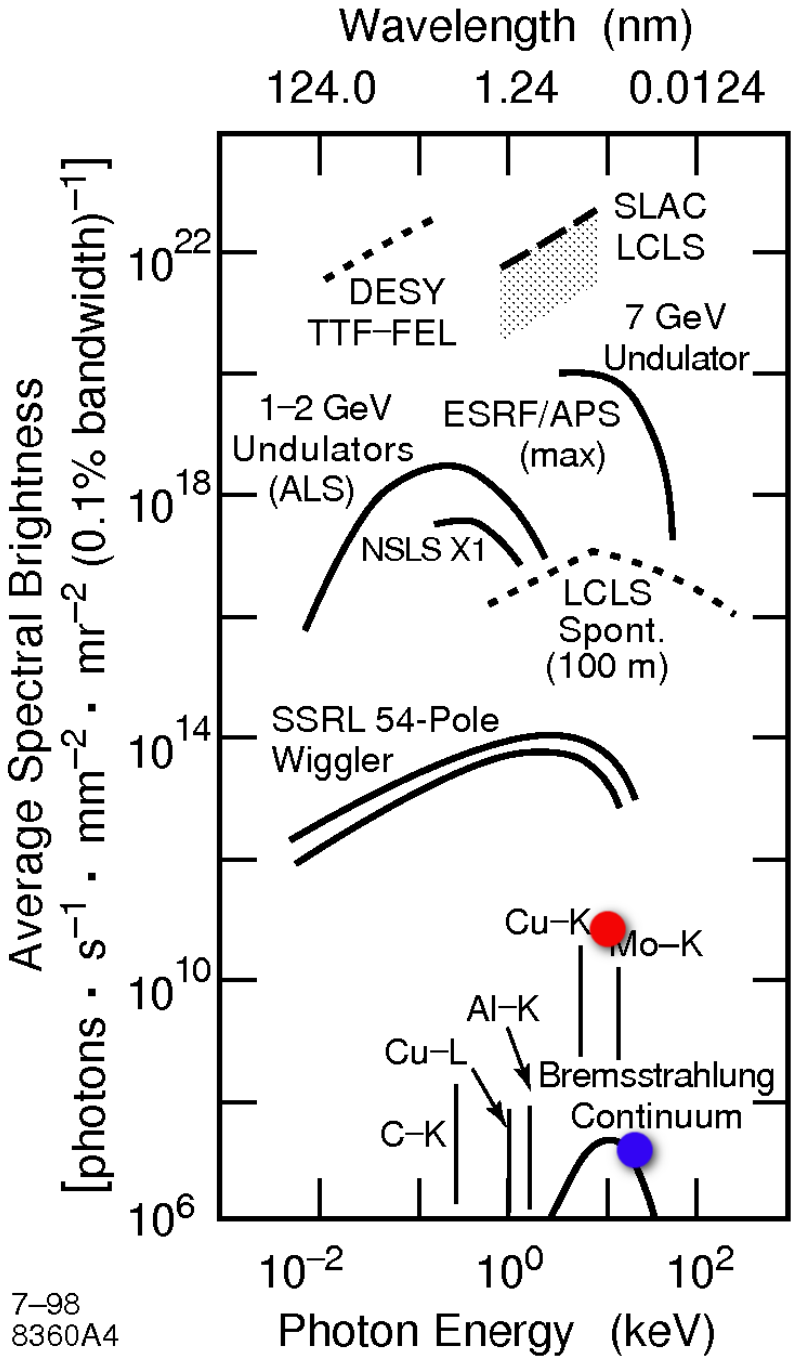

Figure 2.4: Average spectral brightness of lab and synchrotron X-ray sources. A typical Mo lab source is marked in blue, the brightness of ALS 11.3.1 is marked in red, and the brightness of 11-BM in green. From http://www.slac.stanford.edu/.

2.7 Photoluminescence spectroscopy

One of the primary considerations for the evaluation of phosphor materials is the wavelengths of light at which they can be excited, and the wavelength light that they emit. This is measured with a photoluminescence spectrometer, or PL, and the data consists of two sets: the excitation and the emission. A photoluminescence excitation spectra is a measure of what wavelengths of light can be used to generate a single emission frequency, and what the intensity of that emission is. Similarly, a photoluminescence emission spectra contains the wavelengths of light and their emission that are generated by excitation with a single wavelength.

The instrument used in these experiments uses a broad spectrum white light source, typically a xenon lamp. The light from this lamp is passed through a diffraction grating monochromator (M1) to select a single wavelength from the white. This single colour is then passed through slits to control the amount of light reaching the sample. Finely ground powder samples were mounted behind a quartz window that is transparent within the range of wavelengths investigated. After light reaches the sample, some of it is reflected and some will be (potentially) converted to the photoluminescence emission colour. This is passed again through a set of slits, a second monochromator (M2) to select the emission colour to be studied, and collected by a photomultiplier tube (PMT). The PMT converts the incident light flux to a voltage that can then be measured. Thus the path of the light goes from the lamp→M1→slits→sample→slits→M2→PMT. Harmonics of the incident light are naturally generated by the diffraction gratings, and thus a long-pass filter is sometimes inserted before the PMT if needed.

Thus for each data point there is an excitation wavelength, set by M1, an emission wavelength, set by M2, and a intensity as measured by the PMT. In

practice, to collect an emission spectra, the incident monochromator M1 is fixed at a single wavelength and M2 is swept through a range of wavelengths, while for an excitation scan, the M2 is fixed and M1 is swept through a range of excitation wavelengths.

2.8 Time-dependent photoluminescence spectroscopy

The methods explained above for PL spectroscopy are steady-state measurements and take no consideration of the rates in which these excitation and emission processes occur. Time-dependent measurements, for instance to show the rate of radiative decay, can be measured using fast laser pulses and highly sensitive detectors. For instance, the photoluminescence decay curves that will be described in detail in section 3.2.4, used excitation pulses of approximately 100 fs and a PMT system sensitive to single photon events. Monitoring these decay rates can give information about how many radiative recombination pathways exist, and the speed of those recombinations.

Time correlated single photon counting (TCSPC) is an experimental approach that allows the monitoring of fluorescent decay at sub-nanosecond resolution. A laser pulse of several hundred femptoseconds is used to excite a luminescent sample. Collecting the actual luminescence decay would be rather difficult experimentally, and this is overcome by a digital counting technique. For each laser pulse cycle, a single emitted photon is collected. The time from the laser pulse to the collection of a photon is measured. This excitation cycle is repeated millions of times and a histogram of collection events is created, binned by time. The method relies

on the fact that the probability distribution of individual photons is equivalent to the actual time distribution photon emission from the sample. Consequently, the histogram is equivalent to, and can be used as, a intensity versus time plot. In TCSPC, resolution is limited by the peak widths of the excitation, detector, and electronic system time jitter such that:

$$\tau_{min} = \frac{1}{10}\sqrt{FWHM^2_{source} + FWHM^2_{detector} + FWHM^2_{jitter}} \tag{2.20}$$

When only a single radiative decay process is involved, the emission intensity decreases mono-exponentially according to:

$$I_t = I_o e^{\frac{-t}{\tau}} \tag{2.21}$$

where I_t and I_o are the intensities of the emission at time t and at initial time t_o, respectively, and τ is the lifetime of the luminescence. The lifetime τ is the time when the population of the excited state has decreased to $\frac{1}{e}$ ($\sim$37%). If there are two processes involved, the emission intensity decreases bi-exponentially according to:

$$I_t = I_1 e^{\frac{-t}{\tau_1}} + I_2 e^{\frac{-t}{\tau_2}} \tag{2.22}$$

where I_1 and I_2 are the intensities of the emissions of the different processes at t_o, and τ_1 and τ_2 are the lifetimes of each process, and so on for multiple pathway systems.

Excited states return to the ground state by both radiative and non-radiative processes, thus two decay rates $\tau_{non-rad}$ and τ_{rad} can be considered such that:

$$\frac{1}{\tau_{total}} = \frac{1}{\tau_{non-rad}} + \frac{1}{\tau_{rad}} \tag{2.23}$$

2.9 Thermogravimetric analysis

Thermogravimetric analysis monitors the weight loss of a sample as its heat is slowly increased. The system consists of a microbalance inside of a furnace. For hybrid materials, this provides an gauge of sample purity as the mass of the percentage weight loss for the final decomposition product can be readily calculated and compared to the measured value. Typically a mixed metal-organic system will decompose in an oxidizing environment to the most stable oxide of that metal. Additionally, by heating slowly, the temperature at which adsorbed and bound water molecules are removed from the sample can be identified and quantified, and the specific decomposition temperature of the organic components can be identified as well.

Chapter 3

Inorganic phosphor nanoparticles

3.1 Introduction

Yttrium aluminium garnet, $Y_3Al_5O_{12}$, doped with 2% Ce^{3+} (YAG:Ce) converts blue and UV incident light into a broad yellow emission around 550 nm. The compound was first synthesized in 1967 by Blasse at Philips Eindhoven for use in colour televisions [3, 4]. Bright phosphors with short lifetimes, excitable using electrons from a cathode ray tube, were needed for the new screens. Conveniently, its high brightness when excited in the blue make the compound useful for white LED devices wherein a blue emitting LED is combined with a phosphor layer to generate white light. The compound has been retuned slightly by other small chemical additions to optimize it for solid state lighting applications and it is the phosphor material found in most commercially available white LEDs today. The emitting ion, Ce^{3+} has a $4f^1$ configuration with a doublet F ground state ($^2F_{\frac{5}{2}}$ and $^2F_{\frac{7}{2}}$). The Ce^{3+} transition from an excited $5d$ level to the ^2F ground states account for the luminescence and the split ground state results in broadened emission at room temperature [65], ideal for lighting applications. A typical excitation

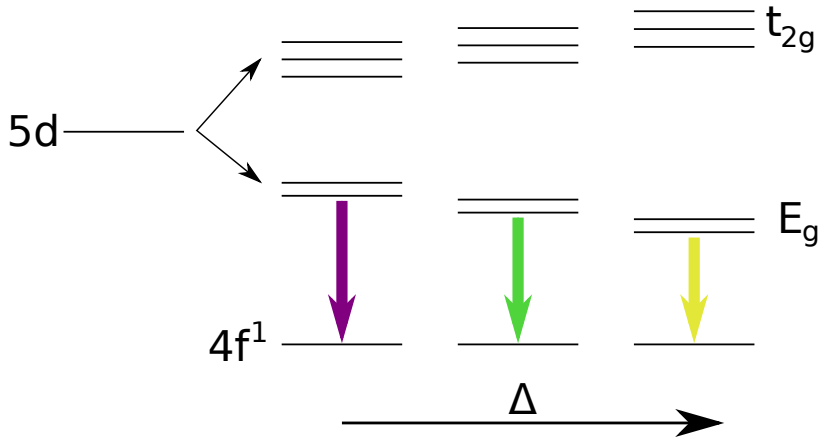

Figure 3.1: $5d \rightarrow 4f^1$ emission processes in Ce^{3+} shown with increasing ligand field splitting. The $4f^1$ level is shielded from most interactions and thus stays at a constant level, while the splitting between the E_g and t_{2g} of the $5d$ level is sensitive to the local environment. The $4f^1$ splitting is omitted for clarity. Adapted from Le Toquin and Cheetham [13].

and emission spectra for YAG:Ce is shown in Figure 3.2. This transition is both spin and parity allowed, resulting in short decay times and high brightness. The participation of the $5d$ energy levels makes the transition sensitive to the crystal field environment [13], and to the symmetry at the Y^{3+} site [29] of the host lattice. This results in a tunable emission colour of the Ce^{3+} ion from the UV to the red. The colour tunability of the Ce^{3+} ion is shown in Figure 3.1. Figure 3.2, shown earlier in Chapter 1 and again here, is a typical emission and excitation spectra for bulk YAG:Ce. It can been seen that the excitation spectra aligns closely with the 440 nm emission from GaN blue LEDs and a broad yellow emission is provided.

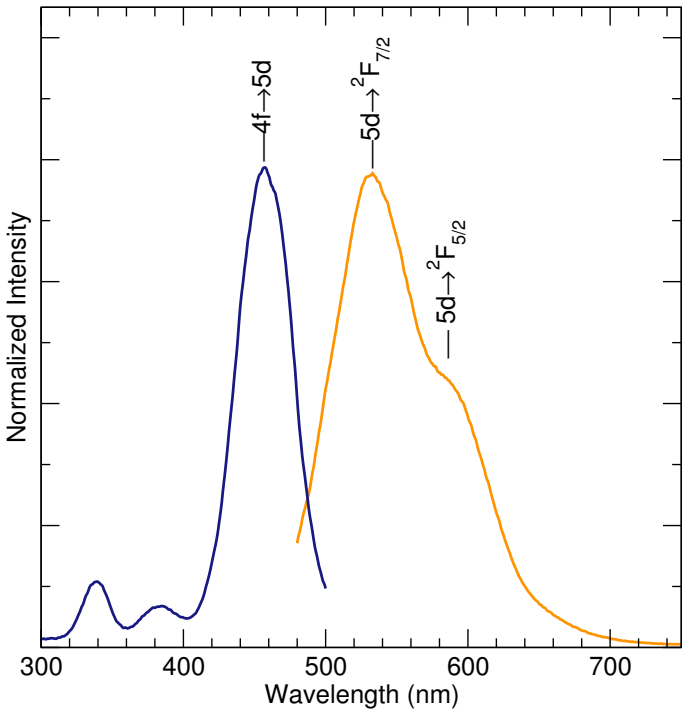

Figure 3.2: photoluminescence excitation and emission spectra for YAG:Ce. λ_{ex}=460 nm, λ_{em}=530 nm. The 4f ground state is split into a doublet of $^2F_{\frac{5}{2}}$ and $^2F_{\frac{7}{2}}$, the transitions to which are both labeled in the emission spectra. Excitations peaks are transitions from the 4f ground state to various 5d levels.

3.1.1 Nanoparticles of phosphors

Presently used lighting phosphors have diameters in the micron range and are typically obtained by spray-pyrolysis [66], sol-gel routes [67], and conventional ceramic methods. Some studies have suggested that the use of phosphors with a diameter smaller than a few hundred nanometres would significantly reduce back-scattering and improve light extraction from LED devices [68–70]. It has also been suggested that reducing particle size will aid in using the phosphor layer more efficiently, as illustrated by Figure 3.3. Conversely, other publications have shown that in practice, reducing particle size leads to a reduction in luminescent efficiency [71]. While it is possible that using smaller phosphor particles will increase

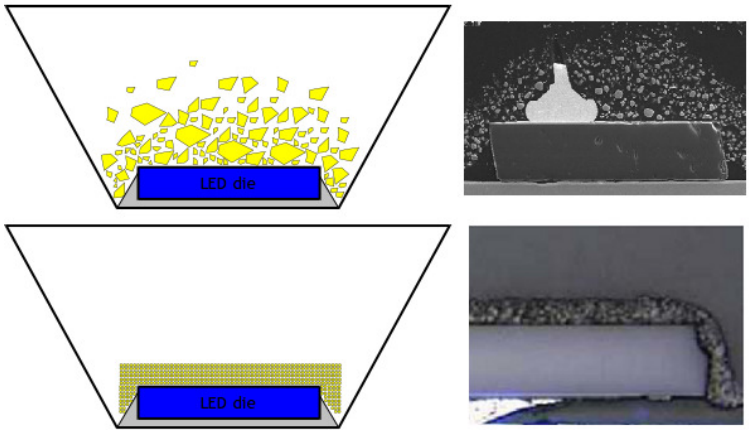

Figure 3.3: TOP: Schematic and cross-section electron micrograph of coarsely milled phosphor particles. BOTTOM: Schematic and micrograph showing how reduced particle size helps in forming a conformal phosphor layer over the emitter. From www.lumileds.com.

total package efficiency, this requires maintaining the bulk luminescent efficiency in the nanoparticles. In an attempt to clarify some of these discrepancies, a study has been performed on YAG:Ce nanoparticles.

There have been many reported synthetic routes to phosphor nanoparticles. Wang and Li prepared $BaAl_{12}O_{19}$ phosphors by reverse microemulsion using polyoxyethylene octylphenol as a surfactant with cyclohexane and water [72]. Zhou, Shi, and Gong prepared the SrY_2O_4:Eu^{3+} phosphor using the same surfactant system [73]. The network forming characteristics of silica gels have been used to form nanoparticles of silicate phosphors such as Zn_2SiO_4:Mn^{2+} [74]. Lou et al. used a surfactant assisted gel growth with tetraethyl orthosilicate (TEOS) to form zinc silicates hydrothermally with a particle size near 100 nm [75]. Wan et al. applied an amine to a precipitation route followed by reaction under mild hydrothermal conditions to achieve luminescent nanoparticles of the same compound at 220°C without further calcination [76].

There are comparatively fewer reports on the synthesis of nanoparticles of YAG:Ce, largely because it requires high calcination temperatures, typically above 1500°C, to achieve highly emissive samples. Nevertheless the number has increased significantly since this work began several years ago due to rising interest in the field [77–82]. Chatterjee et al. prepared $\sim$10 μm spheres of YAG using an emulsion of Span80 and cyclohexane [83]. Caponetti et al. used the surfactant cetyl trimethylammonium bromide (CTAB) in a water/CTAB/1-butanol/n-heptane emulsion to produce YAG:Nd particles $\sim$20 nm in size [84]. Preparations of YAG:Ce nanoparticles by microwave synthesis [85], sonochemical [86], sol-gel [87, 88], co-precipitation [89], and solvothermal [90] methods have also been reported. A novel salted sol-gel and salted sol-gel combustion method was recently reported by Jia [69] in which high yields of dispersible YAG:Ce, $Sr_4Al_{14}O_{25}$:Eu^{2+},Dy^{3+} and $BaMgAl_{10}O_{17}$:Eu^{2+} were achieved with sintering temperatures 400°C to 500°C lower than the reported conventional solid state methods. The degree to which the particles have sintered together during calcination, while critical to gaining the benefits of using nanoparticles, is often not addressed, nor is the quantum efficiency of the luminescence.

The problem that often arises in the processing of inorganic nanoparticles of phosphors is that the temperatures needed to achieve efficient luminescence also lead to particle sintering and ripening. A recent study of YAG:Ce nanoparticles by Su et al. observed an incomplete garnet structure at the surface by high resolution transmission electron microscopy. The proposed that this provides traps for the excited $5d$ electrons, lengthening the decay rate of the excited state and thus quenches radiative emission [91]. Another study on the luminescence of Y_2SiO_5:Ce^{3+} similarly described a change in the radiative lifetime of the cerium ion due to the perturbed electric field at the surface [92]. Jia et al. [93] reported

that the intensity of the photoluminescence emission increased as the nanoparticle phosphor calcination temperature increased. This increase was ascribed to increased crystallinity and subsequent elimination of emission-quenching defects. The low photoluminescence intensity observed in nanoscale samples by Wang et al. [70] was attributed to defects on the crystallite surface and the presence of amorphous phases. In all of these examples the increasing concentration of defects in nanoparticles, both from the increased surface area and from the lower processing temperatures required to prevent sintering, resulted in decreased efficiency.

3.1.2 Emulsion synthesis

An emulsion-based method was used to prepare YAG:Ce nanoparticles in this research. Inverse emulsion syntheses, alternatively referred to as microemulsions, miniemulsions, and nanoemulsions, use surfactants to stabilize aqueous droplets in a non-polar phase [94]. Boutonnet et al. published one of the earliest reports in 1982 on the use of a microemulsion to control the morphology of metal particles reduced from a solution of metal salts [95]. Specifically, emulsions of water/cetyl trimethylammonium bromide/octanol and water/pentaethylene glycol dodecyl ether/hexane were used with salts of platinum, palladium, rhodium, and iridium dissolved in the aqueous phase. Solvent to surfactant ratios were used such that the aqueous phase was surrounded by the hydrocarbon, and thus each droplet of water could independently nucleate metal particles upon reduction with hydrazine or bubbling hydrogen. Using this method they were able to prepare 2 to 5 nm metal particles. Thorough reviews from the Landfester group [96, 97] and a more recent work from Eastoe et al. [98] described the wide range of applications of emulsion methods, from inorganics to metals to polymers, and the

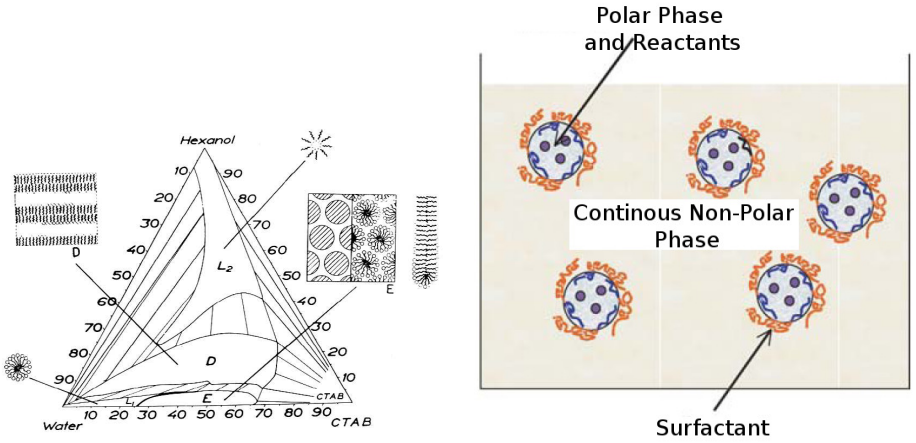

Figure 3.4: LEFT: Ternary phase diagram of the water/hexanol/CTAB system. L1, close to 100% water, indicates the standard emulsion region, while L2, close to 100% hexanol, indicates the inverse emulsion region. RIGHT: Illustration of an inverse emulsion, showing regions of blue aqueous reactants stabilized by orange surfactants in a gray continuous phase [96].

conditions required for the formation of a stable emulsion. In practice, emulsions are typically formed by mixing an aqueous sol of metal nitrates with a solvent and surfactant dispersion. Initially the mixture is biphasic and by applying some form of mixing such as stirring or sonication, self-assembled aggregates form if the ratio of components allows it. A ternary phase diagram showing different regions in the water/hexanol/CTAB system and an illustration of a reverse emulsion are shown in Figure 3.4.

The mechanisms seen in the formation and agglomeration of emulsions were well described in a review by Uskokovic and Drofenik [99]. Most important to our work is that a reagent can be added that diffuses through the continuous phase but only reacts with the dispersed phase. Reactions can then be carried out in the hydrophilic regions of the self-assembled domains. This allows each suspended water droplet in the oil phase to act as an independent reactor and

presumably nucleate an individual particle. Because the droplets are continually colliding, mixing, and reforming, the produced particle size is typically larger than the colloidal dispersion. Nevertheless, it can result in nanoscale particles with a good degree of monodispersity under the proper conditions.

3.1.3 YAG structure

YAG:Ce crystallizes in a cubic garnet structure with space group $Ia\bar{3}d$ and cell edge length 11.99 Å. There is one 8-coordinate Y^{3+} site and two crystallographically distinct Al^{3+} sites, one octahedral and the other tetrahedral. The Ce^{3+} dopants displace yttrium atoms and a maximum in emission intensity is seen from approximately 2% substitution, increasing beyond which leads to concentration quenching via cross-relaxation between cerium atoms. Figure 3.5 shows the crystal structure of YAG, and the individual networks of its constituent metal sites.

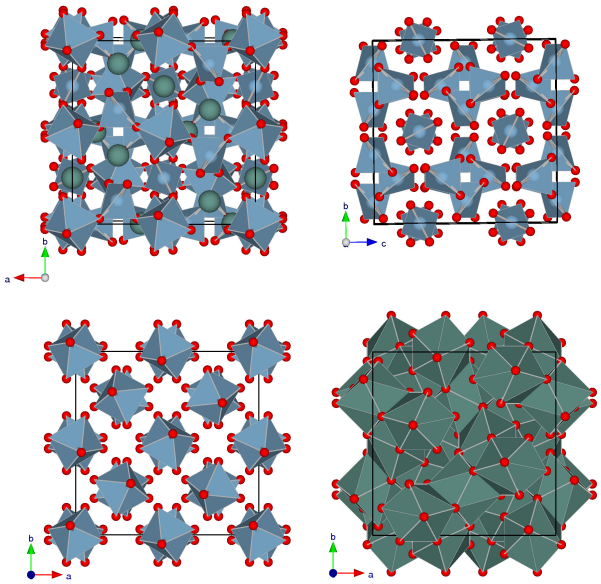

Figure 3.5: Multiple views of the $Y_3Al_5O_{12}$ crystal structure in $Ia\bar{3}d$. TOP LEFT: all atoms, TOP RIGHT: the aluminium tetrahedra, BOTTOM LEFT: aluminium octahedra, BOTTOM RIGHT: the yttrium polyhedra.

3.2 Experimental methods

3.2.1 YAG:Ce nanoparticle synthesis

$Y_3Al_5O_{12}$:2%Ce^{3+} nanoparticles were synthesized by an emulsion-based method, which is a relatively inexpensive and versatile approach that is scalable, avoids the equipment requirements of spray-based approaches, and can give particles of a uniform morphology. The aqueous phase was prepared by dissolving $Y(NO_3)_3{\cdot}(H_2O)_6$, $Al(NO_3)_3{\cdot}(H_2O)_9$, and $Ce(NO_3)_3{\cdot}(H_2O)_6$ in a 1:1.67:0.02 molar ratio to form a 0.1 M solution. The pH of the solution was raised to $\sim$3 using ammonium hydroxide. The continuous phase consisted of a 20:1 volume ratio of cyclohexane and sorbitan monooleate (sold commercially as Span80). The two solutions were combined and placed in an ultrasonic bath for 90 minutes, forming

a white, milky emulsion. This was then refluxed in air at 90°C while stirring for 48 h. The emulsion remained stable throughout the reflux. The particles were hydrolyzed by the addition of tetraethyl ammonium hydroxide under vigorous stirring until the pH reached ∼11. A colour change from white to yellow was also observable when the hydrolysis was complete. At this point, the particles were still suspended, but readily separated by centrifugation at 3000 rpm for 15 min. They were washed several times with H_2O and ethanol to remove unreacted starting materials and remaining solvent, then dried in vacuum at room temperature. The products were calcined in air at temperatures between 700°C and 1300°C for 2 h. Several experimental parameters were varied in the course of this study. The continuous solvent phase was replaced with n-hexane and octane. The ratio of surfactant to solvent was changed from 1:40 to 3:40. The temperature of the reflux was varied between 60°C and 90°C, and duration varied from 0 to 72 h. Finally, the hydrolysis of the suspended particles was performed using different bases such as NH_4OH and triethylamine in place of the tetraethylammonium hydroxide.

3.2.2 Pair distribution function

The pair distribution function (PDF) is a total scattering method of analysing the short and medium range order of crystalline and semi-crystalline materials using data from diffraction experiments [100]. Data contained in both the Bragg peaks and diffuse scattering is extracted from high-Q diffraction data and converted from reciprocal space to real space. In this case, data is considered as intensity versus Q (Å$^{-}1$), where Q is the scattering vector and mathematically related to the incident angle θ described earlier for powder diffraction by:

$$Q = \frac{4\pi sin\,(\theta)}{\lambda} \tag{3.1}$$

Because both the Bragg peaks and the diffuse reflections are used, the intensity data is carefully corrected for instrumental parameters. Diffraction data is collected for empty sample holders and for a known standard of CeO_2 to use as a baseline in these corrections. Beyond the instrument parameters, corrections are also made for multiple scattering events and attenuation The extracted data is normalized to generate the structure factors $S(Q)$ and a sine fourier transform is made of the to create a real-space histogram of atom-atom distances, labelled $G(r)$, to which a structural model is refined. $G(r)$ is defined as:

$$G(r) = 4\pi r[\rho(r) - \rho_0] \tag{3.2}$$

$$= \frac{2}{\pi}\int_0^\infty Q[S(Q) - 1]sin(Qr)dQ \tag{3.3}$$

where Q is the scattering vector and r is the atom-atom pair length in Å. In practice the integral is not calculated to infinity, but either some reasonably long length such that all the data under consideration is modeled, or a purposefully shorter one to model small particles. The calculated model from a structure, G_c, is computed as:

$$G_c(r) = \frac{1}{r}\sum_i\sum_j\left(\frac{b_i b_j}{< b >^2}\delta(r - r_{ij})\right) - 4\pi r\rho_o \tag{3.4}$$

For this reason, the fitting has been referred to as "real-space Rietveld" [101]. For these nanoparticles, synchrotron X-ray powder diffraction data were collected in transmission mode at room temperature on beamline 11-ID-B of the Advanced Photon Source, Argonne National Laboratory. Powder samples were loaded into polyaniline tubes, sealed with glass wool and placed vertically in a sample holder in the path of the beam at room temperature, with an experimental set-up similar to that described by Chupas et al [102]. Scattering data were collected with an image plate system (MAR345) and sample-to-detector distances of 970 mm and

305 mm using high energy X-rays (∼90 KeV). Data for Rietveld analysis (970 mm) were collected using single 30 to 100 s exposures, and data for PDF analysis (305 mm) were collected in three exposures of 10 to 60 s. The image plate data were processed using the program FIT2D [103]. The Rietveld method [104] was used to refine the structures and for quantitative phase analysis using the programs XND [105] and the GSAS-EXPGUI [106, 107] suite. The PDF, $G(r)$ [108, 109], was extracted with the program PDFGetX2 [110], using a maximum momentum transfer of $Q = 20$ Å^{-1}. Full structure profile refinements with the PDF data were carried out in the program PDFFIT2 and PDFgui [111]. A bulk cubic ceria standard provided an effective wavelength of $\lambda \approx 0.1368$ Å for refinements as well as instrument parameters for PDF analysis.

Correlated motion of atom-atom pairs also has an impact on the peak shapes in extracted pair distribution functions. The more closely correlated the atoms, the sharper the PDF peak, in a way similar to, but more complex than thermal atomic displacement effects. This generally makes the correlated motion peak impact dependent upon r, but it also can be used to reveal local structure information. The calculated G_c above is convolved with a gaussian distribution that includes a correlated motion term Q_σ, isotropic atomic displacement parameters, as well as a scale factor.

3.2.3 Optical characterization

Photoluminescence measurements were carried out at room temperature using a Perkin Elmer LS55 fluorescence spectrometer.

Emission quantum yield (QY) measurements were performed on finely ground powder samples mounted in silicone resin on optical quartz substrates. A Lab-

sphere integrating sphere with excitation light from a Spectraphysics Beamlok 2060 line tuneable CW argon-ion (Ar^+) laser at 363 nm was used to illuminate the samples. The experimental setup is similar to the one described in a paper by Greenham et al [112]. The light exiting the sphere passed through appropriate coloured glass or interference filters. Emission was detected using a Newport UV-818 calibrated Si photodiode, amplified with a Stanford Research Systems SR570 and measured using a Keithley 195 digital multimeter.

3.2.4 Time resolved luminescence

Fluorescence lifetime measurements were performed using the Time Correlated Single Photon Counting (TCSPC) technique [113]. Excitation pulses of approximately 100 fs with a wavelength tunable from 360-470 nm were generated using a frequency doubling β-barium borate crystal in combination with a Spectra-Physics Tsunami mode-locked Ti-sapphire laser. The laser repetition rate was reduced to 2 MHz using an acousto-optical pulse picker to avoid chromophore saturation. The TCSPC system was equipped with a Hamamatsu R3809U-51 ultrafast microchannel plate photomultiplier tube detector and a Becker & Hickl SPC-630 counting module, providing a response time $\leq$50 ps. The triggering signal for the TCSPC board was generated by sending a fraction of the laser beam to a Si photodiode. The fluorescence spectrum was monitored using a Roper Scientific PIXIS-400B CCD camera equipped with an Acton Research SP300 monochromator and an ALP long-pass filter. Fluorescence transients were not deconvolved from the instrument response function since their characteristic time constants were much longer than the width of the system response to the excitation pulse. Variable temperature measurements were performed using a liquid nitrogen cryostat with temperature controller down to 77 K or a heating stage up to 500 K.

3.3 Results

Samples of $Y_3Al_5O_{12}$:2%Ce^{3+} (YAG:Ce) were prepared for synchrotron X-ray analysis. Precursors were prepared using an emulsion of water, cyclohexane and Span80, and calcined at 700, 1000, and 1300°C. A bulk sample was made by a traditional ceramics route, calcined at 1600°C, for comparison.

The relationship between the calcining conditions and the photoluminescence intensity was explored in a series of experiments from which electron micrographs are shown in Figure 3.6. Shown in the leftmost micrograph, the precursor was heated to 700°C for 2 h. The individual particles were approximately 40 nm in diameter and did not appear to be fused together. However, heating to 700°C did not develop the crystalline garnet phase and showed no photoluminescence. The centre micrograph image shows the same precursor heated to 1000°C for 2 h and suggests that the particle size is still quite small, although the degree of sintering was not readily identifiable. The sample showed a weak yellow luminescence under UV illumination. In the rightmost image, the precursor was heated to 1300°C for 24 h and displayed a bright yellow luminescence under UV illumination. This heating, however, resulted in extensive condensation and sintering of the particles.

photoluminescence emission spectra at λ_{ex}=460 nm for products of the three calcination temperatures are shown in Figure 3.8. A comparison of the excitation and emission spectra for the 1300°C sample and the bulk sample is shown in Figure 3.7. The emission spectra show an rise in brightness with calcination temperature, increasing from almost no emission after heating to 700°C to a strong intensity from the 1300°C and bulk samples. While the relative intensities in the plot are qualitative, the trend is nevertheless apparent. Quantum efficiency was measured at 42% for the 1300°C and 74% for the bulk samples. Noise on these

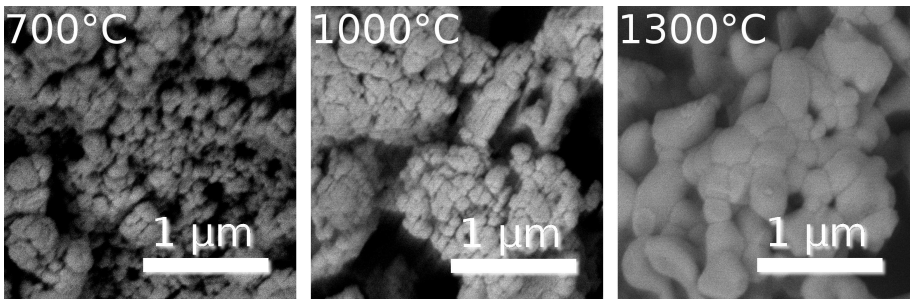

Figure 3.6: LEFT Scanning electron micrographs after heating to 700°C, showing no photoluminescence, CENTRE: 1000°C, which showed weak colour, RIGHT 1300°C heating, which showed intense yellow luminescence.

spectra is largely attributable to scaling and sample preparation effects as the data was not collected in an integrating sphere and so scattering effects become significant.

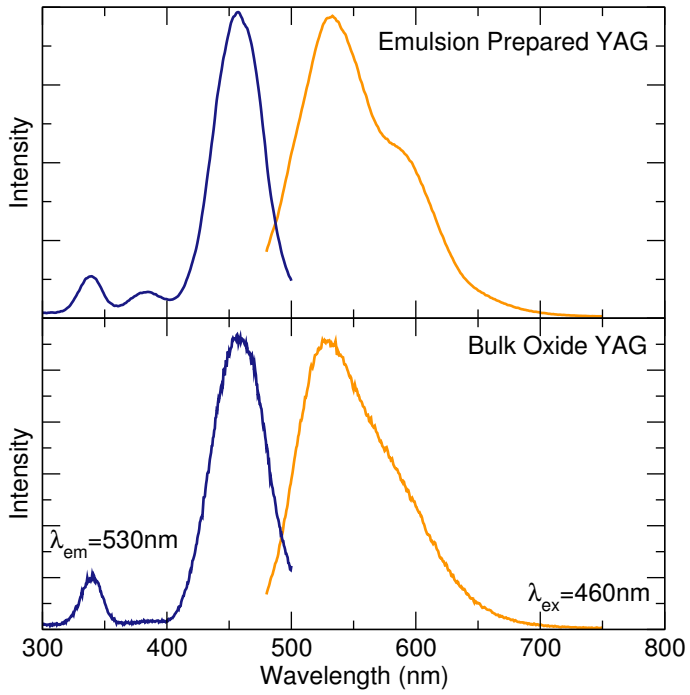

Figure 3.7: TOP: photoluminescence excitation and emission spectra for the emulsion prepared YAG:Ce nanoparticles calcined at 1300°C. BOTTOM: High temperature bulk preparation, showing that the luminescent behaviour is preserved in the nanoparticle samples. The apparent extra excitation peak at 380 nm and emission shoulder at 600 nm are present in the bulk phase as well and are obscured by scaling artefacts.

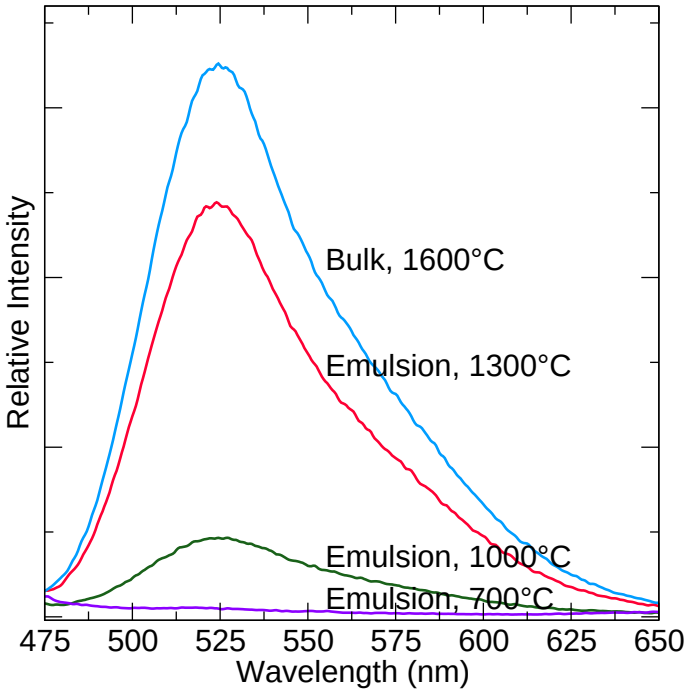

Figure 3.8: photoluminescence emission spectra of the same samples at λ_{ex} =460 nm, showing the increase in intensity with increasing calcination temperature. A high temperature bulk sample is included for comparison

3.3.1 Rietveld refinement using synchrotron data

To better analyse the structural disorder and impurity phases, high resolution X-ray diffraction data were collected. Synchrotron X-ray powder diffraction data shown in Figure 3.9 were collected at the Advanced Photon Source at Argonne National Laboratory. The highly monochromatic incident beam had a wavelength of λ=0.13697(2) nm, determined by refinement of a CeO_2 standard. The short wavelength, sharply defined X-rays, and high flux allows highly accurate phase purity and structural information to be obtained. The powder diffraction data were analysed by the Rietveld method using both XND [105] and GSAS [106, 107] software packages. With the availability of such high quality data, it became apparent that there were significant impurity phases in all of the samples. In addition to the garnet structure, samples were found to contain the monoclinic $Y_4Al_2O_9$ (YAM), a hexagonal perovskite $YAlO_3$ (hex-YAP), and CeO_2 (ceria). Figures 3.10, 3.11, and 3.12 show the refinements and constituent phase contributions for the 1000°C, 1300°C, and bulk samples, respectively. There is a small but unidentified impurity phase in the bulk sample which can mainly been observed in peaks between 2° and 2.5° 2θ. Table 3.1 summarizes the phases present and the relative amounts as determined by GSAS quantitative Rietveld analysis, wherein relative phase amounts are calculated by the scale factors applied to the gaussian profiles of the structure fitting. The increase in grain size, as indicated by the decreased Scherrer broadening, is shown in Figure 3.13, which details the (521) and (440) peaks. The increase in lattice parameter with calcination temperature is also evident in this plot, as the peaks shift to higher angles, and is listed for the garnet phase in Table 3.1.

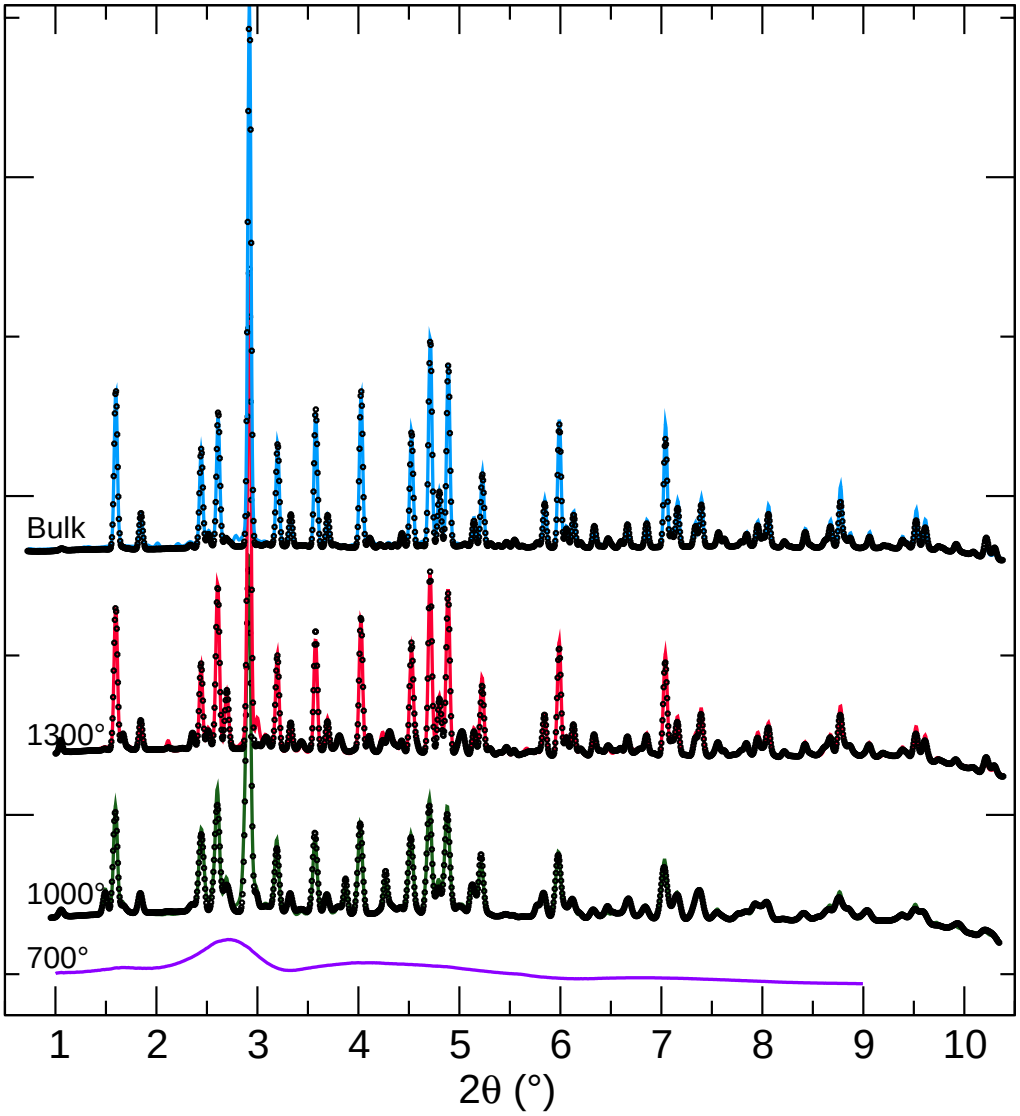

Figure 3.9: Synchrotron X-ray diffractograms at λ=0.136 nm of the 700°C, 1000°C, 1300°C, and bulk YAG samples. The 700°C sample is amorphous, and a sharpening of the peaks can be seen between the 1000°C and the 1300°C sample.

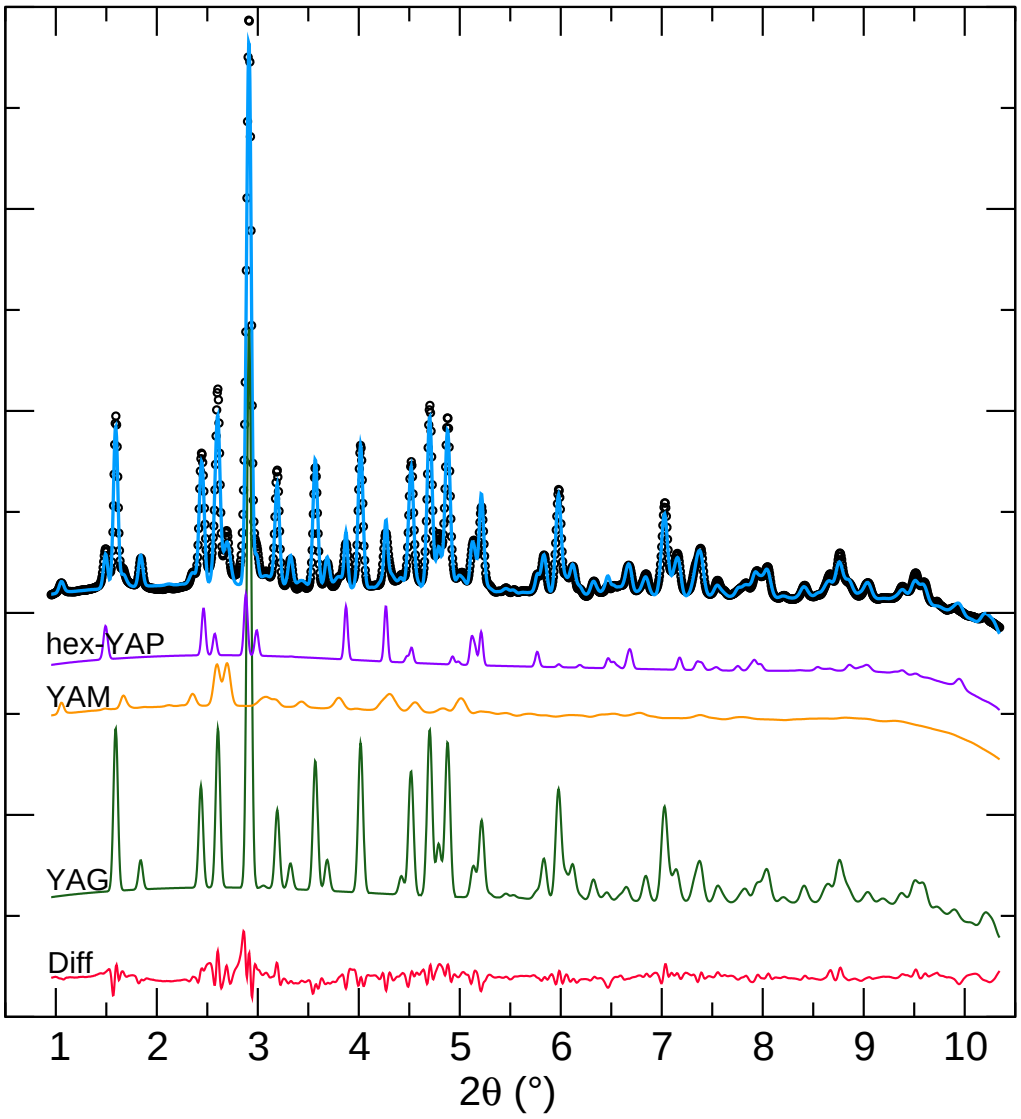

Figure 3.10: Impurity phase identification and Rietveld refinement of the emulsion prepared YAG sample calcined at 1000°C using synchrotron X-rays at λ=0.136 nm. The blue line indicates the total calculated pattern, and below it are the constituent phases and their contributions. YAM is monoclinic $Y_4Al_2O_9$, hex-YAP is hexagonal perovskite $YAlO_3$

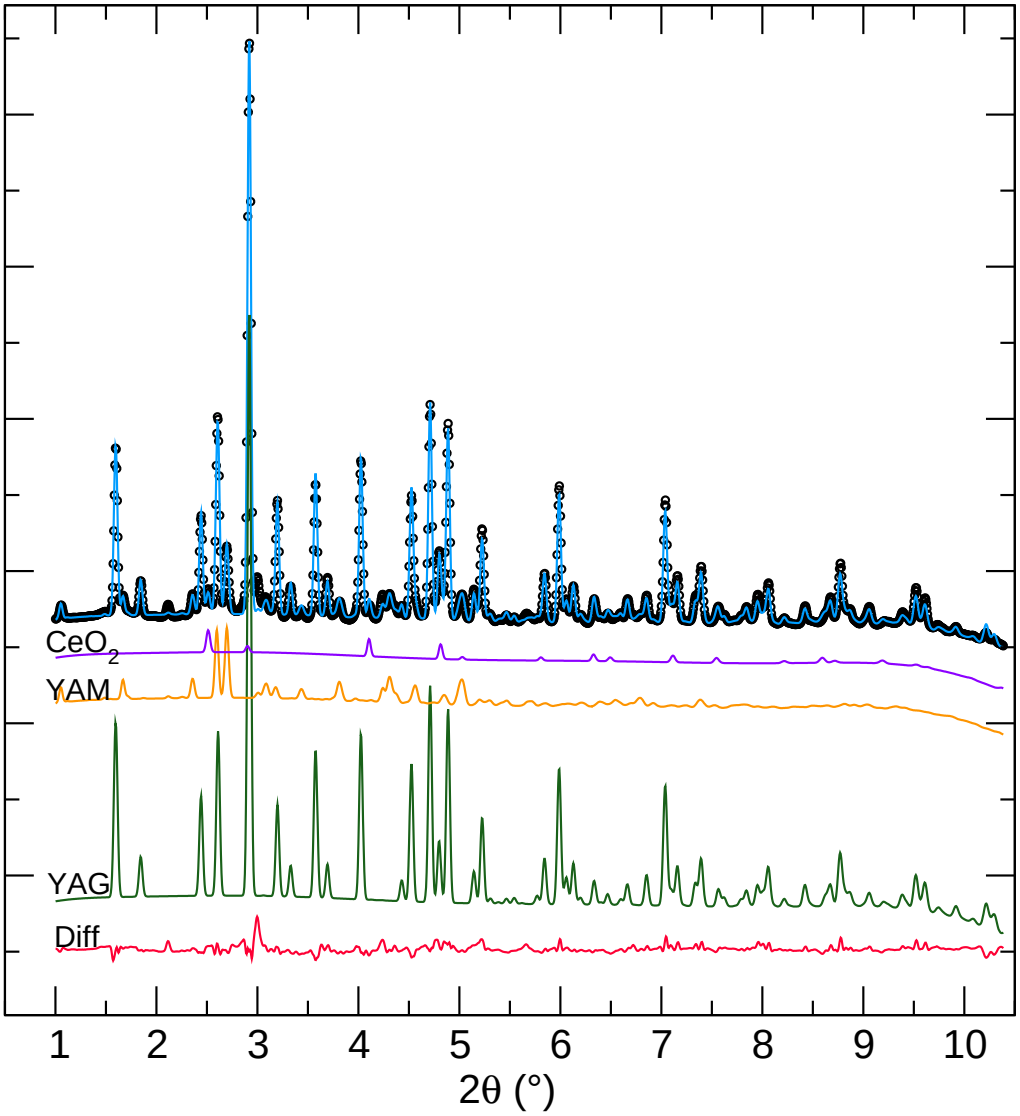

Figure 3.11: Impurity phase identification and Rietveld refinement of the emulsion prepared YAG sample calcined at 1300°C using synchrotron X-rays at λ=0.136 nm. The blue line indicates the total calculated pattern, and below it are the constituent phases and their contributions.

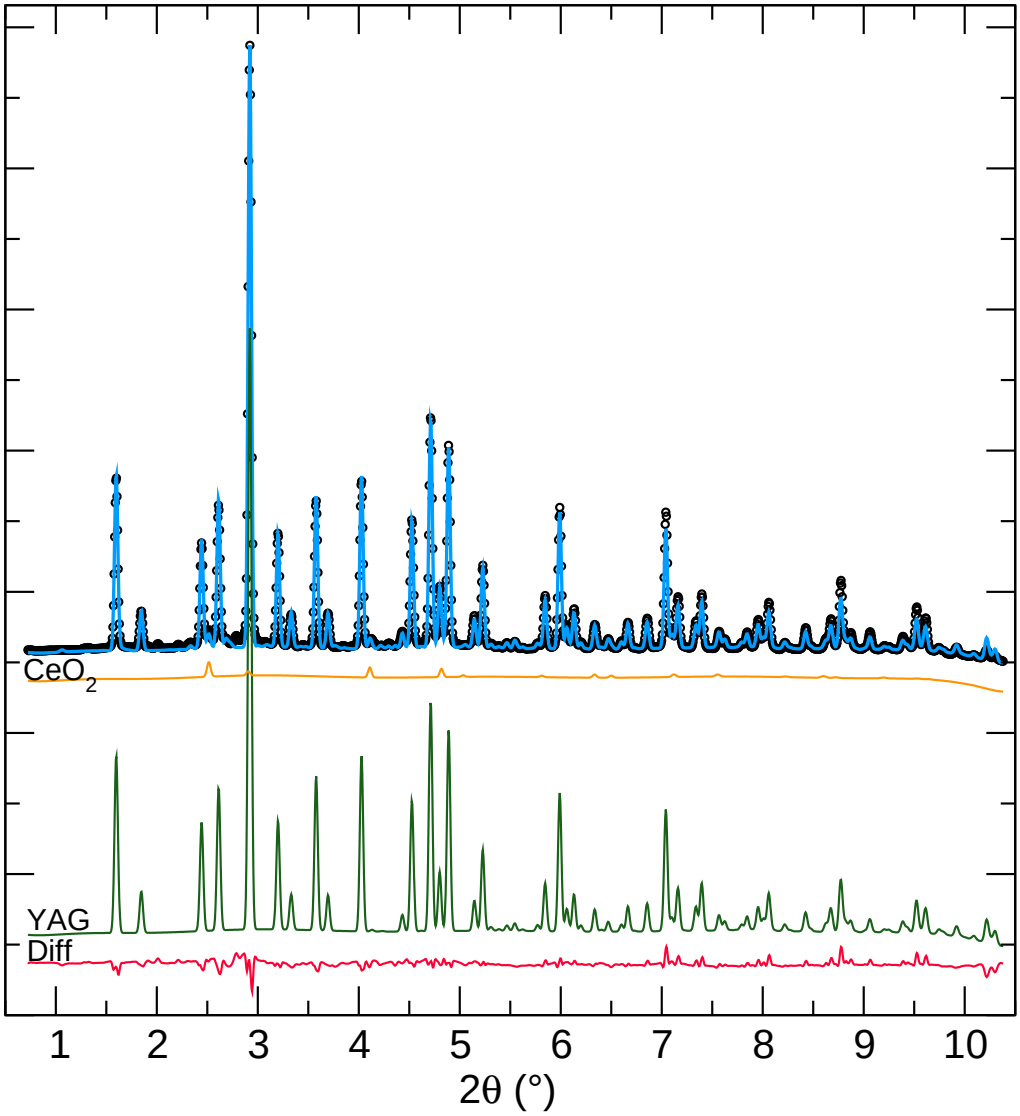

Figure 3.12: Impurity phase identification and Rietveld refinement of the bulk YAG sample calcined at 1600°C using synchrotron X-rays at λ=0.136 nm. The blue line indicates the total calculated pattern, and below it are the constituent phases and their contributions.

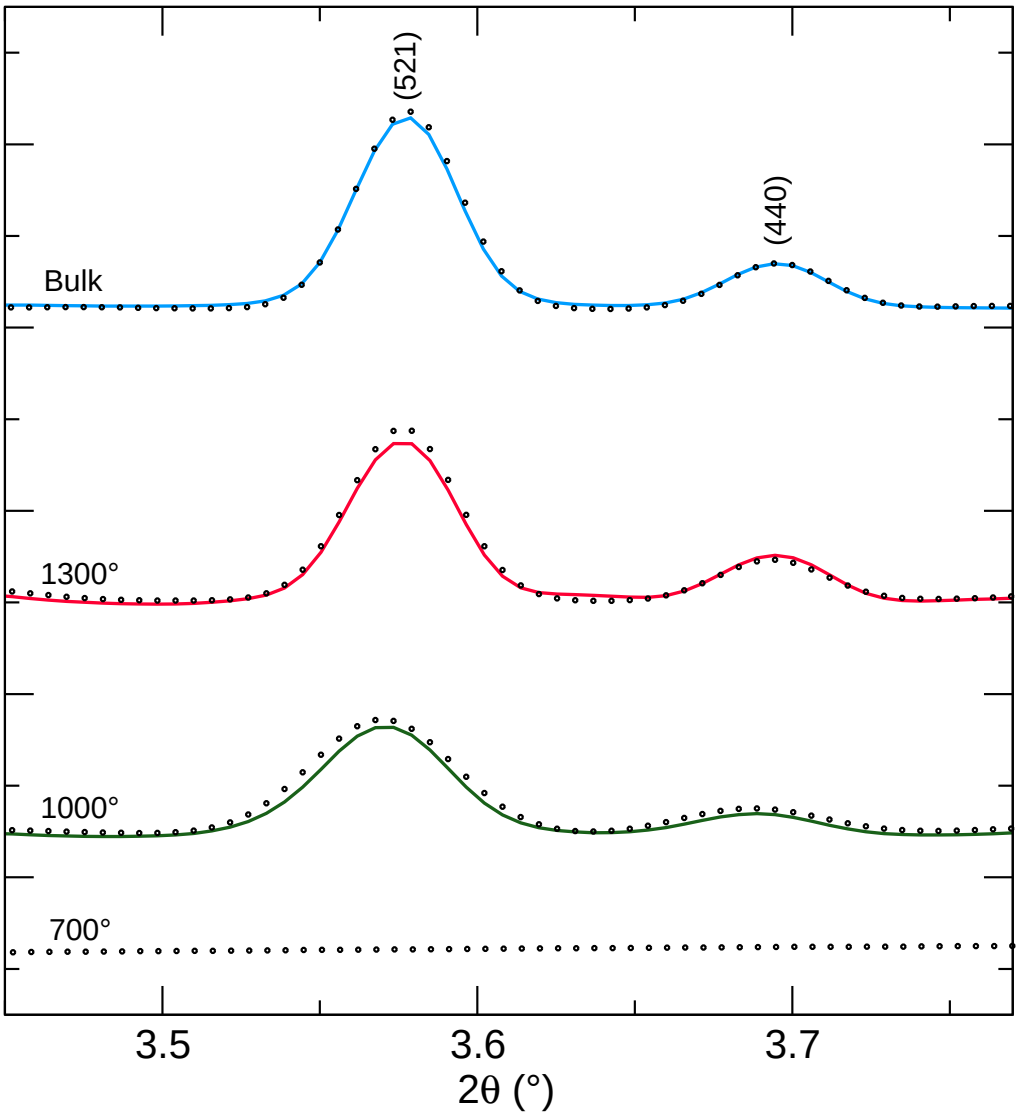

Figure 3.13: Detail of YAG:Ce synchrotron X-ray diffraction and Rietveld refinement showing peak broadening of the (521) and (440) reflections

Table 3.1: Relative phase contributions in the emulsion prepared YAG:Ce and lattice parameter of the garnet phase, as determined by GSAS Rietveld refinements. Lattice parameters for impurity phases are not reported.

Sample	Phase	Lattice Parameter (Å)	Contribution (%)
700°C	Amorphous	n/a	
1000°C	YAG	12.0209(7)	78.86(4)
	YAM	–	11.14(33)
	hex-YAP	–	10.00(19)
1300°C	YAG	12.0013(4)	85.45(8)
	YAM	–	13.58(19)
	CeO_2	–	0.97(4)
Bulk	YAG	11.9989(3)	98.94(1)
	CeO_2	–	1.06(6)

3.3.2 PDF analysis

The synchrotron X-ray data were further analysed by the PDF method. The experimentally determined $G(r)$ spectra are given in Figure 3.14 along with PDF refinements of the 1000°C, 1300°C and bulk YAG:Ce samples to 20 Å in r. In the PDF refinements, impurity phases were included as fractions (determined via Rietveld analysis) and their parameters were not refined. For the cubic YAG phase refinements, the lattice parameter a, the isotropic atomic displacement parameter (constrained for each element to be equivalent among all the phases), and the x, y, and z oxygen positions of the cubic phase were refined. In addition, a scale factor refinement and a peak broadening parameter (Q_σ) accounting for correlated motion were applied. It was found that the low-r range of the experimental PDF is more poorly fitted than the high-r range. A closer look at the atom-atom pairs

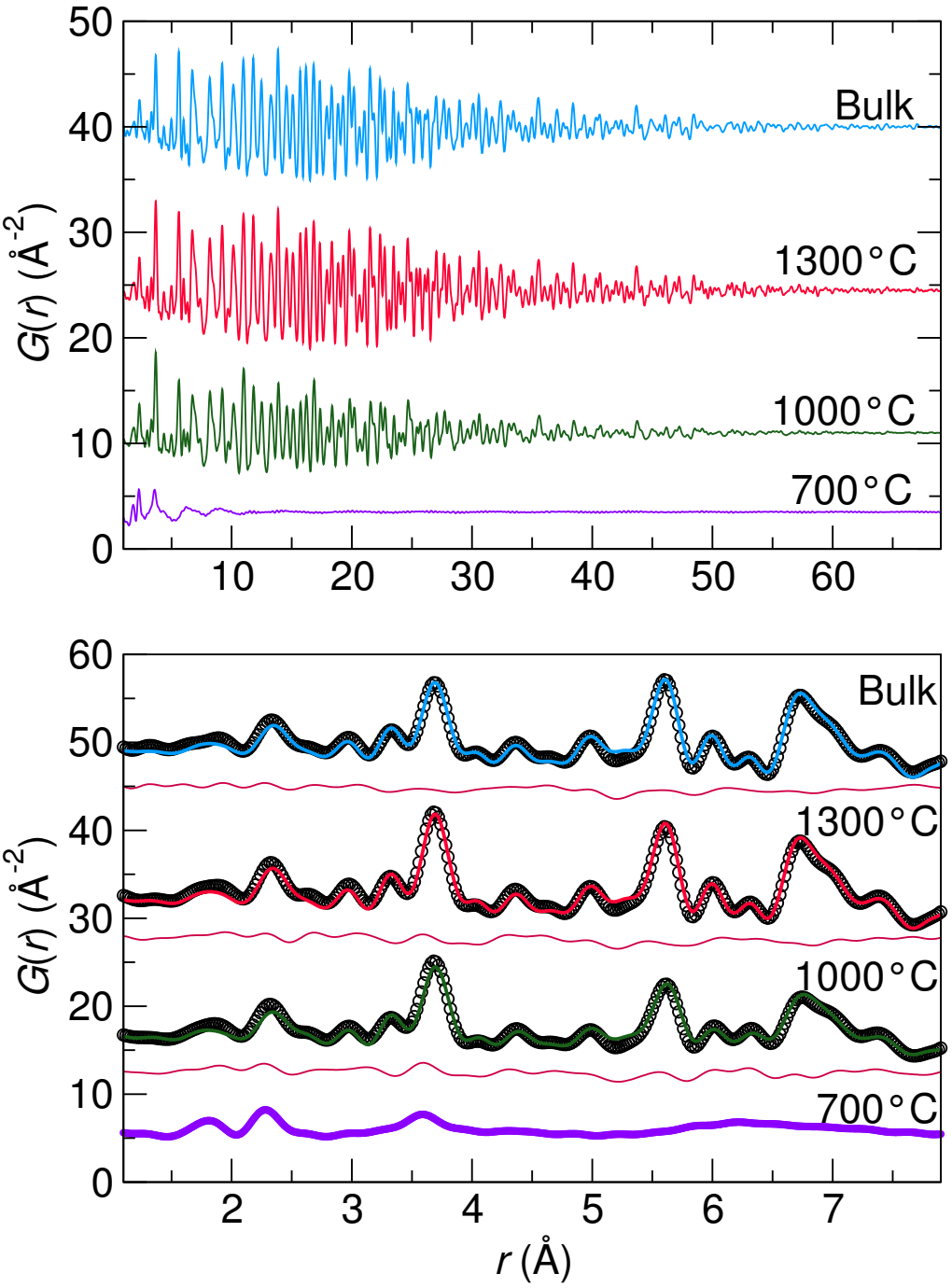

Figure 3.14: TOP: Long range pair distribution functions extracted from synchrotron powder diffraction data, showing the reduced correlation length for the lower temperature preparations. BOTTOM: Short range experimental pair distribut ion functions (solid circles) and fits (lines) to the top three data sets, with difference spectra shown below. Only raw data is given for the 700°C sample data set, though it can been sesen that the first two bond distances in the 700°C sample match those for the more crystalline samples.

Table 3.2: Structural parameters and bond distances from synchrotron PDF refinement of $Ia\bar{3}d$ YAG phase

	Bulk	**1300°C**	**1000°C**
Q_σ	0.85(5)	0.780(4)	0.73(5)
a (Å)	11.989(1)	11.996(1)	12.018(2)
x(O)	0.280(1)	0.279(1)	0.280(2)
y(O)	0.102(1)	0.102(1)	0.104(1)
z(O)	0.200(1)	0.1993(9)	0.0041(4)
U_{iso}(Y) (Å^2)	0.0025(2)	0.0027(2)	0.0041(4)
U_{iso}(Al) (Å^2)	0.0068(7)	0.0069(6)	0.008(1)
U_{iso}(O) (Å^2)	0.011(1)	0.012(1)	0.017(3)
$d_{Y\text{–}O}$ (Å)	(4×)2.30(2)	(4×)2.30(2)	(4×)2.32(3)
	(4×)2.43(1)	(4×)2.43(1)	(4×)2.45(2)
$d_{Al1\text{–}O}$ (Å)	(6×)1.911(2)	(6×)1.90(2)	(6×)1.89(3)
$d_{Al2\text{–}O}$ (Å)	(4×)1.78(2)	(4×)1.78(2)	(4×)1.79(3)
R_{wp} (%)	11.94	12.22	17.77

in the correlations shows the distances poorly captured belong to metal-oxygen distances. Results from the PDF fits and calculated bond lengths are given in Table 3.2. Figure 3.15 shows that the isotropic atomic displacement parameter (U_{iso}) increased at lower calcination temperatures, suggesting an increasingly disordered lattice. The decreasing crystallinity is also reflected in the decreasing Q_σ.

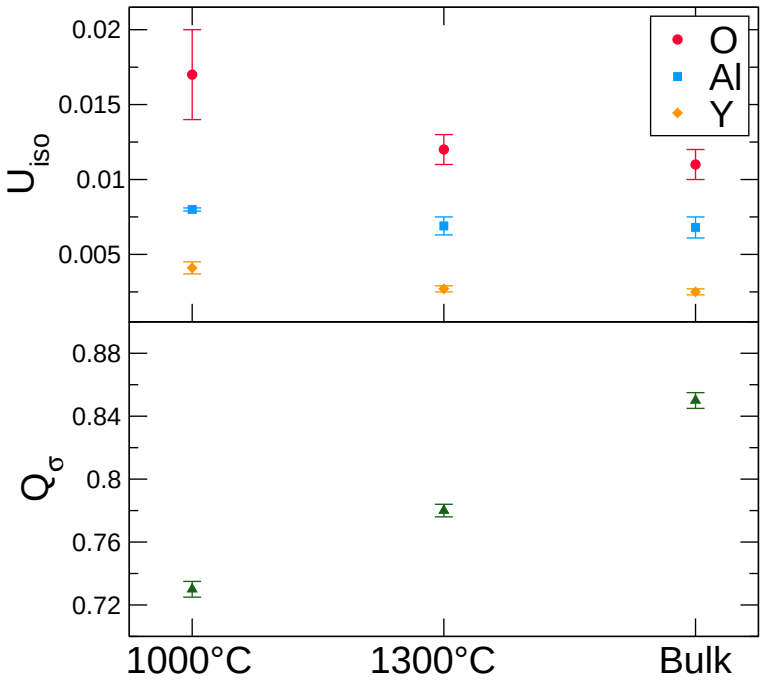

Figure 3.15: TOP: Decreasing isotropic atomic displacement parameter U_{iso}. BOTTOM: Increasing fitting parameter Q_σ, suggesting disorder at lower temperature calcinations.

3.3.3 Luminescent lifetimes

The top of Figure 3.16 shows the intensity decay measured for the emission of the bulk YAG:Ce preparation and for the YAG:Ce nanoparticles at room temperature after a 450 nm laser excitation pulse. The best fit model to the data was a bi-exponential, allowing us to determine the corresponding lifetimes of each decay. The fast process, τ_1, was 6.29 ns for the bulk and 5.18 ns in the 1300°C nanoparticles. The slow process, τ_2, was 58.07 ns for the bulk and 53.36 ns in the nanoparticles. For the bulk YAG:Ce sample the contribution of the fast process is small (∼5%) and the lifetime of the slow process is very close to the 67 ns previously reported by Zych et al. [114], while for the nanoparticles the contribution

of the fast process becomes more significant, around 20%.

We have performed time-resolved experiments at different temperatures to establish the effect of thermal quenching on lifetime and quantum efficiency. As the intensity at initial time I_o is proportional to the quantum efficiency, we were able to determine the temperature dependence using measurements at initial time t_o. The centre of Figure 3.16 shows that the quantum efficiency for the bulk YAG:Ce diminishes from 74% at room temperature to 56% at 473 K. A similar behaviour can be observed for the YAG:Ce nanoparticles in the same temperature range, its quantum efficiency diminishing from 42% to 34%.

The lifetimes of each process measured by the bi-exponential fitting at different temperatures for these samples are shown in the bottom of Figure 3.16. It can be seen that the behaviours are very similar for the lifetime of the fast component τ_1. In the case of the slow process, the lifetime of the YAG:Ce nanoparticles drops slightly at temperatures above 350 K.

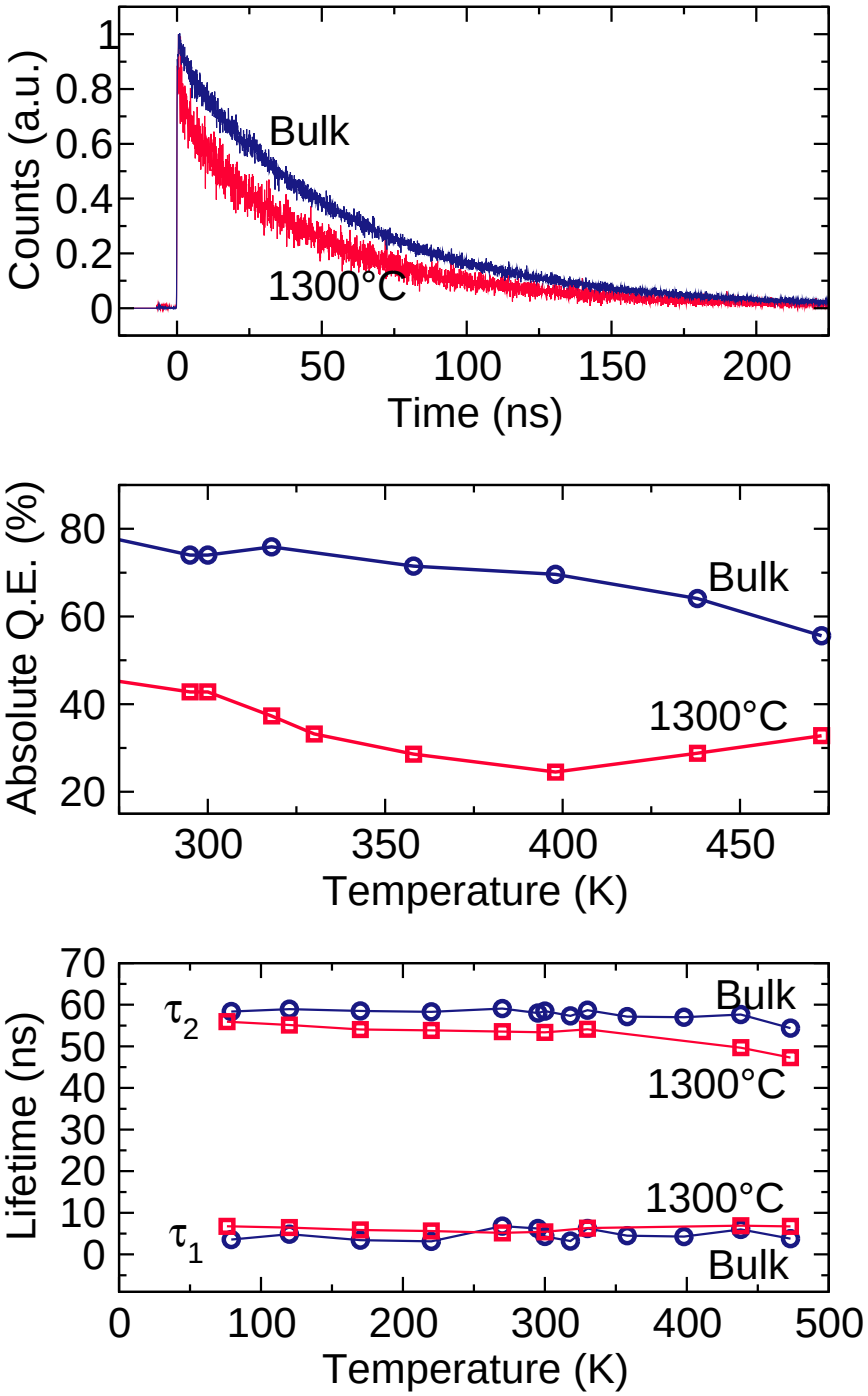

Figure 3.16: TOP: Room temperature emission intensity decay, CENTRE: temperature dependent absolute quantum efficiency, and BOTTOM: temperature dependent luminescent lifetime for YAG:Ce nanoparticles prepared at 1300°C (squares) and bulk YAG:Ce (circles).

3.4 Summary

The difficulties in producing highly efficient yet nanoscale particles of YAG:Ce highlight one of the problems with tuning particle size for inorganic phosphors. While the theoretical benefits of a perfectly phase pure, highly crystalline particle of a phosphor compound with dimensions that would reduce backscattering and improve device processability are apparent, they are much more difficult to implement experimentally. While there certainly have been many reports of nanosized phosphor materials, their efficiency (when reported) is never up to the performance of their bulk counterparts. In our own YAG:Ce preparations, relatively high efficiency was obtained by emulsion-templating with a calcination temperature 300°C lower than the bulk oxide preparation and in a single heating step, which represents a large energy savings on its own. Unfortunately it seems that the calcination conditions required for highly efficient luminescence also lead to sintering of the particles.

Several important conclusions were reached with Rietveld and PDF refinement with synchrotron powder diffraction data in combination with the quantum efficiency and lifetime measurements. First, the high resolution synchrotron X-ray data revealed that additional phases, not detected with laboratory X-rays, are present in the nanoparticle samples calcined at 1000°C and 1300°C. These additional phases no doubt account in part for the loss of photoluminescence efficiency. Second, the PDF results indicate that the order within the garnet phase is lower for the nanoparticles as compared to the bulk sample, which again contributes to the lower efficiency. Third, photoluminescence efficiency and lifetime measurements indicate lower quantum efficiency for the nanoparticles and thus more non-radiative decay mechanisms.

It is clear that all of these factors influence the photoluminescence performance of the YAG nanoparticles.

The research described in this chapter was carried out in collaboration with Katherine Page, who was responsible for the PDF refinements, Gautam Gundiah, who assisted with the synthesis and microscopy, and Nancy Pizzaro, who performed many of the luminescence measurements. It has been published in Chemical Physics Letters as: J. D. Furman, K. Page, N. Pizzaro, G. Gundiah, and A. K. Cheetham. "Local structure and time resolved luminescence of emulsion prepared YAG nanoparticles." *Chem. Phys. Lett.*, **465**, 67 (2008). [DOI: 10.1016/j.cplett.2008.09.045].

Chapter 4

photoluminescence and mechanical properties of rare earth-based inorganic-organic frameworks

4.1 Introduction

The rest of this thesis concerns our attempts to make phosphors for solid state lighting using hybrid inorganic-organic framework materials. In this chapter we investigate the possibility of using rare earth-based hybrids as phosphors. It will be shown that while their excitation and emission spectra make them unsuitable for use in devices, the mechanical properties of dense frameworks are well within the range required for device applications. The use of hybrid materials was also motivated by the possibility of making nanoparticles of these materials. While nanoparticles of these compounds were not synthesized, it is expected that it should be much easier to overcome the crystallinity issues that arose for the YAG:Ce particles because the frameworks are already solution processed under mild conditions.

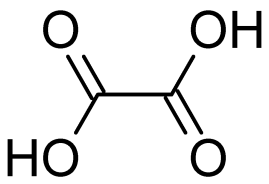

Figure 4.1: Sketch of oxalic acid

Rare earth elements and the dicarboxylate ligand oxalic acid, shown in Figure 4.1, were combined in attempt to make dense, anhydrous framework phosphors. The oxalate anion was selected as a ligand as its lack of C–H bonding and high temperature stability should make a wide range of reaction conditions accessible. Also, the lack of C–O and C–H bonding has been suggested to improve phosphor performance as the resonant vibrations of the bonds couple to excited luminescent ions, providing non-radiative recombination pathways. Anhydrous framework structures can show remarkable thermal stability, typically displaying no weight loss in thermogravimetric measurements up to 400°C, often exceeding the thermal stability of the ligand as a free acid. The O–H bonds in water are also known to reduce luminescent efficiency, particularly when the water molecules coordinate to the metal ions. It was hoped that an anhydrous oxalate phosphor would benefit from both the high stability and limited vibration modes of the oxalate anion as well as the overall stability of that has been seen in other anhydrous frameworks.

In the course of this work it became apparent that no high efficiency phosphors with lighting applications were likely to be found in the rare-earth oxalate family of crystal structures. Excitation of rare-earth containing phosphors only

showed directed metal excitation without any lattice contribution because the antenna effect of the oxalic acid is too far into the UV to be useful for LEDs. Figure 4.2 shows the UV excitation and emission of a cerium-doped lanthanum oxlalate formate $La_{1-x}Ce_x(HCOO)_3$. Additionally, obtaining anhydrous frameworks based

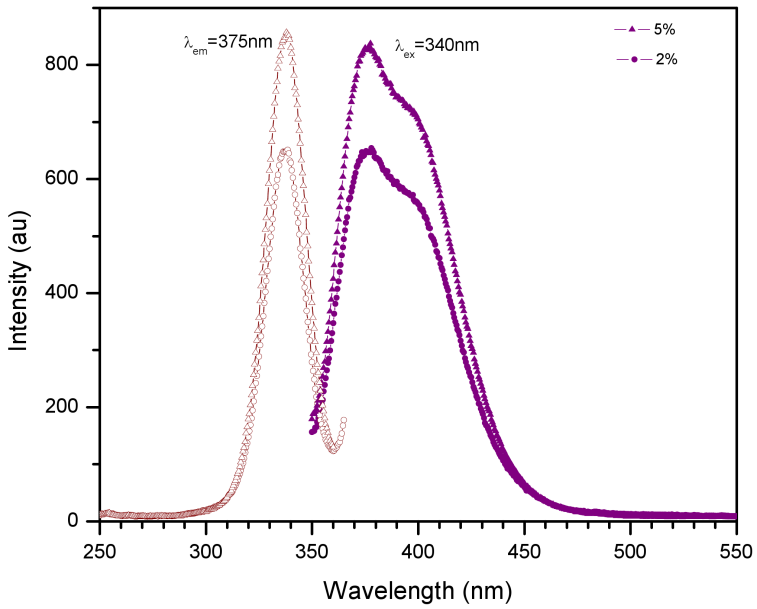

Figure 4.2: Excitation and emission spectra for cerium-doped lanthanum formate $La_{1-x}Ce_x(HCOO)_3$, shown for x=2% and 5% with λ_{ex}=340 nm and λ_{em}=375 nm. Both the excitation and emission are too far into the UV to be useful for solid state lighting applications [115].

on oxalic acid proved to be difficult if not impossible. An example of green Tb^{3+} luminescence from a (Tb/La)-oxalate decahydrate solid solution series with the formula $La_xTb_{1-x}(C_2O_4)\cdot 10H_2O$ [116] is shown in Figure 4.3 for x=0, 0.1, 0.2, 0.5, and 1. The emission in this case comes from direct excitation of the terbium ions in the lattice, and its intensity rises with increasing terbium substitution. Excitation transitions in the terbium sample correspond to the $^7F_6 \rightarrow^5 L_6$ centred at 330 nm and the $^7F_6 \rightarrow^5 D_3$ centred near 380nm. The three prominent luminescent

peaks at 490 nm, 550 nm, and 575 nm correspond to the $^5D_4 \rightarrow^7 F_6$, $^5D_4 \rightarrow^7 F_5$, and $^5D_4 \rightarrow^7 F_4$ transitions, respectively. The inset shows the excitation spectra, which does not have a useful excitation range for white LEDs applications. Interestingly, however, no concentration quenching was seen for these samples and the maximum emission intensity came from the pure terbium compound.

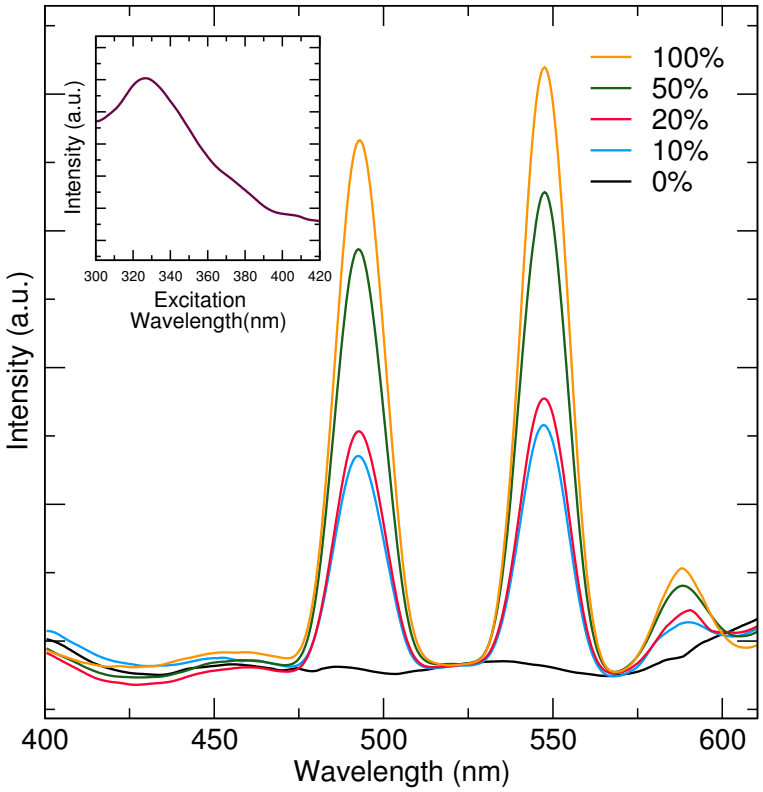

Figure 4.3: Emission spectra from (Tb/La) oxalate up to 100% terbium. Inset: Excitation spectra for 100% terbium oxalate. λ_{ex}=330 nm and λ_{em}=550 nm.

Nevertheless, some routes to large single crystals of known materials were found, namely a mixed ligand cerium oxalate formate with the formula $Ce(C_2O_4)(HCO_3)$. This compound was previously reported by Trombe et al. [117] and serendipitously rediscovered in this work. Well faceted, relatively large crys-

tals were synthesized hydrothermally, with edge lengths up to 500μm, making them ideal for a study of the mechanical properties of hybrid framework materials. The structure is highly anisotropic and crystallographically aligned with the crystal facets, which allowed for probing of how the bonding arrangement down a crystal axis effected its mechanical properties.

The luminescence of the anhydrous cerium oxalate formate, the mechanical properties of which will be discussed later in this chapter, was investigated by photoluminescence spectroscopy. However, no emission was observed for excitations at any wavelength although a UV emission was expected. This might be because the signal was simply too weak to be detected, or because the stokes shift was so small that the emission could not be resolved from the excitation. Either way, the luminescent properties of this compound were clearly not suitable for use as a solid state lighting phosphor. However, we continued to test the mechanical properties of the compound in order to ascertain whether inorganic-organic frameworks as a class would be sufficiently robust for applications in lighting.

4.1.1 Known oxalate framework structures

The known lanthanide oxalates from lanthanum to erbium all crystallize in a monoclinic decahydrate with the formula $M_2(C_2O_4)_3{\cdot}10H_2O$ [118]. The structure shows a 2-dimensional honeycomb structure of six-membered rings, as was described for the lanthanum oxalate decahydrate by Huang et al. [116]. This 2-D honeycomb structure is also seen with other oxalate frameworks such as zinc and tin [119]. Figure 4.4 shows a sheet of gadolinium(III) oxalate decahydrate ($Gd_2(C_2O_4)_3{\cdot}10H_2O$) along with the isostructural tin oxalate.

Similar reported hybrid structures with oxalate ligands have been reported

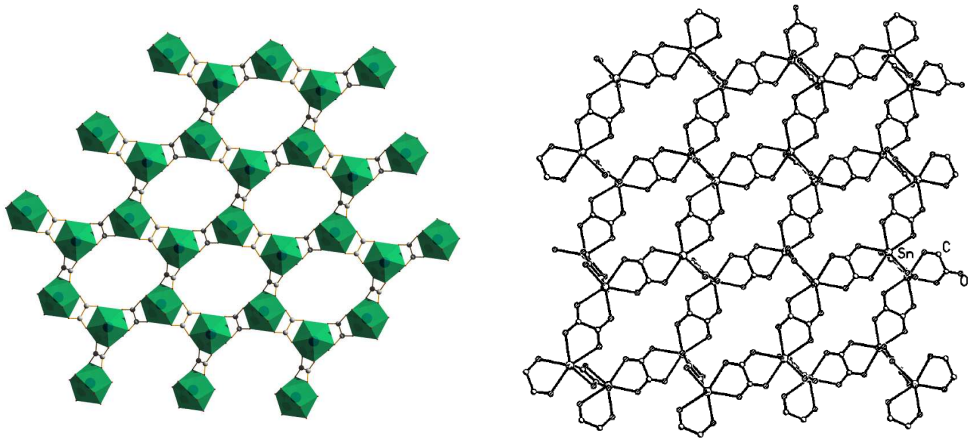

Figure 4.4: LEFT: Gadolinium oxalate decahydrate ($Gd_2(C_2O_4)_3{\cdot}10H_2O$), viewed down the b axis showing the honeycomb structure. The water in the pores is omitted for clarity. RIGHT: isostructural tin oxalate hydrate from Natarajan et al. [119].

with mixed metal ions. The Louër group has prepared a mixed oxalate hydrate structure with a $[MM'(C_2O_4)_4]^{-2}$ framework that is charge balanced by interstitial K^+ or Cd^{2+} ions [120]. The structure, shown in Figure 4.5, shows a honeycomb structure in the (111) plane with alternating metal sites around the 6-membered ring and open sites in the pores that are filled by either the small potassium and cadmium cations or water. In their work, and those they cited, structures were reported for $[MM'(C_2O_4)_4]^{2-}$ charge compensated with K^+, Cd^{2+}, Ca^{2+}, Sr^{2+}, and NH_4^+, where M and M' were various combinations of Y, Cd, Zr, Ca, In, Sr, Mn, U, Bi, and Er [121–127]. Those preparations were all carried out at room temperature and resulted in hydrated compounds. These structure types were not investigated in this work because their porosity generally leads to lower thermal and chemical stability than needed for solid state lighting phosphors.

Reports of dense, anhydrous, inorganic-organic framework oxalates are rare

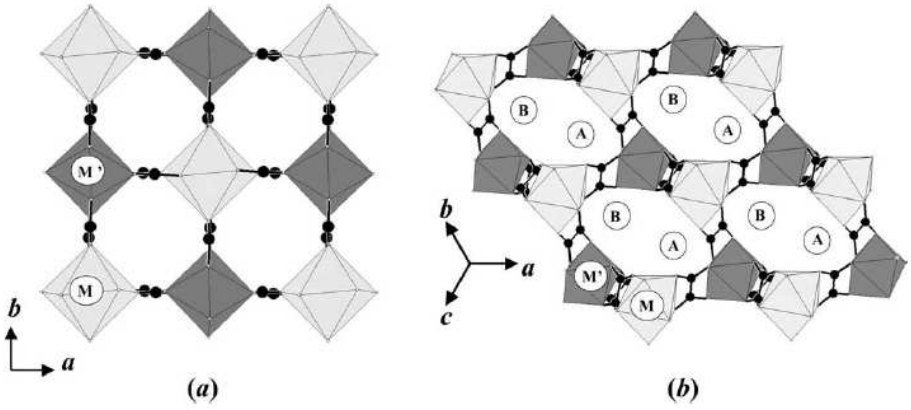

Figure 4.5: the (a) c-axis projection and (b) (111) plane of the $[MM'(C_2O_4)_4]^{-2}$ structure reported by Louër et al. [120]. The A and B sites filling the pores are occupied either by the small charge compensating cations or water molecules.

but a few exist. A strontium oxalate compound was grown hydrothermally at 240°C as reported by Price et al. [128]. The strontium cations are 8 coordinated by oxygen and form edge sharing polyhedra chains linked by oxalate ligands. Another similar anhydrous structure from the Louër group was an anhydrous β-Cd oxalate [129]. The compound was prepared hydrothermally at 150°C from cadmium nitrate and potassium oxalate, and contains MO_6 octahedra chains linked by oxalate ions. Trifa et al. prepared anhydrous barium strontium oxalate crystals by very slow evaporation at room temperature [130]; it adopts a structure of chains formed by bidentate oxalate ligands which then connected into a 3-dimensional structure via monodentate oxalates. Evaporation of the crystals took over a year, however, which makes it not a particularly attractive method.

Reports of several anhydrous oxalates structures have come from thermal decomposition of hydrated forms. This typically requires structure solution from powder diffraction, a difficult and sometimes impracticable method depending on

the complexity of the crystal structure. For example, Christensen et al. reported two partially solved anhydrous barium oxalate structures in 2002 from powder diffraction data of a thermally decomposed hydrated oxalate [131].

All of these anhydrous structures, however, involve divalent metal cations. The luminescent rare earth species investigated here almost always assume a 3+ state, with the notable exception of Eu^{2+}, which is difficult to stabilize in an aqueous reaction. In the course of this research it became apparent that obtaining anhydrous trivalent lanthanide oxalates was out of reach and that combining the stability benefits of an anhydrous oxalate system with rare earth luminescent ions was not going to be possible.

4.1.2 Mechanical properties

Very little is known about the mechanical properties of inorganic-organic hybrid frameworks. Hybrids have mostly been studied in the past for their porosity, where mechanical strength is not a property of primary concern. However, as the potential applications of hybrid framework materials moves into optical and electronic devices, it becomes critical to understand their mechanical stiffness and hardness.

Measuring hardness and Young's modulus on sub-millimetre crystals proposes some practical problems as all of the measurements being considered are orders of magnitude smaller than the traditional metallurgical samples for which these tests were originally developed. One cannot, for example, clamp both ends of a sample in a tensometer and measure the extension versus applied load. However, advances in indentation techniques have been scaled down to provide sub-micron resolution and thus allow for so-called "nanoindentation" experiments. In these tests, a small indentation is made in a sample using a tip with known geometry and

elastic properties, and the displacement depth and applied pressure are measured. From this data, the material's modulus and hardness can be extracted.

The parameter of primary concern is the Young's modulus (E). This is the measurement of a material's stiffness while it undergoes elastic deformation and is typically reported in gigapascals (GPa). Hardness (H) is a measurement of resistance to plastic deformation. When measuring polycrystalline samples, a test at one length scale does not necessarily translate to others because the effects of grain size and boundaries become more significant as displacements increase. However when testing single crystals, a measurement at any length scale should be accurate or nearly accurate at all length scales. Furthermore, any potential device applications would likely involve stresses on the order of what is tested by nanoindentation.

There have been a few reports published on nanoporous framework materials [132–135], but none on dense hybrid structures until the recent publication of Tan, Furman and Cheetham [136] on the cerium oxalate formate described herein, and another work from the Cheetham group by Tan, Merrill, Orton and Cheetham [137] studying copper phosphonoacetate polymorphs. Both of these studies provided highly anisotropic crystal structures which led to highly anisotropic and impressive mechanical properties.

4.2 Experimental methods

4.2.1 Synthesis of cerium oxalate formate

$Ce(C_2O_4)(HCO_2)$ was prepared by hydrothermal synthesis. The synthesis was modified from that reported by Romero et al. [117] to yield larger crystals. A

mixture of 0.15 mmol $Ce(OH)_4$ and 1 mmol oxalic acid in 10 mL deionized water was sealed in a 23 mL PTFE-lined auto clave. The autoclave was heated at 200°C for 5 days. During heating, a portion of oxalic acid decomposed to formic acid and the cerium(IV) was reduced to cerium(III) by the acidic solution. The final products, consisting of colourless block crystals ($\approx 200 \times 50 \times 45\,\mu$m), were recovered by filtration, washed with water and ethanol, and then dried in air.

4.2.2 Single crystal structure and orientation

Single crystal X-ray diffraction was carried out to confirm the crystal structure of $Ce(C_2O_4)(HCO_2)$ and to index the primary crystal facets. A representative single-crystal was selected under a cross-polarizing microscope and glued onto a glass fibre using epoxy. The crystal structure determination was performed on a Bruker single crystal diffractometer at Southampton University using a Nonius FR591 rotating anode source with a molybdenum target ($\lambda = 0.71073$ Å) and a KappaCCD detector with graphite monochromator. A hemisphere of intensity data were collected at 120 K. An empirical correction on the basis of symmetry equivalent reflections was applied using the SADABS program. The structure was solved by direct methods using SHELXTL and difference Fourier syntheses. The hydrogen atoms were found in the Fourier difference map and constrained to chemically reasonable positions. Crystal faces were identified using Bruker Face Indexing.

4.2.3 Nanoindentation testing

The mechanical properties of cerium oxalate formate were evaluated using an MTS NanoindenterXP at the Gordon Laboratory of the University of Cambridge. The instrument is held in an isolation cabinet, protecting it from thermal and

acoustic interference. This device is equipped with a continuous stiffness measurement attachment which allows for multiple measurements during a single indentation. It has a maximum depth of 2 μm with a resolution of 0.01 nm and with 50 nN load resolution. Two indenting tips were used on the nanoindenter. A diamond 3-sided pyramid Berkovich tip which provides a sharp tip radius of approximately 100 nm was used to measure sample modulus and hardness. A spherical diamond indenter, with a much larger tip radius of $\approx$10 μm, was used to examine the plastic deformation regime as it delays the sample yielding, the point at which the transition to from elastic to plastic deformation takes place. Amorphous silica (E=72 GPa, H=9 GPa) was used as a calibration standard for all experiments.

High quality, untwinned single crystals were selected using a cross-polarizing light microscope and cold mounted in epoxy. Controlling surface roughness is extremely important for indentation experiments as the radius of the Berkovich tip is on the order of, or smaller than, some crystal surface features. To overcome this, the samples were polished using progressively finer diamond slurries and then finally colloidal silica. AFM of the surfaces after polishing revealed an average (RMS) roughness of less than 10 nm. Multiple crystals were mounted for each crystal face to collect a wide range of data, especially since each individual crystal could only be tested on a single crystal facet. An optical micrograph of an indented sample is shown in Figure 4.6. A schematic of tip loading and unloading with some elastic recovery given by $h_{max} - h_f$ is shown in Figure 4.7. Modulus and hardness were measured for multiple samples on each crystal face by applying the small dynamic force of a 2 nm sinusoid at 45 Hz over a constant loading rate of 0.05 s^{-1} to a total displacement of 500 nm.

Young's modulus (E), a measurement of stiffness, is defined as the ratio be-

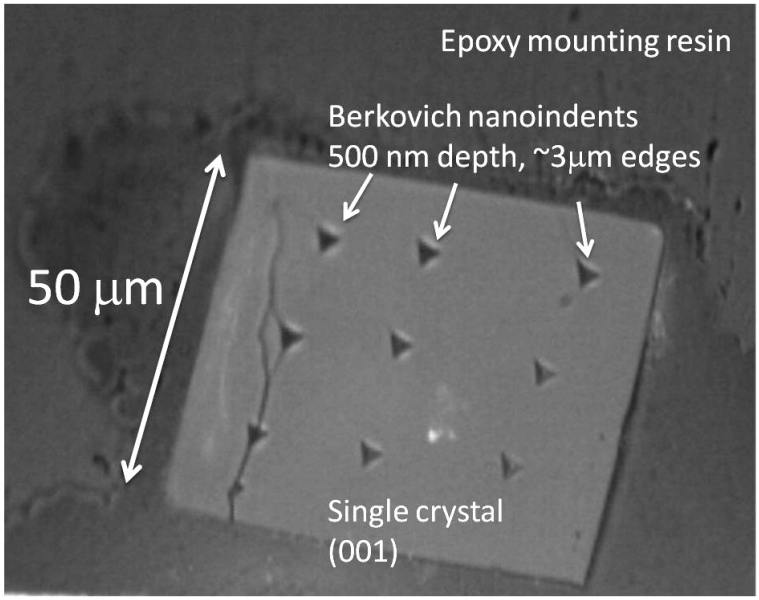

Figure 4.6: Optical micrograph of a resin mounted single crystal polished to show the (001) face after indenting to a depth of 500 nm with a Berkovich tip

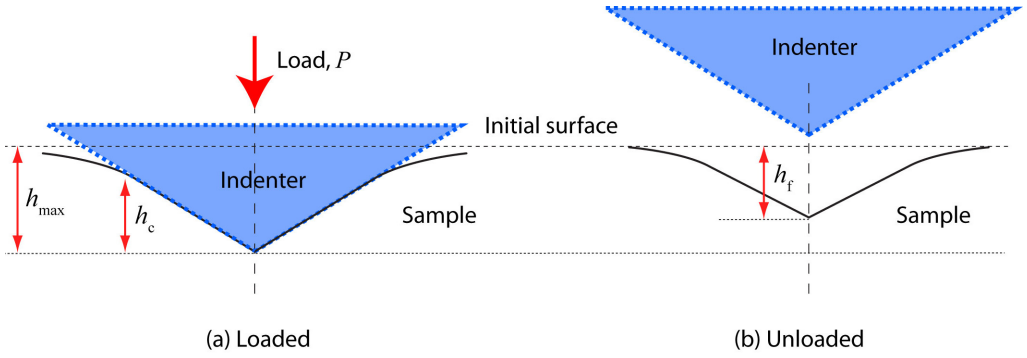

Figure 4.7: LEFT: Schematic of tip indentation at maximum loading, RIGHT: after unloading, showing height of elastic recovery h_f

tween stress and strain. Using the dynamic measurement method described, the modulus as a function of the penetration depth can be calculated from the measured elastic contact stiffness (S). This is known as the reduced modulus E_r:

$$E_r = \frac{\sqrt{\pi}}{2\beta}\frac{S}{\sqrt{A_c}} \tag{4.1}$$

where A_c is the contact area of the tip as determined by the calibration standards and β is a constant dependent on the tip geometry, equal to 1 for a spherical tip and 1.034 for the Berkovich tip. The sample modulus E is extracted from E_r using the method of Oliver and Pharr [138, 139]:

$$E_r = \left[\left(\frac{1-\nu_s^2}{E}\right) + \left(\frac{1-\nu_i^2}{E_i}\right)\right]^{-1} \tag{4.2}$$

where E_i and ν_i are the elastic modulus and Poisson's ratio of the indenter. For the diamond tips used, E_i=1141 GPa and ν_i=0.07.

Hardness was calculated from the ratio of applied load P to the contact area A_c:

$$H = \frac{P}{A_c} \tag{4.3}$$

where A_c is calculated from the tip geometry as it was for the modulus calculations, taking into account the tip penetration depth and the elastic recovery:

$$h_c = h_{max} - 0.75\frac{P}{S} \tag{4.4}$$

The elastic work (W_{elas}) and plastic work (W_{plas}) combine to make the total work (W_{total}). The total work is calculated as the integrated area under the loading

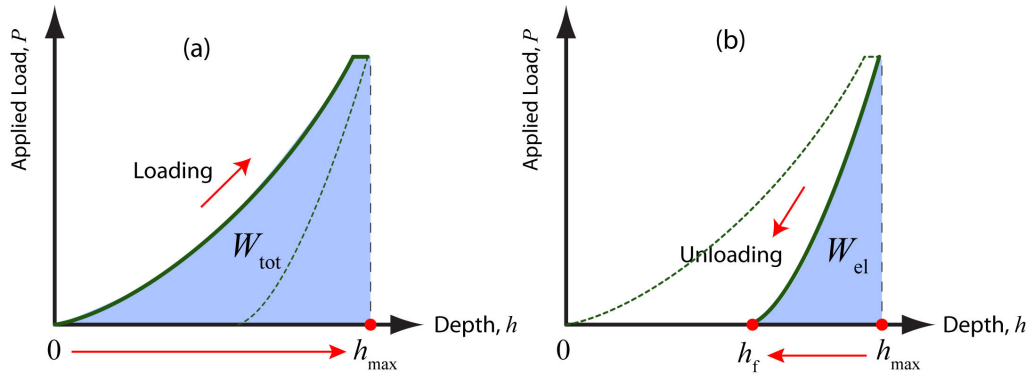

Figure 4.8: Representative load–displacement curves showing (a) the integration of total work and (b) the unloading hysteresis leading to the calculation of the elastic work

curve as a function of depth, $P(h)$, as shown in Figure 4.8, thus:

$$W_{tot} = \int_0^{h_{max}} P(h)dh \tag{4.5}$$

$$W_{elas} = \int_{h_f}^{h_{max}} P(h)dh \tag{4.6}$$

$$W_{plas} = W_{tot} - W_{elas} \tag{4.7}$$

$$\tag{4.8}$$

Using a spherical indenter, the indentation stress P_m is represented by the applied pressure divided by the area:

$$P_m = \frac{P}{\pi a^2} \tag{4.9}$$

where a is the contact radius. P_m is linearly proportional to strain in the elastic

regime:

$$P_m = \left(\frac{4E_r}{3\pi}\right)\left(\frac{a}{R}\right) \tag{4.10}$$

where R is the tip radius and E_r is the reduced modulus from above. This elastic regime applies under low strain levels prior to the yield pressure P_y.

Standard AFM measurements were made after indenting using a Veeco Dimension V in tapping mode. Scans were made 512×512 resolution with the gain and proportional gain set to 4 and 40, respectively. An amplitude setpoint of 310 mV was applied and the scan rate was set at 0.4 Hz.

4.3 Results

4.3.1 Structure of cerium oxalate formate

Cerium oxalate formate with composition $Ce(C_2O_4)(HCO_2)$ was prepared hydrothermally. It was found that this structure has previously been reported by J. C. Trombe [117]. The synthesis includes only oxalic acid as a ligand, a portion of which is decomposed in-situ to form formic acid after the breaking of the C–C bond. The FTIR and TGA data of this compound (Figure 4.9) suggested that it was anhydrous. The TGA shows no mass loss up to 450°C and the FTIR shows no O–H bond vibrations at 3600 cm^{-1}. The presence of an FTIR peak at 1427 cm^{-1} suggested that some of the oxalic acid may have decomposed to formic acid. This was confirmed by single crystal X-ray diffraction which revealed the structure shown in 4.10. Details of the structure refinement are given in Table 4.1.

The inorganic connectivity in the cerium oxalate formate compound is 1-dimensional and the organic connectivity is 2-dimensional. The zig-zag 1-D in-

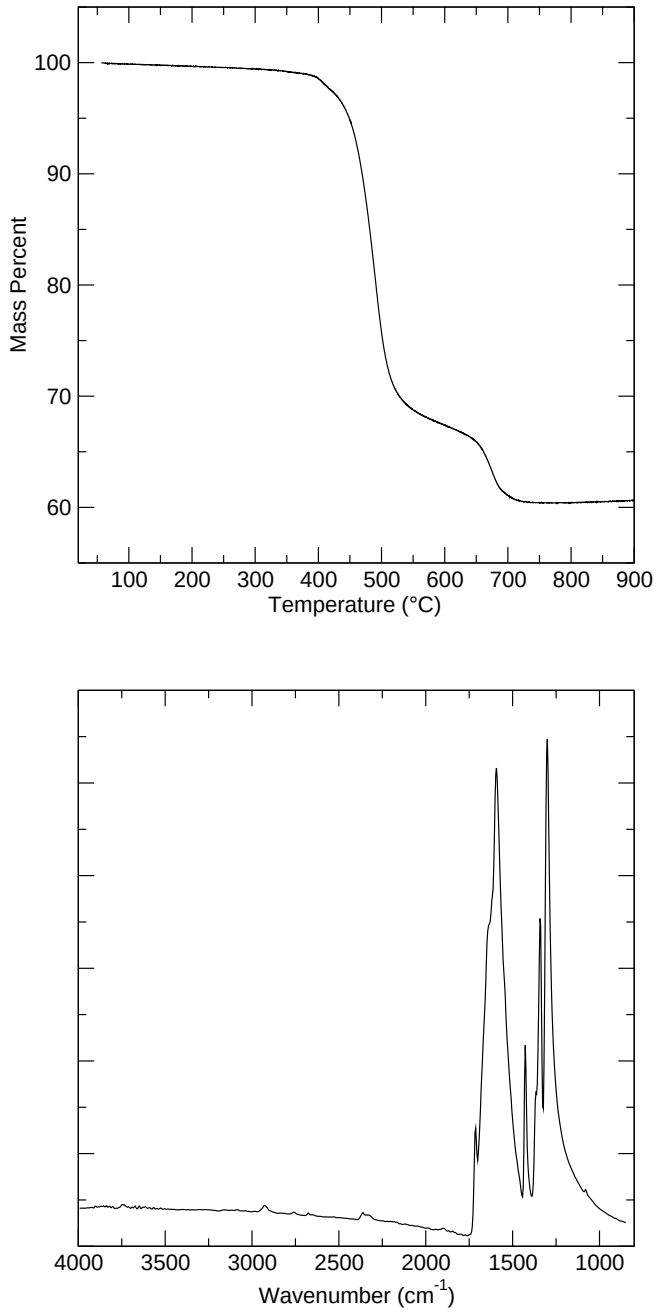

Figure 4.9: TOP: Thermogravimetric analysis of cerium oxalate formate, BOTTOM: FTIR spectra. The TGA data shows that the compound is stable to nearly 400°C and is likely anhydrous. This is supported by the lack of vibrational coupling around 3400 cm^{-1} in the FTIR data, although the peak at 1427 cm^{-1} suggests the presence of formic acid along with oxalic acid.

Table 4.1: Summary of single crystal diffraction data for structures cerium oxalate formate

	Cerium Oxalate Formate
Formula	$Ce(C_2O_4)(HCO_2)$
MW (g/mol)	271.95
System	Orthorhombic
Space Group	$Pnm2_1$
a (Å)	7.3963(5)
b (Å)	10.885(1)
c (Å)	6.7901(5)
V (Å^3)	546.66(7)
Z	4
μ (mm^{-1})	8.480
ρ (g·cm^{-2})	3.395
Measurement Temp (K)	120 K
Radiation Source	MoK_α
Radiation λ (Å)	0.71073
Scan Mode	Omega
Absorption Correction	SADABS
Solution Method	SHELX, $\|F\|^2$
2θ Range (°)	3.54–35.98
data/restraints/parameters	5551/1/52
R1/wR2 [I>2σ(I)]	1.71%/4.32%
R1/wR2 (all data)	1.74%/4.44%
Goodness of Fit	1.079
Dimensionality	2-dimensional
Hydration	Anhydrous

organic chain is built from face sharing 9-coordinate CeO_9 polyhedra. The chains form along the $\langle 100 \rangle$ direction. The formate anions bridge the chains to form sheets along the $\langle 010 \rangle$ direction. The oxalate anions then bridge the sheets along the $\langle 001 \rangle$ direction, completing the 2-D organic connectivity and the 3-D framework structure. The crystal habit of the compound are long rectangular prisms where the two long faces are the (100) and (010) planes and the short end is the (001) face, as shown in Figure 4.11. Detailed images of the bonds present with respect to the three crystallographic facets are shown in Figures 4.12, 4.13, and 4.14 with the faces drawn in and the uninvolved atoms omitted to further illustrate the anisotropy of the indentation directions (see below).

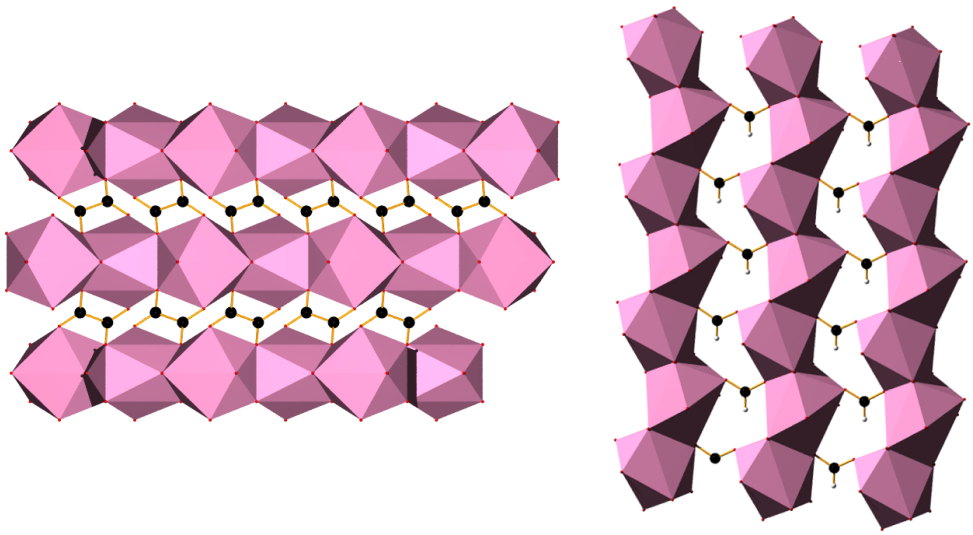

Figure 4.10: Anhydrous cerium oxalate formate structure. LEFT: Oxalate ligands connect nine coordinated edge sharing lanthanum polyhedra in one direction while in the other direction, RIGHT: formate ligands complete the coordination of the metal cations and link the chains to form a 2-D sheet.

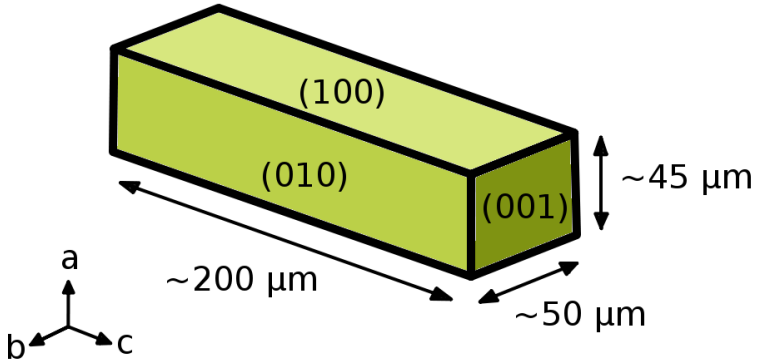

Figure 4.11: Typical crystal habit of cerium oxalate formate, showing rectangular prism shape and crystallographic faces as determined by single crystal diffraction

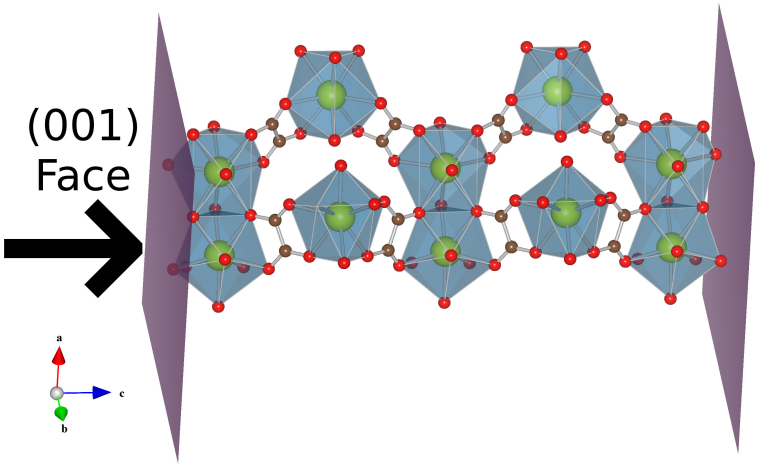

Figure 4.12: Bonding arrangements showing the (001) facet indentation direction dominated by oxalate bonding in cerium oxalate formate

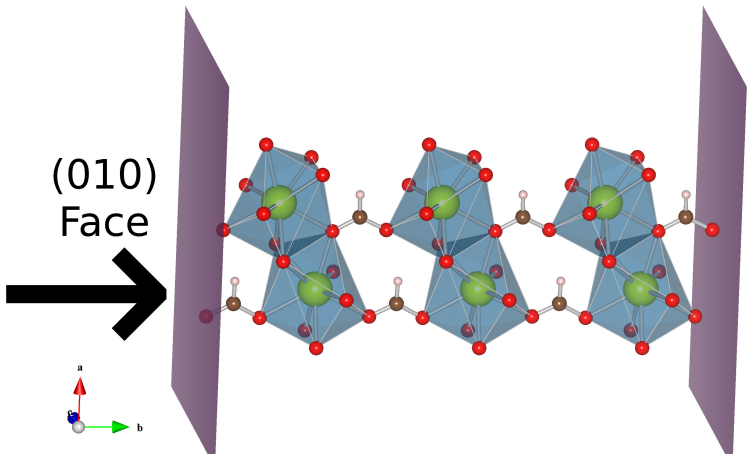

Figure 4.13: Bonding arrangements showing the (010) facet indentation direction dominated by formate bonding in cerium oxalate formate

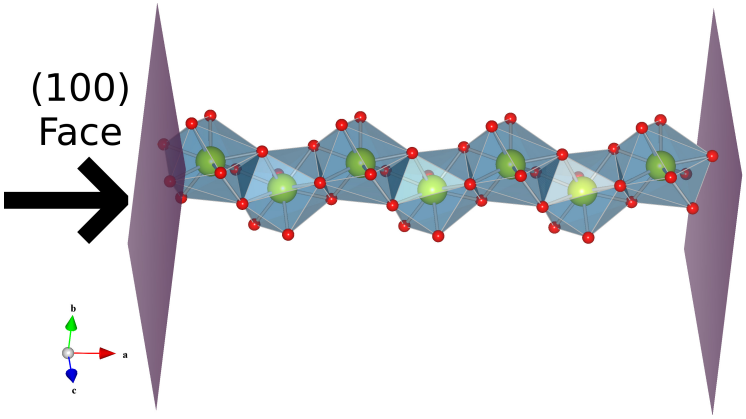

Figure 4.14: Bonding arrangements showing the (100) facet indentation direction dominated by inorganic metal-oxygen-metal bonding in cerium oxalate formate

4.3.2 Mechanical properties

Young's modulus and hardness were determined for cerium oxalate formate on each crystallographic facet and distinct properties were observed for each direction, as seen in Figure 4.15. Each data point is representative of 10 to 20 indentations. Table 4.2 shows the Young's modulus (E) and hardness (H) averaged for all of the penetration depths from 50 nm to 500 nm. The ratio of the average elastic moduli for the three orthogonal orientations was found to be E(001):E(010):E(100)= 1.82:1.00:1.20, indicating a difference in stiffness between the (010) and (001) planes of 82%. Thus when indented down the oxalate chains, a much greater stiffness (78 GPa) is measured than along the (010) formate ligands (43 GPa) or the (100) inorganic chains (52 GPa). The bidentate oxalate ligands can be very stiff, but not when loaded orthogonal to the backbone. The monodentate formate ligands do not have bonding parallel to the direction of loading but rather following the bond angle of the carboxylic acid group, leading to the lowest measured stiffness. The inorganic chains show a stiffness slightly higher than the formic acid but much less that than that of the oxalic acid chain. This was initially surprising, considering the other report from the Cheetham group on copper phosphonoacetates [137] showed the highest modulus along the metal-organic-metal inorganic chains. However, in that structure the copper atoms were tetrahedrally and octahedrally coordinated, which is a much more rigid and well defined polyhedra structure than the 9-coordinate polyhedra of the cerium. Also, the inorganic chains in this cerium structure show a metal-oxygen-metal bond angle of 132° unlike the nearly 180° bonding of the oxalate chains.

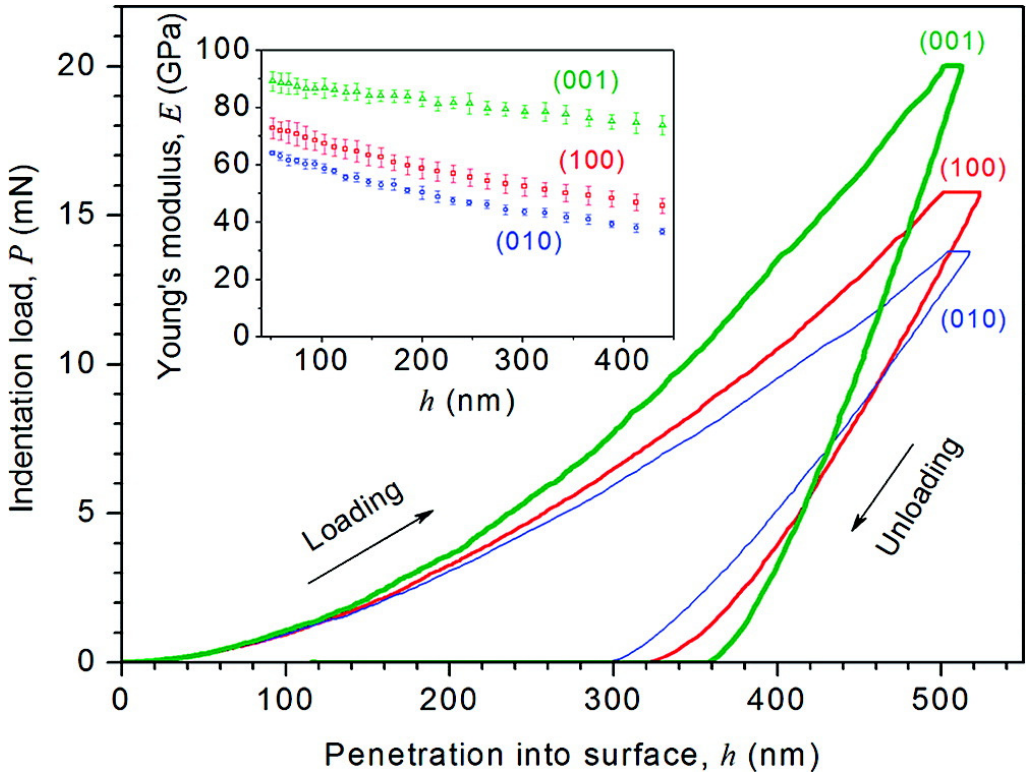

Figure 4.15: Loading and unloading of cerium oxalate formate for (001), (010), and (100) faces using sharp Berkovich tip, showing distinct behaviour for each direction. Inset: Young's modulus as a function of penetration

Table 4.2: Averaged anisotropic Young's modulus, hardness, and yield pressure for measurements from penetration depths of 50 nm to 500 nm for cerium oxalate formate

Crystal facet Primary structural element	(001) Oxalate	(010) Formate	(100) Inorganic Chains
Young's modulus E (GPa)	78.2 ± 2.5	43.0 ± 1.4	51.8 ± 2.8
Hardness H (GPa)	4.55 ± 0.14	3.94 ± 0.06	4.11 ± 0.07
Yield Pressure P_y (GPa)	2	1.2	1.4

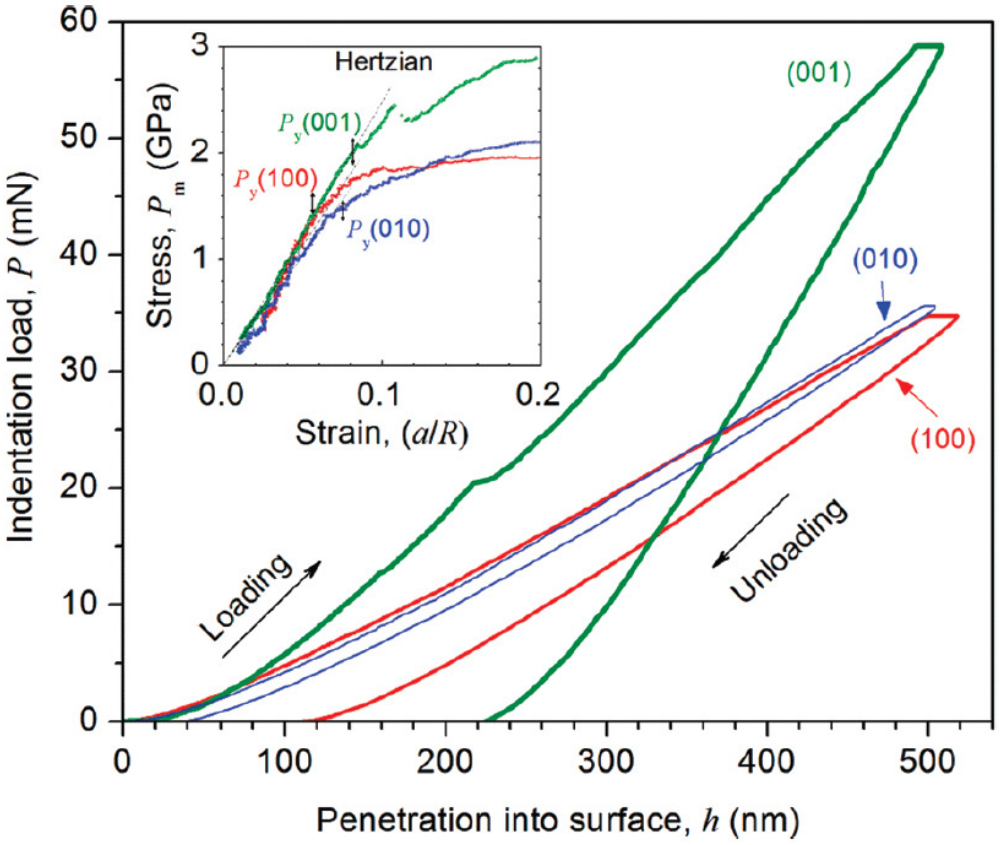

Figure 4.16: Loading and unloading of cerium oxalate formate for (001), (010), and (100) faces using spherical tip, showing distinct behaviour for each direction. Inset: stress–strain curves with yield pressure P_y indicated. Note the continued rise in stress for the (001) direction after the elastic-plastic transition, indicative of strain hardening behaviour.

4.3.3 Plastic deformation

Measurements of the plastic deformation characteristics of cerium oxalate formate were made using a spherical indenter rather than the pyramidal Berkovich tip. The strain field from this geometry is less localized, delaying the onset of plastic deformation and thus giving a better view of the elastic-plastic transition. Representative loading and unloading curves are shown in Figure 4.16, with the inset showing the calculated stress–strain curves. In the stress–strain curves, the yield pressure (P_y) is defined as the critical stress marking the onset of plastic deformation. This was the highest for the (001)-oriented facet probing along the length of the oxalate ligand, again showing that the mechanical properties are the strongest against yielding along the C–C backbone of the oxalate anion. As shown in Table 4.2, $P_{y,(001)} > P_{y,(100)} > P_{y,(010)}$. The percent of elastic work was calculated to be 91.7%, 72.3%, and 54.4% for the (010), (100), and (001) facet, respectively, at 500 nm indentation height, as shown in Table 4.3

In the stress–strain behaviour there is evidence of strain hardening but only in the (001) direction. The behaviour in that plane shows a power law response following $P_m \propto \left(\frac{a}{R}\right)^n$ where n is the strain exponent. This same behaviour is associated with dislocation entanglement in more fully characterized systems. Con-

Table 4.3: Elastic work for each crystal facet in cerium oxalate formate

Crystal Facet	Elastic Work W_{el} (nJ)	Total Work W_{tot} (nJ)	Percentage Elastic Work $\frac{W_{el}}{W_{tot}} \times 100\%$
(010)	7.36	8.03	91.7%
(100)	6.19	8.56	82.3%
(001)	7.12	13.1	54.4%

versely, almost purely elastic behaviour is seen for the (100) and (010) facets, most likely because there are less dislocation interactions along these directions. This explanation is supported by atomic force microscopy (AFM) of the residual indents following experiments using a Berkovich tip. Pile-up is a mechanical deformation phenomenon in which the height a material at just outside the border of the indenter rises up above the initial height as material is displaced. Pile-up generally reduces the accuracy of indentation measurements, but here the anisotropic pile-up behaviours give insight into the materials properties. In Figure 4.17, it can been seen that the least pile-up occurs for the (001) face, which is consistent with strain hardening. The (010) and (100) planes, whose stress–strain curves suggest a lesser extent of strain hardening in the plastic regime, show a large amount of pile-up. However, these images also show some cracking, indicated by the large peaks in several of the height profiles and larged raised areas in the images, that make this evaluation more difficult.

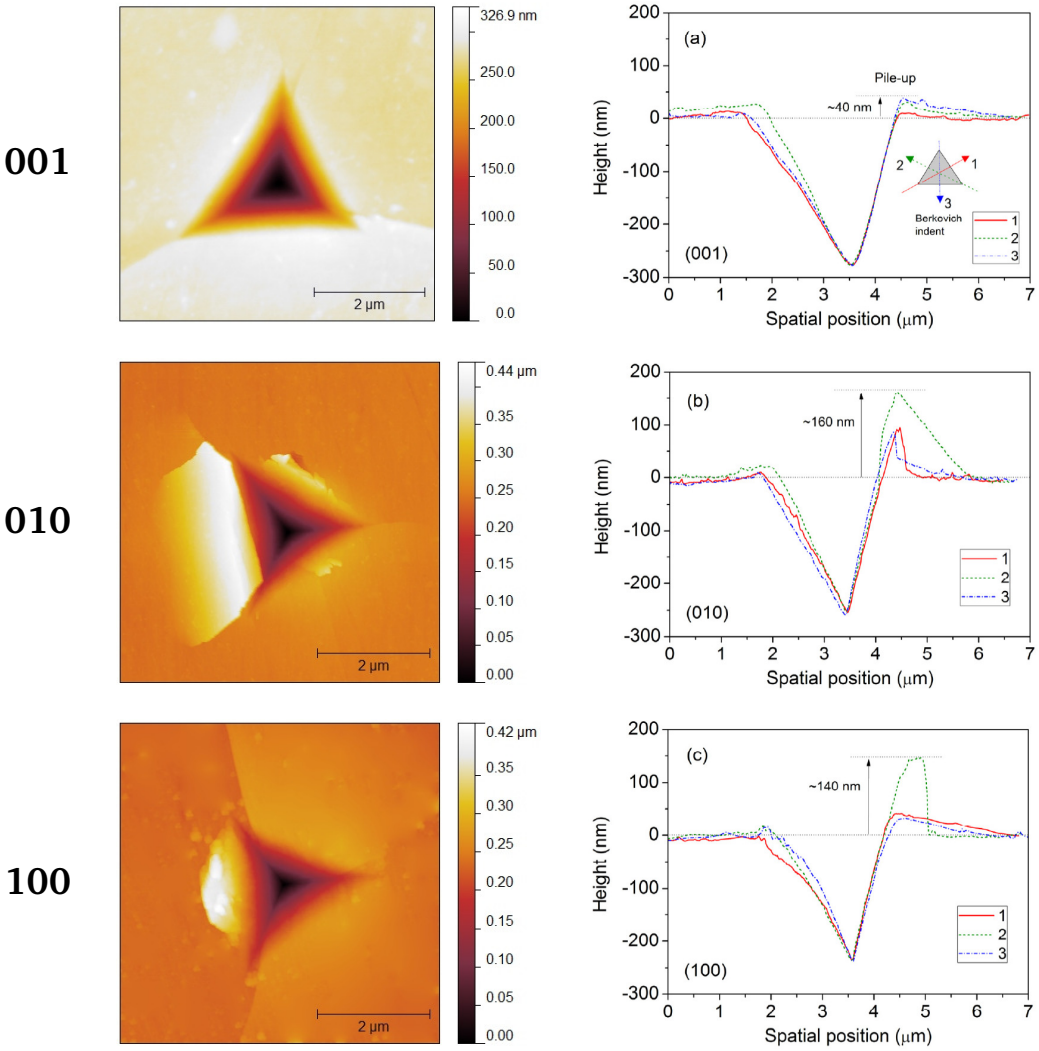

Figure 4.17: Representative AFM topologies and height profiles of residual Berkovich indents for the (001), (010), and (100) facets, (TOP, MIDDLE, BOTTOM, respectively). The red, blue, and green lines follow the trace across the crystal indent as shown in the (001) inset. Note the (010) and (100) images are rotated slightly anti-clockwise.

4.4 Summary

The oxalate formate system is a good model for studying the mechanical behaviour of inorganic-organic hybrids due do its relative structural simplicity. For a class of a compounds where the most common space group is $P\bar{1}$, the orthorhombic setting provides relatively high symmetry. The small ligand with multiple bonding arrangements can lead to a wide variety of interesting structures.

While the oxalate and oxalate/formate structures were not particularly exciting as luminescent materials, they provide useful insight into the physical properties of this class of materials, a nearly unexplored field at the time of this research. Understanding the mechanical properties of hybrid frameworks becomes important if they are to become device materials, as consideration must be given to processing constraints and device lifetime behaviour. The structural anisotropy of the oxalate formate, crystal habit alignment with atomic moieties, and ability to grow relatively large high quality single crystals make structure-property relationships easier to identify. Large anisotropies in the Young's modulus, hardness, and plastic deformation characteristic were found between the crystal facets of cerium oxalate formate crystals. Particularly, it was shown that indenting along the oxalate-dominated direction resulted in comparatively high modulus and hardness measurements. In that direction, strain hardening behaviour indicative of dislocation entanglement occurs, while in the other crystal directions, the deformation occurs without hardening [109, 140]. From these measurements it was shown that ligand behaviour and alignment with crystal faces can be very important in predicting mechanical properties and that the inorganic chains in a compound are not necessarily the stiffest element. This is not without precedent given the extremely impressive mechanical properties that have been reported for carbon

nanotubes, such as tensile moduli along the length of the tube on the order of 1000 GPa, where the carbon–carbon bonding is very carefully constructed [141].

The data points collected for these materials, as well as some other hybrid framework materials which have been studied since the time this work was carried out [136, 137, 142, 143], are plotted on an Ashby plot of Elastic modulus/hardness in Figure 4.18. The impressive strength of the oxalate-formate structures is apparent here; nearly approaching the values of zirconia and other classical ceramic materials. It is also the strongest of all the hybrid frameworks studied to date. As a consequence of this work, we can confidently conclude that dense inorganic-organic frameworks can exhibit mechanical properties that are comfortably within the range required for a wide range of device applications, including solid state lighting.

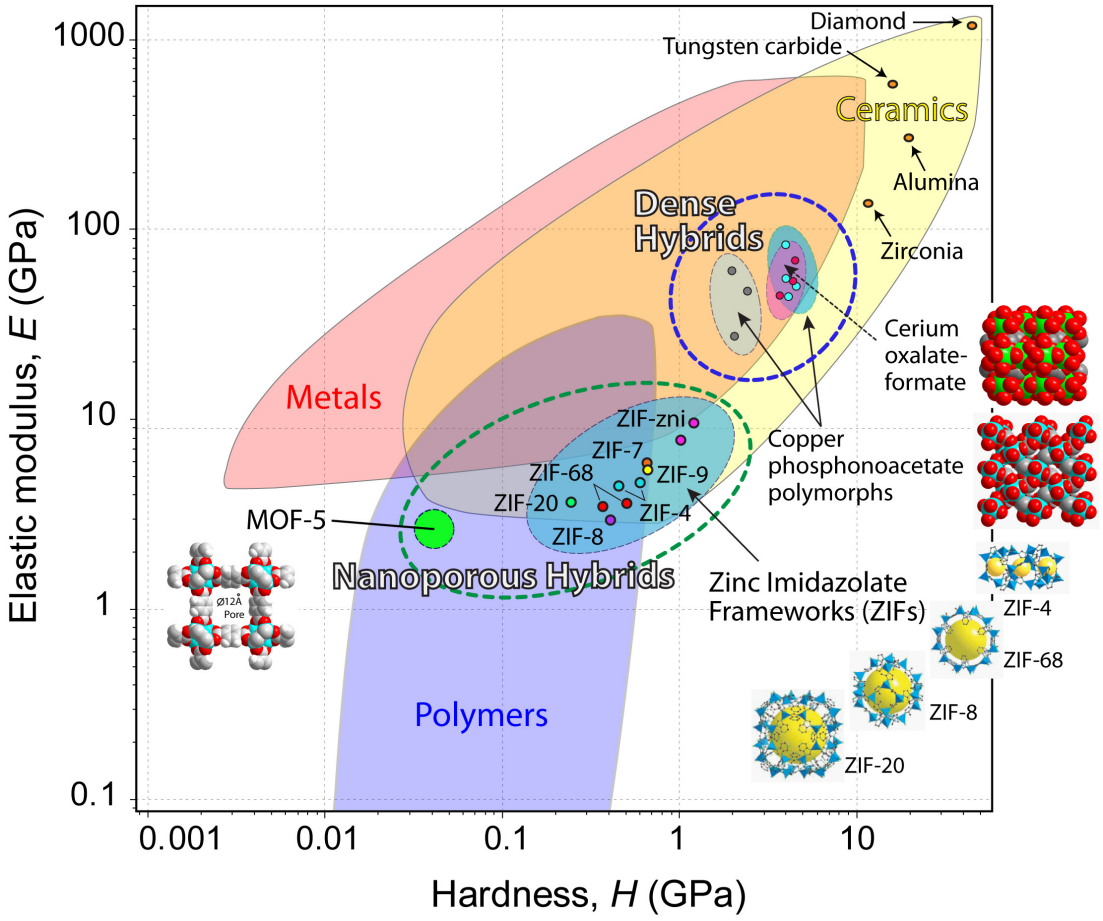

Figure 4.18: Ashby plot showing the elasticity and plasticity of various framework materials with respect to classical metals, ceramics, and polymers. The data points for the cerium oxalate formate show very high strength, approaching nearly that of zirconia. The more porous frameworks show lower moduli and hardness, as expected.

The research described in this chapter was carried out in collaboration with Jin-Chong Tan who performed the mechanical testing and analysis. It has been published in the Journal of the American Chemical Society as: J. C. Tan and J. D. Furman and A. K. Cheetham. "Relating Mechanical Properties and Chemical Bonding in an Inorganic-Organic Framework Material: A Single-Crystal Nanoindentation Study." *J. Am. Chem. Soc.*, **131**, 14252 (2009). [DOI: 10.1021/ja9060307].

Chapter 5

Anthraquinone dicarboxylic acid frameworks

5.1 Introduction

In the previous chapter, the photoluminescence and mechanical properties of a dense cerium oxalate formate framework were evaluated for use in solid state lighting devices. It became apparent in the course of that research that luminescent quenching from coordinated water molecules was a major problem. Additionally, achieving blue excitation in an antenna compound requires an organic molecule that is larger than those that typically forms highly stable framework framework structures. Broad emission spectra in the green and red, available mainly by incorporating Ce^{3+} and Eu^{2+}, are difficult to realize in an inorganic-organic structure because the ligand field strength needed to shift trivalent cerium emission into the visible range is not available and the divalent state of europium is not stable under aqueous reaction conditions. A new approach is taken here, by moving both the photoluminescence excitation and emission processes onto the

ligand. It is shown that by including an intrinsically luminescent organic molecule in an inorganic-organic structure, its thermal and chemical stability, as well as its luminescent efficiency, might be increased. Luminescent quenching from coordinated water molecules providing non-radiative relaxation pathways is eliminated, or at least reduced, because the photoluminescence is moved away from the metal ions. Furthermore, we shall show that the broad emissions needed for can be achieved in a hybrid framework system.

Creating new framework phosphor materials with ligand-based luminescence requires the selection of commercially available ligands with suitable characteristics or synthesizing new organic molecules. Polycyclic organics such as naphthalene and anthracene are known to show photoluminescence properties, but the synthesis of dicarboxylic acid derivatives is complicated by limited solubility and production of side products. The ligand anthraquinone-2,3-dicarboxylic acid, shown in Figure 5.1 is a commercially available derivative of anthracene. The 9 and 10 positions of the fused polycyclic anthracene are substituted with ketone groups and dicarboxylic acid groups are attached at the 2 and 3 positions. The structure can also be viewed as 1,4-benzoquinone fused between molecules of benzene and phthalic acid. This molecule was selected as a potential luminescent ligand as it was thought that the electron withdrawing ketone groups in the centre fused ring would shrink the HOMO–LUMO gap as compared to anthraquinone and thus red–shift the emission spectra from the typical blue/violet seen for anthracene compounds [144]. Prior to this work, no framework structures have been published using the anthraquinone-2,3-dicarboxylic acid ligand.

The *ortho* arrangement of the dicarboxylic acid groups in this ligand is generally not ideal for synthesizing hybrid frameworks with 3-dimensional connectivity. Higher connectivity is desired because it is typically accompanied by higher ther-

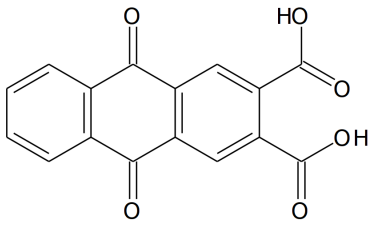

Figure 5.1: Anthraquinone-2,3-dicarboxylic acid (H_2AQDC).

mal stability and structural rigidity. While the 2,3-dicarboxlate ligand is available commercially, the 2,6- and 2,7- species are not. Attempts were made to synthesize those ligands so that a direct comparison between anthraquinone ligands with different binding modes could be made, but the compounds could not be obtained with sufficient purity.

Yamanashi et al. studied the luminescence of anthraquinone at 77 K and at room temperature in various solvents [145]. They observed three strong emission peaks, located approximately at 450 nm, 500 nm, and 540 nm, when excited in the UV at low temperatures. The position of these peaks shifts slightly depending on the solvent. Scott and Watson reported on the relative intensities of the luminescent emission peaks in anthraquinone [146]. Their conclusions were in agreement with earlier work by Drott and Dearman [147], who assign the visible fluorescent emissions to singlet π–π^* transitions. They also assigned an n–π^* phosphorescent transition in the system. They consider anthraquinone as essentially behaving like two weakly interacting *ortho*-substituted benzene molecules from a luminescence standpoint, and the two lower energy emissions are assigned to two excited dipole states of benzene. The optical properties of the ligand shown in Figure 5.1 have not been reported.

Four new structures containing anthraquinone dicarboxylic acid (AQDC) and

calcium, zinc, manganese, and nickel are presented here. Their crystal structures, luminescent behaviour, and thermogravimetric analysis are presented.

5.2 Experimental methods

5.2.1 Synthesis

2,3-anthraquinone dicarboxylic acid was obtained from TCI America. All other chemicals and reagents were obtained from Sigma-Aldrich and used without further purification. Compounds were prepared by combining 0.02 mmol of H_2AQDC with 0.02 mmol metal acetate (metal: Ca, Mn, Ni, Zn) in 5 mL H_2O in a sealed glass pressure vessel and heated at 90°C for 2 days. Crystals were recovered by filtration while hot to prevent recrystallization of unreacted ligand on cooling, and washed in water and acetone. Synthesis of compounds containing other metals, particularly the remaining alkaline earth metals magnesium, strontium, and barium, and d^{10} cadmium, were attempted but crystal structures were not obtained.

5.2.2 Structure of anthraquinone frameworks

Structures were determined using single crystal X-ray diffraction. Data were collected on a Siemens SMART-CCD diffractometer at UCSB equipped with a normal focus, 2.4 kW sealed tube X-ray source (MoKα radiation, λ = 0.71073 Å) operating at 45 kV and 30 mA. Suitable single crystals were selected under a polarizing microscope and glued to a glass fibre and a hemisphere of intensity data was collected at room temperature. Data were integrated with Bruker Saint version 6.02 [61]. SADABS [62] was used to perform an empirical absorption correct and

structures were then solved by direct methods and difference Fourier synthesis and were refined against $|F|^2$ using the SHELXL software package [63]. All extinction coefficients refined to within three esd's of zero and were therefore removed from the refinements. Non-hydrogen atoms were refined anisotropically. Riding hydrogen atoms were assigned to the carbon atoms on the AQDC ligands. Hydrogen atoms on the water molecules were found in the Fourier difference map and were refined isotropically. Hydrogen atoms were restrained to chemically appropriate positions, resulting in increased residual error. Room temperature powder X-ray diffraction data were obtained via the mail-in service of Argonne National Laboratory's Advanced Photon Source beamline 11-BM in order to to determine bulk phase purity. Structure models were refined using the Rietveld method as implemented in GSAS and EXPGUI to fit the collected patterns [106].

5.2.3 Material properties

Thermogravimetric analysis was carried on on a Mettler 851e in air. Samples were loaded into alumina crucibles and heated at 10°C per minute to 800°C. Luminescence measurements were carried out using a standard Acton spectrophotometer with samples dispersed in acetone, contained in NMR tubes, and cooled in an optically transparent dewar of liquid nitrogen to 77 K. UV-visible absorption spectra were collected using a Shimadzu UV3600 spectrometer fitted with an integrating sphere. Samples were blended 20:1 by weight in $BaSO_4$ and measured in diffuse reflectance mode.

Table 5.1: Summary of anthraquinone framework compounds

	CaAQDC	MnAQDC	NiAQDC	ZnAQDC
Formula	$CaC_{16}H_{14}O_{10}$	$MnC_{16}H_{14}O_{10}$	$NiC_{16}H_{20}O_{15}$	$ZnC_{16}H_{14}O_{10}$
Space Group	$P\bar{1}$	$P\bar{1}$	$P2_1/c$	$P\bar{1}$
Bound Water	2	2	5	2
Pore Water	2	2	2	2
Inorg. Dimen.	0-D	0-D	0-D	0-D
Organic Dimen.	2-D	2-D	0-D	1-D
π-π dist.	3.65 Å	3.48 Å	3.58 Å	3.46 Å

5.3 Results

5.3.1 Crystal structures

Results of the single crystal diffraction experiment are shown in Table 5.2 and the key features are summarized in Table 5.1. The dimensionality of the structures is described in terms of both the inorganic connectivity, where metal–oxygen–metal bonds give rise to an extended structure, and organic connectivity, where bonding through the ligands gives rise to the extended structure, as described in Cheetham et al.[35]. This is also given as a shorthand I^xO^y where x is the inorganic dimensionality and y is the organic dimensionality, and $x + y$ is the overall dimensionality of the structure. The crystal structure of the parent ligand has not been reported in the literature and attempts to recrystallize X-ray quality samples were unfortunately unsuccessful. The calcium containing structure, abbreviated CaAQDC, formed with the composition $Ca(AQDC)(H_2O)_2{\cdot}2H_2O$, where the AQDC anion is $C_{16}H_6O_6^{2-}$. The asymmetric unit of CaAQDC consists of a single 2,3-anthraquinone molecule bound to a 7-coordinate calcium cation, as shown in Figure 5.2. The CaO_7 polyhedron is completed by oxygen atoms from adjacent

AQDC ligands and two bound water molecules. Two zeolitic water molecules sit in the pore space. The Ca polyhedra form edge-sharing dimers (Ca-Ca distance 3.88 Å) that are bridged by the carboxylic acid groups to form a 2-dimensional sheet, as seen in Figure 5.3. The ligands then extend outward from this sheet and are interdigitated with those from the adjacent sheet, π-stacked at a separation of 3.65 Å, as seen in Figure 5.4. The manganese containing compound, abbreviated MnAQDC, formed with the composition $Mn(AQDC)(H_2O)_2{\cdot}2H_2O$ and is isostructural to CaAQDC, although the π stacking is reduced to 3.48 Å due to the increased cation size.

The nickel containing compound, abbreviated NiAQDC, formed with the composition $Ni(AQDC)(H_2O)_5{\cdot}2H_2O$. The basic unit of NiAQDC consists of a 2,3-anthraquinone ligand with a unidentate bond through one of its carboxylic acid oxygen atoms to a NiO_6 octahedron, as shown in Figure 5.5. The octahedron is completed by 5 bound H_2O molecules. Each asymmetric unit consists of two isolated ligand-metal complexes along with 4 zeolitic water molecules. The compound is molecular and the extended structure is formed by a network of hydrogen bonding between the bound water polyhedra and π-stacking of the ligands at a separation of 3.58 Å, as seen in Figure 5.9.

The zinc containing compound, abbreviated ZnAQDC, formed with the composition $Zn(AQDC)(H_2O)_2{\cdot}2H_2O$. The asymmetric unit of ZnAQDC is similar to that of CaAQDC, although in this case the local coordination of the ZnO_5 trigonal bipyramid polyhedra is completed by oxygen atoms from two adjacent ligands and two axially bound water molecules, as seen in Figure 5.7. A 1-dimension ribbon of ZnO_5 dimers (Zn-Zn distance 3.924 Å, Figure 5.8) is formed by carboxylate group bridging of the metal centres. A hydrogen-bonded extended network, seen in Figure 5.9, is formed by π-stacking between the ligands of adjacent ribbons at

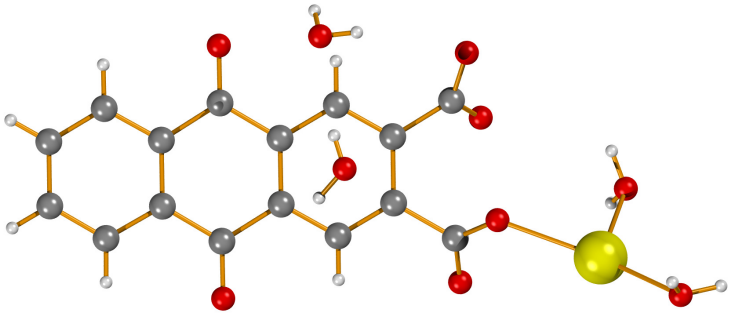

Figure 5.2: Asymmetric unit of CaAQDC and isostructural MnAQDC

a separation of 3.46 Å.

The equivalent isotropic atomic displacement parameters for the carbon atoms of the ligand were extracted from the single crystal structure data and plotted as a function of their separation from the metal cation in Figure 5.10. These can be seen as an estimate of the thermal vibrations in the system. This plot shows a steep increase in mean squared displacement on moving away from the bound metal atoms. In addition, the anisotropic nature of that displacement, shown in Figure 5.11, indicates that the ligands librate as a rigid body around an axis formed by the metal centres.

Table 5.2: Anthraquinone single crystal solution and structure data. Dimensionality is given as inorganic connectivity and the metal-oxygen-metal connectivity, as desribed in Cheetham et al.[35]

	CaAQDC	MnAQDC	NiAQDC	ZnAQDC
Formula	$CaC_{16}H_{10}O_8{\cdot}2H_2O$	$MnC_{16}H_{10}O_8{\cdot}2H_2O$	$NiC_{16}H_{16}O_{11}{\cdot}2H_2O$	$ZnC_{16}H_{10}O_8{\cdot}2H_2O$
MW (g/mol)	406.35	421.21	479.03	431.64
Crystal System	Triclinic	Triclinic	Monoclinic	Triclinic
Space Group	$P\bar{1}$	$P\bar{1}$	$P21/c$	$P\bar{1}$
a (Å)	5.960(2)	5.799(2)	16.308(3)	7.629(2)
b (Å)	7.634(3)	7.477(3)	7.410(1)	7.843(2)
c (Å)	18.603(7)	18.493(7)	16.183(3)	15.045(5)
α (°)	90.145(6)	89.639(6)	90	91.409(6)
β (°)	95.804(6)	85.173(6)	106.064(4)	95.784(5)
γ (°)	97.105(6)	83.485(7)	90	115.160(5)
V (Å^3)	835.5(6)	793.8(5)	1879.2(7)	808.4(4)
Z	2	2	4	2
μ (mm^{-1})	0.433	0.891	1.104	1.578
ρ (g·cm^{-2})		1.762	1.693	1.773
Measurement Temp (K)	298	298	298	298
Radiation Source	Mo$K\alpha$	Mo$K\alpha$	Mo$K\alpha$	Mok_α
Radiation λ (Å)	0.71073	0.71073	0.71073	0.71073
Scan Mode	Omega	Omega	Omega	Omega
Absorption Correction	SADABS	SADABS	SADABS	SADABS
Solution Method	SHELX,$\lvert F\rvert^2$	SHELX, $\lvert F\rvert^2$	SHELX, $\lvert F\rvert^2$	SHELX, $\lvert F\rvert^2$
2θ Range (°)	2.97-29.36	2.21-25.68	1.30-26.02	2.73-26.02
data/parameters/restraints	3224/270/12	2965/274/12	3675/313/21	3124/269/12
R1/wR2 [I>2σ(I)]	5.00%/10.35%	8.06%/18.26%	6.22%/12.84%	6.63%/10.36%
R1/wR2 (all data)	8.75%/11.80%	13.59%/20.93%	11.31%/15.87%	16.81%/13.45%
Goodness of Fit	0.817	1.041	1.083	0.947
dimensionality	I^0O^2	I^0O^2	I^0O^0	I^0O^1
hydration	2 bound, 2 pore-space	2 bound, 2 pore-space	5-bound, 2 pore-space	2-bound, 2 pore-space

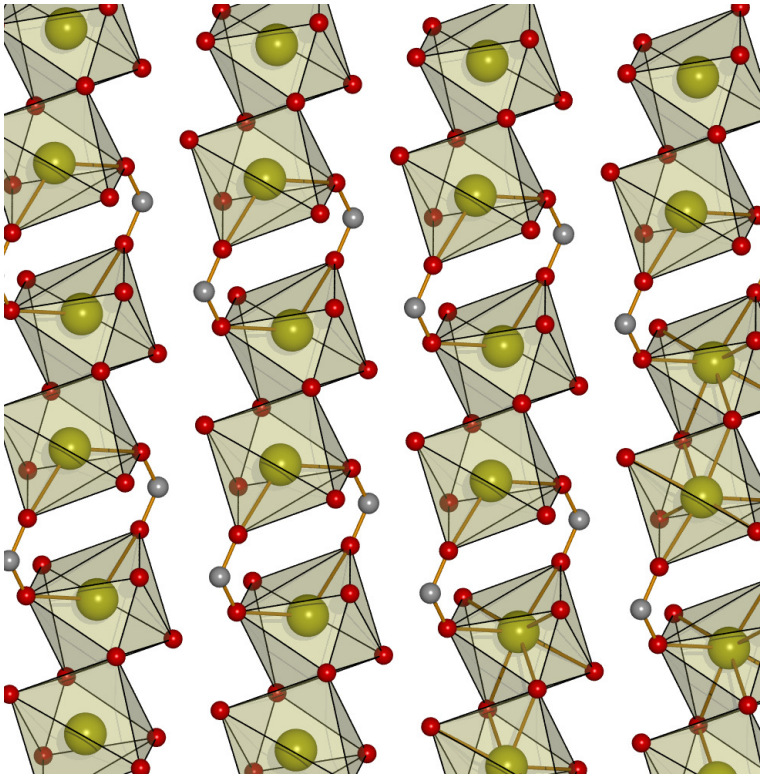

Figure 5.3: Calcium sheets in CaAQDC and MnAQDC, showing isolated edge sharing MO_7 dimers, bridged by carboxylic acid groups. Hydrogen atoms are omitted for clarity.

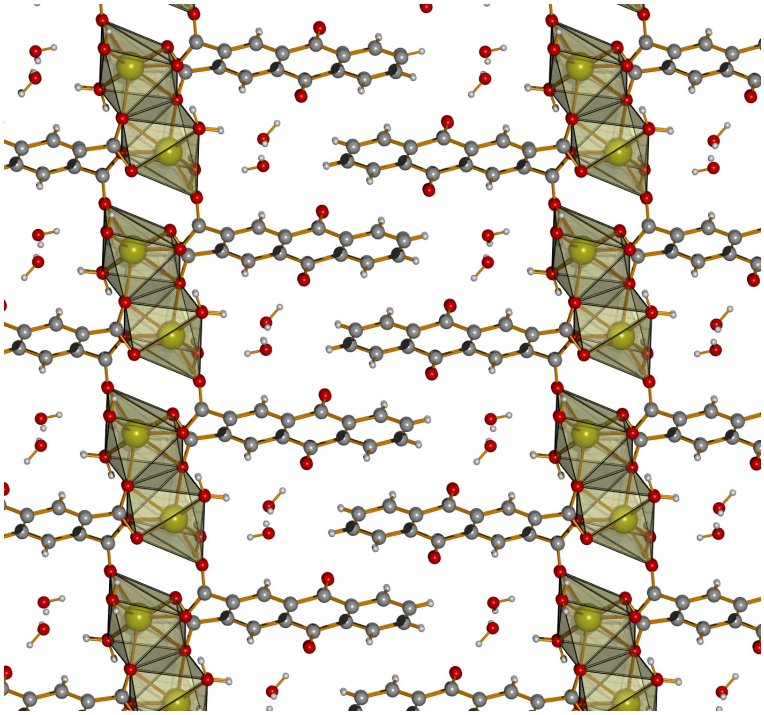

Figure 5.4: Extended structure of CaAQDC and MnAQDC

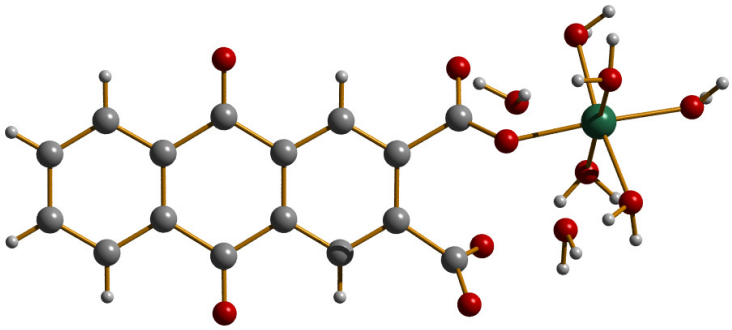

Figure 5.5: Asymmetric unit of NiAQDC

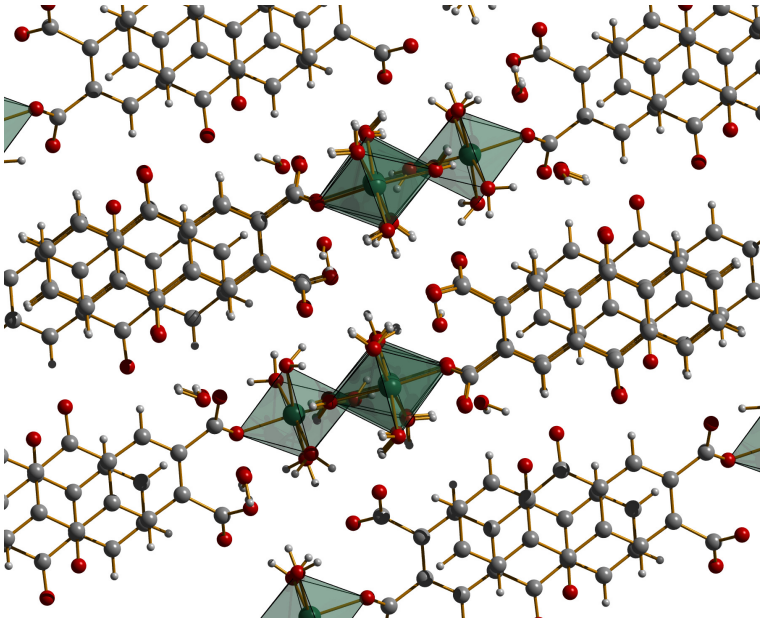

Figure 5.6: Extended structure of NiAQDC

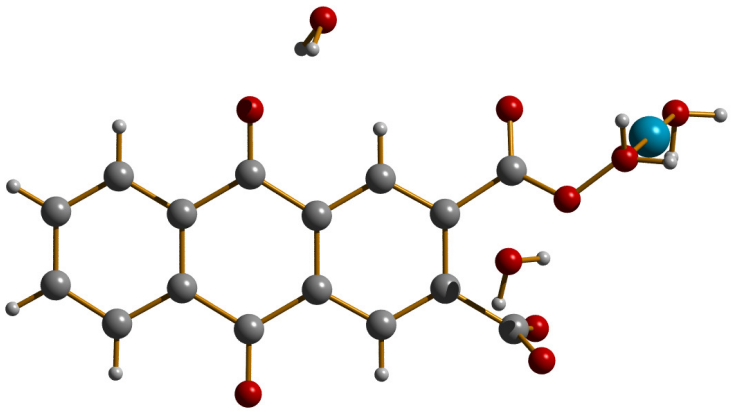

Figure 5.7: Asymmetric unit of ZnAQDC

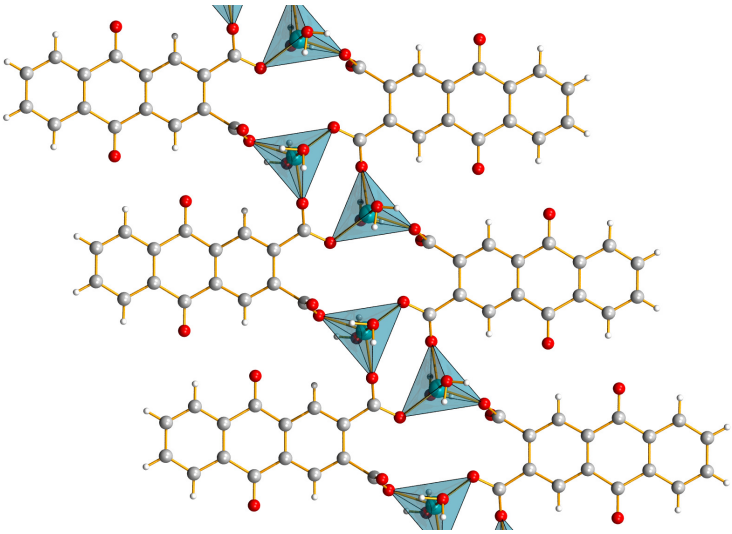

Figure 5.8: 1-D ribbon structure of ZnAQDC

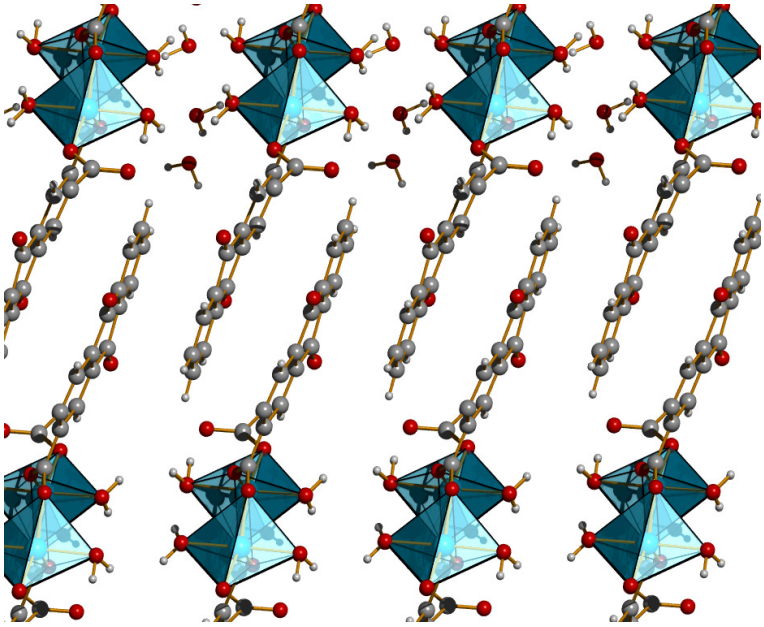

Figure 5.9: Extended structure of ZnAQDC

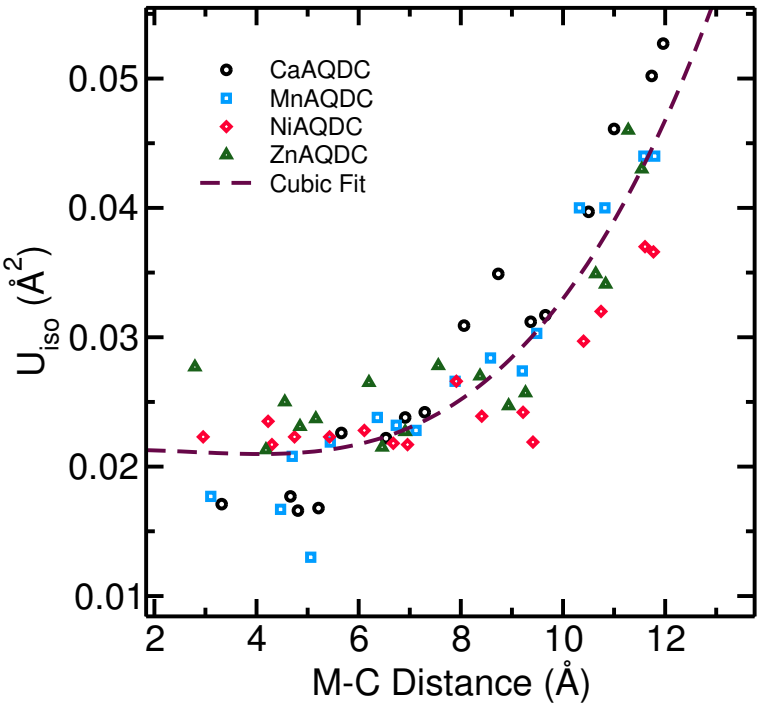

Figure 5.10: Equivalent isotropic atomic displacement parameters of the carbon atoms in anthraquinone containing frameworks plotted as a function of their distance from the associated metal atom. Note the large increase in displacement parameters moving away from the bound metal site, suggesting the presence of large thermal vibrations in the system.

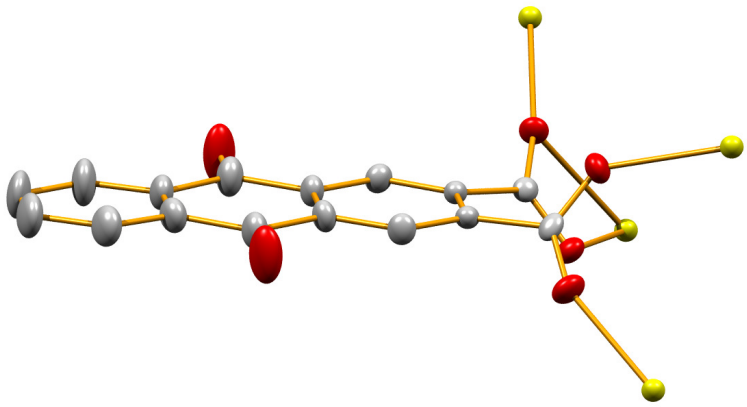

Figure 5.11: Anisotropic displacement parameters for a portion of the CaAQDC structure, showing the increase in displacement perpendicular to the ligand backbone on increasing distance from the metal ions. Ellipsoids plotted at 50% probability.

5.3.2 Powder diffraction

High resolution powder diffraction spectra were collected at Argonne National Laboratory beamline 11-BM to verify bulk homogeneity in the prepared samples. The high flux and sharp wavelength distribution reveal impurity phases that would be otherwise invisible using a standard laboratory source X-ray diffractometer. Data for CaAQDC, MnAQDC and NiAQDC were collected using synchrotron radiation with a wavelength (λ) of 0.458 Å. Data for ZnAQDC were collected using 0.413 Å synchrotron radiation. Plots of the collected data and refined structures are shown in Figures 5.12, 5.13, 5.14, and 5.15. A summary of the refined crystal parameters and refinement statistics is shown in Table 5.3. These refinements indicate that the compounds have excellent phase purity.

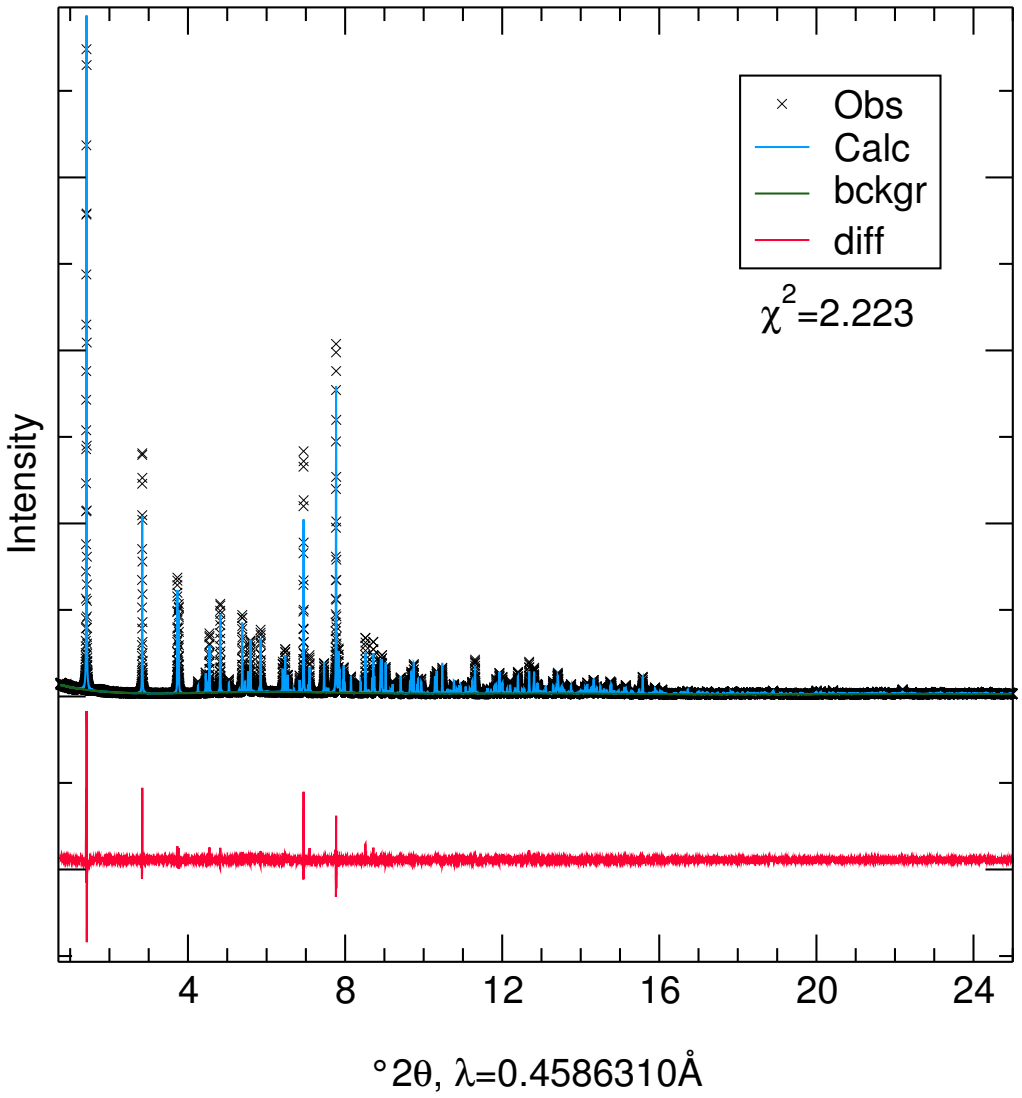

Figure 5.12: Synchrotron powder diffraction data for CaAQDC and Rietveld refinement of the model initially determined by single crystal experiment.

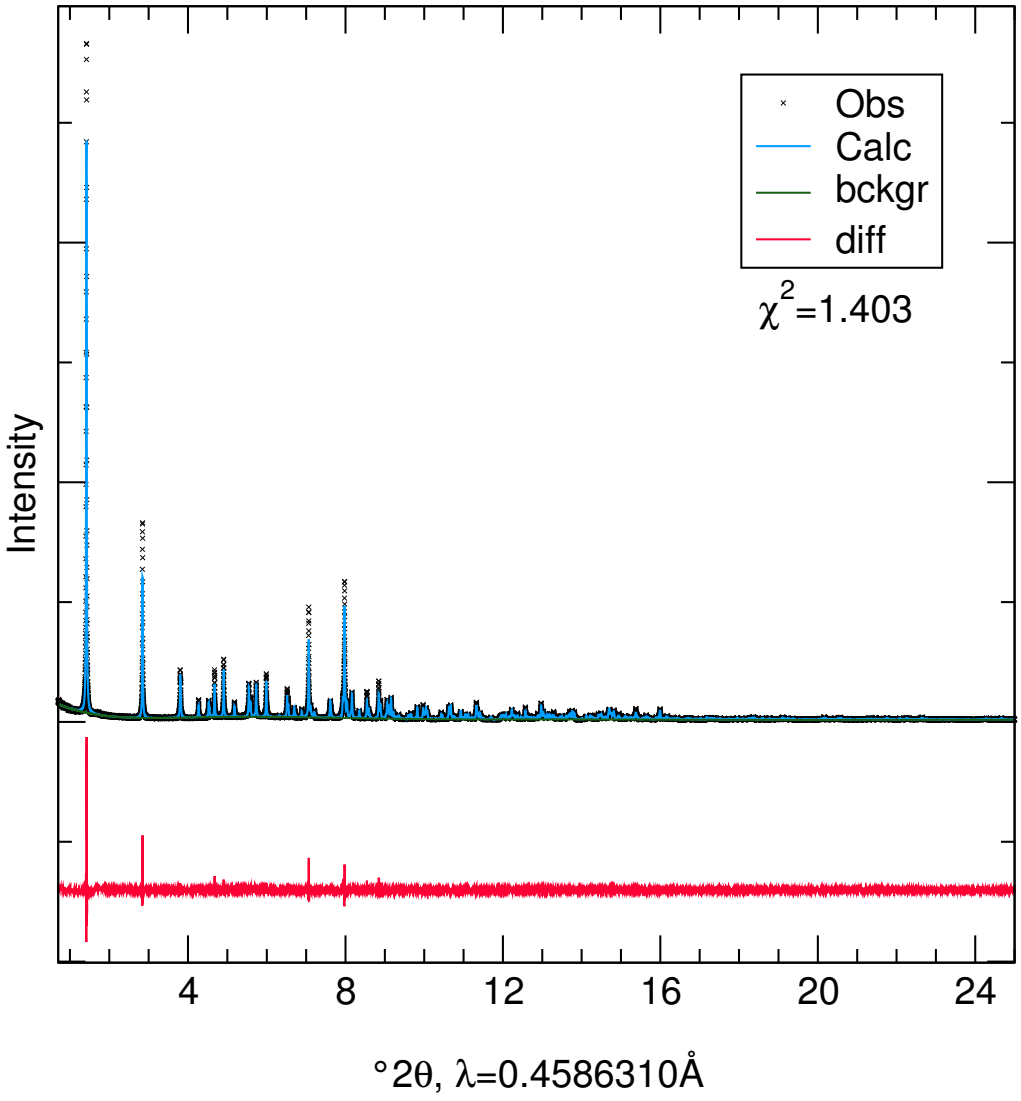

Figure 5.13: Synchrotron powder diffraction data for MnAQDC and Rietveld refinement of the model initially determined by single crystal experiment.

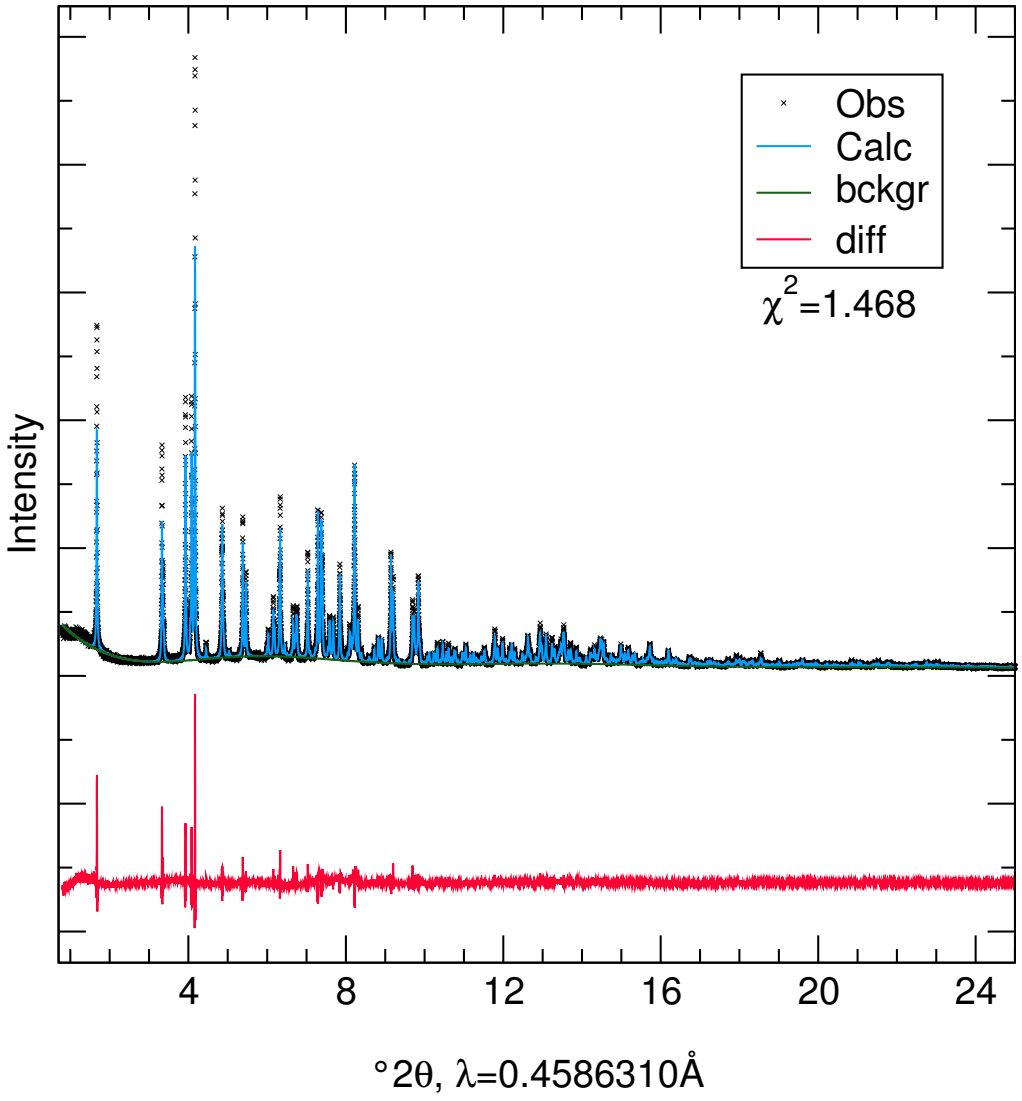

Figure 5.14: Synchrotron powder diffraction data for NiAQDC and Rietveld refinement of the model initially determined by single crystal experiment.

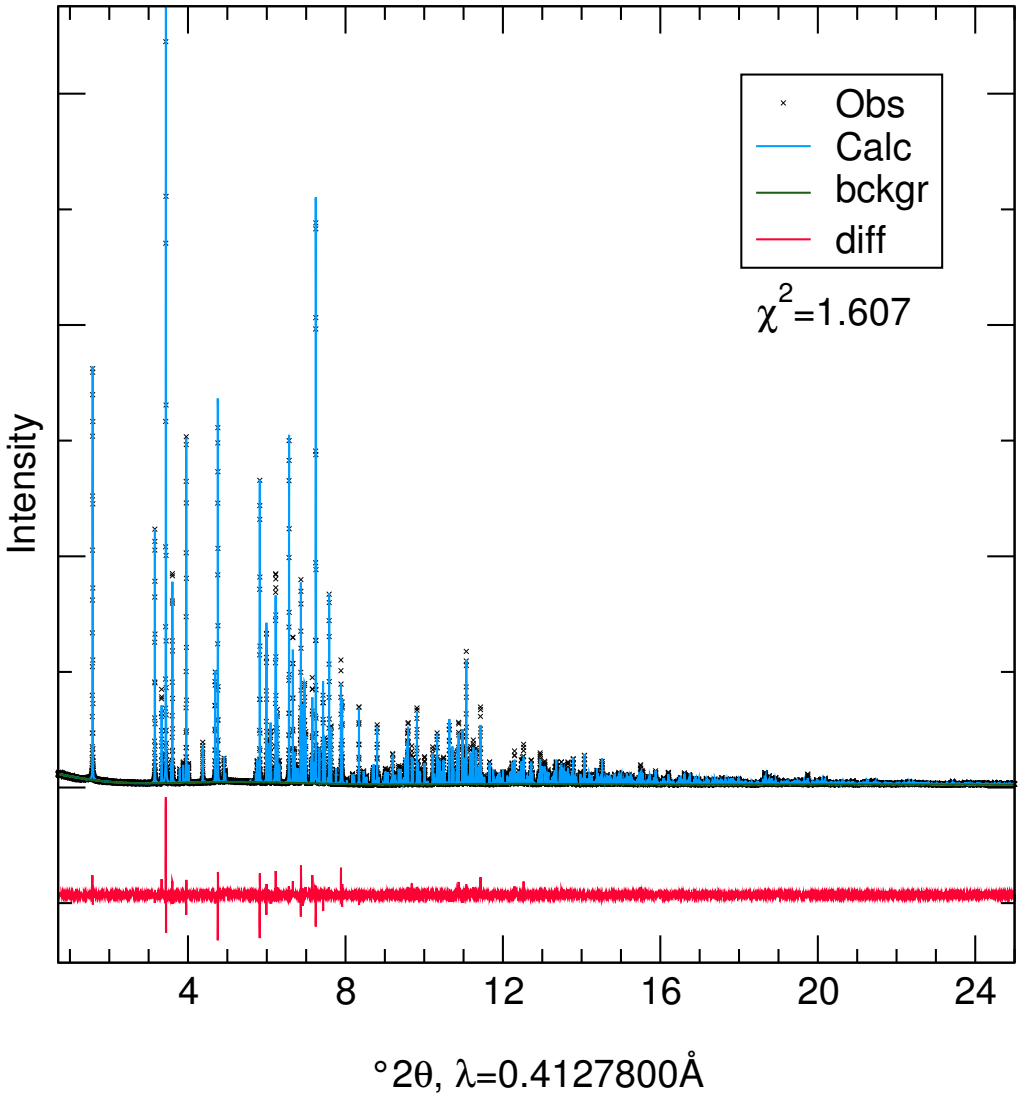

Figure 5.15: Synchrotron powder diffraction data for ZnAQDC and Rietveld refinement of the model initially determined by single crystal experiment.

Table 5.3: Structure and refinement parameters from synchrotron powder X-ray diffraction data

Compound	CaAQDC	MnAQDC	NiAQDC	ZnAQDC
Formula	$C_{16}H_{14}CaO_{10}$	$C_{16}H_{14}MnO_{10}$	$C_{16}H_{20}NiO_{13}$	$C_{16}H_{14}O_{10}Zn$
Crystal System	triclinic	triclinic	monoclinic	triclinic
Space Group	$P\bar{1}$	$P\bar{1}$	$P2_1/c$	$P\bar{1}$
a (Å)	5.80099(6)	5.80099(6)	16.30970(15)	7.654318(10)
b (Å)	7.48853(6)	7.48853(6)	7.41339(5)	7.865764(12)
c (Å)	18.53285(17)	18.53285(17)	16.19017(15)	15.096604(20)
α (°)	89.7232(11)	89.7232(11)	90.0	91.41250(10)
β (°)	85.1458(9)	85.1458(9)	106.1139(7)	95.76910(10)
γ (°)	83.5310(8)	83.5310(8)	90.0	115.10700(10)
Volume (Å^3)	797.080(10)	797.080(10)	1880.649(23)	816.5880(10)
Observations	49149	49199	48199	48501
Variables	21	85	24	20
wRp	11.55%	10.75%	9.31%	9.87%
Rp	9.73%	9.09%	8.03%	8.04%
χ^2	2.223	1.403	1.468	1.607

5.3.3 Luminescence

No measurable luminescence was observed at room temperature for any samples due to thermal quenching. Solid state luminescence measurements were therefore carried out at 77 K on the diprotonated ligand H_2AQDC, and on the framework compounds CaAQDC, MnAQDC, and ZnAQDC, as shown in Figure 5.16. When cooled to 77 K and excited at λ=365 nm, the ligand H_2AQDC shows broad emission with peaks at 469 nm, 508 nm, 556 nm, and 608 nm. The excitation spectrum, collected at 520 nm, shows a maxima at 335 nm, decreases slowly beginning at 370 nm, and then sharply at 440 nm. The calcium-containing CaAQDC shows significantly broader peaks that spread into a very broad emission centred at 530 nm. To the eye the sample appeared a greenish-white colour. The excitation spectrum is nearly constant from 300 nm up to a steep decrease that begins at 435 nm, just short of what is needed for today's solid state lighting devices. The excitation spectra of ZnAQDC and MnAQDC are similar to that of H_2AQDC with strong absorption in the 300 nm to 350 nm range. The ZnAQDC emission shows several resolved peaks, blue-shifted approximately 40 nm from those of the H_2AQDC. For the MnAQDC sample, a broad, red/near-IR peak with a maximum at 715 nm was observed. Visually the manganese-containing sample appears a dim red, as most of its luminescence is beyond the range of the eye and for the part that does overlap with the visible spectrum our sensitivity is limited. The origin of this significant red-shift was not confidently determined, and the features of the luminescence in all samples were difficult to interpret due to the limited comparison points in the literature. It is possible that the red/IR luminescence in the manganese occurs as a result of eximer emission on the ligand or from the metal following a ligand to metal charge transfer (LMCT) process. Brillante et al. described pressure sensitive eximer emission in crystals of pure anthraquinone, which displayed a broad

emission near the wavelengths seen for MnAQDC. They showed that the eximer character increased as the molecules were brought closer together by increasing external pressure. The MnAQDC luminescence origin could potentially be probed more directly through some ultra-fast time-dependent measurements, as eximer emission should have a much different time relationship than LMCT. The luminescence of the nickel-containing NiAQDC structure is quenched by the paramagnetic state of the d^8 metal centres.

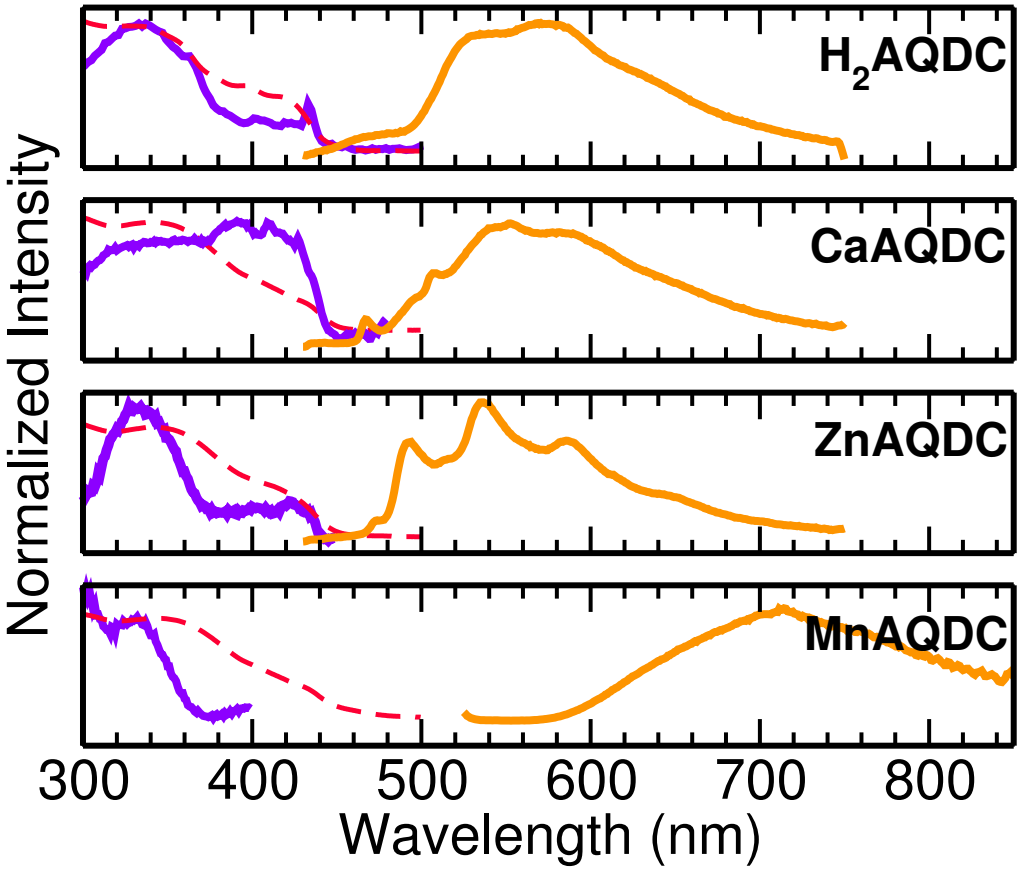

Figure 5.16: photoluminescence excitation and emission spectra for AQDC compounds, λ_{ex}=365 nm, λ_{em}=520 nm for all except for the MnAQDC, where λ_{em}=700 nm. Dotted red line is the UV-Vis absorption.

The UV-Vis absorption spectrum of H_2AQDC, shown in Figure 5.16 as a red dashed line, is nearly identical to the photoluminescence excitation spectra. For MnAQDC and ZnAQDC the UV absorption intensity exceeds that of the luminescent excitation spectra, suggesting a non-ideal photoluminescence mechanism. In the calcium containing structure, however, the drop-off in excitation intensity occurs at at wavelength that exceeds that of the UV absorption drop-off, extending from 375 nm to 440 nm. While the excitation is nearly flat band for that entire range, it drops off too far into the UV to be used by the current GaN based blue emitters, which rely on the 430 nm to 480 nm excitation range of YAG:Ce.

Further characterization of the luminescence was carried out by collecting emission spectra at temperatures from 77 K up to room temperature, as shown in Figure 5.17. Because the samples did not luminesce at room temperature, no absolute quantum efficiency measurements could be made. As a means of quantifying the thermal quenching and developing a relative quantum efficiency with respect to temperature, the integrated intensity of the variable temperature emission spectra were calculated and adjusted such that the intensity at room temperature was 0, as seen in Figure 5.18. This plot shows mostly similar quenching behaviour for all of the samples, with the most pronounced drop-off observed for ZnAQDC.

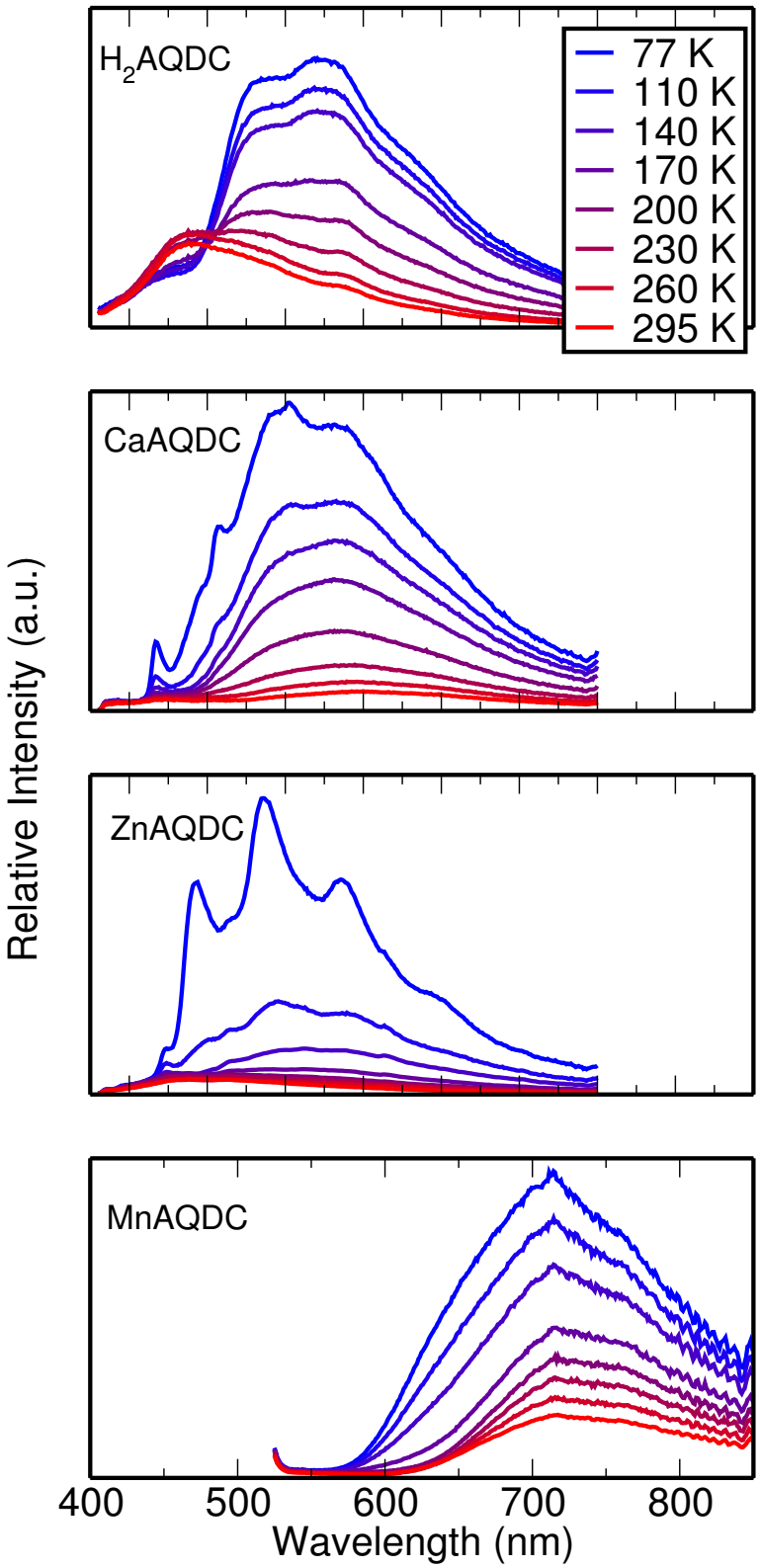

Figure 5.17: Variable temperature photoluminescence emission for AQDC compounds, λ_{ex}=365 nm.

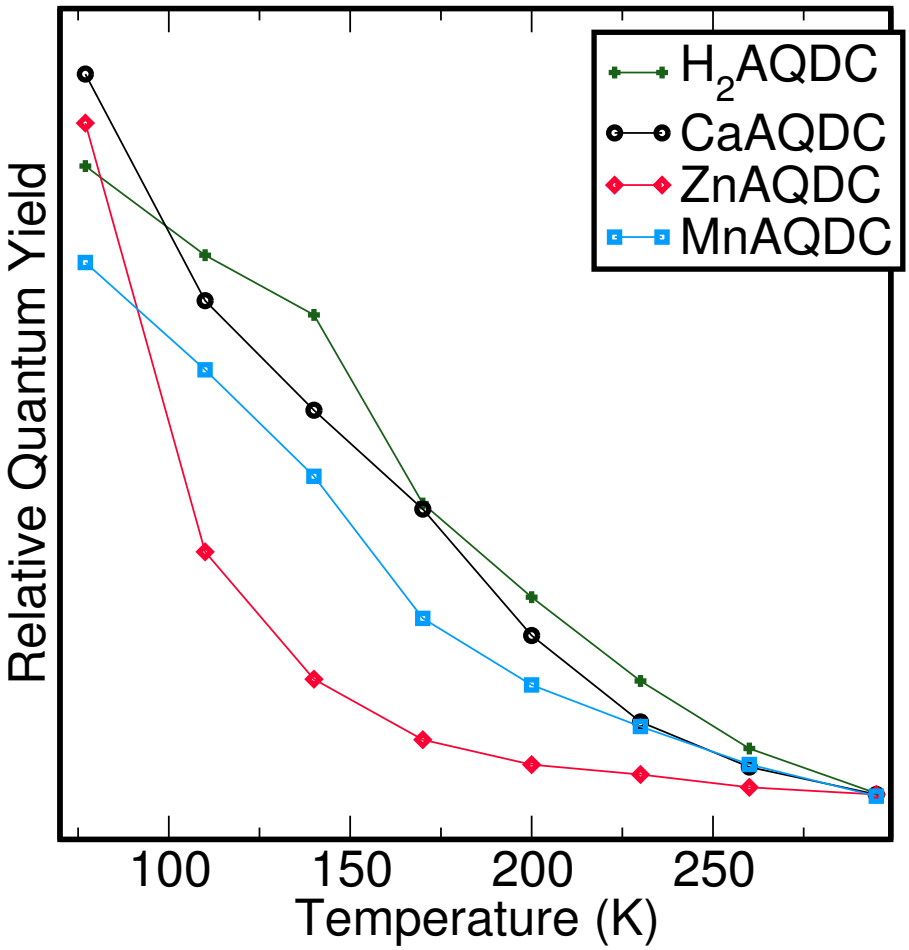

Figure 5.18: Integrated intensity of the luminescent emission from AQDC compounds, representing the relative quantum efficiency with respect to temperature.

5.3.4 Thermal analysis

Thermogravimetric analysis conducted in air is shown in Figure 5.19. Results were consistent in all samples with the degree of hydration determined by single-crystal diffraction. The ligand H_2AQDC shows a small degradation step at 250°C and then a full decomposition with zero residue at 375°C. It is significantly less stable than the hybrid framework structures. The isostructural CaAQDC and MnAQDC both show a few unresolved dehydration steps from 20°C to 150°C. The CaAQDC structure is then stable on heating to 480°C where it undergoes a weight loss on conversion to $CaCO_3$. A second decomposition step beginning at 650°C indicates a conversion to calcium(II) oxide. The decomposition steps in MnAQDC are overlapping and a broad weight loss beginning at 400°C and ending at 525°C indicates a conversion to manganese(II) oxide. An initial dehydration occurs in ZnAQDC between 20°C and 100°C. A broad decomposition step from 350°C to 520°C ending at 19% of the initial mass indicates a transformation to zinc(II) oxide. NiAQDC similarly goes through dehydration steps up to 150°C, followed by a decomposition between 380°C and 450°C to nickel(II) oxide. Decomposition data is summarized in Table 5.4.

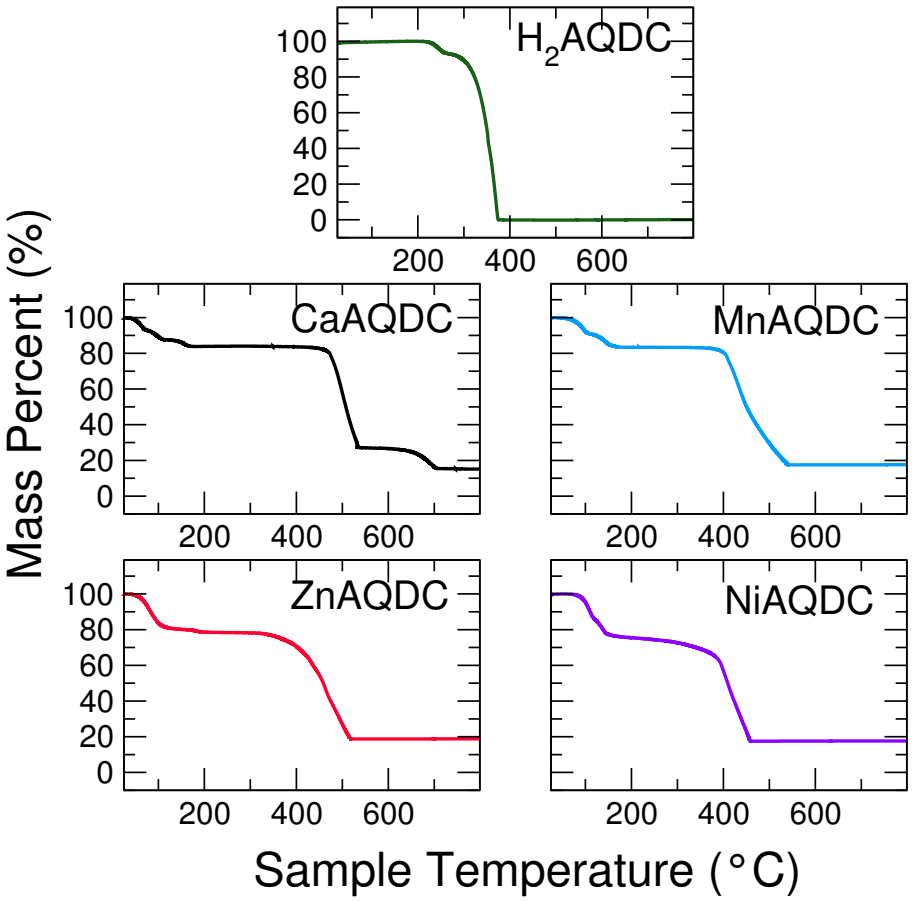

Figure 5.19: Thermogravimetric analysis of H_2AQDC, CaAQDC, MnAQDC, NiAQDC, and ZnAQDC as labeled.

Table 5.4: Thermogravimetric analysis of anthraquinone frameworks

Compound	Initial Mass ($g \cdot mol^{-1}$)	Final Mass Percent (%)	Observed final mass ($g \cdot mol^{-1}$)	Decomposition product	Ideal decomposition mass ($g \cdot mol^{-1}$)	Error (%)
H_2AQDC	268.23	0	0	None	0	0
CaAQDC	406.35	15.0	60.95	CaO	56.08	8.7
MnAQDC	421.21	17.5	73.71	MnO	70.94	3.9
NiAQDC	479.03	17.6	84.31	NiO	74.69	12.8
ZnAQDC	431.64	18.8	81.15	ZnO	81.41	0.3

5.4 Summary

The closed-shell Zn^{2+} and Ca^{2+} frameworks show a bright luminescence from the ligand, but it is only visible when the samples are cooled to low temperatures. At liquid nitrogen temperatures, the thermal quenching from the vibrational states in the ligand is reduced and radiative recombination is possible. This is consistent with the large thermal vibrations seen in the structure due to the polycyclic ligand backbone being bound to the cations only at one end (Figure 5.11). These large thermal motions should result in increased phonon scattering and be the cause of the luminescence quenching at room temperature. One might expect greater stability from a more *para* binding ligand rather than the *ortho* AQDC.

In spite of the fact that these compounds do not show photoluminescence at room temperature, the observations, particularly for CaAQDC, demonstrate that ligand-based luminescence can be tuned towards the requirements for solid state lighting applications. The system shows an excitation spectra extending far into the visible range, from 300 nm to 435 nm. In addition, the emission spectra is extremely broad with a FWHM of approximately 150 nm, covering nearly the whole visible range and approximately double that of YAG:Ce. Figure 5.20 shows the excitation and emission spectra of CaAQDC in comparison to YAG:Ce.

In the thermogravimetric analysis, enhanced thermal stability of the organic ligand within the framework structure was observed in comparison with that of the free acid. In the calcium-containing structure the ligand is stable within the structure to 575°C, approximately 200°C higher than in H_2AQDC. This shows the potential benefits of including intrinsically luminescent organic compounds within a hybrid framework rather than simply as an organic crystal or in a polymer.

In summary, several new blue-excited photoluminescence hybrid frameworks

have been described. Unfortunately, the thermal quenching in this system is such that the luminescence is only seen at low temperatures. This makes these compounds ultimately unsuitable for any sort of device application. They are, nevertheless, a good model compound from which much can be learned about the behaviour and design characteristics of ligand-based luminescence in hybrid frameworks. As the optical properties of more and more framework compounds are investigated, the structural and chemical parameters that are important for highly efficient photoluminescence will become apparent. From this study we can see that having a large degree of vibrational motion results in severe thermal quenching. In the following chapter, a different ligand will be used for ligand-based emission that will improve upon these results.

The research described in this chapter was carried out in collaboration with Min Tang who assisted with the synthesis, and Alexander Mikhailovsky who performed some of the optical characterization. A manuscript is currently being prepared for publication.

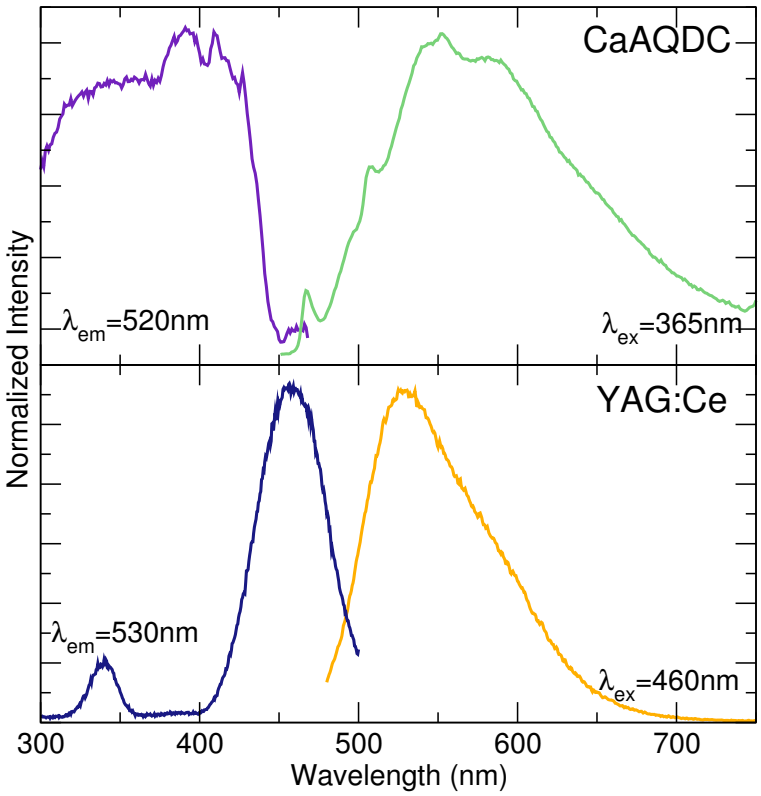

Figure 5.20: TOP: Excitation and emission spectra of CaAQDC, BOTTOM: Excitation and emission for YAG:Ce. Note the increased width of both spectra for the anthraquinone structure.

Chapter 6

Fluorenone-based luminescent frameworks

6.1 Introduction

In the previous chapter, novel framework materials using ligand-centred luminescence were introduced as an approach to developing new phosphors for solid state lighting. The calcium anthraquinone displayed excellent excitation and emission spectra, but the temperature dependence of the luminescence made it unsuitable for device applications. It was suggested that this thermal quenching could be tied to the flexibility of the ligand and that moving to a more linear-bonding ligand may improve properties. In this chapter, new phosphor materials using the intrinsic luminescence of the 9-fluorenone-2,7-dicarboxylic acid, a *para*-binding ligand, is investigated. This ligand is shown in Figure 6.1 along with the anthraquinone dicarboxylate used in Chapter 5 for comparison.

The fluorene molecule is well known for its use in optical materials, typically

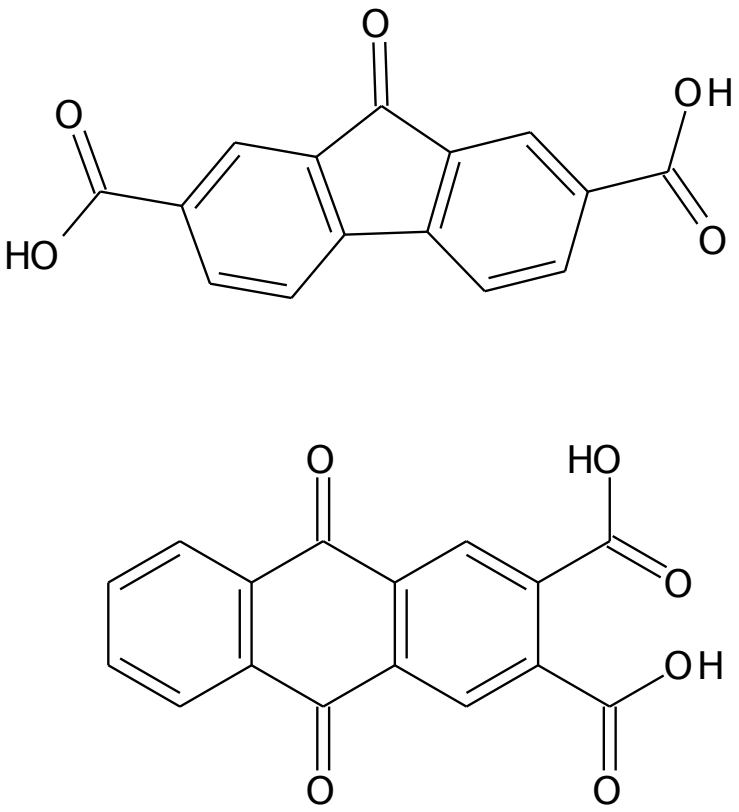

Figure 6.1: TOP: 9-fluorenone-2,7-dicarboxylic acid. BOTTOM: anthraquinone-2,3-dicarboxylic acid

as an organic backbone in larger molecular compounds and polymers [148]. It consists of a pentene ring with a benzene fused on either side, forming a 6–5–6 polyaromatic chain. 9-Fluorenone-2,7-dicarboxylic acid (H_2FDC) is a commercially available fluorene derivative that has a ketone group at the 9- position of fluorene on the pentene ring and carboxylic acids at the 2- and 7- positions. This results in a nearly linear bonding arrangement similar to that provided by the common framework ligands terephthalic acid and oxalic acid. This ligand also shows yellow luminescence under blue and UV excitation. On account of these structural and optical properties, H_2FDC was considered a good candidate for developing

inorganic-organic hybrid phosphors for solid state lighting.

Five novel framework structures containing the FDC ligand and calcium, strontium, barium, manganese or cadmium are described below. Except for the manganese structure, they all show blue-excited photoluminescence.

6.2 Experimental methods

6.2.1 Synthesis

9-fluorenone-2,7-dicarboxylic acid was obtained from Trans World Chemicals and used without further purification. All other reagents were obtained from Sigma-Aldrich. Hydrothermal reactions were carried out in 23mL PTFE lined Parr brand autoclaves using deionized water.

6.2.2 Preparation of Na_2FDC

Preliminary reactions with H_2FDC showed limited solubility in water, even at hydrothermal temperatures. To obtain single crystals of the CaFDC, it was necessary to first make the sodium salt of the ligand, which shows high solubility in water. The other fluorenone frameworks were all synthesized using H_2FDC.

The sodium salt of FDC (Na_2FDC) was prepared by combining equimolar amounts of NaOH and H_2FDC in water. The solution was stirred overnight and evaporated to dryness on a hot plate. The crude product was refluxed in ethanol for 1 h, separated by filtration, and dried in vacuo. The sodium salt shows high water solubility at room temperature whereas the acid was only sparingly soluble in water. Its provided single crystals of CaFDC, although in very low yield.

6.2.3 Preparation of CaFDC

$Ca(FDC)(H_2O)_2$ CaFDC was prepared from 0.05 mmol of calcium acetate, 0.05 mmol Na_2FDC, and 5 mL H_2O. The mixture was stirred, sealed in an autoclave, and heated to 150°C for 2 days before cooling to room temperature. Tiny yellow needle crystals were recovered by filtration and washed with water and acetone. Phase pure powders in greater yield were prepared by reacting 0.1 mmol calcium acetate, 0.1 mmol H_2FDC, and 0.25 mL 1M sodium hydroxide in 10 mL H_2O hydrothermally at 175°C for 2 days.

6.2.4 Preparation of SrFDC

$Sr(FDC)(H_2O)_5 \cdot 2H_2O$ SrFDC was prepared from 0.05 mmol strontium acetate, 0.05 mmol H_2FDC, 0.05 mmol imidazole, and 5 mL H_2O. The mixture was stirred, sealed in an autoclave, and heated to 180°C for 2 days before cooling to room temperature. Small yellow plate crystals were recovered by filtration. Although imidazole was not incorporated into the structure, its presence was required to obtain single crystal products. Phase pure powders in greater yield were prepared by reacting 0.1 mmol strontium acetate, 0.1 mmol H_2FDC, and 0.25 mL 1M sodium hydroxide in 10 mL H_2O hydrothermally at 175°C for 2 days.

6.2.5 Preparation of BaFDC

$Ba(FDC)(H_2O)$ BaFDC was prepared from 0.1 mmol barium acetate, 0.1 mmol H_2FDC, 0.18 mL 1M sodium hydroxide, and 5 mL H_2O. The mixture was stirred, sealed in an autoclave, and heated to 180°C for 2 days before cooling to room temperature. Small yellow plate crystals were recovered by filtration. Phase pure

powders were prepared by reacting 0.1 mmol barium acetate, 0.05 mmol H_2FDC, and 0.18 mL 0.5 M potassium hydroxide in 10 mL H_2O hydrothermally at 180°C for 2 days.

6.2.6 Preparation of CdFDC

$Cd(FDC)(H_2O)_2 \cdot 2H_2O$ CdFDC was prepared from 0.05 mmol cadmium acetate, 0.05 mmol H_2FDC, 0.09 mL 0.5 M potassium hydroxide, and 5 mL H_2O. The mixture was stirred, sealed in an autoclave, and heated to 180°C for 2 days before cooling to room temperature. Small yellow plate crystals were recovered by filtration. Phase pure powders were prepared by reacting 0.1 mmol cadmium acetate, 0.05 mmol H_2FDC, and 0.18 mL 0.5 M potassium hydroxide in 10 mL H_2O hydrothermally at 180°C for 2 days.

6.2.7 Preparation of MnFDC

$Mn(FDC)(H_2O)_2$ MnFDC was prepared from 0.05 mmol manganese acetate, 0.05 mmol H_2FDC, and 5 mL H_2O. The mixture was stirred, sealed in an autoclave, and heated to 200°C for 2 days before cooling to room temperature. Small yellow needle crystals were recovered by filtration. The reaction products were phase pure.

6.2.8 Structure determination

All structures were determined using single crystal X-ray diffraction. Data collection for CaFDC, BaFDC, CdFDC, and MnFDC, was performed at beamline 11.3.1 on the Advanced Light Source at Lawrence Berkeley National Laboratory

(λ=0.7749 Å). A crystal was mounted on a Kaptan loop using paratone-N oil and placed in a N_2 cryostream at 100 K. Data were collected using a Bruker D8 goniometer and APEX2 detector. Data integration and corrections for Lorentz and polarization effects were performed using Bruker SAINT version 7.56a [61]. SADABS was used to perform an absorption correction [62]. The high brightness synchrotron source allowed for the analysis of very small crystals. For samples BaFDC and MnFDC, a true single crystal could not be found and so data was collected on a twin. CELL_NOW was used to determine that the orientation matrices and the domains were related by a 180° rotation around the reciprocal axis (001) [149]. The integration was performed with both matrices. TWINABS was used to produce a merged reflection file, for structure solution and initial refinement, and a split reflection file for for final structure refinement. These computational software methods allowed for the correct crystallographic cell to be identified and the intensity from the twinned reflections to be correctly assigned.

Data were collected for SrFDC on a Siemens SMART-CCD diffractometer at UCSB equipped with a normal focus, 2.4 kW sealed tube X-ray source (MoK_α radiation, λ = 0.7107 Å) operating at 45 kV and 30 mA and integrated with Bruker Saint version 6.02 [61]. Suitable single crystals were selected under a polarizing microscope and glued to a glass fibre and a hemisphere of intensity data was collected at room temperature. SADABS was used to perform an absorption correct and structures were then solved by direct methods and difference Fourier synthesis and were refined against $|F|^2$ using the SHELXL software package [62, 63].

Details of the structure determination are shown in Table 6.2. For all diffraction experiments, extinction coefficients refined to within three esd's of zero and were therefore removed from the refinement. Non-hydrogen atoms were refined anisotropically. Riding hydrogens were assigned to the carbon atoms on the FDC

ligands. Hydrogen atoms on the water molecules were found in the Fourier difference map and were refined isotropically. Where necessary, hydrogen atoms were restrained to chemically appropriate positions, resulting in increased residual error.

Powder diffraction data were collected at the Advanced Photon Source synchrotron X-ray beamline 11-BM at λ=0.5892 Å for CaFDC and MnFDC. Data for SrFDC, BaFDC and CdFDC were collected on a Bruker D8 with Cu$K\alpha$ source. Models were refined to the data using GSAS and EXPGUI [106, 107] to confirm purity of the bulk sample.

Room temperature photoluminescence spectra were collected on a Perkin-Elmer LS55 spectrometer using finely ground powders mounted behind a quartz window. Quantum yield data were collected on solid samples mounted on quartz slides in silicone resin. The samples were placed within an integrating sphere and excited with a 405 nm laser. Temperature dependent emission spectra were collected using the same 405 nm excitation and a LN_2 cooled cryostat or resistive heating stage in combination with an Acton Research spectrometer. Thermal analysis was carried out a Mettler 851e in air, heating in alumina crucibles at 10°C per minute to 1000°C. Luminescent lifetime measurements were carried out in the same method described in Section 3.2.4 using laser excitation at 400 nm.

6.2.9 Heat capacity measurements

In addition to standard structural and optical characterization, specific heat measurements were carried out to evaluate vibrational modes in the materials as an attempt to explain differences in quantum yield between the compounds. Measurements of the fluorenone compound heat capacities were carried out on a

Quantum Design Physical Properties Measurement System (PPMS) using a 2-τ relaxation technique [150]. Powder samples were mixed 1:1 by weight with silver powder, finely ground, and cold pressed into rectangular pellets which were then cut down to approximately 3 mm$\times$3 mm$\times$0.5 mm. The addition of the silver raises the thermal conductivity of the overall sample, increasing sensitivity [151]. Pellets are attached to a calorimeter using the thermally conductive Apiezon N grease. The contribution to the specific heat from the silver and grease are measured separately and subtracted. The sample holder contains both a resistance heater and a thermocouple. A power pulse is delivered to the heater for a fixed amount of time and the temperature change caused by delivering that heat to the sample is measured. The system temperature is lowered and allowed to stabilize between pulses, in this case from 80 K down to 2 K. The behaviour of the temperature relaxation and contributions from the instrument are modelled internally and converted to specific heat.

6.3 Theory of specific heat measurements

Specific heat relates the total energy of a system (U) to the temperature (T) by:

$$\frac{\partial U}{\partial T} = \int C_p dT \tag{6.1}$$

It is related to the extrinsic property of heat capacity, the amount of heat needed to raise the temperature of a material by some amount. The specific heat is sensitive to changes in pressure, volume, magnetic field, and others, and so experimentally these parameters are selectively held constant and a value is often reported as the heat capacity at constant pressure C_p or at constant volume C_v in units of

J·mol^{-1}·K^{-1}.

The partition function Z in statistical mechanics encodes how probabilities are divided, or partitioned, between microstates of a system:

$$Z = \sum_i e^{\frac{-\epsilon_i}{k_B T}} \tag{6.2}$$

where i are all the states of a system and ϵ_i is the energy at that state. This allows the rotational, electronic, magnetic, and lattice contributions to Z to be separated such that:

$$Z = Z_{rotation} \cdot Z_{electronic} \cdot Z_{magnetic} \cdot Z_{lattice} \tag{6.3}$$

And when combined with Equation 6.1 above, it is found that:

$$C_v = C_{v,rotation} + C_{v,electronic} + C_{v,magnetic} + C_{v,lattice} \tag{6.4}$$

Thus contributions to the specific heat by individual processes can be simply subtracted out of the total value. This is particularly useful in measurements, where the contribution of a sample holder or thermal grease can be removed as a baseline.

In 1819, Dulong and Petit introduced a rule stating that all solid elements at room temperature have the molar heat capacity $3R$, or 24.9 J·K^{-1}. This can be derived using classical oscillators with energy $k_B T$, moving with 3 degrees of freedom. However, an understanding the relationship of specific heat to temperature was not clear until the application of quantum theory [152]. The 1907 Einstein model treated each atom in a lattice as a single harmonic oscillator with quantized frequencies. This models the energy as localized vibrations rather than collective phonon vibrations. These vibrations can exist down to low temperatures, whereas

classical collective modes cannot [153]. Thus the total energy in a system U can be derived as the sum of the quantized oscillators:

$$U_{\text{tot}} = 3\sum_i n_i \left(i + \frac{1}{2}\right) h\nu \tag{6.5}$$

where i is the i^{th} energy level, n_i is the number of moles, h is Plank's constant and the multiplier 3 arises from the three degrees of freedom in the x, y, and z directions. Extracting the heat capacity from this total energy approximation gives a relatively good match to measured values, approaching Dulong-Petit behaviour at high temperature and decreasing to 0 at 0 K. There was still, however, a slight mismatch between empirical data and the theoretical model at low temperatures.

Debye further refined Einstein's approach by constraining the range of frequencies available to the oscillators. The upper limit is set by the interatomic distances and the distribution increases parabolically per unit volume. This refinement of the model gives a very close fit to empirical data for many well behaved systems, and more closely follows the increase in specific heat with temperature than the Einstein model, as shown in Figure 6.2. The characteristic Debye temperature, θ_D, indicates the cross-over point from low temperature quantized behaviour, where the atoms vibrate independently, to the high temperature classical region, where vibrations are coupled through the lattice. The Debye frequency ω_D is given as:

$$\omega_D = \left(\frac{6\pi^2 sN}{V}\right)^{1/3} \left(\frac{1}{c_L^3} + \frac{1}{c_T^3}\right)^{-1/3} \tag{6.6}$$

where s is the number of atoms per formula unit, N is the number of molecules per mole, V is the volume of the crystal, and c_L and c_T are the velocities of the longitudinal and transverse phonons [154]. This relates to the debye temperature

θ_D by:

$$\theta_D = \frac{\hbar\omega_D}{k_B} \tag{6.7}$$

The specific heat then follows the function:

$$C_v = 9Rs\left(\frac{T}{\theta_D}\right)^3 \int_0^{x_D} \frac{x^4 e^x dx}{(e^x - 1)^2} \tag{6.8}$$

where:

$$x = \frac{\hbar\omega}{k_b T} \tag{6.9}$$

$$x_D = \frac{\hbar\omega_D}{k_b T} \tag{6.10}$$

In practice, the integral in Equation 6.8 is approximated by an odd-series taylor expansion such that:

$$C_v = \beta_3 T^3 + \beta_5 T^5 + \beta_7 T^7 \ldots \tag{6.11}$$

The cubic term of that expansion, β_3, can be used to extract the Debye temperature from the low temperature limit of the integral above, such that:

$$C_v = \frac{12\pi^4}{5}\left(\frac{Rs}{\theta_D^3}\right) T^3 = \beta_3 T^3 \tag{6.12}$$

$$\theta_D = \left(\frac{12\pi^4}{5}\frac{Rs}{\beta_3}\right)^{1/3} \tag{6.13}$$

The specific heat decreases sharply at low temperature as individual degrees of freedom are effectively “frozen” out of the vibration modes available to the atoms. While we are not considering the luminescence of materials at these low temperatures, the behaviour of the phonons provides insight into lattice dynamics at all temperatures.

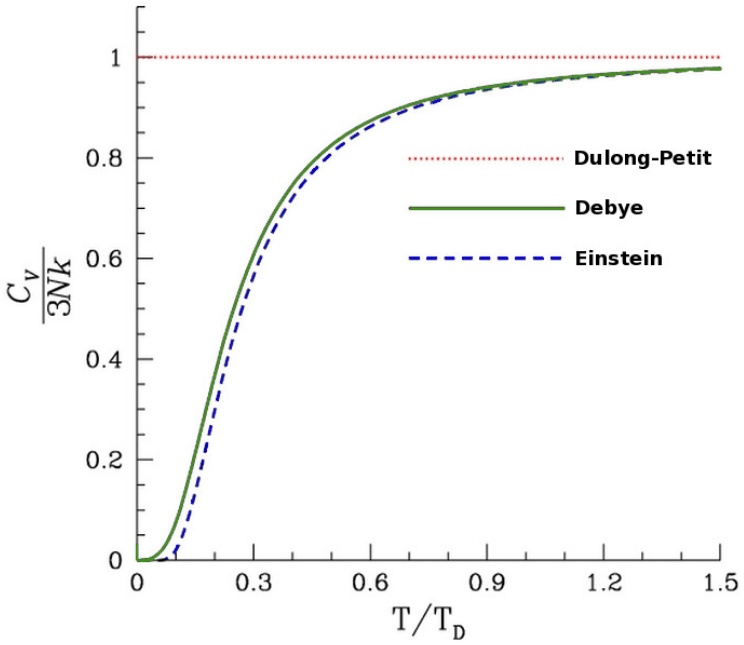

Figure 6.2: Specific heat as described by the Dulong-Petit law (dotted red), Debye model (green), and Einstein model (dashed blue), showing convergence at high temperature. The Einstein model deviates from the expected behaviour shown in the Debye model at low temperatures [152].

6.4 Results

6.4.1 Structures

Five new compounds were discovered and their structures were determined by single crystal X-ray diffraction. Interestingly, none of the compounds are isostructural, despite containing the same ligand and cations from the same groups. Table 6.1 summarizes the structures that will be described here, and it is given in detail in Table 6.2. The π-stacking behaviour of all the structures is shown in Figure 6.15. The crystal structure of the free ligand is not reported in the literature and attempts to recrystallize the ligand for structure determination were unfortunately unsuccessful.

The structure of CaFDC (Figure 6.3) consists of isolated CaO_6 octahedra linked through FDC ligands as seen in Figure 6.4. Each octahedron connects to four FDC ligand oxygen atoms and two coordinating water molecules, while each dicarboxylic acid oxygen atom of the FDC ligand is bound to a different metal. The octahedra arrange in sheets which are pillared by FDC ligands to form a 3-dimensional structure. The ligands are π-stacked with their ketone groups aligned at a sepa-

Table 6.1: Summary of fluorenone framework compounds

	CaFDC	SrFDC	BaFDC	CdFDC	MnFDC
Formula	$CaC_{15}O_7H_{10}$	$Sr_2C_{30}O_{17}H_{26}$	$BaC_{15}O_6H_8$	$CdC_{15}O_8H_{12}$	$MnC_{15}O_7H_{10}$
Space Group	$P2_1$	$P\bar{1}$	$P1$	$P2_1/c$	$C2/c$
Bound Water	2	$2\frac{1}{2}$	1	2	2
Pore Water	0	1	0	1	0
Inorg. Dimen.	0-D	1-D	2-D	0-D	0-D
M-O-M Dimen.	3-D	2-D	1-D	2-D	3-D
π-π	3.41 Å	3.38 Å	3.30 Å	3.33 Å	3.39 Å

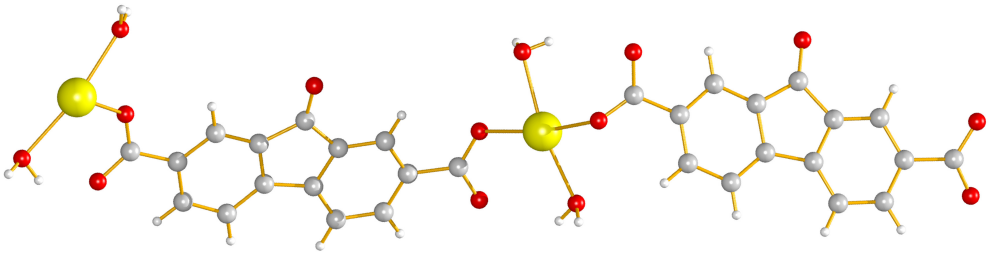

Figure 6.3: Asymmetric unit of CaFDC.

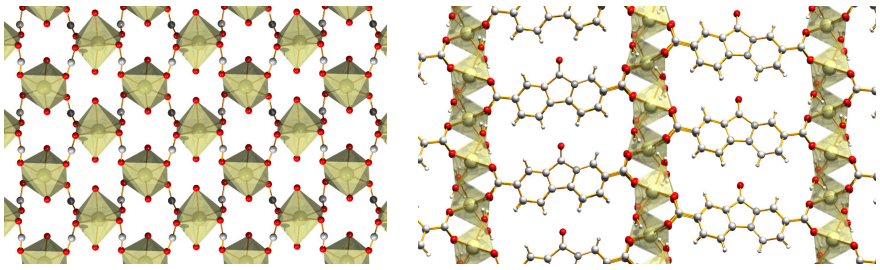

Figure 6.4: LEFT: Sheet of isolated CaO octahedra of CaFDC with hydrogen atoms omitted for clarity viewed down the c axis, RIGHT: The extended structure viewed down the a axis.

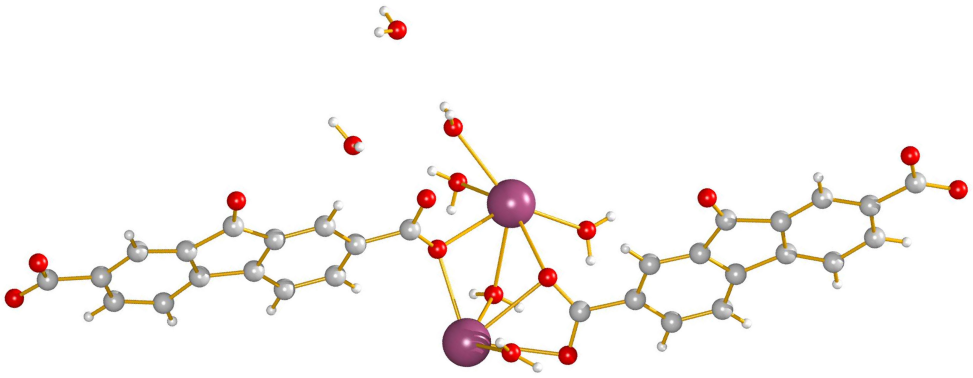

Figure 6.5: Asymmetric unit of SrFDC.

ration of 3.41 Å.

The structure of Sr(FDC)$(H_2O)_5 \cdot 2H_2O$ (Figure 6.5) consists of edge-sharing SrO_8 polyhedra that form 1-dimensional chains (Figure 6.6a). These chains are linked in-plane by the carboxylic acid groups of the FDC ligand to form a sheet, and the sheets are in turn bridged by the FDC to form an extended 3-dimensional framework, seen in Figure 6.6. The strontium atoms in the chains are arranged in pairs of two Sr1 atoms followed by two Sr2 atoms, with atom-atom distances of Sr1-Sr1 4.5681(11) Å, Sr1-Sr2 3.9935(10) Å, and Sr2-Sr2 4.0965(10) Å. The Sr1 polyhedra are completed by 2 coordinating water molecules, 3 bridging water molecules, and 3 oxygen atoms from ligand carboxylic acid groups. The Sr2 polyhedra consists of 1 coordinating water, 1 bridging water, and 6 oxygen atoms from the ligand. Two unbound water molecules sit in the pore space. One of the four oxygen atoms from the two dicarboxylic acid grounds on each FDC ligand is uncoordinated. The ligands π-stack less perfectly than those of CaFDC, with the ketone groups alternating in direction and a separation of 3.38 Å.

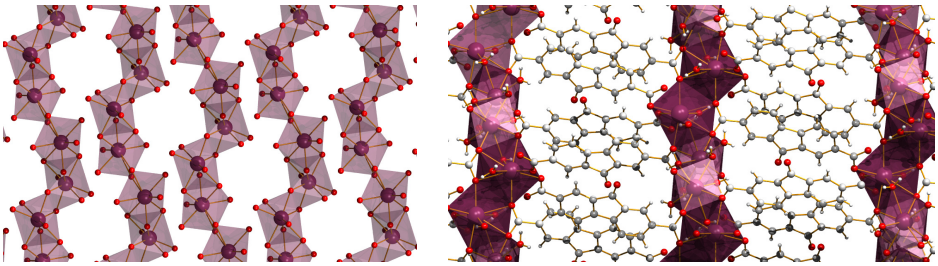

Figure 6.6: LEFT: 1-Dimensional edge sharing SrO_8 chains in SrFDC, hydrogen and carbon atoms omitted for clarity. RIGHT: Extended structure of SrFDC.

The asymmetric unit of Ba(FDC)(H_2O) [BaFDC] consists of two Ba atoms and two FDC units, similar to that of CaFDC (Figure 6.7). The structure crystallized in non-centrosymmetric triclinic space group $P1$. Both metal sites form a BaO_7 polyhedron, where one oxygen atom is from a bound H_2O. The O5 and O8 carboxylic acid oxygen molecules on the FDC units bridge Ba1 to Ba2 such that the each Ba1 is surrounded by three Ba2 and each Ba2 is surrounded by 3 Ba1. For both Ba1 and Ba2, one neighbouring polyhedra is edge sharing with a Ba-Ba distance 4.3277(5) Å while the other two are corner sharing with a Ba-Ba distances of 4.4593(5) Å and 4.1745(4) Å. Thus an inorganic 2-D sheet is formed with a distorted honeycomb structure of 6-membered rings, shown in Figure 6.8. The extended 3-D structure is formed by pillaring of the inorganic sheets with the FDC ligand units, as shown in Figure 6.9. The fluorenone ligands are π-stacked at a separation of 3.30 Å.

The asymmetric unit of Cd(FDC)(H_2O)$_2$·2H_2O [CdFDC] consists of a single FDC ligand with bidentate bonding to a cadmium (Figure 6.10), along with a single pore space water molecule. The compound crystallized in monoclinic space group $P2_1/c$. The metal site sits at the centre of a CdO_7 polyhedra where two of

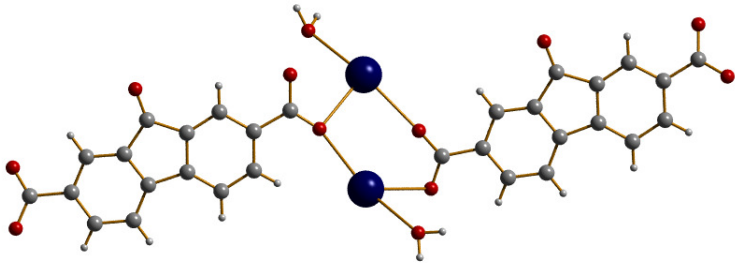

Figure 6.7: Asymmetric unit of BaFDC.

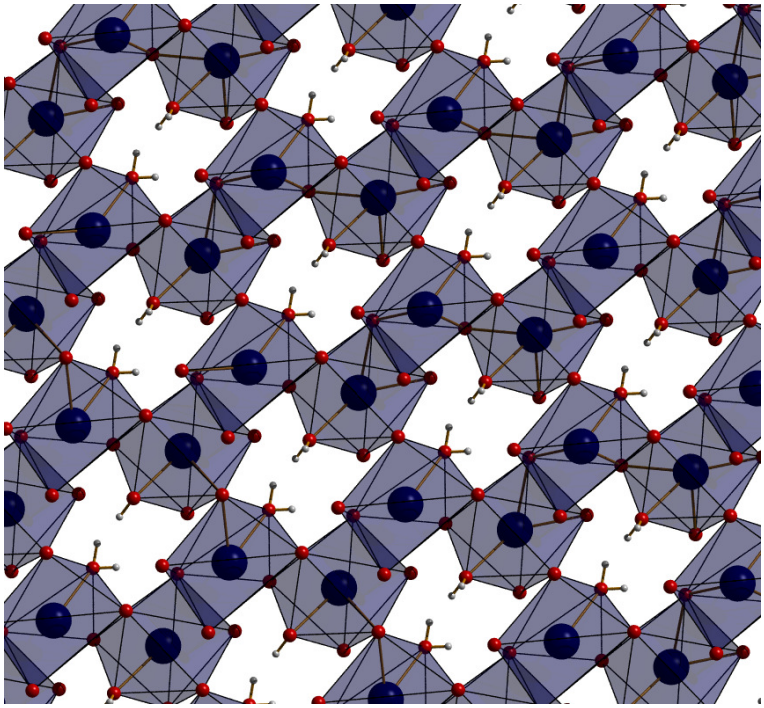

Figure 6.8: 2-Dimensional inorganic sheet of BaFDC.

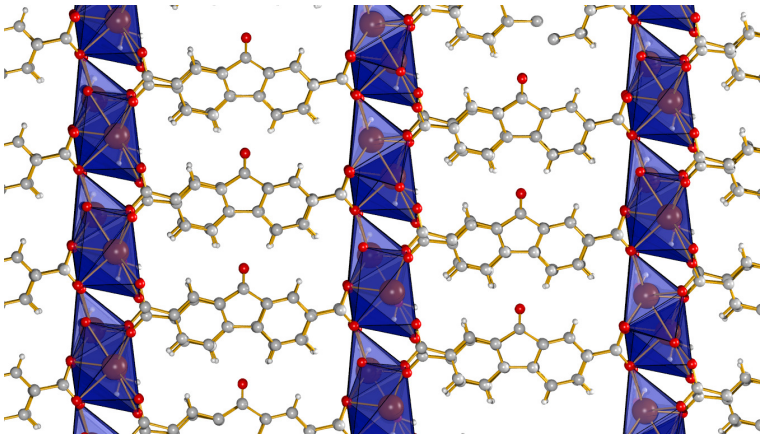

Figure 6.9: Extended 3-Dimensional structure of BaFDC, showing the linking of inorganic sheets by ligand units.

those oxygens are bound H_2O molecules. While both carboxylic acid groups are bidentate bonded to Cd1, the oxygen O4 is also bonded to an adjacent cadmium, resulting in an extended 2-D sheet structure, shown in Figure 6.11, with the pore space water molecule omitted for clarity. The extended structure is composed of these 2-dimensional sheets stacked in an ABAB fashion, as shown in Figure 6.12, with the FDC ligands π–stacked at a separation of 3.33 Å and rotated slightly out of parallel.

The asymmetric unit of $Mn(FDC)(H_2O)_2$ [MnFDC] consists of half of a FDC ligand, one Mn atom and one bound water molecule. The higher symmetry monoclinic space group $C2/c$ has an inversion centre through the ketone group of the ligand such that the structure can be seen as folded over on itself through that plane. Each oxygen of the carboxylic acid groups bonds to a single octahedral manganese atom, where the coordination is completed by two bound water molecules and adjacent ligands. A three dimensional structure is formed by sheets of isolated polyhedra connected by FDC in the a direction. The FDC are π–stacked

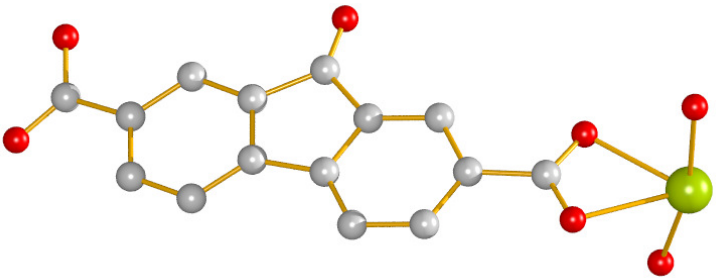

Figure 6.10: Asymmetric unit of CdFDC.

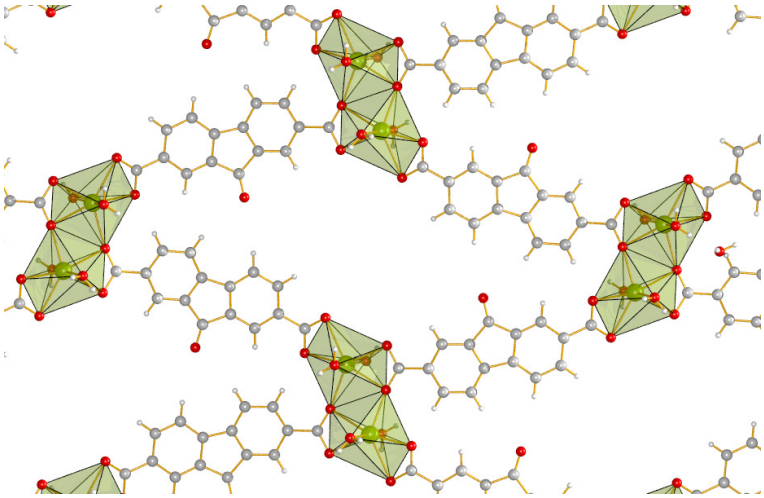

Figure 6.11: 2-Dimensional inorganic sheet of CdFDC, pore waters omitted for clarity.

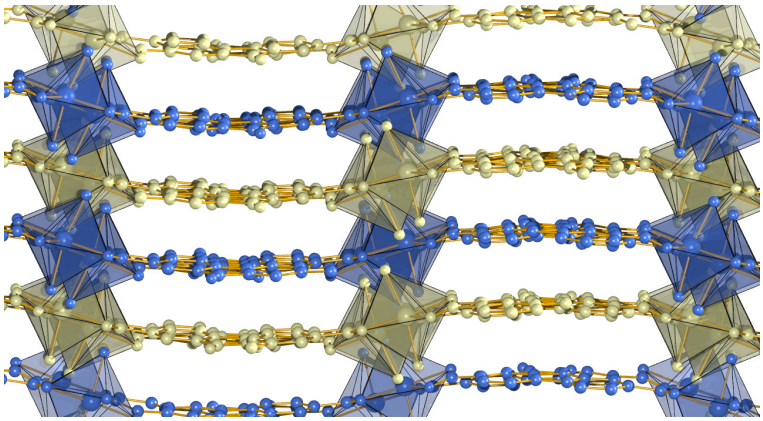

Figure 6.12: Extended structure of CdFDC, with alternating layers shown in blue and yellow.

at a separation of 3.39 with their ketone groups alternating in orientation.

Figures 6.16, 6.17, 6.18, 6.19 and 6.20 show Rietveld refinements of the structures determined by single crystal to the powder X-ray diffraction data. Data for CaFDC and MnFDC were collected at the Advanced Photon Source synchrotron X-ray beamline 11-BM at λ=0.5892 Å. Data for SrFDC, BaFDC, and CdFDC were collected on a Bruker D8 with CuKα. Unit cell parameters and refinement statistics are summarized in Table 6.3. The fitting statistics of these compounds are slightly elevated, particularly CaFDC, indicating that there may be some small impurity phases present.

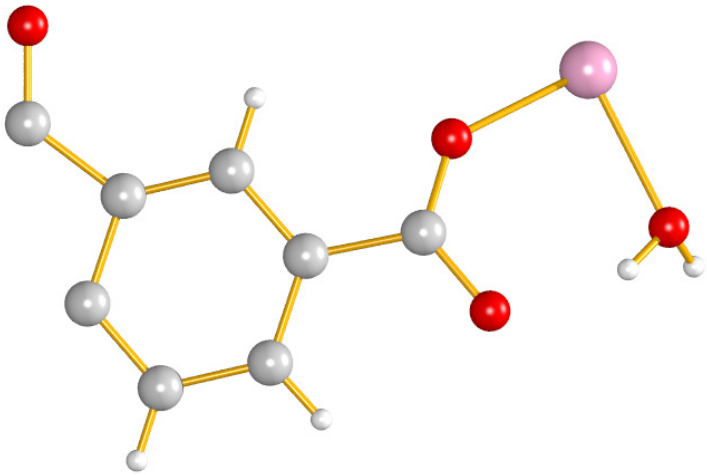

Figure 6.13: Asymmetric unit of MnFDC.

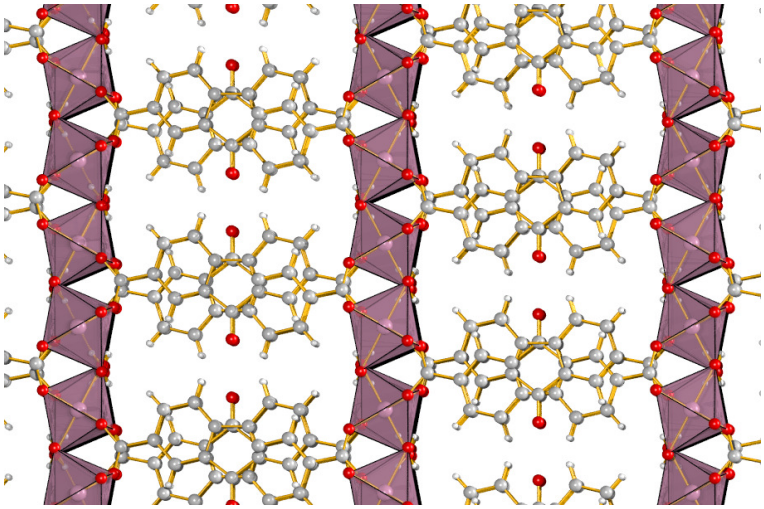

Figure 6.14: Extended structure of MnFDC.

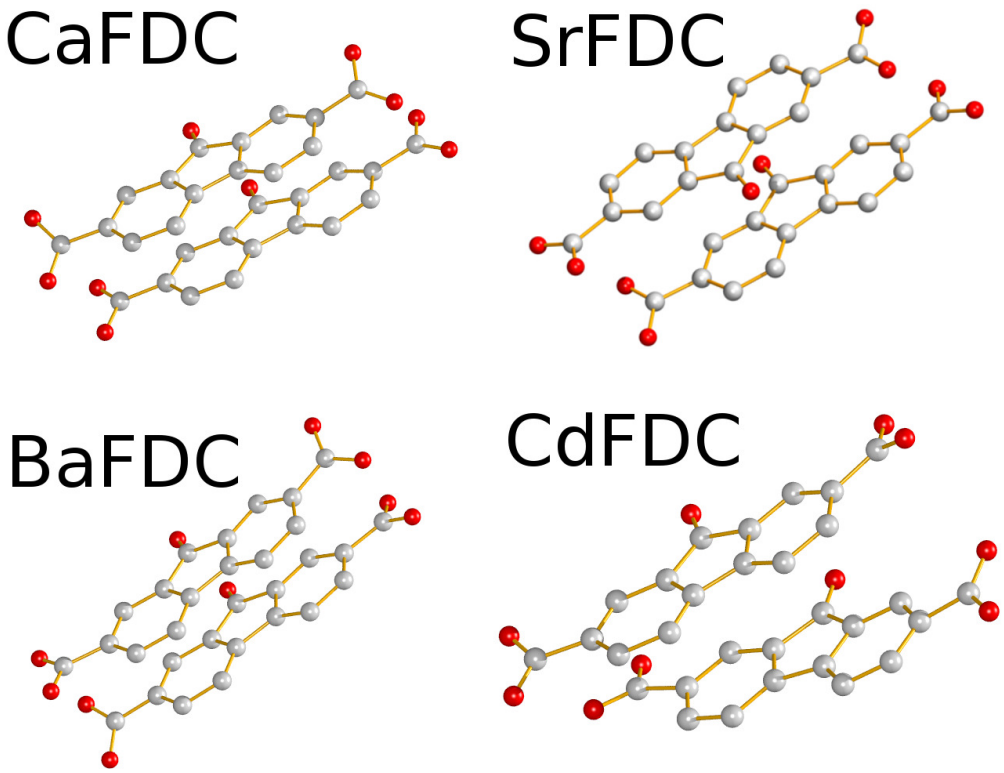

Figure 6.15: Adjacent ligand pairs for the luminescent fluorenone containing frameworks. The spacing between the layers and angle between the planes formed by them are nearly the same for all. The degree of skew as measured by the ketone group pointing direction shows some variability.

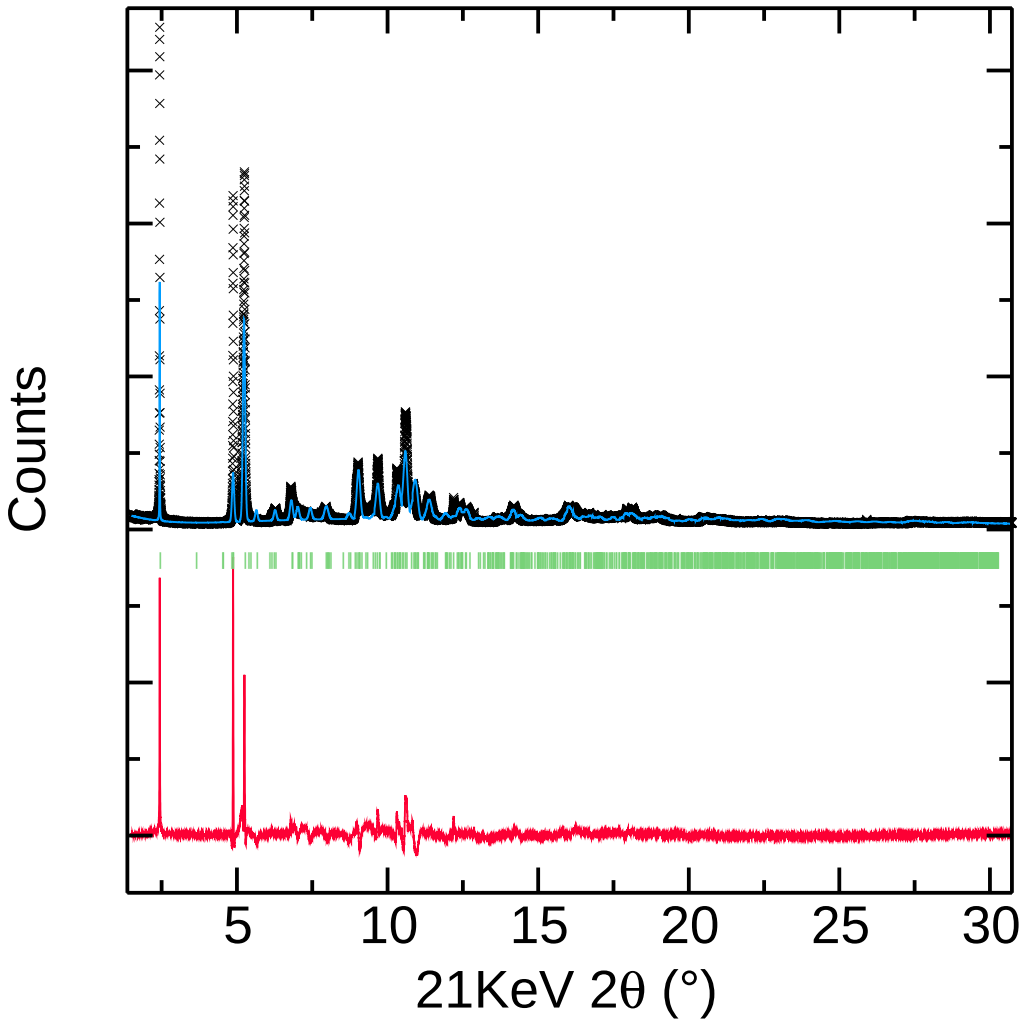

Figure 6.16: Synchrotron X-ray powder diffraction spectra (APS 11-BM, λ=0.7749 Å) of bulk sample of CaFDC and Rietveld refinement of model determined by single crystal diffraction (χ^2=10.560).

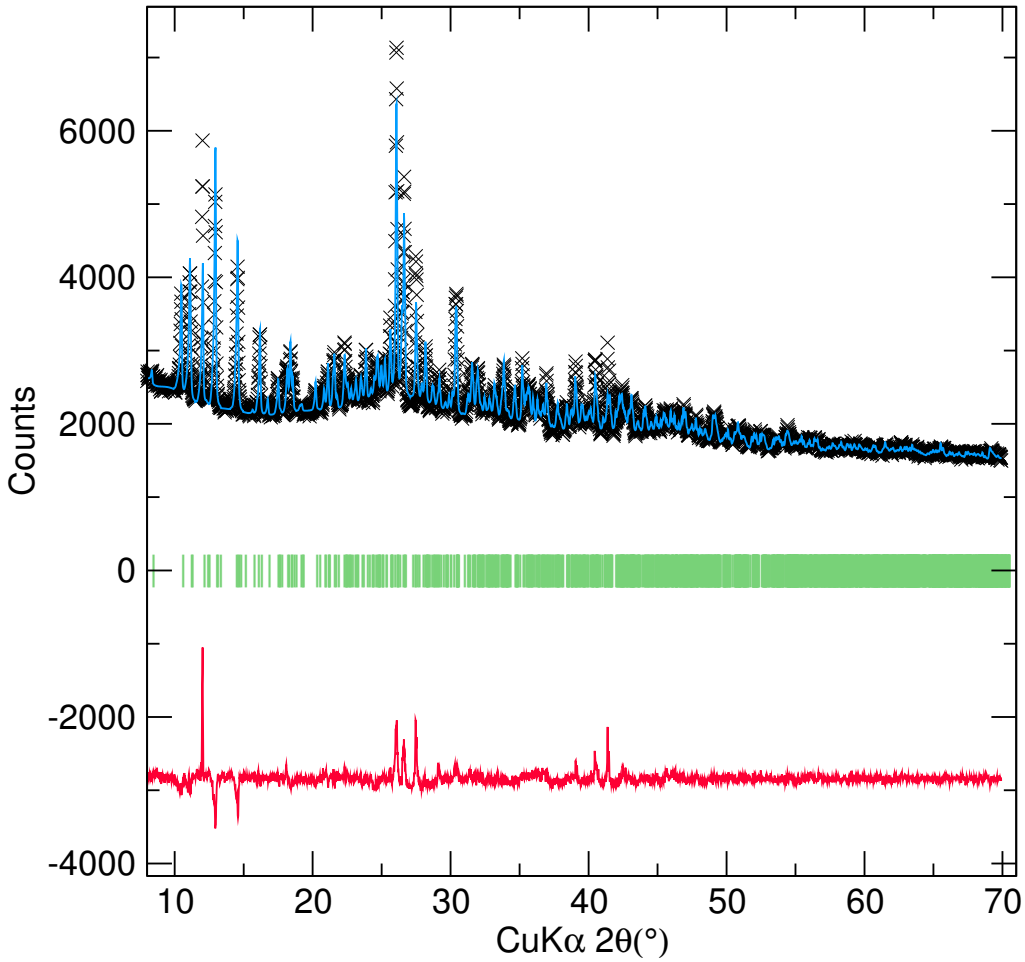

Figure 6.17: X-ray powder diffraction spectra of bulk sample of SrFDC and Rietveld refinement of model determined by single crystal diffraction (χ^2=5.046).

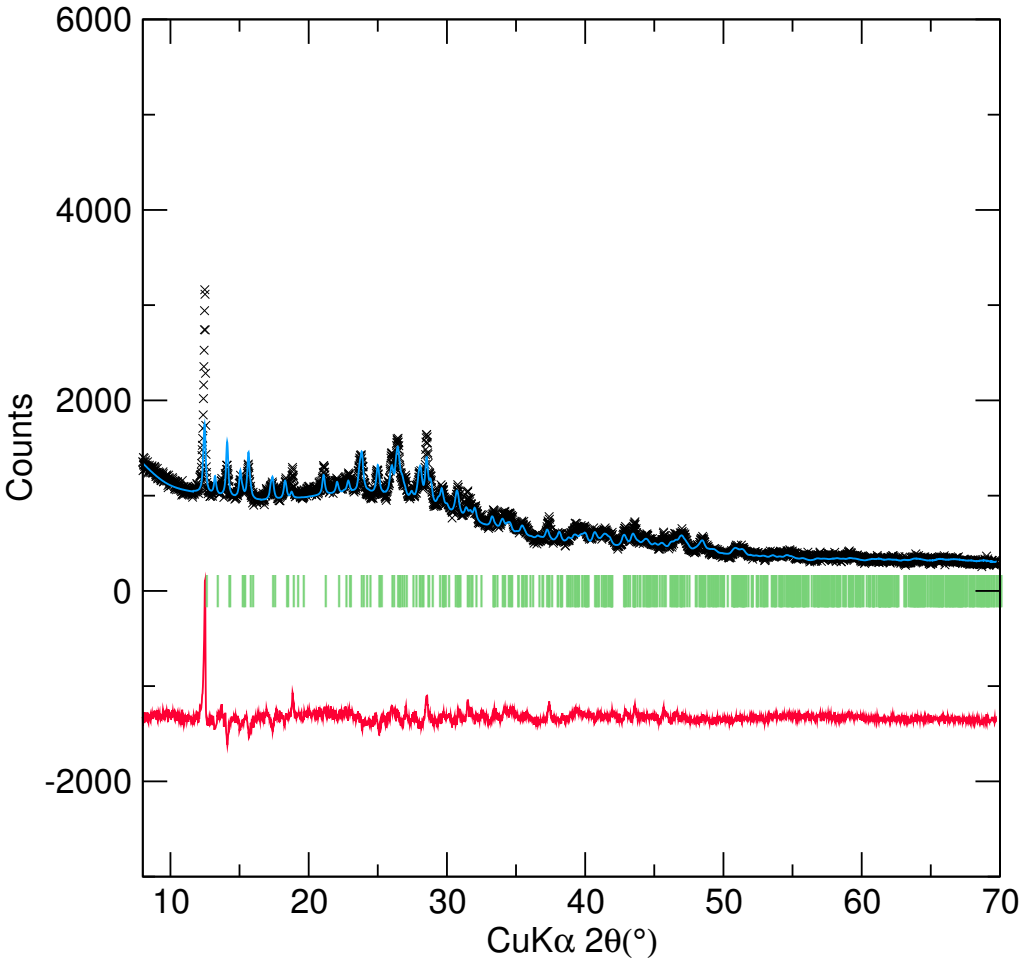

Figure 6.18: X-ray powder diffraction spectra of bulk sample of BaFDC and Rietveld refinement of model determined by single crystal diffraction (χ^2=5.592).

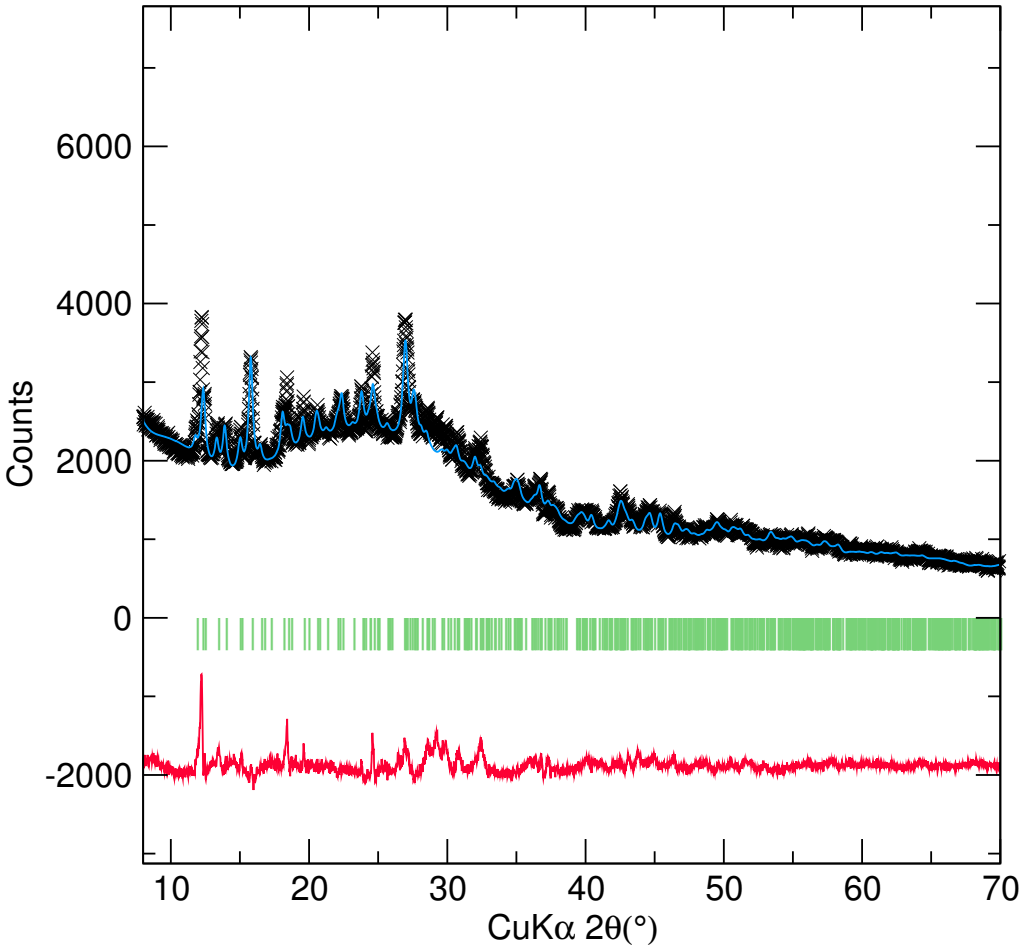

Figure 6.19: X-ray powder diffraction spectra of bulk sample of CdFDC and Rietveld refinement of model determined by single crystal diffraction (χ^2=4.430).

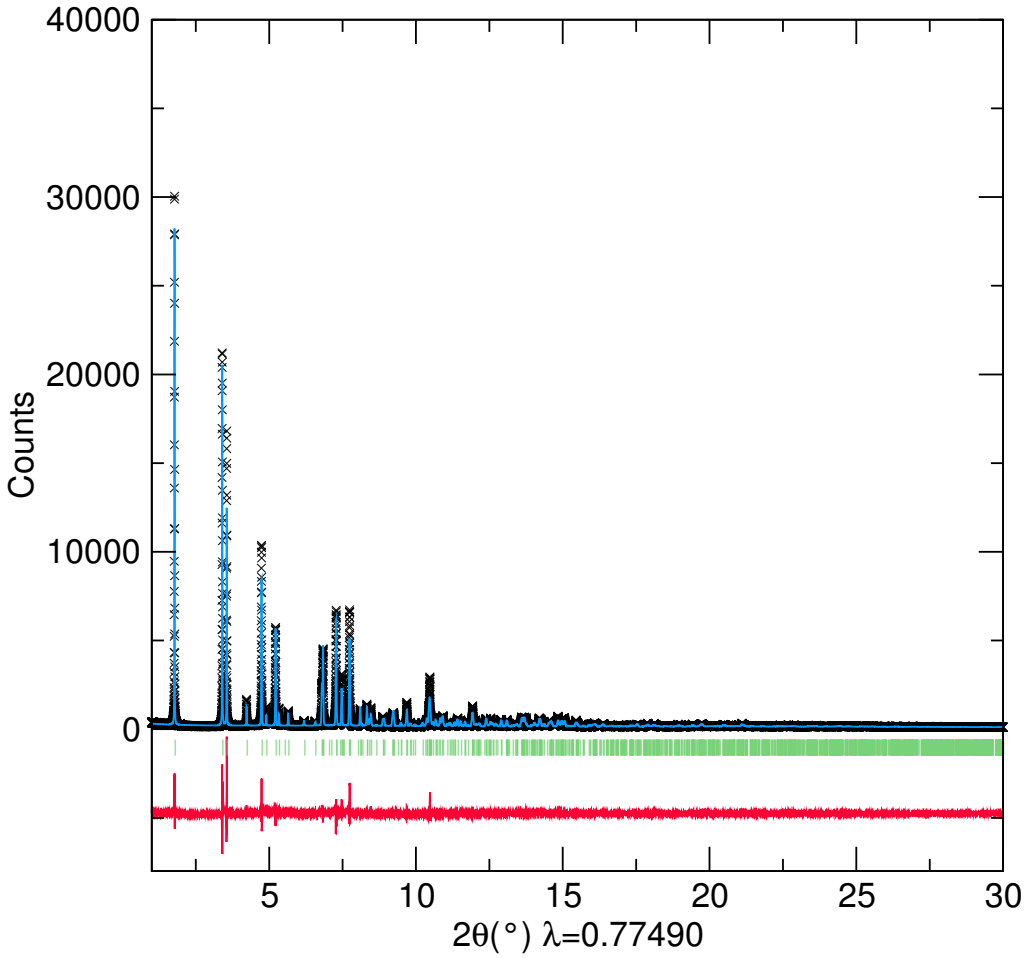

Figure 6.20: X-ray powder diffraction spectra of bulk sample of MnFDC and Rietveld refinement of model determined by single crystal diffraction (χ^2=4.329).

Table 6.2: Crystallographic data for fluorenone structures from single crystal diffraction data. Dimensionality is given as inorganic connectivity and the metal-oxygen-metal connectivity, as desribed in Cheetham et al.[35]

	CaFDC	SrFDC	BaFDC	CdFDC	MnFDC
Formula	$CaC_{15}O_7H_{10}$	$Sr_2C_{30}O_{17}H_{26}$	$BaC_{15}O_6H_8$	$CdC_{15}O_8H_{12}$	$MnC_{15}O_7H_{10}$
MW (g/mol)	342.31	833.75	421.55	432.65	357.17
System	Monoclinic	Triclinic	Triclinic	Monoclinic	Monoclinic
Space Group	$P2_1$	$P\bar{1}$	$P1$	$P2_1/c$	$C2/c$
a (Å)	7.5411(16)	8.578(2)	6.7676(6)	7.7123(2)	26.943(2)
b (Å)	6.6118(14)	11.836(3)	7.2311(7)	28.5057(8)	7.2476(6)
c (Å)	27.999(6)	15.626(4)	14.1591(13)	6.6459(2)	6.9261(5)
α (°)	90	72.437(4)	82.763(2)	90.00	90.00
β (°)	97.065(3)	78.722(5)	84.102(2)	105.050(2)	97.703(2)
γ (°)	90	85.437(4)	66.047(2)	90.00	90.00
V (Å^3)	1385.4(5)	1483.1(7)	627.17(10)	1410.95(7)	1340.27(18)
Z	4	2	2	4	4
ρ (g/cm^3)	1.641	1.867	2.232	2.037	1.770
μ (mm^{-1})	0.613	3.683	3.994	1.982	1.287
Measurement Temp (K)	100	298	100	100	100
Radiation Source	Synchrotron	Mok_α	Synchrotron	Synchrotron	Synchrotron
Radiation λ (Å)	0.7749	0.7107	0.7749	0.7749	0.7749
Scan Mode	Omega	Omega	Omega	Omega	Omega
Absorption Correction	SADABS	SADABS	SADABS	SADABS	SADABS
Solution Method	SHELX,$\lvert F\rvert^2$	SHELX, $\lvert F\rvert^2$	SHELX, $\lvert F\rvert^2$	SHELX, $\lvert F\rvert^2$	SHELX, $\lvert F\rvert^2$
2θ Range (°)	2.97-29.36	4.834-51.953	3.17-33.59	3.08-33.61	3.95-33.60
data/parameters/restraints	5824/440/130	5902/487/21	3737/398/3	4304/235/15	2016/116/0
R1/wR2 [I>2σ(I)]	8.19%/21.84%	5.71%/18.06%	2.67%/6.87%	2.57%/6.76%	2.58%/6.31%
R1/wR2 (all data)	8.56%/22.22%	10.13%/13.00%	2.61%/6.83%	2.88%/6.95%	3.12%/6.60%
Goodness of Fit	1.046	1.03	1.054	1.044	1.044
hydration	2 bound	$2\frac{1}{2}$ bound, 1 unbound	1 bound	2 bound, 1 unbound	2 bound
dimensionality	I^0O^3	I^1O^2	I^2O^1	I^0O^2	I^0O^3

Table 6.3: Summary of refined Rietveld models to powder diffraction data

	CaFDC	SrFDC	BaFDC	CdFDC	MnFDC
Formula	$CaC_{15}O_7H_{10}$	$Sr_2C_{30}O_{17}H_{26}$	$BaC_{15}O_6H_8$	$CdC_{15}O_8H_{12}$	$MnC_{15}O_7H_{10}$
SG	$P2_1$	$P\bar{1}$	$P1$	$P2_1/c$	$C2/c$
a (Å)	7.5515(4)	8.5904(4)	6.7996(17)	7.7388(21)	26.89540(22)
b (Å)	6.6325(3)	11.8583(6)	7.2493(21)	28.502(6)	7.21464(6)
c (Å)	27.962(1)	15.6506(7)	14.274(4)	6.7446(16)	6.99755(5)
α (°)	90	72.484(4)	82.836(33)	90.00	90.00
β (°)	97.49(1)	78.663(4)	83.848(31)	105.286(23)	97.4052(11)
γ (°)	90	85.464(4)	67.018(19)	90.00	90.00
V (Å^3)	1388.5(1)	1490.37(8)	641.36(22)	1435.0(4)	1346.484(15)
χ^2	10.560	5.048	5.592	4.430	4.329

6.4.2 Room temperature luminescence

The excitation curve of the parent ligand H_2FDC (Figure 6.21), measured at λ_{em}=500 nm, shows strong peaks near 390 nm and 440 nm and then decreases sharply. The accompanying emission curve, measured at λ_{ex}=440 nm, shows a broad emission centred at 515 nm. Room temperature excitation and emission curves of H_2FDC, CaFDC, SrFDC, BaFDC, and CdFDC show broad emission that is yellow for the ligand itself, and shifted slightly for each framework structure. MnFDC did not show visible photoluminescence, presumably due to the paramagnatism of the Mn^2+ cation and thus the lone pair electrons interacting with the fluorenone π-electron system. The excitation curve of CaFDC (Figure 6.22), measured under the same conditions, is mostly constant into the blue and drops sharply at 460 nm. The emission curve, measured at λ_{ex}=440 nm, peaks at 503 nm with a long tail into the red. Similarly, the excitation of SrFDC (Figure 6.23) drops sharply at 460 nm and the emission peaks at 526 nm. The excitation spectra for BaFDC (Figure 6.24), measured at λ_{em}=535 nm, peaks at 400 nm and 445 nm. The emission spectra, measured at λ_{ex}=365 nm, has a maximum at 517 nm. The excitation spectra for CdFDC (Figure 6.25), measured at λ_{em}=535 nm, peaks at 394 nm, 450 nm, 468 nm. The emission spectra, measured at λ_{ex}=365 nm, has a maximum at 428 nm. These emission spectra overlayed on a single graph (Figure 6.26) show a consistent peak shape, blue-shifted from the H_2FDC emission for CaFDC and red-shifted for the other structures.

This luminescence of the fluorenone chromophore comes from a triplet state in the π electron system. Thus the emission colour is determined by the spacing between the ground state and the triplet state. There is a general trend in the red-shifting of the emission color with atomic mass, and thus it is likely that the increasing atomic size of the cation is leading to a lowering of the triplet state

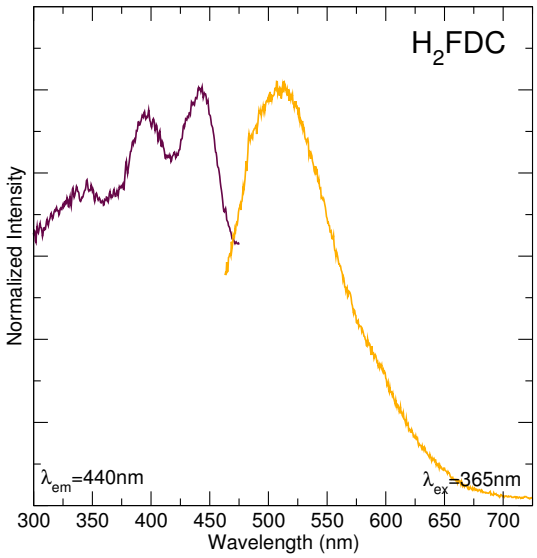

Figure 6.21: photoluminescence excitation and emission spectra for the free ligand H_2FDC, λ_{ex} =365 nm, λ_{em} =440 nm.

energy by way of increasing the configurational coordinate value of the stokes shift, and thus a red-shifted emission color is observed.

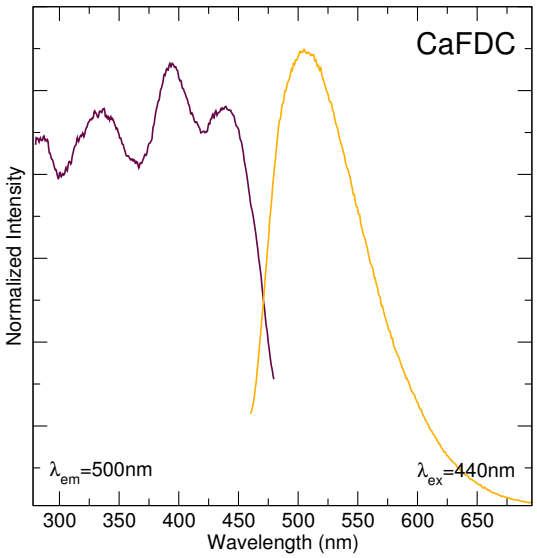

Figure 6.22: photoluminescence excitation and emission spectra for CaFDC, λ_{ex} =440 nm, λ_{em} =500 nm.

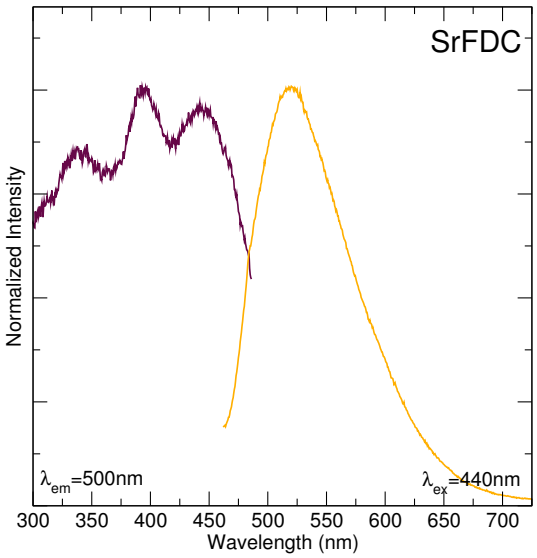

Figure 6.23: photoluminescence excitation and emission spectra for SrFDC, λ_{ex} =440 nm, λ_{em} =500 nm.

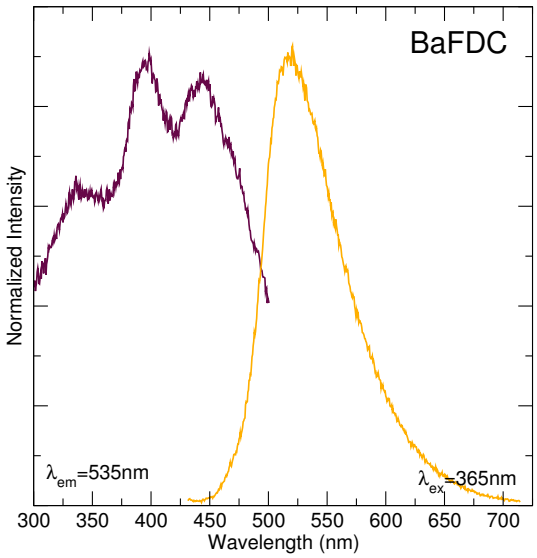

Figure 6.24: photoluminescence excitation and emission spectra for BaFDC, λ_{ex} =365 nm, λ_{em} =535 nm.

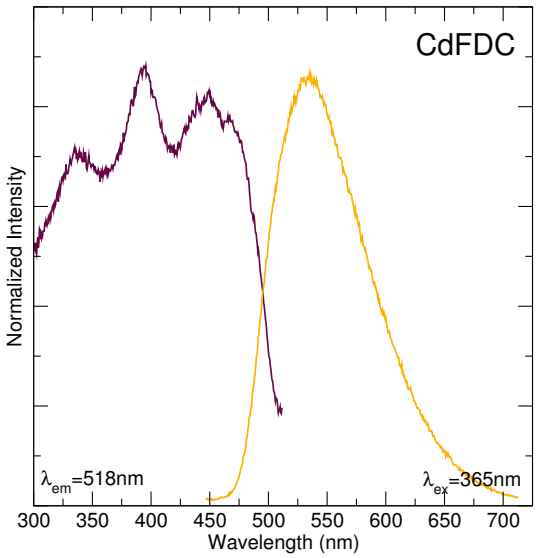

Figure 6.25: photoluminescence excitation and emission spectra for CdFDC, λ_{ex} =365 nm, λ_{em} =535 nm.

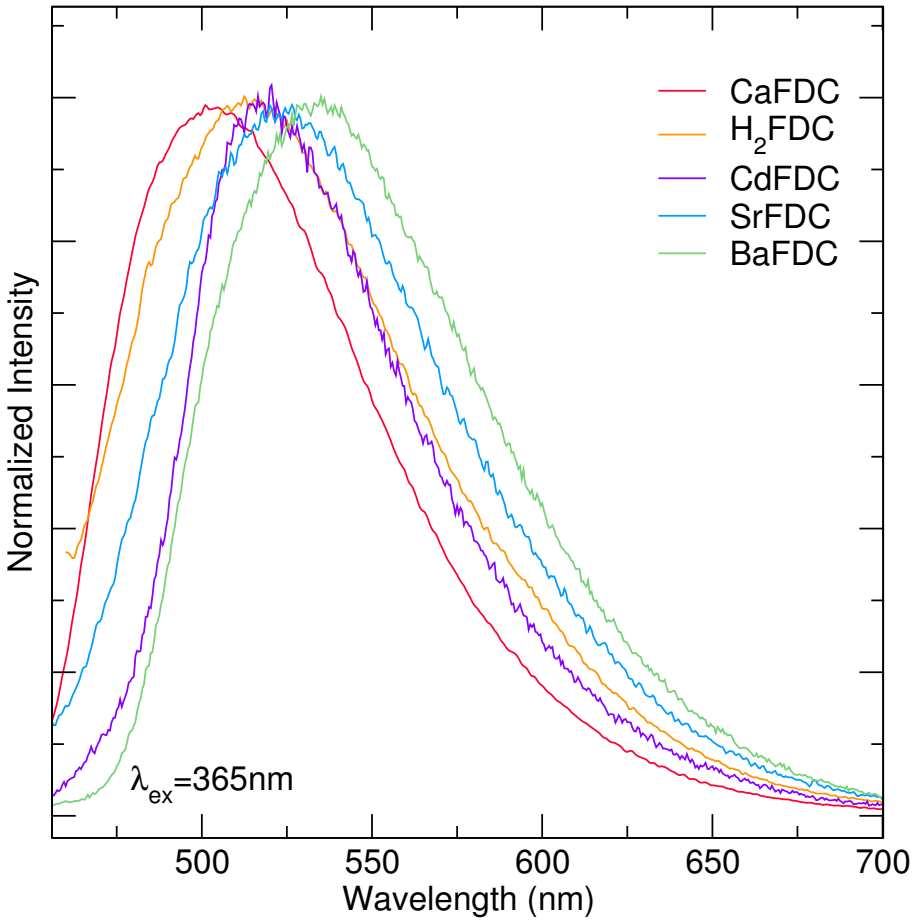

Figure 6.26: Normalized photoluminescence emission spectra for all fluorenone compounds. The CaFDC is blue shifted from the H_2FDC emission and all of the others are red shifted. λ_{ex}=365 nm.

6.4.3 Temperature dependent luminescence

Temperature dependent emission spectra for H_2FDC and the luminescent fluorenone frameworks are shown in Figures 6.27 through 6.31. Samples were all measured down to 77 K, although the maximum temperature varied slightly due to sample stability. An inverse-S type curve is expected for thermal quenching of luminescent states. H_2FDC and CaFDC exhibit this quite clearly, while the other compounds may but the decay occurs over a wider range than the compound is otherwise chemically stable.

The room temperature quantum yield (QY) of CaFDC was measured at 7.4%, SrFDC at 2.8%, BaFDC at 2.8% and CdFDC at 2.6%, and the ligand H_2FDC at 2.4%. These were performed as a single measurement and so the error is not calculated, but the system is considered to have an error less that 5%. Moreover, while the absolute value of the quantum yield may have some inaccuracy, the relative values are significant. From this it can be said that the QY of the SrFDC, BaFDC, CdFDC, and H_2FDC are statistically similar, while the efficiency of the CaFDC is increased. The extracted temperature dependent QY data is shown in Figure 6.32. Notably, at 77 K the QY is of CaFDC is 15%, approximately double its value at room temperature.

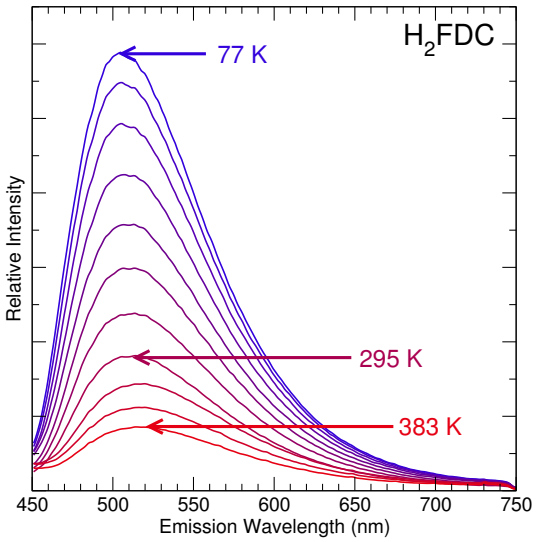

Figure 6.27: Temperature dependent emission spectra (λ_{ex} =405 nm) of H_2FDC, increasing in temperature from 77 K (blue) to 383 K (red).

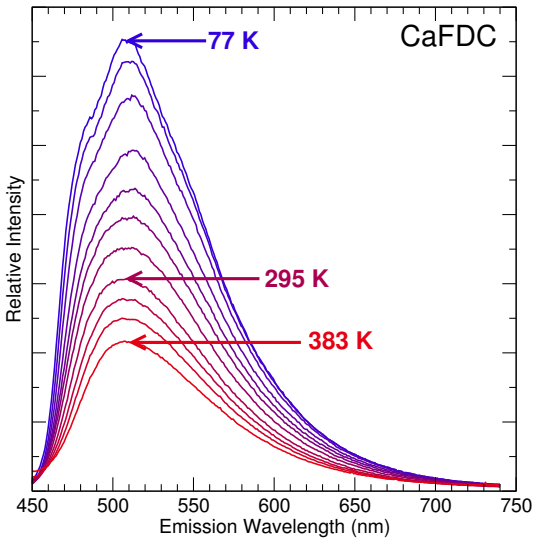

Figure 6.28: Temperature dependent emission spectra (λ_{ex} =405 nm) of CaFDC, increasing in temperature from 77 K (blue) to 383 K (red).

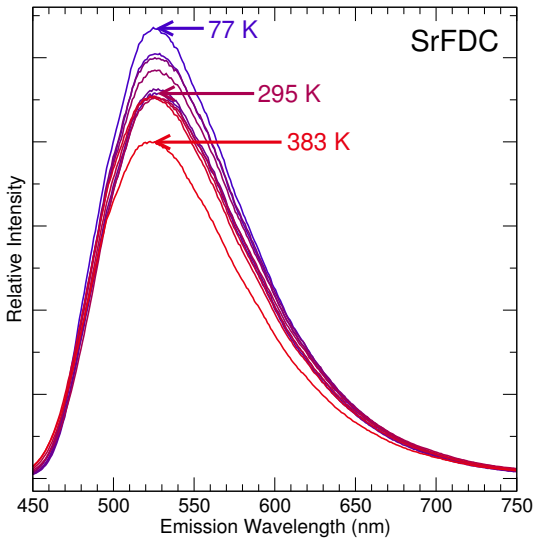

Figure 6.29: Temperature dependent emission spectra (λ_{ex} =405 nm) of SrFDC, increasing in temperature from 77 K (blue) to 383 K (red).

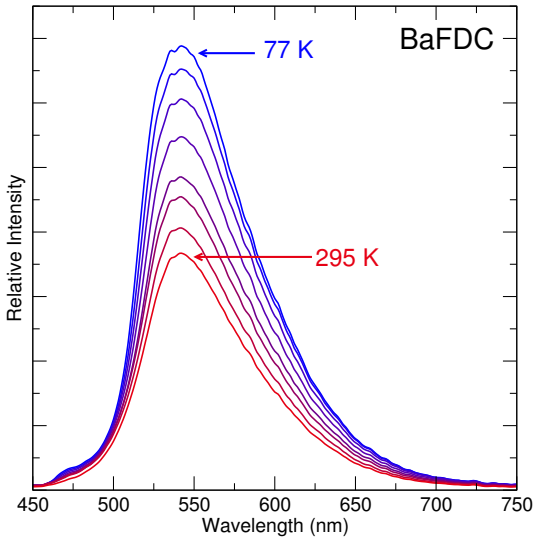

Figure 6.30: Temperature dependent emission spectra (λ_{ex} =405 nm) of BaFDC, increasing in temperature from 77 K (blue) to 295 K (red). High temperature data was omitted for clarity due to an emission colour shift.

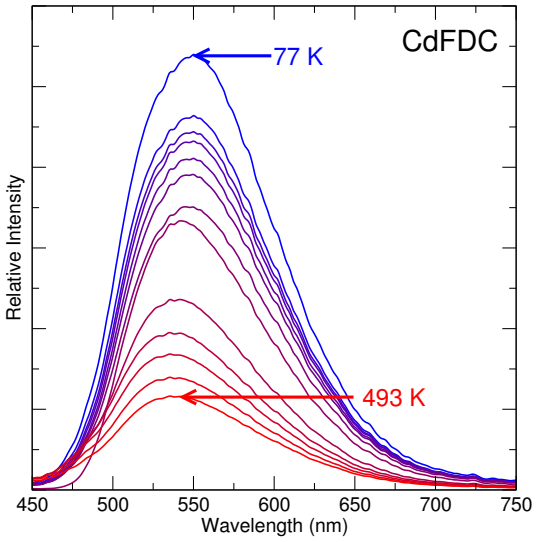

Figure 6.31: Temperature dependent emission spectra (λ_{ex} =405 nm) of CdFDC, increasing in temperature from 77 K (blue) to 493 K (red).

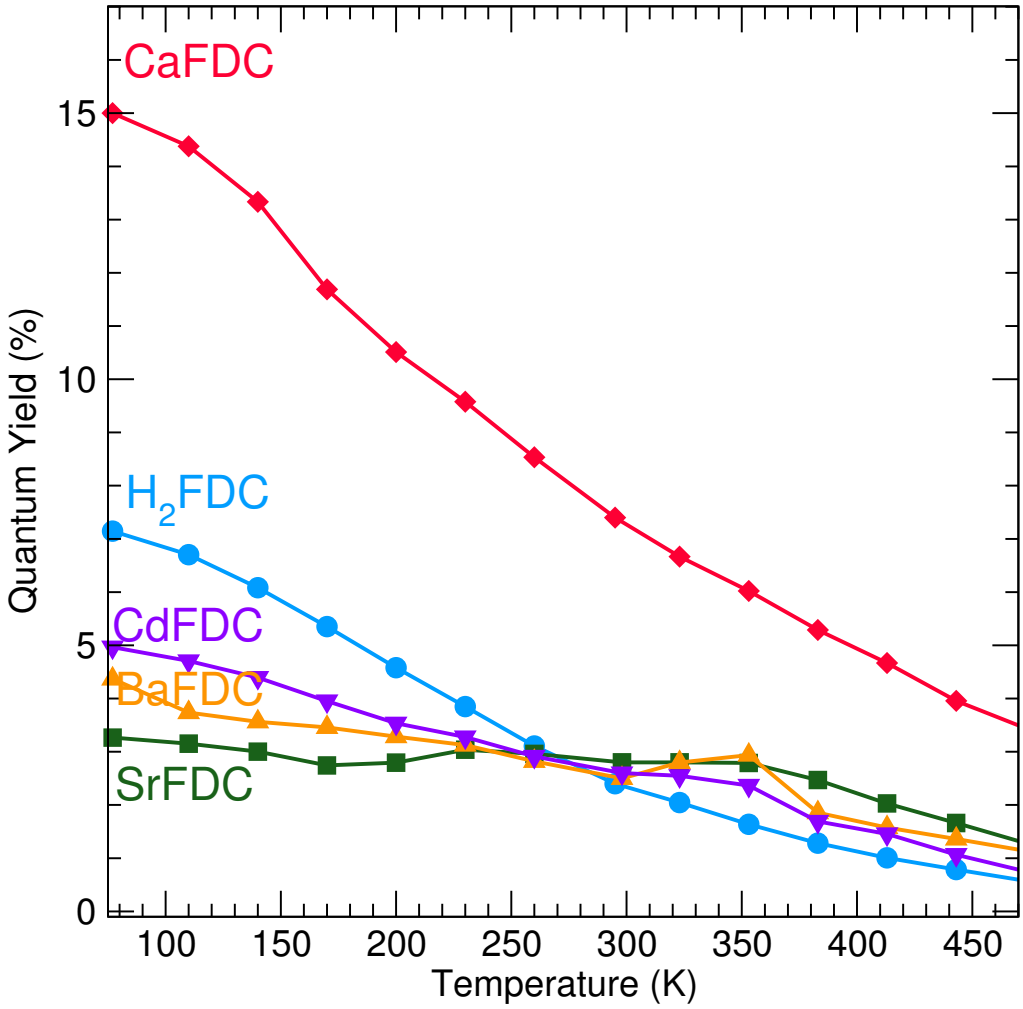

Figure 6.32: Temperature dependent QY of fluorenone compounds.

6.4.4 Luminescent lifetimes

The luminescent decay for compounds CaFDC, SrFDC, BaFDC, and CdFDC were measured and are shown in Figures 6.33. Laser excitation was used at 400 nm and the emission wavelength was monitored at the maximum of the emission peak, as listed in the figures. The data are fitted to a double exponential decay as shown in the red line in the plots and summarized in Table 6.4 according to:

$$I_t = I_1 e^{\frac{-t}{\tau_1}} + I_2 e^{\frac{-t}{\tau_2}} \tag{6.14}$$

where I_1 and I_2 are the intensities of the emissions of the different processes at t_o, and their ratio gives the contribution of each process to the radiative deactivation. τ_1 and τ_2 are the lifetimes of each process. The RMS error in the curve fitting is also listed. For the BaFDC, the sensitivity of the detection system was limited for such rapid decay and so the first 2 ns were omitted from the curve fitting. Fitting the full data resulted in the nearly the same coefficients, but with a large RMS error value. For comparison, the decay constant for YAG:Ce is typically on the order of 50 ns, depending on the crystallinity of the sample [155, 156].

Table 6.4: Summary of luminescent lifetime decay exponentials for FDC compounds

Compound	I_1 (a.u.)	I_2 (a.u.)	τ_1 (ns)	τ_2 (ns)	$\frac{I_1}{I_2}$	fitting RMS
CaFDC	10230	5339	11.4	3.3	1.92	8.27%
SrFDC	10850	3820	12.4	4.3	2.84	6.78%
BaFDC	4169	11854	7.2	2.0	0.35	13.55%
CdFDC	8061	7138	11.7	2.8	1.13	11.81%

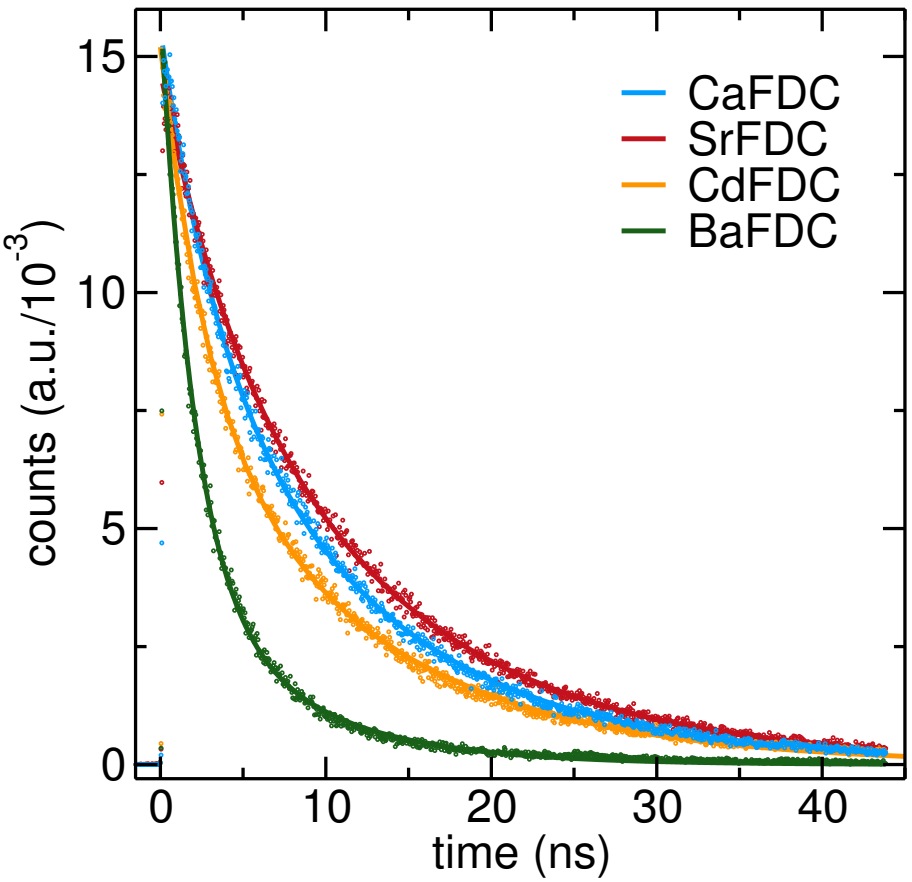

Figure 6.33: Luminescent lifetime for all fluorenone framework compounds.

6.4.5 Thermal analysis

Thermogravimetric analysis (TGA) was carried out in air for the fluorenone samples up to 1000°C, at which point they decomposed to their constituent oxides or carbonates, depending on the metal species. The decomposition products are summarized in Table 6.5. Thermal gravimetric analysis in air of CaFDC (Figure 6.35) shows removal of the two water molecules in two steps near 115°C and 200°C. An anhydrous phase is then present on heating until 560°C, where the compound decomposes to calcium carbonate and then finally to calcium oxide at 713°C. Analysis of SrFDC (Figure 6.36) shows dehydration steps ending at at 127°C and 270°C corresponding to a loss of 3.5 water molecules to an anhydrous structure that is stable to 400°C. Decomposition to strontium carbonate is completed at 560°C, and a final decomposition to strontium oxide occurs between 800°C and 960°C. BaFDC (Figure 6.37) shows multiple small dehydration steps corresponding to a loss of 1 water molecule, followed by a large weight loss step starting at 430°C and ending at 557°C, where the compound decomposes to barium carbonate. CdFDC (Figure 6.38) shows dehydration steps up to 150°C corresponding to the loss of 3 water molecules, as expected from the formula, and then a large weight loss starting at 350°C and ending at 500°C where the compound decomposes to cadmium oxide. MnFDC (Figure 6.39) shows a dehydration step between 120°C and 220°C corresponding to a loss of two water molecules, followed by decomposition and oxidation to manganese dioxide between 420°C and 510°C.

Table 6.5: Thermogravimetric analysis of fluorenone frameworks

Compound	Initial Mass ($g \cdot mol^{-1}$)	Final Mass Percent (%)	Observed final mass ($g \cdot mol^{-1}$)	Decomposition product	Ideal decomposition mass ($g \cdot mol^{-1}$)	Error (%)
CaFDC	342.31	16.5	56.5	CaO_2	56.1	0.7
SrFDC	416.88	25.5	106.3	SrO	103.6	2.6
BaFDC	421.55	43.2	182.3	$BaCO_3$	197.3	7.6
CdFDC	432.65	31.4	135.8	CdO	128.4	5.7
MnFDC	357.17	24.3	86.8	MnO_2	88.69	0.2

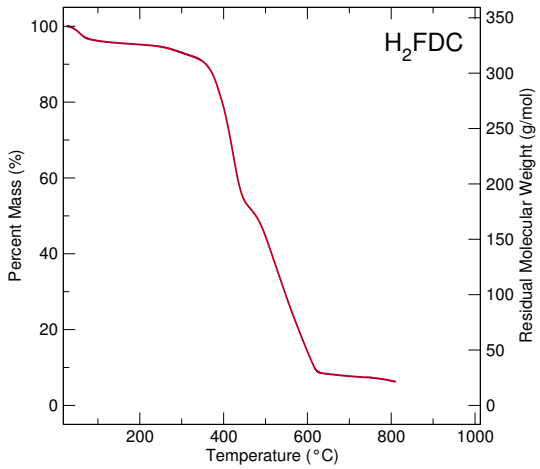

Figure 6.34: Thermogravimetric analysis of H_2FDC in air.

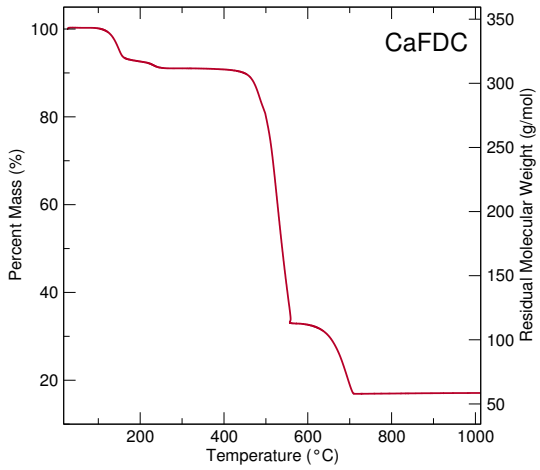

Figure 6.35: Thermogravimetric analysis of CaFDC in air.

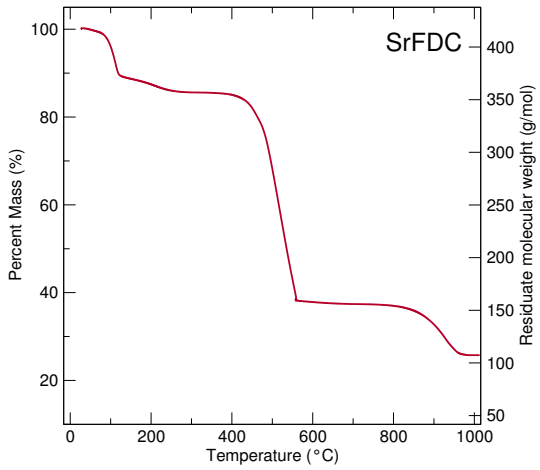

Figure 6.36: Thermogravimetric analysis of SrFDC in air.

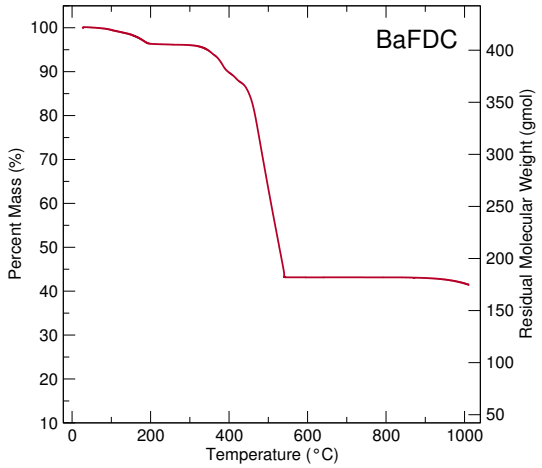

Figure 6.37: Thermogravimetric analysis of BaFDC in air.

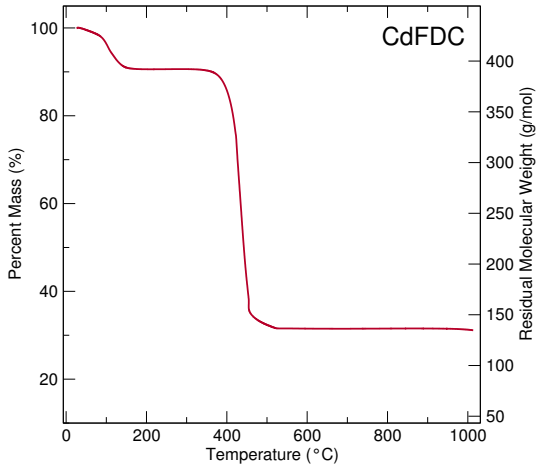

Figure 6.38: Thermogravimetric analysis of CdFDC in air.

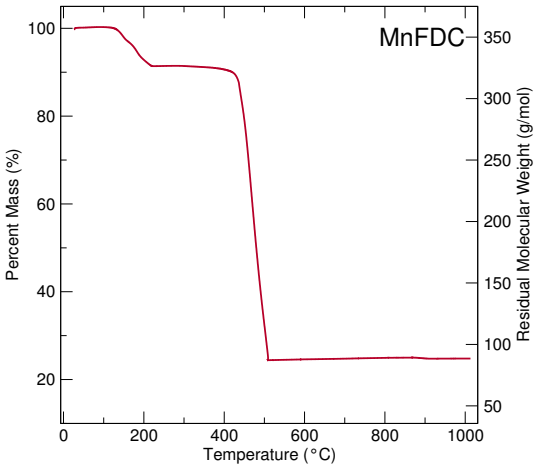

Figure 6.39: Thermogravimetric analysis of MnFDC in air.

6.4.6 Specific heat

The specific heat, as measured, is shown in Figure 6.40 and the calculations to extract the characteristic Debye temperatures are shown in Figure 6.41. They are summarized in Table 6.6, which lists the coefficients for fitting of Equation 6.8 to a 4 term taylor expansion, as described in Section 6.3. Figure 6.42 shows the specific heat plotted as C_p/T^3 against T/θ_D as a semi-log plot [157]. This plot helps to reveal deviations from the expected Debye behaviour [151] The data for H_2FDC is anomalous and has been omitted, because considering continuous lattice vibrations in a system without an extended covalent network is fundamentally different. This is not unexpected as the work of Talon et al. showed a large deviation from expected Debye behaviour for molecular solids as compared to amorphous and crystalline extended network solids. The behaviour of the fluorenone-containing frameworks shows no sharp peaks or discontinuities that would indicate a first or second order phase transition. They do all show a

Table 6.6: Summary of fitting functions for heat capacity data with formula $AT + BT^3 + CT^5 + DT^7$, Debye temperature θ_D, and RMS error of the fit.

Compound	A	B	C	D	θ_D	RMS Error
H_2FDC	0.0268584	0.00479257	-2.39301e-5	7.57669e-8	225 K	12.4%
CaFDC	0	0.00189032	-1.08458e-6	9.13224e-9	324 K	8.43%
SrFDC	0	0.00262637	2.00472e-7	-8.61947e-9	381 K	3.70%
BaFDC	0	0.00612649	-5.428e-6	-2.67416e-9	267 K	1.47%
CdFDC	0	0.0261431	1.17412e-6	-1.42275e-8	299 K	3.70%

broad peak at around 10 K. The increased value of C_p/T^3 at low temperature for BaFDC as compared to the calcium-containing framework suggests that increased collective vibrations present in the lattice may be quenching the luminescent processes by providing non-radiative recombination pathways as compared to the more localized vibrations in CaFDC. Similarly, the work of Ramos et al. showed higher values in the C_p/T^3 curves for glasses as compared to crystalline solids of the same composition [158]. Furthermore, the lowest Debye temperature in the framework structures was extracted for BaFDC, suggesting a lower temperature crossover to collective vibrations in the lattice. This may explain why, despite the broad structural and chemical similarity of the BaFDC and CaFDC samples, the luminescence of the barium compound is so reduced.

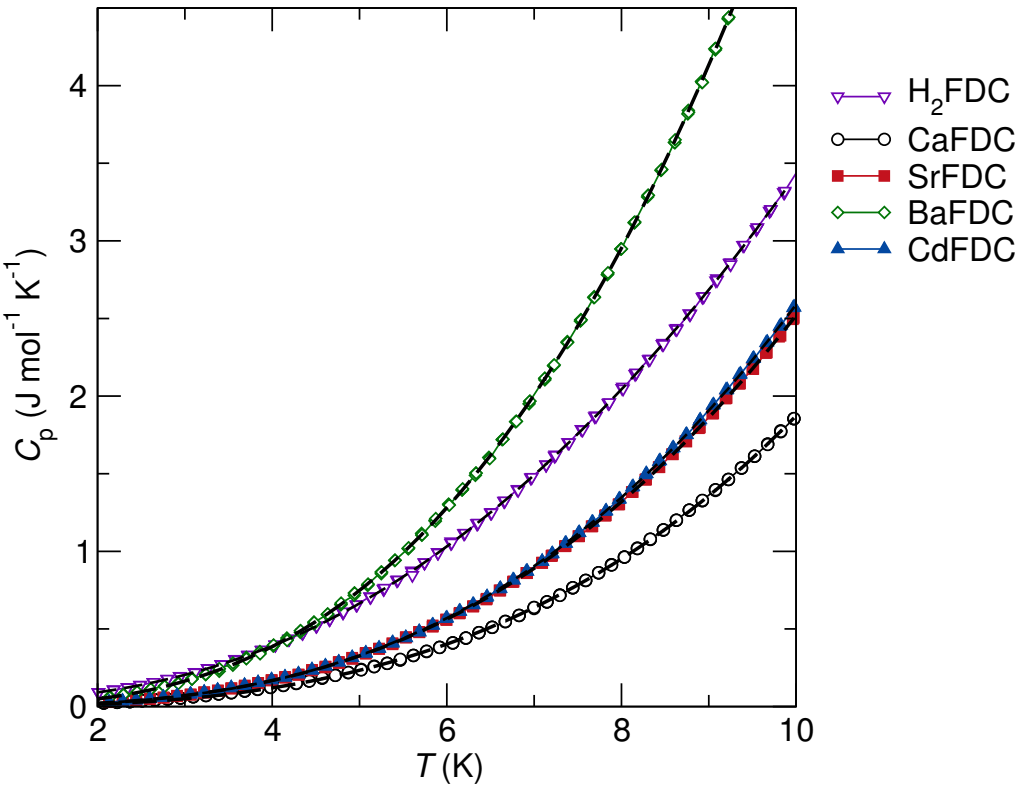

Figure 6.40: Heat capacity of ligand H_2FDC and fluorenone frameworks.

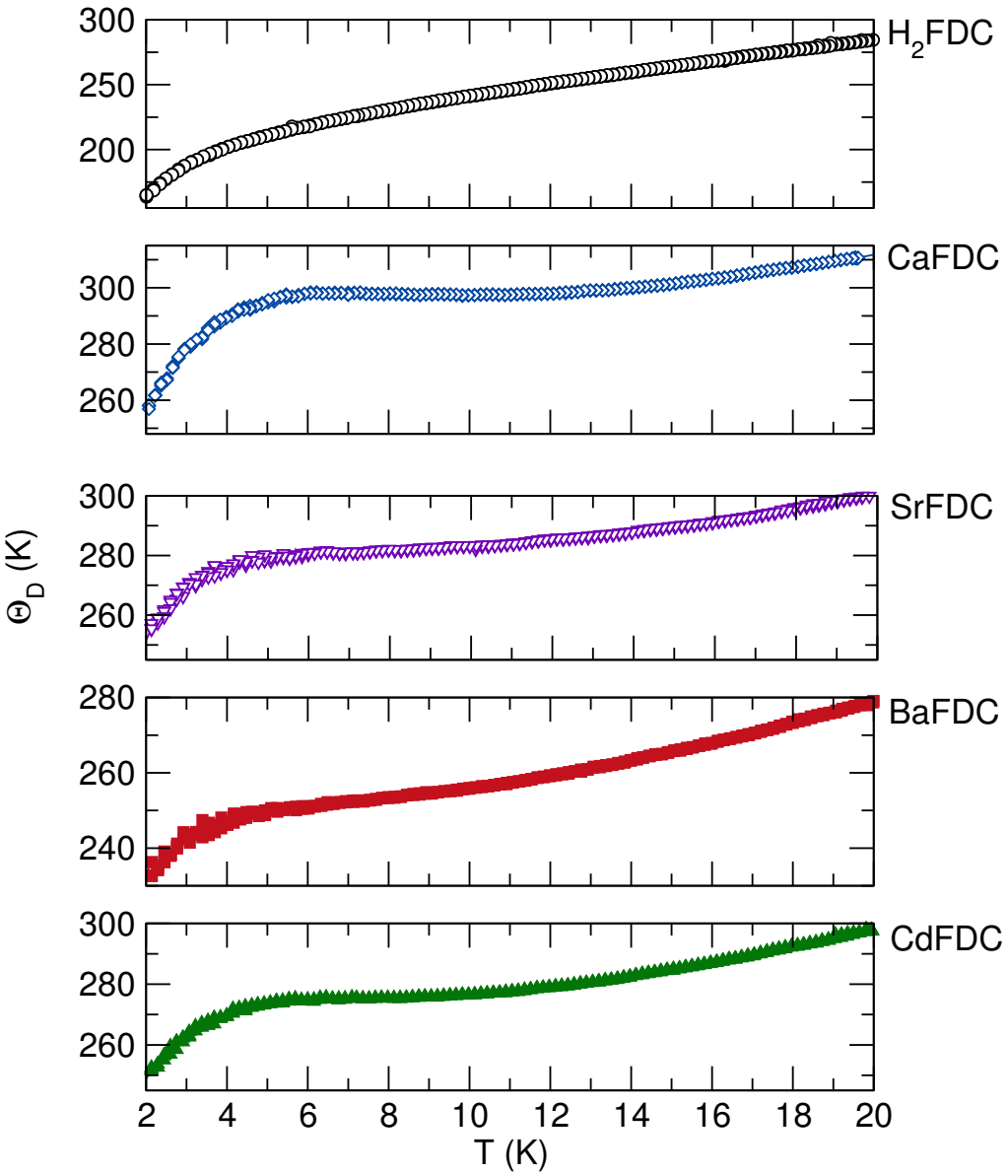

Figure 6.41: Debye temperature for the ligand H_2FDC and fluorenone frameworks.

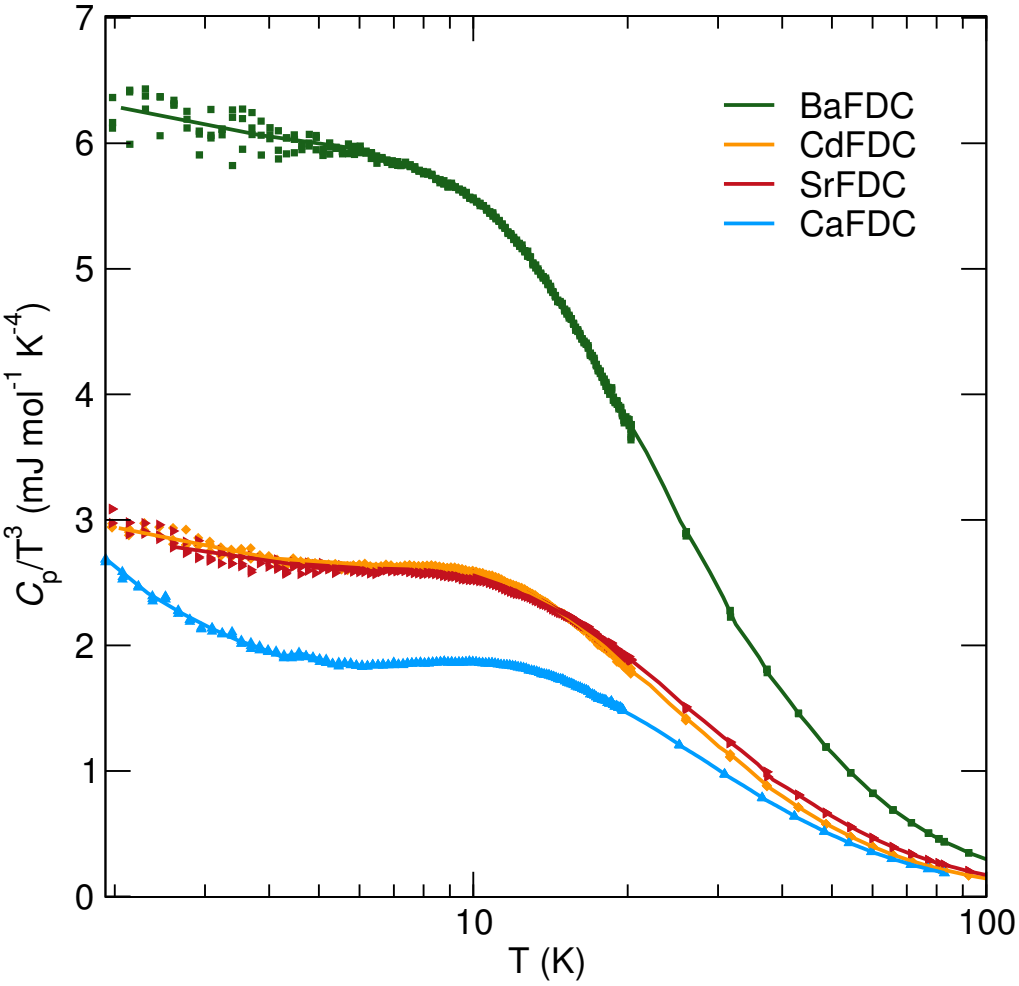

Figure 6.42: Heat capacity data plotted as C_p/T^3 vs. T/θ_D heat capacity for fluorenone frameworks

6.4.7 Bonding modes

The bonding modes of the carboxylic acid groups to the metal atoms for the five fluorenone containing structures are shown in Figures 6.43 through 6.48. Because the structures of CaFDC and SrFDC were determined and the luminescent properties of those compounds were studied earlier in the course of this thesis than the final three compounds, it was initially believed that the increased QY of CaFDC may have been explained by increased rigidity in the structure with respect to both SrFDC and H_2FDC. For CaFDC, each oxygen of the dicarboxylic acid groups is bound to a single calcium atom, while one of every four dicarboxylate oxygen atoms in SrFDC is unbound and "loose" to vibrate in a way that might quench luminescence. The H_2FDC is a hydrogen-bonded molecular crystal with presumably all unbound oxygen atoms, although a specific crystal structure has not been published and efforts to recrystallized samples for X-ray were unsuccessful. With the addition of the BaFDC and CdFDC, the relationship becomes less clear. By this analysis one would expect that the highly bonding bonded BaFDC, shown in Figure 6.46, would lead to the highest QY. However, measurements revealed that it is approximately the same as SrFDC and H_2FDC. While it is certainly possible that the bonding arrangements of the ligands to the metals impact the luminescence, the specific nature of that relationship is not clear. Pairs of adjacent ligands are shown in Figure 6.15, where it can be seen that no significant differences exist in the interligand spacing and angles. The skew of the ketone groups does change between samples but not in any way that shows a trend with the luminescence data.

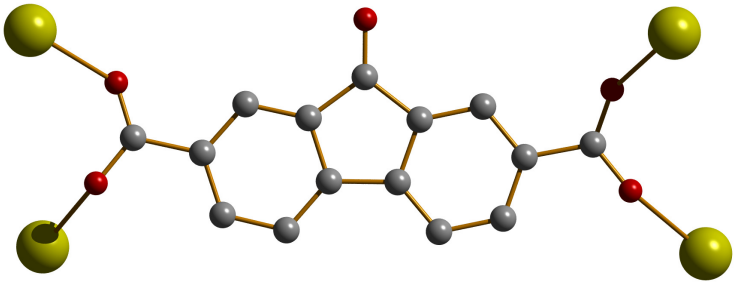

Figure 6.43: Bonding mode of CaFDC

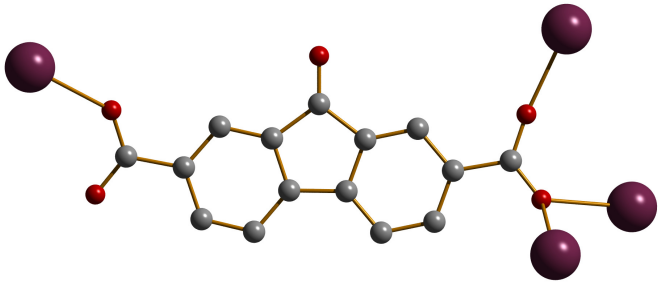

Figure 6.44: First bonding mode of SrFDC

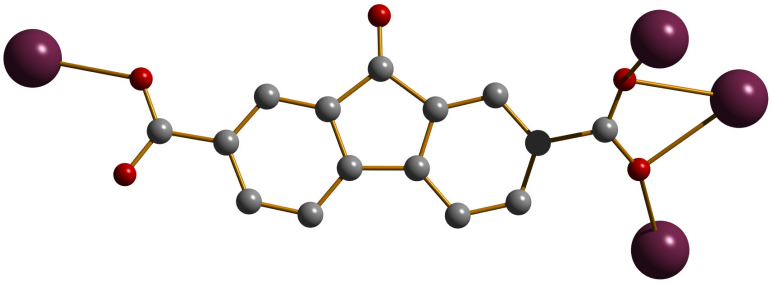

Figure 6.45: Second bonding mode of SrFDC

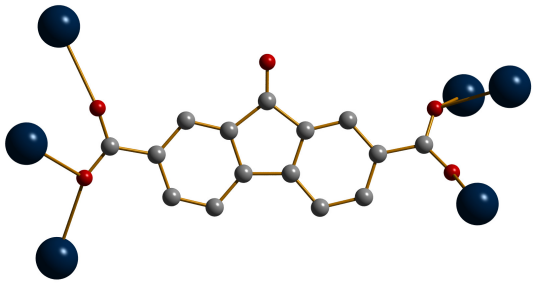

Figure 6.46: Bonding mode of BaFDC

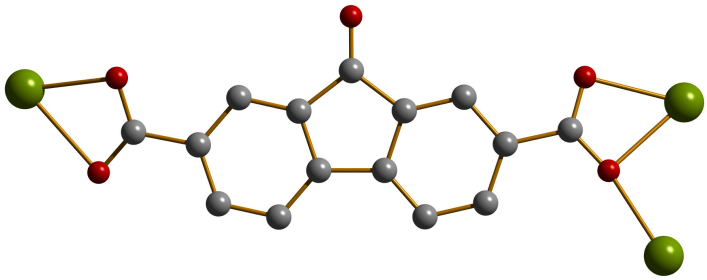

Figure 6.47: Bonding mode of CdFDC

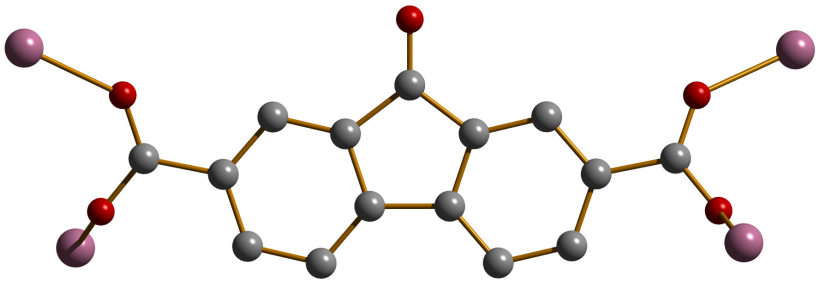

Figure 6.48: Bonding mode of MnFDC

6.5 Discussion

Five new fluorenone frameworks have been discoved. They represent a new approach to the development of solid state lighting phosphors as they show many of the properties required for the application, in a previously unexplored class of materials. The CaFDC compound is remarkable in that it contains only calcium, carbon, oxygen, and hydrogen and is synthesized in water at mild temperatures. Cerium doped YAG, for comparison, is synthesized by a high temperature ceramics route using rare earth elements. Luminescent molecules like fluorenone and its derivatives have long been used in strictly organic applications where it has been cross-linked into polymers [159] and combined into OLEDs [160]. Other classes of inorganic-organic framework structures have been used with both metal centred and antenna type structures with potential applications in sensors and scintillators. This is the first reported example of a ligand-centred luminescent framework that, in terms of excitation and emission spectra, meets most of the requirements for solid state lighting. It is also the first report of frameworks based upon this ligand. The photoluminescence of these compounds can be excited in the near UV and blue, between 380 nm and 460 nm, and gives broad emissions that peak between 500 nm and 535 nm. The tunability of that peak is provided by changing the metal cation. That control is essential for high performance phosphor materials. Figure 6.49 shows the excitation and emission spectra of CaFDC in comparison to YAG:Ce, similar to the comparison made in Figure 5.20 in the previous chapter for CaAQDC. With a FWHMs around 100 nm, the emission broadness of CaFDC is slightly larger than that of Ce^{3+}:YAG phosphors.

It was suggested in the beginning of Chapter 5 that by placing an organic chromophore into a framework structure, its luminescence could be enhanced by

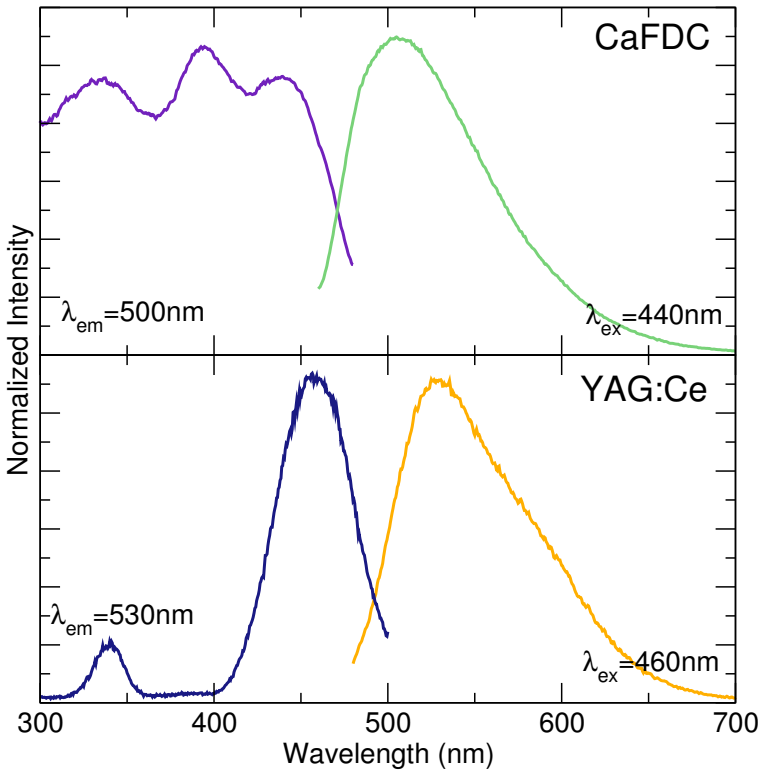

Figure 6.49: TOP: Excitation and emission spectra of CaFDC, BOTTOM: Excitation and emission for YAG:Ce. Note the increased band width for the fluorenone structure.

virtue of increased structural rigidity. In the CaFDC, this is clearly evident in the doubling of quantum efficiency as compared to the parent ligand. The behaviour of the other frameworks is more complex, as they show photoluminescence efficiencies closer to that of the H_2FDC. It is proposed that the inclusion of the organic chromophore in a rigid framework network is indeed beneficial in all of the framework structures, and that there are peculiarities in the SrFDC, BaFDC, and CdFDC cases that quench the enhanced luminescence.

Even though the structures are broadly related and have similar compositions, certain details in dimensionality, hydration, and coordination are quite different.

A lack of structural rigidity in SrFDC comes from an one of the four carboxylate group oxygen atoms on each ligand being unbound, as shown in Figure 6.44 and 6.45, as well as pore space waters. This "loose" C–O bond can provide vibrational routes to recombination and quench photoemission. The O–H vibrations on the pore space water near the luminescent chromophore also provide non-radiative routes to the ground state. BaFDC forms with the nearly the composition and degree of hydration as the calcium structure, however it shows much lower efficiency. The large contribution to the lattice specific heat and the significantly shorter lifetime indicate that some rapid process is present, likely based in oscillations of the edge and corner sharing barium polyhedra, that quenches the excited states before they are able to radiatively recombine. Moreover, the low Debye temperature of BaFDC (267 K as opposed to 324 K for CaFDC) indicates that the phonon modes in this compound are more collective than they are localized. For efficient luminescence in this model, the excited states should be as localized as possible to reduce cross-relaxation between the ligands. Interestingly, SrFDC actually shows the highest Debye temperature at 381 K, but since the quenching mechanism is thought to reside in the light carbon and oxygen atoms rather than a heavy cation, the contributions of those oscillations to the lattice specific heat are smaller. The cadmium structure, CdFDC, shows only 2-dimensional connectivity with some pore space water, both of which provide routes to non-radiative recombination. The lower dimensionality of this structure is less rigid and allows for more thermal vibrations to quench luminescence. The behaviour of MnFDC, with its paramagnetic d^5 metal centers, is indicative of the importance of using filled outer shell cations to prevent electronic processes on the metal from quenching organic luminescence. For CaFDC, however, there is no pore space water, isolated metal atoms, and symmetrically bound chromophore groups, resulting in efficient

photoluminescence.

Organic and polymer systems generally show a reduction in quantum yield with increasing π-stacking. It has been reported in the literature that increased π-stacking leads to a reduction in quantum yield for conjugated polymers because of increased aggregate formation and thus increased non-radiative cross-relaxation between ligands [161–163]. The theoretical analysis of Cornil et al. considered cofacial dimers of stilbene molecules and found that with an interchain distance below 5Å the molecular orbitals of the dimer pair begin to delocalize with a chain spacing below 5Å. [164]. It would appear that this is not the case for these framework systems as the most perfect π-stacking in terms of alignment is seen in the calcium structure, which is also the brightest. However, the average separation distances show a downward trend with cation size, from 3.41 Å for CaFDC to 3.38 Å for SrFDC to 3.30 Å for BaFDC and 3.33 Å for CdFDC. Moreover, we do not expect to see the dimerization that is possible for purely organic systems because the chromophores are so tightly held in place. Similarly, Chen et al. described two unique Zn(II)-norfloxin networks where the more π-stacked arrangement showed nearly double the QY of the tilted structure [165]. It is believed that in the fluorenone frameworks the contributions to structural rigidity from the π-π bonding outweighs any electronic interactions and that the slightly larger separation in CaFDC provides just enough electronic isolation that the cross-relaxation effects are reduced.

Another trend that is apparent in these compounds is increasing inorganic dimensionality with increasing cation size. The alkali earth compounds CaFDC, SrFDC, and BaFDC showed 0-, 1-, and 2-dimensional inorganic connectivity, respectively. This trend was recently highlighted in work by Eduardo Falcão et al. [166] using a thiazolothiazoledicarboxylate ligand, where the inorganic connec-

tivity increased from isolated magnesium polyhedra to calcium dimers to strontium chains to a barium 2-dimensional sheet. For those compounds it was proposed that the increasing cation size allows for more bound water molecules to act as bridges rather than just capping ligands. This is apparent for the strontium structure, where bridging waters help form the inorganic chains. It is not, however, the case for the barium structure, where all of the M–O–M linkages are by carboxylic acid groups. Nevertheless, the increasing inorganic connectivity appears to be detrimental to luminescent efficiency, likely due to metal–metal oscillations quenching excited states on the organic chromophore. This suggests that small cations will lead to isolated metal polyhedra, which in turn may lead to brighter phosphors.

6.6 Summary

For a previously unexplored approach to phosphor development for solid state lighting, the fluorenone-containing compounds described here show remarkably applicable photoluminescence excitation and emission properties. While they do fall short in terms of the brightness and temperature dependent behaviour requirements that are essential for commercial viability of a phosphor, the CaFDC excitation and emission exceeds the performance of YAG:Ce by giving broader emission. Its excitation requires light about 10 nm further into the blue, but it also allows for a much wider range of UV and blue excitation as compared to YAG:Ce.

With the knowledge gained here, it is now possible to propose some design criteria for framework phosphors. Isolating metal cations in a 3-dimensional network, thus an I^0O^3 network, is the most important, will most likely be achieved by using small cations. Increasing π-π stacking separation and reducing pore-space

water also impact performance. The intrinsic quantum efficiency of the parent ligand chromophore is also a critical design consideration. These compounds, and the anthraquinones from the previous chapter, clearly suggest that this approach to the development of new luminescent materials warrants further study and that with proper combinations of metal, ligand, and structure, highly stable and emissive compounds may well be accessible.

The research described in this chapter was carried out in collaboration with Brent Melot, who performed the heat capacity measurements, Simon Teat who assisted with the synchrotron X-ray single crystal crystallography, Alexander Mikhailovsky who performed many of the optical measurements, and Alina Warner who assisted with some of the synthesis. The structure and luminescence of CaFDC and SrFDC have been published in Chemistry of Materials as: J. D. Furman, A. Y. Warner, S. J. Teat, A. A. Mikhailovsky and A. K. Cheetham. "Tunable, ligand-based emission from inorganic-organic frameworks: A new approach to phosphors for solid state lighting and other applications." *Chem. Mater.*, **22**, 2255-2260 (2010). [DOI: 10.1021/cm9030733]. A manuscript describing the structure of BaFDC, CdFDC, and MnFDC, and luminescent properties of all five compounds has been published as: J. D. Furman, B. C. Melot, S. J. Teat, A. A. Mikhailovsky and A. K. Cheetham. "Towards enhanced ligand-centered photoluminescence in inorganic-organic frameworks for solid state lighting." *Phys. Chem. Chem. Phys.*, 2010 [In Press].

Chapter 7

Conclusions and future work

In the 17 years since the commercialization of the first bright blue LEDs, the potential benefits of illumination by solid state devices have captivated researchers studying everything from physics to political science. While initial developments have been promising and the increases in output light efficiency have come continuously over the years, two large barriers still remain: colour quality and power limitations. This work addresses the colour available from devices.

The benefits of using oxide nanoparticle phosphors were investigated in Chapter 3 for YAG:Ce. It was found that the structural disorder present in nanoparticles as a result of the lower temperature processing needed to avoid sintering led to reduced quantum yield. This outweighed any scattering reduction that small phosphor particles might provide. While it has not been shown, nanoparticles of the hybrid frameworks should be much more easily synthesized as their processing is already in water at low temperatures. It is possible that reduced scattering benefits could be realized in those compounds without loss of quantum yield.

The physical robustness of dense inorganic-organic framework compounds was shown in Chapter 4 for cerium oxalate formate. While it turned out to not be a

useful compound for phosphor applications, it was an ideal system for studying the mechanical properties of this class of materials. It was shown to be nearly as strong as classical ceramic materials and is certainly suitable for use in solid state device applications.

Novel phosphor materials, utilizing unique ligand-based luminescence in hybrid frameworks, were introduced in the anthraquinones of Chapter 5 and the fluorenones of Chapter 6. This approach to solid state lighting phosphors is without precedent. There have been evaluations of ligand-based luminescence from hybrid frameworks reported, but all are excited much too far into the UV for use in GaN-based devices. The anthraquinone and fluorenone frameworks both meet most of the criteria for solid state lighting applications. The excitation and emission of YAG:Ce, CaAQDC, and CaFDC are shown in Figure 7.1. A vertical blue band indicates the excitation with of a typical 450 nm GaN-based LED, showing that the CaFDC is suitable for excitation at this wavelength, while the CaAQDC is not. The width of the excitation band in the CaFDC is slightly larger than the width for YAG:Ce, and CaAQDC is significantly larger. As the next generation of LED emitters moves further into the UV, the blue-shifted excitation and very broad emission of the CaAQDC may be highly applicable. Moreover, the CaAQDC spectrum was collected at 77 K because of thermal quenching. Low temperatures typically sharpen emission profiles and so it is likely that if the CaAQDC emission could be stabilized at room temperature, its would be nearly white in colour.

Most remarkable in both of these framework structures, however, is that they contain only calcium, carbon, oxygen, and hydrogen, and they are prepared in water under mild hydrothermal conditions. By comparison, YAG:Ce is prepared from rare earth oxides at more than 1600°C, often requiring long calcination times and controlled atmospheres.

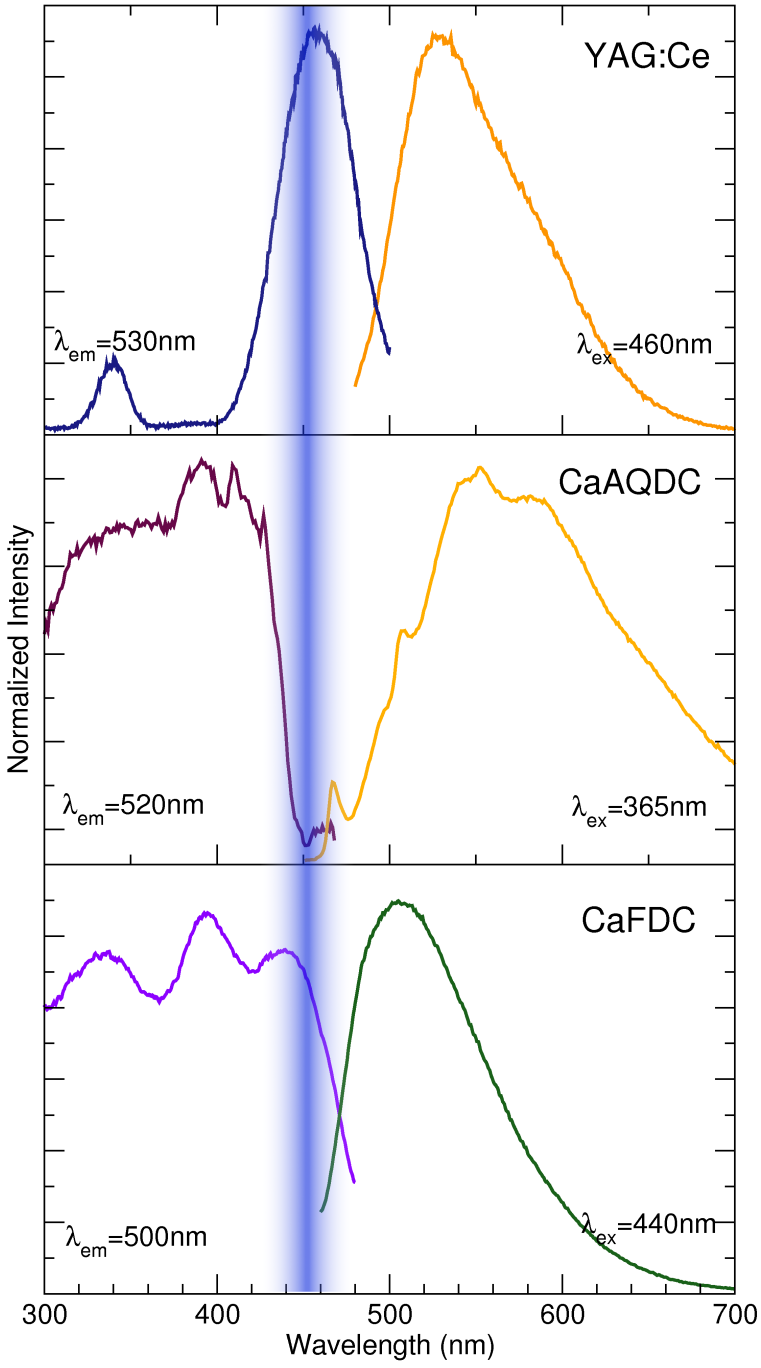

Figure 7.1: Comparison of excitation and emission for TOP: YAG:Ce, MIDDLE: CaAQDC, and BOTTOM: CaFDC. The vertical blue band shows a typical emission width for a 450 nm blue LED emitter. The CaAQDC excitation is too far into the UV, but the CaFDC is well suited for this excitation.

The quantum yield enhancement seen in the calcium fluorenone with respect to its parent ligand shows that placing an organic chromophore in a framework structure can significantly enhance its luminescence. The CaFDC showed 15% QY at 77 K while H_2FDC showed only 7%. The ligand-based inorganic-organic framework approach also provides precise colour tunability by simply changing the metal cation. In the fluorenone framework compounds, the emission peak locations change only about 7 nm with each cation change. Additionally, placing the organic ligands in a framework structure increased their thermal stability. For example, anthraquinone dicarboxylic acid was shown to decompose at 375°C, while the ligand within the CaAQDC structure is stable to 480°C.

One of the great benefits of the hybrid framework systems is the nearly limitless extent of ligand, metal, and structure combinations available. From the structure and luminescence of the compounds described here, some important design criteria for further work in ligand-based luminescence can be developed. The most important consideration is the rigidity of the ligand in the structure. It was seen for the anthraquinones that the *ortho* bonding arrangement lead to large thermal vibrations and luminescence quenching. The lack of rigidity from the unbound oxygen atoms in SrFDC and the 2-dimensional CdFDC also reduced efficiency. The second parameter is the isolation of the metal centres. The increased inorganic connectivity in the BaFDC resulting in what appears to be a rigid structure showing reduced luminescence. We know from this and previous work that smaller cations in structures tend to result in lower inorganic connectivity, and so small metal cations such as magnesium and calcium should outperform strontium and barium. A third parameter is the degree of hydration, with particular concern for pore space water. The O–H bonds of water molecules can quench excited states, and since the pore waters are closer to the chromophores, they tend to have

more influence. Finally, the π-stacking and separation appear to have an impact on luminescent efficiency, though the details of this interaction are not yet clear.

Already it is apparent that nearly ideal excitation and emission spectra are available from hybrid framework phosphors. It is also clear that including organic chromophores in a framework structure can enhance their quantum efficiency and tune their emission color. Finally, the thermal behaviour of all of these compounds showed that the decomposition temperature of the ligand is increased by its inclusion in a hybrid network. If a single compound could incorporate all of these criteria outlined above using a ligand of higher intrinsic quantum efficiency, the conditions for a commercialized phosphor may be achievable.

Chapter 8

Appendix

8.1 Cerium oxalate formate structure details

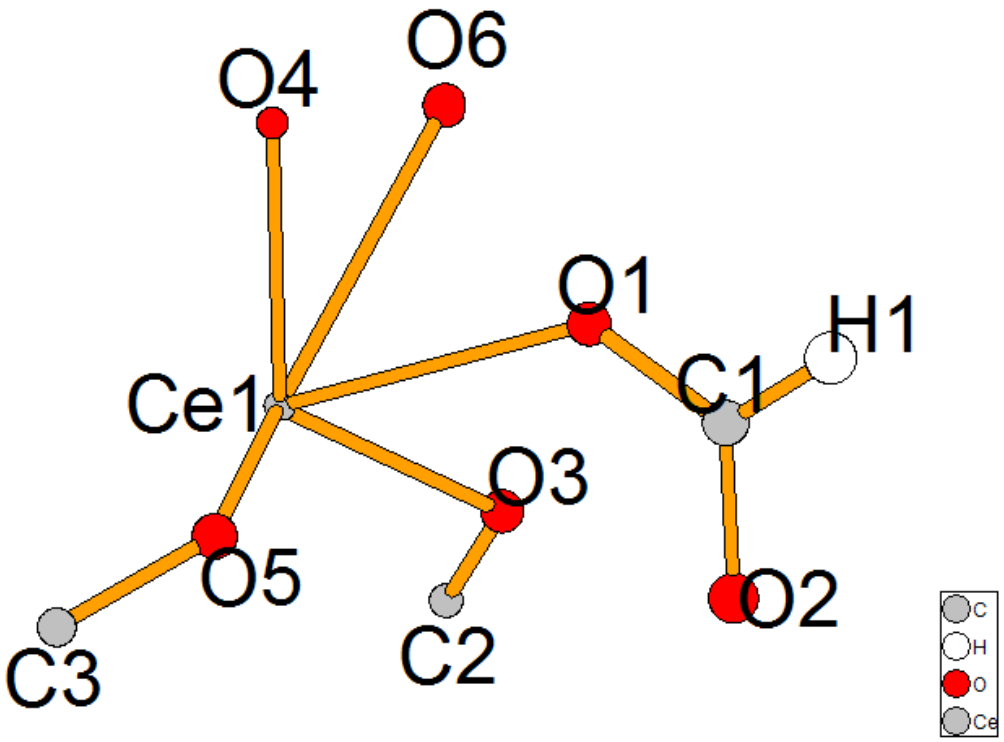

Figure 8.1: Asymmetric unit with atom numbers for cerium oxalate formate.

Table 8.1: Crystal data and structure refinement for cerium oxalate formate.

Parameter	Value
Empirical formula	C_3HO_6Ce
Formula weight	273.16 g·mol^{-1}
Collection Temperature	120(2) K
Wavelength	0.71073Å
Crystal system	Orthorhombic
Space Group	$Pnm2_1$
Unit cell dimensions	
a	7.3963(5)Å
b	10.885(1)Å
c	6.7901(5)Å
α	90°
β	90°
γ	90°
Volume	546.66(7)Å^3
Z	4
Calculated density	3.395 g/m^3
Absorption coefficient	8.480 mm^{-1}
F(000)	500
Crystal size	0.7×0.2×0.2 mm
Theta range for data collection	4.11° to 27.46°
Limiting indices	$-9 \leq h \leq 8$, $-8 \leq k \leq 7$, $-14 \leq l \leq 12$
Reflections collected / unique	3243 / 1113 [R(int) = 0.0297]
Data Completeness	97.4%
Absorption correction	Semi-empirical by equivalents
Refinement method	Full-matrix least-squares on F^2
Data / restraints / parameters	1113 / 1 / 46
Goodness-of-fit on F^2	1.079
Final R indices [I>2sigma(I)]	R1 = 0.0171, wR2 = 0.0432
R indices (all data)	R1 = 0.0174, wR2 = 0.0444
Absolute structure parameter	0.52(7)
Largest diff. peak and hole	0.805 and -0.737 e·Å^{-3}

Table 8.2: Crystal coordinates [Å] and equivalent isotropic displacement parameters [Å^2] for cerium oxalate formate. U_{eq} is defined as one third of the trace of the orthogonalized U_{ij} tensor.

	x	y	z	U_{eq}
C(1)	0.6284(4)	0.8721(4)	0.4605(16)	0.0114(7)
H(1)	0.7580	0.8757	0.4598	0.014
C(2)	0.0961(9)	0.9551(10)	0.1934(5)	0.0059(13)
C(3)	0.0851(9)	0.9505(10)	0.7384(5)	0.0077(14)
O(1)	0.5452(3)	1.0371(3)	0.4632(9)	0.0099(4)
O(4)	0.4216(8)	1.3488(7)	0.5937(4)	0.0052(13)
O(6)	0.4196(9)	1.3611(7)	0.3380(4)	0.0100(15)
O(3)	0.2302(7)	0.9861(7)	0.2497(5)	0.0095(12)
O(2)	0.5548(3)	0.7069(3)	0.4588(9)	0.0128(5)
O(5)	0.2306(7)	0.9721(8)	0.6705(4)	0.0106(12)
Ce(1)	0.210526(18)	1.12998(2)	0.4638(3)	0.00462(9)

Table 8.3: Anisotropic displacement parameters [Å^2] for cerium oxalate formate. The anisotropic displacement factor exponent takes the form $-2\pi^2[h^2a^{*2}U^{11}+...+2hka^*b^*U^{12}]$.

	U^{11}	U^{22}	U^{33}	U^{23}	U^{13}	U^{12}
Ce(1)	0.00426(13)	0.00472(12)	0.00489(12)	0.0003(2)	0.0000(3)	-0.00043(4)

Table 8.4: Symmetry operations used in the following tables for cerium oxalate formate.

	Operation
#1	'x,y,z'
#2	'-x,-y,z+1/2'
#3	'-x+1/2,y+1/2,z+1/2'
#4	'x+1/2,-y+1/2,z'

Table 8.5: Bond Lengths [Å] for cerium oxalate formate.

	Angle	Symm. op. atom 1	Symm. op. atom 3
C(1)-O(1)	1.269(3)		
C(1)-H(1)	0.9500		
C(2)-O(3)	1.175(8)		
C(2)-O(4)	1.301(8)	3	
C(2)-C(3)	1.551(4)	2	
C(3)-O(6)	1.235(8)	3	
C(3)-O(5)	1.303(8)		
C(3)-C(2)	1.551(4)	2	
O(1)-Ce(1)	2.531(2)		
O(1)-Ce(1)	2.551(2)	4	
O(4)-C(2)	1.301(8)	3	
O(4)-Ce(1)	2.545(6)	4	
O(4)-Ce(1)	2.558(6)		
O(6)-C(3)	1.235(8)	3	
O(6)-Ce(1)	2.530(6)	4	
O(6)-Ce(1)	2.575(6)		
O(3)-Ce(1)	2.515(7)		
O(2)-Ce(1)	2.543(2)	4	
O(5)-Ce(1)	2.480(7)		
Ce(1)-O(6)	2.530(6)	4	
Ce(1)-O(2)	2.543(2)	4	
Ce(1)-O(4)	2.545(6)	4	
Ce(1)-O(1)	2.551(2)	4	
Ce(1)-Ce(1)	4.00560(11)	4	
Ce(1)-Ce(1)	4.00560(11)	4	

Table 8.6: Bond Angles [°] for cerium oxalate formate.

	Angle	Symm. op. atom 1	Symm. op. atom 3
O(3)-C(2)-C(3)	118.7(5)		2
O(4)-C(2)-C(3)	113.6(4)	3	2
O(6)-C(3)-O(5)	124.7(7)	3	
O(6)-C(3)-C(2)	116.7(5)	3	2
O(5)-C(3)-C(2)	118.5(4)		2
C(1)-O(1)-Ce(1)	133.05(18)		
C(1)-O(1)-Ce(1)	122.90(18)		4
Ce(1)-O(1)-Ce(1)	104.03(7)		4
C(2)-O(4)-Ce(1)	120.6(5)	3	4
C(2)-O(4)-Ce(1)	135.4(5)	3	
Ce(1)-O(4)-Ce(1)	103.44(18)	4	
C(3)-O(6)-Ce(1)	118.8(5)	3	4
C(3)-O(6)-Ce(1)	137.7(5)	3	
Ce(1)-O(6)-Ce(1)	103.4(2)	4	
C(2)-O(3)-Ce(1)	119.9(5)		
C(1)-O(2)-Ce(1)	127.43(19)		4
C(3)-O(5)-Ce(1)	120.5(4)		
O(5)-Ce(1)-O(3)	131.38(8)		
O(5)-Ce(1)-O(6)	123.03(17)		4
O(3)-Ce(1)-O(6)	64.02(18)		4
O(5)-Ce(1)-O(1)	80.7(2)		
O(3)-Ce(1)-O(1)	81.2(2)		
O(6)-Ce(1)-O(1)	145.2(2)	4	
O(5)-Ce(1)-O(2)	70.3(2)		4
O(3)-Ce(1)-O(2)	70.2(2)		4
O(6)-Ce(1)-O(2)	68.37(15)	4	4
O(1)-Ce(1)-O(2)	102.35(7)		4
O(5)-Ce(1)-O(4)	64.92(17)		4
O(3)-Ce(1)-O(4)	125.28(16)		4
O(6)-Ce(1)-O(4)	66.08(7)	4	4
O(1)-Ce(1)-O(4)	145.2(2)		4
O(2)-Ce(1)-O(4)	71.85(16)	4	4
O(5)-Ce(1)-O(1)	114.1(2)		4
O(3)-Ce(1)-O(1)	111.4(2)		4
O(6)-Ce(1)-O(1)	65.01(17)	4	4
O(1)-Ce(1)-O(1)	132.68(6)		4
O(2)-Ce(1)-O(1)	124.95(7)	4	4
O(4)-Ce(1)-O(1)	63.69(17)	4	4
O(5)-Ce(1)-O(4)	73.55(17)		
O(3)-Ce(1)-O(4)	133.91(17)		
O(6)-Ce(1)-O(4)	142.31(18)	4	
O(1)-Ce(1)-O(4)	63.80(18)		
O(2)-Ce(1)-O(4)	143.0(2)	4	
O(4)-Ce(1)-O(4)	99.64(16)	4	
O(1)-Ce(1)-O(4)	77.35(16)	4	
O(5)-Ce(1)-O(6)	134.51(18)		
O(3)-Ce(1)-O(6)	73.29(17)		
O(6)-Ce(1)-O(6)	101.69(18)	4	
O(1)-Ce(1)-O(6)	64.65(18)		
O(2)-Ce(1)-O(6)	142.8(2)	4	
O(4)-Ce(1)-O(6)	138.84(19)	4	
O(1)-Ce(1)-O(6)	75.44(17)	4	
O(4)-Ce(1)-O(6)	65.25(8)		
O(5)-Ce(1)-Ce(1)	96.85(12)		4
O(3)-Ce(1)-Ce(1)	95.94(11)		4
O(6)-Ce(1)-Ce(1)	139.57(12)	4	4
O(1)-Ce(1)-Ce(1)	38.16(4)		4
O(2)-Ce(1)-Ce(1)	140.50(5)	4	4
O(4)-Ce(1)-Ce(1)	137.59(12)	4	4
O(1)-Ce(1)-Ce(1)	94.53(5)	4	4

Table 8.7: Continued: Bond Angles [°] for cerium oxalate formate.

	Angle	Symm. op. atom 1	Symm. op. atom 3
O(4)-Ce(1)-Ce(1)	38.17(12)		4
O(6)-Ce(1)-Ce(1)	37.92(14)		4
O(5)-Ce(1)-Ce(1)	103.16(11)		4
O(3)-Ce(1)-Ce(1)	102.02(11)		4
O(6)-Ce(1)-Ce(1)	38.71(13)	4	4
O(1)-Ce(1)-Ce(1)	170.49(4)		4
O(2)-Ce(1)-Ce(1)	87.16(5)	4	4
O(4)-Ce(1)-Ce(1)	38.39(12)	4	4
O(1)-Ce(1)-Ce(1)	37.81(5)	4	4
O(4)-Ce(1)-Ce(1)	108.66(12)		4
O(6)-Ce(1)-Ce(1)	107.44(13)		4
Ce(1)-Ce(1)-Ce(1)	132.332(7)	4	4

8.2 CaAQDC structure details

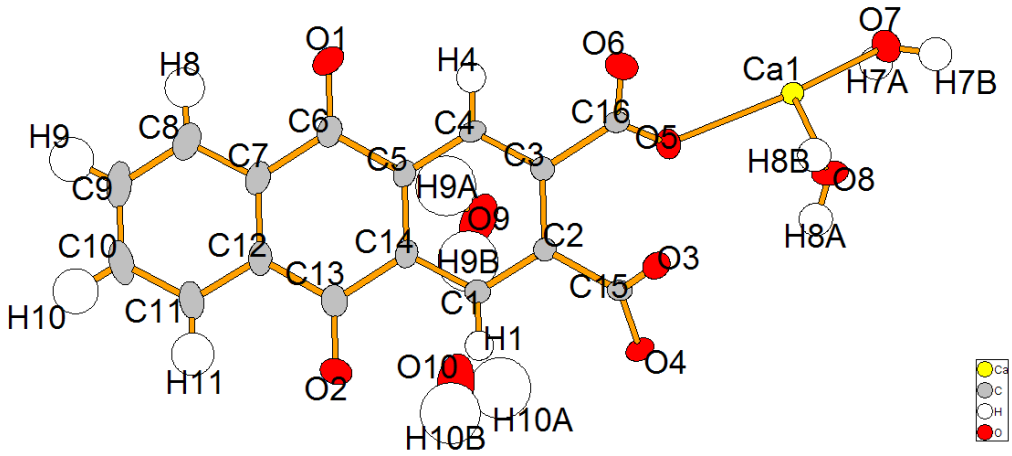

Figure 8.2: Asymmetric unit with atom numbers for CaAQDC.

Table 8.8: Crystal data and structure refinement for CaAQDC.

Parameter	Value
Empirical formula	$C_{16}H_{14}O_{10}Ca$
Formula weight	406.35 g·mol^{-1}
Collection Temperature	293(2) K
Wavelength	0.71073Å
Crystal system	Triclinic
Space Group	$P\bar{1}$
Unit cell dimensions	
a	5.960(2)Å
b	7.634(3)Å
c	18.603(7)Å
α	90.145(6)°
β	95.804(6)°
γ	97.105(6)°
Volume	835.5(6)Å^3
Z	2
Calculated density	1.615 g/m^3
Absorption coefficient	0.433 mm^{-1}
F(000)	420
Crystal size	0.5×0.3×0.3 mm
Theta range for data collection	2.89° to 26.02°
Limiting indices	$-7 \leq h \leq 7$, $-9 \leq k \leq 9$, $-22 \leq l \leq 13$
Reflections collected / unique	6129 / 3224 [R(int) = 0.0684]
Data Completeness	97.5%
Absorption correction	Semi-empirical from equivalents
Max. and min. transmission	0.878 and 0.856
Refinement method	Full-matrix least-squares on F^2
Data / restraints / parameters	3224 / 24 / 268
Goodness-of-fit on F^2	0.912
Final R indices [I>2sigma(I)]	R1 = 0.0509, wR2 = 0.0915
R indices (all data)	R1 = 0.0885, wR2 = 0.1015
Largest diff. peak and hole	0.366 and -0.387 e·Å^{-3}

Table 8.9: Crystal coordinates [Å] and equivalent isotropic displacement parameters [Å^2] for CaAQDC. U_{eq} is defined as one third of the trace of the orthogonalized U_{ij} tensor.

	x	y	z	U_{eq}
Ca(1)	0.01213(10)	0.26769(7)	1.04132(3)	0.01654(18)
C(1)	0.6884(5)	0.3306(4)	0.78485(17)	0.0226(7)
H(1)	0.8315	0.3957	0.7927	0.027
C(2)	0.5723(5)	0.2767(3)	0.84306(16)	0.0170(7)
C(3)	0.3530(5)	0.1825(4)	0.83117(17)	0.0180(7)
C(4)	0.2585(5)	0.1416(4)	0.76142(17)	0.0231(7)
H(4)	0.1142	0.0785	0.7536	0.028
C(5)	0.3768(5)	0.1938(4)	0.70275(17)	0.0240(7)
C(6)	0.2704(6)	0.1454(4)	0.62827(18)	0.0316(8)
C(7)	0.3997(6)	0.2041(4)	0.56716(18)	0.0315(8)
C(8)	0.3061(6)	0.1657(5)	0.49654(19)	0.0404(9)
H(8)	0.1591	0.1075	0.4879	0.049
C(9)	0.4297(7)	0.2134(5)	0.4390(2)	0.0505(11)
H(9)	0.3654	0.1874	0.3920	0.061
C(10)	0.6455(8)	0.2985(5)	0.4511(2)	0.0537(12)
H(10)	0.7287	0.3284	0.4123	0.064
C(11)	0.7407(7)	0.3403(5)	0.5206(2)	0.0463(10)
H(11)	0.8872	0.3997	0.5283	0.056
C(12)	0.6196(6)	0.2944(4)	0.57910(18)	0.0320(8)
C(13)	0.7244(6)	0.3457(5)	0.65262(19)	0.0350(9)
C(14)	0.5935(5)	0.2885(4)	0.71416(17)	0.0244(8)
C(15)	0.6889(5)	0.3018(4)	0.91869(17)	0.0168(7)
C(16)	0.2163(5)	0.1346(4)	0.89378(16)	0.0176(7)
O(1)	0.0841(4)	0.0587(4)	0.61889(14)	0.0555(8)
O(2)	0.9125(4)	0.4300(4)	0.66229(14)	0.0578(8)
O(3)	0.6881(3)	0.1670(2)	0.95728(11)	0.0231(5)
O(4)	0.7935(3)	0.4496(2)	0.93883(11)	0.0232(5)
O(5)	0.2042(3)	0.2595(3)	0.93706(11)	0.0261(5)
O(6)	0.1237(3)	-0.0191(3)	0.89812(12)	0.0290(6)
O(7)	-0.2439(4)	0.3960(3)	1.10960(14)	0.0285(6)
H(7A)	-0.251(5)	0.497(4)	1.0962(17)	0.034
H(7B)	-0.214(5)	0.385(4)	1.1575(19)	0.034
O(8)	0.3471(4)	0.1697(3)	1.09909(13)	0.0292(6)
H(8A)	0.472(6)	0.228(4)	1.0913(18)	0.035
H(8B)	0.350(6)	0.073(4)	1.0879(18)	0.035
O(9)	0.2223(7)	0.6670(5)	0.7472(2)	0.0962(16)
H(9A)	0.161(9)	0.582(7)	0.716(3)	0.115
H(9B)	0.348(9)	0.692(8)	0.744(3)	0.115
O(10)	0.6948(8)	0.8097(6)	0.7490(2)	0.0966(14)
H(10A)	0.690(10)	0.831(8)	0.790(3)	0.116
H(10B)	0.825(9)	0.765(8)	0.753(3)	0.116

Table 8.10: Anisotropic displacement parameters [Å^2] for CaAQDC. The anisotropic displacement factor exponent takes the form $-2\pi^2[h^2a^{*2}U^{11} + ... + 2hka^*b^*U^{12}]$.

	U^{11}	U^{22}	U^{33}	U^{23}	U^{13}	U^{12}
Ca(1)	0.0188(3)	0.0138(3)	0.0161(4)	-0.0009(2)	0.0016(3)	-0.0014(2)
C(1)	0.0214(17)	0.0228(16)	0.022(2)	0.0011(14)	0.0020(15)	-0.0035(13)
C(2)	0.0194(16)	0.0149(14)	0.0163(18)	-0.0005(13)	0.0025(14)	-0.0004(12)
C(3)	0.0210(17)	0.0146(14)	0.0180(19)	-0.0006(13)	0.0032(14)	0.0001(12)
C(4)	0.0187(17)	0.0261(17)	0.022(2)	-0.0023(14)	-0.0020(15)	-0.0054(13)
C(5)	0.0258(18)	0.0289(17)	0.0158(19)	-0.0040(14)	0.0012(15)	-0.0016(14)
C(6)	0.037(2)	0.0362(19)	0.019(2)	-0.0021(16)	0.0017(17)	-0.0041(17)
C(7)	0.039(2)	0.0349(19)	0.019(2)	-0.0044(16)	0.0003(17)	0.0000(16)
C(8)	0.049(2)	0.047(2)	0.022(2)	-0.0017(18)	-0.0033(19)	-0.0008(18)
C(9)	0.074(3)	0.058(3)	0.018(2)	0.0016(19)	0.005(2)	0.003(2)
C(10)	0.074(3)	0.062(3)	0.024(2)	0.006(2)	0.020(2)	-0.006(2)
C(11)	0.054(3)	0.061(3)	0.021(2)	0.0003(19)	0.012(2)	-0.008(2)
C(12)	0.044(2)	0.0335(19)	0.017(2)	0.0007(15)	0.0055(17)	-0.0016(17)
C(13)	0.037(2)	0.044(2)	0.022(2)	0.0006(17)	0.0054(17)	-0.0042(18)
C(14)	0.0295(19)	0.0265(17)	0.0156(19)	-0.0011(14)	0.0017(15)	-0.0027(14)
C(15)	0.0114(16)	0.0189(16)	0.0199(19)	0.0000(14)	0.0013(13)	0.0014(12)
C(16)	0.0116(15)	0.0232(16)	0.0170(18)	0.0059(14)	-0.0032(13)	0.0014(13)
O(1)	0.0434(17)	0.084(2)	0.0285(17)	-0.0115(14)	-0.0019(13)	-0.0285(16)
O(2)	0.0439(17)	0.086(2)	0.0336(18)	-0.0059(15)	0.0104(14)	-0.0361(15)
O(3)	0.0278(12)	0.0184(11)	0.0212(13)	0.0041(10)	-0.0024(10)	-0.0009(9)
O(4)	0.0251(12)	0.0179(11)	0.0237(14)	-0.0039(9)	-0.0013(10)	-0.0057(9)
O(5)	0.0305(13)	0.0268(12)	0.0214(14)	-0.0045(10)	0.0079(10)	0.0014(10)
O(6)	0.0313(13)	0.0207(12)	0.0332(15)	0.0072(10)	0.0042(11)	-0.0054(10)
O(7)	0.0368(14)	0.0213(12)	0.0284(15)	0.0012(12)	0.0095(12)	0.0022(11)
O(8)	0.0237(13)	0.0200(12)	0.0416(17)	-0.0012(11)	-0.0010(12)	-0.0026(10)
O(9)	0.150(4)	0.081(3)	0.041(2)	-0.0071(18)	-0.004(3)	-0.041(3)
O(10)	0.128(4)	0.113(3)	0.045(2)	-0.001(2)	0.010(3)	0.000(3)

Table 8.11: Symmetry operations used in the following tables for CaAQDC.

	Operation
#1	'x,y,z'
#2	'-x,-y,-z'

Table 8.12: Bond Lengths [Å] for CaAQDC.

	Angle	Symm. op. atom 1	Symm. op. atom 3
Ca(1)-O(4)	2.329(2)	2	
Ca(1)-O(5)	2.354(2)		
Ca(1)-O(8)	2.374(2)		
Ca(1)-O(7)	2.378(2)		
Ca(1)-O(3)	2.405(2)	1	
Ca(1)-O(4)	2.687(2)	1	
Ca(1)-C(15)	2.867(3)	1	
Ca(1)-Ca(1)	3.8826(17)	2	
Ca(1)-Ca(1)	4.3434(19)	2	
Ca(1)-H(7A)	2.75(3)		
Ca(1)-H(8B)	2.72(3)		
C(1)-C(2)	1.380(4)		
C(1)-C(14)	1.398(4)		
C(1)-H(1)	0.9300		
C(2)-C(3)	1.408(4)		
C(2)-C(15)	1.506(4)		
C(3)-C(4)	1.380(4)		
C(3)-C(16)	1.508(4)		
C(4)-C(5)	1.391(4)		
C(4)-H(4)	0.9300		
C(5)-C(14)	1.396(4)		
C(5)-C(6)	1.490(4)		
C(6)-O(1)	1.217(4)		
C(6)-C(7)	1.477(5)		
C(7)-C(8)	1.390(5)		
C(7)-C(12)	1.399(5)		
C(8)-C(9)	1.384(5)		
C(8)-H(8)	0.9300		
C(9)-C(10)	1.364(5)		
C(9)-H(9)	0.9300		
C(10)-C(11)	1.377(5)		
C(10)-H(10)	0.9300		
C(11)-C(12)	1.388(5)		
C(11)-H(11)	0.9300		
C(12)-C(13)	1.476(5)		
C(13)-O(2)	1.218(4)		
C(13)-C(14)	1.486(4)		
C(15)-O(3)	1.256(3)		
C(15)-O(4)	1.257(3)		
C(15)-Ca(1)	2.867(3)	1	
C(16)-O(6)	1.240(3)		
C(16)-O(5)	1.260(3)		
O(3)-Ca(1)	2.405(2)	1	
O(4)-Ca(1)	2.329(2)	2	
O(4)-Ca(1)	2.687(2)	1	
O(6)-Ca(1)	2.311(2)	2	
O(7)-H(7A)	0.82(3)		
O(7)-H(7B)	0.90(3)		
O(8)-H(8A)	0.84(3)		
O(8)-H(8B)	0.77(3)		
O(9)-H(9A)	0.88(5)		
O(9)-H(9B)	0.76(5)		
O(10)-H(10A)	0.78(5)		
O(10)-H(10B)	0.88(5)		

Table 8.13: Bond Angles [°] for CaAQDC.

	Angle	Symm. op. atom 1	Symm. op. atom 3
O(4)-Ca(1)-O(8)	85.18(8)	2	
O(5)-Ca(1)-O(8)	83.50(8)		
O(6)-Ca(1)-O(7)	81.33(8)	2	
O(4)-Ca(1)-O(7)	79.80(8)	2	
O(5)-Ca(1)-O(7)	150.30(8)		
O(8)-Ca(1)-O(7)	120.75(9)		
O(6)-Ca(1)-O(3)	81.54(8)	2	1
O(4)-Ca(1)-O(3)	129.78(7)	2	1
O(5)-Ca(1)-O(3)	82.27(8)		1
O(8)-Ca(1)-O(3)	140.81(8)		1
O(7)-Ca(1)-O(3)	86.89(8)		1
O(6)-Ca(1)-O(4)	129.09(8)	2	1
O(4)-Ca(1)-O(4)	78.82(8)	2	1
O(5)-Ca(1)-O(4)	72.68(7)		1
O(8)-Ca(1)-O(4)	151.99(8)		1
O(7)-Ca(1)-O(4)	78.99(8)		1
O(3)-Ca(1)-O(4)	51.06(6)	1	1
O(6)-Ca(1)-C(15)	106.75(8)	2	1
O(4)-Ca(1)-C(15)	104.60(8)	2	1
O(5)-Ca(1)-C(15)	72.43(8)		1
O(8)-Ca(1)-C(15)	153.06(8)		1
O(7)-Ca(1)-C(15)	85.96(9)		1
O(3)-Ca(1)-C(15)	25.70(7)	1	1
O(4)-Ca(1)-C(15)	25.89(7)	1	1
O(6)-Ca(1)-Ca(1)	155.29(6)	2	2
O(4)-Ca(1)-Ca(1)	42.77(5)	2	2
O(5)-Ca(1)-Ca(1)	75.70(5)		2
O(8)-Ca(1)-Ca(1)	124.10(6)		2
O(7)-Ca(1)-Ca(1)	76.21(6)		2
O(3)-Ca(1)-Ca(1)	87.07(5)	1	2
O(4)-Ca(1)-Ca(1)	36.05(4)	1	2
C(15)-Ca(1)-Ca(1)	61.87(6)	1	2
O(6)-Ca(1)-Ca(1)	56.14(6)	2	2
O(4)-Ca(1)-Ca(1)	149.67(6)	2	2
O(5)-Ca(1)-Ca(1)	68.31(5)		2
O(8)-Ca(1)-Ca(1)	76.29(6)		2
O(7)-Ca(1)-Ca(1)	130.36(6)		2
O(3)-Ca(1)-Ca(1)	64.52(5)	1	2
O(4)-Ca(1)-Ca(1)	107.12(5)	1	2
C(15)-Ca(1)-Ca(1)	83.56(6)	1	2
Ca(1)-Ca(1)-Ca(1)	136.18(4)	2	2
O(6)-Ca(1)-H(7A)	97.6(7)	2	
O(4)-Ca(1)-H(7A)	67.6(7)	2	
O(5)-Ca(1)-H(7A)	134.8(7)		
O(8)-Ca(1)-H(7A)	127.3(7)		
O(7)-Ca(1)-H(7A)	16.4(6)		
O(3)-Ca(1)-H(7A)	87.3(7)	1	
O(4)-Ca(1)-H(7A)	66.7(7)	1	
C(15)-Ca(1)-H(7A)	79.3(7)	1	
Ca(1)-Ca(1)-H(7A)	59.9(7)	2	
Ca(1)-Ca(1)-H(7A)	142.5(7)	2	
O(6)-Ca(1)-H(8B)	68.2(7)	2	
O(4)-Ca(1)-H(8B)	99.6(7)	2	
O(5)-Ca(1)-H(8B)	78.9(7)		
O(8)-Ca(1)-H(8B)	15.5(7)		
O(7)-Ca(1)-H(8B)	129.0(7)		
O(3)-Ca(1)-H(8B)	125.3(7)	1	
O(4)-Ca(1)-H(8B)	151.6(7)	1	
C(15)-Ca(1)-H(8B)	140.7(7)	1	
Ca(1)-Ca(1)-H(8B)	135.1(7)	2	

Table 8.14: Continued: Bond Angles [°] for CaAQDC.

	Angle	Symm. op. atom 1	Symm. op. atom 3
Ca(1)-Ca(1)-H(8B)	60.8(7)	2	
H(7A)-Ca(1)-H(8B)	139.2(10)		
C(2)-C(1)-C(14)	120.8(3)		
C(2)-C(1)-H(1)	119.6		
C(14)-C(1)-H(1)	119.6		
C(1)-C(2)-C(3)	119.7(3)		
C(1)-C(2)-C(15)	120.0(3)		
C(3)-C(2)-C(15)	120.0(3)		
C(4)-C(3)-C(2)	119.6(3)		
C(4)-C(3)-C(16)	119.9(3)		
C(2)-C(3)-C(16)	120.5(3)		
C(3)-C(4)-C(5)	120.7(3)		
C(3)-C(4)-H(4)	119.6		
C(5)-C(4)-H(4)	119.6		
C(4)-C(5)-C(14)	119.9(3)		
C(4)-C(5)-C(6)	119.2(3)		
C(14)-C(5)-C(6)	120.9(3)		
O(1)-C(6)-C(7)	121.7(3)		
O(1)-C(6)-C(5)	120.5(3)		
C(7)-C(6)-C(5)	117.8(3)		
C(8)-C(7)-C(12)	118.9(3)		
C(8)-C(7)-C(6)	120.1(3)		
C(12)-C(7)-C(6)	121.0(3)		
C(9)-C(8)-C(7)	120.5(4)		
C(9)-C(8)-H(8)	119.7		
C(7)-C(8)-H(8)	119.7		
C(10)-C(9)-C(8)	120.2(4)		
C(10)-C(9)-H(9)	119.9		
C(8)-C(9)-H(9)	119.9		
C(9)-C(10)-C(11)	120.3(4)		
C(9)-C(10)-H(10)	119.8		
C(11)-C(10)-H(10)	119.8		
C(10)-C(11)-C(12)	120.5(4)		
C(10)-C(11)-H(11)	119.8		
C(12)-C(11)-H(11)	119.8		
C(11)-C(12)-C(7)	119.5(3)		
C(11)-C(12)-C(13)	119.0(3)		
C(7)-C(12)-C(13)	121.5(3)		
O(2)-C(13)-C(12)	121.0(3)		
O(2)-C(13)-C(14)	121.4(3)		
C(12)-C(13)-C(14)	117.6(3)		
C(5)-C(14)-C(1)	119.2(3)		
C(5)-C(14)-C(13)	121.2(3)		
C(1)-C(14)-C(13)	119.5(3)		
O(3)-C(15)-O(4)	123.1(3)		
O(3)-C(15)-C(2)	116.7(2)		
O(4)-C(15)-C(2)	120.0(3)		
O(3)-C(15)-Ca(1)	56.10(15)		1
O(4)-C(15)-Ca(1)	69.02(16)		1
C(2)-C(15)-Ca(1)	159.36(18)		1
O(6)-C(16)-O(5)	125.7(3)		
O(6)-C(16)-C(3)	118.9(3)		
O(5)-C(16)-C(3)	115.4(3)		
C(15)-O(3)-Ca(1)	98.20(17)		1
C(15)-O(4)-Ca(1)	171.8(2)		2
C(15)-O(4)-Ca(1)	85.09(17)		1
Ca(1)-O(4)-Ca(1)	101.18(8)	2	1
C(16)-O(5)-Ca(1)	130.90(19)		
C(16)-O(6)-Ca(1)	154.7(2)		2
Ca(1)-O(7)-H(7A)	108(2)		

Table 8.15: Continued: Bond Angles [°] for CaAQDC.

	Angle	Symm. op. atom 1	Symm. op. atom 3
Ca(1)-O(7)-H(7B)	113(2)		
H(7A)-O(7)-H(7B)	115(3)		
Ca(1)-O(8)-H(8A)	117(2)		
Ca(1)-O(8)-H(8B)	109(3)		
H(8A)-O(8)-H(8B)	108(3)		
H(9A)-O(9)-H(9B)	112(6)		
H(10A)-O(10)-H(10B)	97(6)		

8.3 MnAQDC structure details

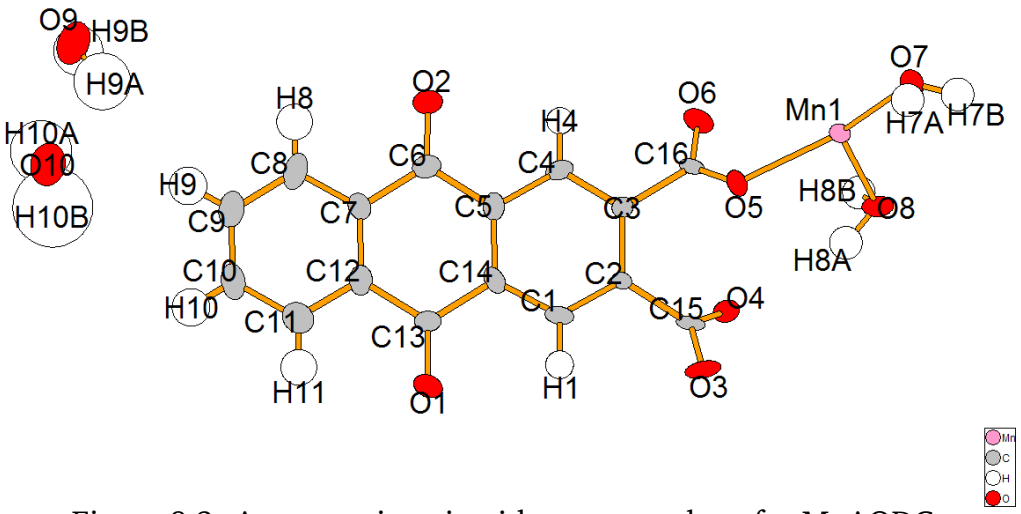

Figure 8.3: Asymmetric unit with atom numbers for MnAQDC.

Table 8.16: Crystal data and structure refinement for MnAQDC.

Parameter	Value
Empirical formula	$C_{16}H_{14}O_{10}Mn$
Formula weight	421.21 g·mol^{-1}
Collection Temperature	293(2) K
Wavelength	0.71073Å
Crystal system	Triclinic
Space Group	$P\bar{1}$
Unit cell dimensions	
a	5.799(2)Å
b	7.477(3)Å
c	18.493(7)Å
α	89.639(6)°
β	85.173(6)°
γ	83.485(7)°
Volume	793.8(5)Å^3
Z	2
Calculated density	1.762 g/m^3
Absorption coefficient	0.891 mm^{-1}
F(000)	430
Crystal size	0.1×0.08×0.02 mm
Theta range for data collection	2.21° to 25.68°
Limiting indices	$-7 \leq h \leq 7$, $-9 \leq k \leq 8$, $-22 \leq l \leq 22$
Reflections collected / unique	6413 / 2965 [R(int) = 0.0777]
Data Completeness	98.8%
Absorption correction	Semi-empirical from equivalents
Max. and min. transmission	0.982 and 0.918
Refinement method	Full-matrix least-squares on F^2
Data / restraints / parameters	2965 / 12 / 274
Goodness-of-fit on F^2	1.041
Final R indices [I>2sigma(I)]	R1 = 0.0806, wR2 = 0.1826
R indices (all data)	R1 = 0.1359, wR2 = 0.2093
Largest diff. peak and hole	1.242 and -0.554 e·Å^{-3}

Table 8.17: Crystal coordinates [Å] and equivalent isotropic displacement parameters [Å^2] for MnAQDC. U_{eq} is defined as one third of the trace of the orthogonalized U_{ij} tensor.

	x	y	z	U_{eq}
Mn(1)	0.48607(17)	0.75368(14)	1.04047(6)	0.0157(3)
C(1)	-0.1858(12)	0.8437(10)	0.7845(4)	0.0238(17)
H(1)	-0.3318	0.9100	0.7907	0.029
C(2)	-0.0732(10)	0.7944(8)	0.8436(3)	0.0130(14)
C(3)	0.1443(11)	0.6930(9)	0.8355(4)	0.0167(15)
C(4)	0.2459(12)	0.6461(9)	0.7671(4)	0.0219(16)
H(4)	0.3920	0.5797	0.7617	0.026
C(5)	0.1272(12)	0.6992(10)	0.7050(4)	0.0232(16)
C(6)	0.2343(12)	0.6450(10)	0.6314(4)	0.0266(17)
C(7)	0.1067(13)	0.7054(10)	0.5682(4)	0.0274(18)
C(8)	0.2026(15)	0.6631(12)	0.4990(4)	0.040(2)
H(8)	0.3522	0.6031	0.4919	0.048
C(9)	0.0753(17)	0.7102(12)	0.4391(4)	0.044(2)
H(9)	0.1408	0.6829	0.3922	0.053
C(10)	-0.1457(16)	0.7964(12)	0.4501(4)	0.044(2)
H(10)	-0.2318	0.8257	0.4106	0.053
C(11)	-0.2430(15)	0.8408(12)	0.5200(4)	0.040(2)
H(11)	-0.3932	0.8998	0.5271	0.048
C(12)	-0.1170(14)	0.7975(11)	0.5787(4)	0.0303(18)
C(13)	-0.2257(12)	0.8534(10)	0.6513(4)	0.0284(18)
C(14)	-0.0919(12)	0.7991(10)	0.7148(4)	0.0228(16)
C(15)	-0.1978(11)	0.8308(9)	0.9189(4)	0.0208(16)
C(16)	0.2806(11)	0.6410(9)	0.9002(4)	0.0177(15)
O(1)	-0.4161(9)	0.9432(9)	0.6593(3)	0.0493(17)
O(2)	0.4233(9)	0.5537(9)	0.6248(3)	0.0514(18)
O(3)	-0.2845(8)	0.9862(7)	0.9338(3)	0.0301(13)
O(4)	-0.2148(8)	0.6984(6)	0.9577(3)	0.0231(12)
O(5)	0.2932(8)	0.7686(6)	0.9444(2)	0.0220(11)
O(6)	0.3677(8)	0.4840(7)	0.9050(3)	0.0286(12)
H(7A)	0.741(14)	0.992(3)	1.095(4)	0.040(12)
H(7B)	0.718(13)	0.890(9)	1.1482(12)	0.040(12)
O(7)	0.7431(9)	0.8749(7)	1.1006(3)	0.0245(12)
H(8A)	0.056(10)	0.699(8)	1.067(3)	0.040(12)
H(8B)	0.164(12)	0.541(4)	1.077(4)	0.040(12)
O(8)	0.1720(8)	0.6512(7)	1.0946(3)	0.0281(13)
H(9A)	0.608(16)	0.882(13)	0.281(5)	0.12(5)
H(9B)	0.637(17)	0.728(9)	0.257(6)	0.09(5)
O(9)	0.7141(14)	0.8246(11)	0.2474(4)	0.064(2)
H(10A)	0.18(2)	0.564(5)	0.242(8)	0.14(6)
H(10B)	0.040(7)	0.69(2)	0.259(11)	0.24(10)
O(10)	0.1933(14)	0.6813(12)	0.2471(4)	0.065(2)

Table 8.18: Anisotropic displacement parameters [Å^2] for MnAQDC. The anisotropic displacement factor exponent takes the form $-2\pi^2[h^2a^{*2}U^{11} + ... + 2hka^*b^*U^{12}]$.

	U^{11}	U^{22}	U^{33}	U^{23}	U^{13}	U^{12}
Mn(1)	0.0152(6)	0.0141(6)	0.0174(6)	-0.0010(4)	-0.0031(4)	0.0017(4)
C(1)	0.017(4)	0.021(4)	0.032(4)	-0.003(3)	-0.005(3)	0.007(3)
C(2)	0.013(3)	0.011(3)	0.015(3)	0.002(3)	-0.002(3)	0.002(3)
C(3)	0.018(3)	0.015(4)	0.017(4)	-0.001(3)	-0.001(3)	-0.002(3)
C(4)	0.021(4)	0.016(4)	0.026(4)	0.003(3)	0.005(3)	0.006(3)
C(5)	0.030(4)	0.024(4)	0.017(4)	0.001(3)	-0.003(3)	-0.006(3)
C(6)	0.022(4)	0.026(4)	0.030(4)	-0.003(3)	0.001(3)	0.002(3)
C(7)	0.030(4)	0.032(5)	0.020(4)	0.006(3)	-0.005(3)	0.001(4)
C(8)	0.046(5)	0.053(6)	0.020(4)	-0.002(4)	0.004(4)	-0.011(4)
C(9)	0.064(6)	0.041(5)	0.023(5)	0.005(4)	-0.001(4)	0.007(5)
C(10)	0.057(6)	0.050(6)	0.023(5)	0.004(4)	-0.010(4)	0.007(5)
C(11)	0.037(5)	0.044(6)	0.038(5)	0.002(4)	-0.008(4)	0.001(4)
C(12)	0.035(4)	0.035(5)	0.020(4)	-0.001(3)	-0.004(3)	-0.001(4)
C(13)	0.021(4)	0.034(5)	0.028(4)	-0.008(4)	-0.004(3)	0.009(3)
C(14)	0.027(4)	0.023(4)	0.020(4)	0.001(3)	-0.010(3)	0.000(3)
C(15)	0.012(3)	0.016(4)	0.033(4)	-0.005(3)	-0.006(3)	0.007(3)
C(16)	0.008(3)	0.021(4)	0.023(4)	0.007(3)	-0.001(3)	0.001(3)
O(1)	0.034(3)	0.074(5)	0.033(3)	-0.003(3)	-0.009(3)	0.027(3)
O(2)	0.034(3)	0.080(5)	0.033(3)	-0.008(3)	-0.003(3)	0.026(3)
O(3)	0.017(3)	0.022(3)	0.048(3)	-0.015(2)	0.003(2)	0.006(2)
O(4)	0.021(3)	0.022(3)	0.025(3)	0.000(2)	0.002(2)	0.001(2)
O(5)	0.025(3)	0.025(3)	0.018(3)	-0.001(2)	-0.009(2)	-0.002(2)
O(6)	0.026(3)	0.024(3)	0.035(3)	0.004(2)	-0.010(2)	0.004(2)
O(7)	0.030(3)	0.022(3)	0.022(3)	0.000(2)	-0.007(2)	0.000(2)
O(8)	0.021(3)	0.025(3)	0.037(3)	-0.002(2)	0.000(2)	0.004(2)
O(9)	0.085(5)	0.062(5)	0.038(4)	-0.003(4)	0.004(4)	0.012(5)
O(10)	0.073(5)	0.074(6)	0.046(4)	-0.009(4)	-0.006(4)	0.000(4)

Table 8.19: Symmetry operations used in the following tables for MnAQDC.

	Operation
#1	'x,y,z'
#2	'-x,-y,-z'

Table 8.20: Bond Lengths [Å] for MnAQDC.

	Angle	Symm. op. atom 1	Symm. op. atom 3
Mn(1)-O(5)	2.174(5)		
Mn(1)-O(3)	2.185(5)	2	
Mn(1)-O(7)	2.208(5)		
Mn(1)-O(8)	2.215(5)		
Mn(1)-O(4)	2.218(5)	1	
C(1)-C(2)	1.348(9)		
C(1)-C(14)	1.383(9)		
C(1)-H(1)	0.9300		
C(2)-C(3)	1.393(9)		
C(2)-C(15)	1.526(9)		
C(3)-C(4)	1.380(9)		
C(3)-C(16)	1.513(9)		
C(4)-C(5)	1.420(9)		
C(4)-H(4)	0.9300		
C(5)-C(14)	1.397(10)		
C(5)-C(6)	1.486(10)		
C(6)-O(2)	1.221(8)		
C(6)-C(7)	1.477(10)		
C(7)-C(8)	1.376(10)		
C(7)-C(12)	1.397(10)		
C(8)-C(9)	1.403(11)		
C(8)-H(8)	0.9300		
C(9)-C(10)	1.368(12)		
C(9)-H(9)	0.9300		
C(10)-C(11)	1.393(11)		
C(10)-H(10)	0.9300		
C(11)-C(12)	1.375(11)		
C(11)-H(11)	0.9300		
C(12)-C(13)	1.476(10)		
C(13)-O(1)	1.224(8)		
C(13)-C(14)	1.492(10)		
C(15)-O(4)	1.227(8)		
C(15)-O(3)	1.236(8)		
C(16)-O(6)	1.229(8)		
C(16)-O(5)	1.272(8)		
O(3)-Mn(1)	2.185(5)	2	
O(4)-Mn(1)	2.218(5)	1	
O(6)-Mn(1)	2.162(5)	2	
O(7)-H(7A)	0.88(2)		
O(7)-H(7B)	0.89(2)		
O(8)-H(8A)	0.91(2)		
O(8)-H(8B)	0.89(2)		
O(9)-H(9A)	0.90(2)		
O(9)-H(9B)	0.90(2)		
O(10)-H(10A)	0.89(2)		
O(10)-H(10B)	0.89(2)		

Table 8.21: Bond Angles [°] for MnAQDC.

	Angle	Symm. op. atom 1	Symm. op. atom 3
O(5)-Mn(1)-O(7)	145.88(19)		
O(3)-Mn(1)-O(7)	81.38(19)	2	
O(6)-Mn(1)-O(8)	77.69(19)	2	
O(5)-Mn(1)-O(8)	84.82(19)		
O(3)-Mn(1)-O(8)	82.25(19)	2	
O(7)-Mn(1)-O(8)	122.9(2)		
O(6)-Mn(1)-O(4)	86.14(18)	2	1
O(5)-Mn(1)-O(4)	81.69(18)		1
O(3)-Mn(1)-O(4)	127.04(19)	2	1
O(7)-Mn(1)-O(4)	83.24(18)		1
O(8)-Mn(1)-O(4)	145.60(19)		1
C(2)-C(1)-C(14)	122.3(6)		
C(2)-C(1)-H(1)	118.9		
C(14)-C(1)-H(1)	118.9		
C(1)-C(2)-C(3)	119.9(6)		
C(1)-C(2)-C(15)	119.4(6)		
C(3)-C(2)-C(15)	120.3(6)		
C(4)-C(3)-C(2)	120.0(6)		
C(4)-C(3)-C(16)	118.4(6)		
C(2)-C(3)-C(16)	121.5(6)		
C(3)-C(4)-C(5)	119.9(6)		
C(3)-C(4)-H(4)	120.0		
C(5)-C(4)-H(4)	120.0		
C(14)-C(5)-C(4)	118.7(6)		
C(14)-C(5)-C(6)	121.3(6)		
C(4)-C(5)-C(6)	119.9(6)		
O(2)-C(6)-C(7)	122.1(7)		
O(2)-C(6)-C(5)	119.7(7)		
C(7)-C(6)-C(5)	118.2(6)		
C(8)-C(7)-C(12)	119.8(7)		
C(8)-C(7)-C(6)	120.2(7)		
C(12)-C(7)-C(6)	119.9(6)		
C(7)-C(8)-C(9)	120.2(8)		
C(7)-C(8)-H(8)	119.9		
C(9)-C(8)-H(8)	119.9		
C(10)-C(9)-C(8)	119.5(8)		
C(10)-C(9)-H(9)	120.3		
C(8)-C(9)-H(9)	120.3		
C(9)-C(10)-C(11)	120.5(8)		
C(9)-C(10)-H(10)	119.7		
C(11)-C(10)-H(10)	119.7		
C(12)-C(11)-C(10)	120.0(8)		
C(12)-C(11)-H(11)	120.0		
C(10)-C(11)-H(11)	120.0		
C(11)-C(12)-C(7)	119.9(7)		
C(11)-C(12)-C(13)	117.7(7)		
C(7)-C(12)-C(13)	122.4(7)		
O(1)-C(13)-C(12)	121.7(7)		
O(1)-C(13)-C(14)	121.0(6)		
C(12)-C(13)-C(14)	117.3(6)		
C(1)-C(14)-C(5)	119.2(6)		
C(1)-C(14)-C(13)	120.3(6)		
C(5)-C(14)-C(13)	120.5(6)		
O(4)-C(15)-O(3)	125.9(7)		
O(4)-C(15)-C(2)	115.9(6)		
O(3)-C(15)-C(2)	118.1(6)		
O(6)-C(16)-O(5)	126.8(6)		
O(6)-C(16)-C(3)	118.3(6)		
O(5)-C(16)-C(3)	114.9(6)		
C(15)-O(3)-Mn(1)	171.8(5)		2

Table 8.22: Continued: Bond Angles [°] for for MnAQDC.

	Angle	Symm. op. atom 1	Symm. op. atom 3
C(15)-O(4)-Mn(1)	109.9(4)		1
C(16)-O(5)-Mn(1)	126.5(4)		
C(16)-O(6)-Mn(1)	156.0(5)		2
Mn(1)-O(7)-H(7A)	114(5)		
Mn(1)-O(7)-H(7B)	120(5)		
H(7A)-O(7)-H(7B)	90(4)		
Mn(1)-O(8)-H(8A)	103(5)		
Mn(1)-O(8)-H(8B)	108(5)		
H(8A)-O(8)-H(8B)	91(4)		
H(9A)-O(9)-H(9B)	85(4)		
H(10A)-O(10)-H(10B)	86(4)		

8.4 NiAQDC structure details

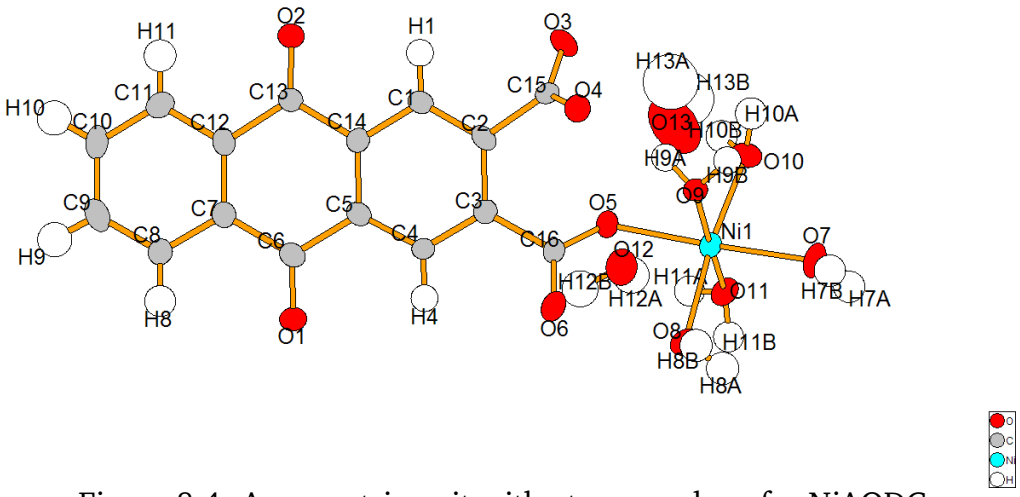

Figure 8.4: Asymmetric unit with atom numbers for NiAQDC.

Table 8.23: Crystal data and structure refinement for NiAQDC.

Parameter	Value
Empirical formula	$C_{16}H_{20}O_{13}Ni$
Formula weight	479.03 g·mol^{-1}
Collection Temperature	293(2) K
Wavelength	0.71073Å
Crystal system	Monoclinic
Space Group	$P2_1/c$
Unit cell dimensions	
a	16.308(3)Å
b	7.4101(15)Å
c	16.183(3)Å
α	90°
β	106.064(4)°
γ	90°
Volume	1879.2(7)Å^3
Z	4
Calculated density	1.693 g/m^3
Absorption coefficient	1.104 mm^{-1}
F(000)	992
Crystal size	0.4×0.35×0.25 mm
Theta range for data collection	1.30° to 26.02°
Limiting indices	$-20 \leq h \leq 20$, $-9 \leq k \leq 8$, $-19 \leq l \leq 19$
Reflections collected / unique	13851 / 3675 [R(int) = 0.0809]
Data Completeness	99.7%
Absorption correction	Semi-empirical from equivalents
Max. and min. transmission	0.758 and 0.648
Refinement method	Full-matrix least-squares on F^2
Data / restraints / parameters	3675 / 21 / 313
Goodness-of-fit on F^2	1.083
Final R indices [I>2sigma(I)]	R1 = 0.0622, wR2 = 0.1284
R indices (all data)	R1 = 0.1131, wR2 = 0.1587
Largest diff. peak and hole	0.625 and -0.509 e·Å^{-3}

Table 8.24: Crystal coordinates [Å] and equivalent isotropic displacement parameters [Å^2] for NiAQDC. U_{eq} is defined as one third of the trace of the orthogonalized U_{ij} tensor.

	x	y	z	U_{eq}
O(3)	0.3620(2)	1.0703(5)	0.5594(2)	0.0339(9)
C(6)	-0.0149(3)	0.7478(8)	0.3714(3)	0.0266(12)
Ni(1)	0.41465(4)	1.08704(9)	0.28644(4)	0.0211(2)
C(1)	0.1960(3)	0.8873(7)	0.5244(3)	0.0228(12)
H(1)	0.2192	0.9086	0.5829	0.027
C(2)	0.2458(3)	0.9082(7)	0.4685(3)	0.0223(11)
C(3)	0.2102(3)	0.8826(7)	0.3801(3)	0.0217(11)
C(4)	0.1257(3)	0.8320(7)	0.3496(3)	0.0223(11)
H(4)	0.1022	0.8152	0.2909	0.027
C(5)	0.0751(3)	0.8057(7)	0.4051(3)	0.0218(12)
C(7)	-0.0637(3)	0.7056(7)	0.4348(3)	0.0242(12)
C(8)	-0.1458(3)	0.6364(7)	0.4058(4)	0.0297(13)
H(8)	-0.1691	0.6108	0.3478	0.036
C(9)	-0.1925(3)	0.6058(8)	0.4637(4)	0.0370(15)
H(9)	-0.2477	0.5604	0.4442	0.044
C(10)	-0.1584(3)	0.6419(8)	0.5503(4)	0.0366(15)
H(10)	-0.1907	0.6222	0.5886	0.044
C(11)	-0.0758(3)	0.7074(8)	0.5798(4)	0.0320(14)
H(11)	-0.0522	0.7301	0.6381	0.038
C(12)	-0.0284(3)	0.7389(7)	0.5218(3)	0.0219(11)
C(13)	0.0593(3)	0.8127(7)	0.5559(3)	0.0239(12)
C(14)	0.1112(3)	0.8343(7)	0.4934(3)	0.0217(11)
C(15)	0.3405(3)	0.9430(7)	0.5080(3)	0.0235(12)
C(16)	0.2631(3)	0.9131(7)	0.3180(3)	0.0223(11)
O(1)	-0.0493(2)	0.7385(7)	0.2946(2)	0.0484(12)
O(2)	0.0881(2)	0.8531(6)	0.6308(2)	0.0399(11)
O(4)	0.3915(2)	0.8319(5)	0.4891(2)	0.0277(9)
O(5)	0.3129(2)	1.0467(5)	0.3335(2)	0.0245(8)
O(6)	0.2528(2)	0.8092(5)	0.2562(3)	0.0407(11)
O(7)	0.5246(2)	1.1090(5)	0.2472(3)	0.0307(9)
H(7A)	0.537(3)	1.171(6)	0.206(3)	0.037
H(7B)	0.556(3)	1.020(5)	0.236(3)	0.037
O(8)	0.3649(2)	0.9207(6)	0.1827(2)	0.0325(9)
H(8A)	0.384(3)	0.965(6)	0.142(3)	0.039
H(8B)	0.396(3)	0.825(4)	0.181(3)	0.039
O(9)	0.4747(2)	0.8762(5)	0.3663(2)	0.0236(8)
H(9A)	0.457(3)	0.880(7)	0.411(2)	0.028
H(9B)	0.5268(13)	0.889(7)	0.395(3)	0.028
O(10)	0.4699(2)	1.2703(5)	0.3803(2)	0.0311(9)
H(10A)	0.505(3)	1.247(7)	0.4305(19)	0.037
H(10B)	0.438(3)	1.334(7)	0.405(3)	0.037
O(11)	0.3562(2)	1.3107(5)	0.2178(2)	0.0283(9)
H(11A)	0.307(2)	1.347(7)	0.224(3)	0.034
H(11B)	0.335(3)	1.309(8)	0.1631(13)	0.034
O(12)	0.2201(2)	1.4402(6)	0.2615(3)	0.0405(10)
H(12A)	0.203(3)	1.550(4)	0.245(4)	0.049
H(12B)	0.1655(17)	1.407(7)	0.245(4)	0.049
O(13)	0.3566(4)	1.4826(9)	0.4210(5)	0.095(2)
H(13A)	0.385(6)	1.446(11)	0.475(3)	0.114
H(13B)	0.362(6)	1.592(5)	0.445(5)	0.114

Table 8.25: Anisotropic displacement parameters [Å^2] for NiAQDC. The anisotropic displacement factor exponent takes the form $-2\pi^2[h^2a^{*2}U^{11} + ... + 2hka^*b^*U^{12}]$.

	U^{11}	U^{22}	U^{33}	U^{23}	U^{13}	U^{12}
Ni(1)	0.0197(3)	0.0237(4)	0.0216(4)	0.0018(3)	0.0084(3)	0.0009(3)
C(1)	0.019(2)	0.028(3)	0.020(3)	-0.003(2)	0.003(2)	0.001(2)
C(2)	0.016(2)	0.022(3)	0.026(3)	-0.004(2)	0.002(2)	0.000(2)
C(3)	0.019(2)	0.024(3)	0.022(3)	0.001(2)	0.006(2)	0.002(2)
C(4)	0.019(2)	0.031(3)	0.016(3)	0.000(2)	0.004(2)	-0.002(2)
C(5)	0.018(2)	0.023(3)	0.022(3)	0.000(2)	0.002(2)	0.001(2)
C(6)	0.022(3)	0.033(3)	0.024(3)	-0.006(3)	0.005(2)	-0.003(2)
C(7)	0.021(3)	0.027(3)	0.025(3)	-0.001(2)	0.007(2)	-0.001(2)
C(8)	0.026(3)	0.040(4)	0.025(3)	-0.003(3)	0.010(2)	-0.006(2)
C(9)	0.025(3)	0.040(4)	0.045(4)	-0.003(3)	0.008(3)	-0.010(3)
C(10)	0.026(3)	0.048(4)	0.040(4)	0.005(3)	0.016(3)	-0.006(3)
C(11)	0.026(3)	0.047(4)	0.023(3)	0.002(3)	0.008(2)	0.004(3)
C(12)	0.017(2)	0.020(3)	0.029(3)	0.001(2)	0.007(2)	0.002(2)
C(13)	0.019(2)	0.032(3)	0.020(3)	0.002(2)	0.003(2)	0.000(2)
C(14)	0.019(2)	0.026(3)	0.021(3)	0.001(2)	0.007(2)	0.002(2)
C(15)	0.021(2)	0.035(3)	0.015(3)	0.001(3)	0.005(2)	-0.001(2)
C(16)	0.019(2)	0.028(3)	0.020(3)	0.005(3)	0.006(2)	-0.001(2)
O(1)	0.028(2)	0.095(4)	0.021(2)	-0.005(2)	0.0060(18)	-0.017(2)
O(2)	0.029(2)	0.067(3)	0.023(2)	-0.007(2)	0.0075(18)	-0.014(2)
O(3)	0.0202(18)	0.047(2)	0.034(2)	-0.019(2)	0.0062(16)	-0.0078(18)
O(4)	0.0182(17)	0.038(2)	0.027(2)	0.0031(18)	0.0062(16)	0.0058(16)
O(5)	0.0236(18)	0.026(2)	0.027(2)	-0.0031(16)	0.0119(16)	-0.0047(15)
O(6)	0.049(3)	0.046(3)	0.035(2)	-0.017(2)	0.027(2)	-0.024(2)
O(7)	0.030(2)	0.028(2)	0.040(2)	0.0080(19)	0.0214(18)	0.0029(17)
O(8)	0.032(2)	0.043(2)	0.024(2)	-0.001(2)	0.0110(16)	0.0072(19)
O(9)	0.0191(17)	0.032(2)	0.0195(19)	-0.0019(17)	0.0059(15)	0.0014(16)
O(10)	0.030(2)	0.035(2)	0.025(2)	-0.0061(19)	0.0032(17)	0.0016(18)
O(11)	0.0252(19)	0.036(2)	0.025(2)	0.0085(19)	0.0097(17)	0.0088(17)
O(12)	0.032(2)	0.043(3)	0.047(3)	0.008(2)	0.013(2)	0.0079(19)
O(13)	0.071(4)	0.066(4)	0.146(6)	-0.052(4)	0.027(4)	0.004(3)

Table 8.26: Symmetry operations used in the following tables for NiAQDC.

	Operation
#1	'x,y,z'
#2	'-x,y+1/2,-z+1/2'
#3	'-x,-y,-z'
#4	'x,-y-1/2,z-1/2'

Table 8.27: Bond Lengths [Å] for NiAQDC.

	Angle	Symm. op. atom 1	Symm. op. atom 3
C(6)-O(1)	1.217(6)		
C(6)-C(5)	1.481(7)		
C(6)-C(7)	1.494(7)		
Ni(1)-O(5)	2.031(3)		
Ni(1)-O(10)	2.050(4)		
Ni(1)-O(8)	2.060(4)		
Ni(1)-O(7)	2.068(3)		
Ni(1)-O(11)	2.074(4)		
Ni(1)-O(9)	2.090(4)		
C(1)-C(2)	1.382(7)		
C(1)-C(14)	1.391(6)		
C(1)-H(1)	0.9300		
C(2)-C(3)	1.401(7)		
C(2)-C(15)	1.521(6)		
C(3)-C(4)	1.381(6)		
C(3)-C(16)	1.512(6)		
C(4)-C(5)	1.391(7)		
C(4)-H(4)	0.9300		
C(5)-C(14)	1.402(7)		
C(7)-C(12)	1.388(7)		
C(7)-C(8)	1.389(7)		
C(8)-C(9)	1.380(7)		
C(8)-H(8)	0.9300		
C(9)-C(10)	1.383(8)		
C(9)-H(9)	0.9300		
C(10)-C(11)	1.386(7)		
C(10)-H(10)	0.9300		
C(11)-C(12)	1.390(7)		
C(11)-H(11)	0.9300		
C(12)-C(13)	1.488(7)		
C(13)-O(2)	1.209(6)		
C(13)-C(14)	1.496(7)		
C(15)-O(4)	1.266(6)		
C(16)-O(6)	1.236(6)		
C(16)-O(5)	1.260(6)		
O(7)-H(7A)	0.878(19)		
O(7)-H(7B)	0.877(19)		
O(8)-H(8A)	0.866(19)		
O(8)-H(8B)	0.877(19)		
O(9)-H(9A)	0.855(19)		
O(9)-H(9B)	0.856(19)		
O(10)-H(10A)	0.871(19)		
O(10)-H(10B)	0.873(19)		
O(11)-H(11A)	0.874(19)		
O(11)-H(11B)	0.858(19)		
O(12)-H(12A)	0.88(2)		
O(12)-H(12B)	0.89(2)		
O(13)-H(13A)	0.91(2)		
O(13)-H(13B)	0.89(2)		

Table 8.28: Bond Angles [°] for NiAQDC.

	Angle	Symm. op. atom 1	Symm. op. atom 3
O(5)-Ni(1)-O(8)	92.22(14)		
O(10)-Ni(1)-O(8)	173.33(16)		
O(5)-Ni(1)-O(7)	174.29(15)		
O(10)-Ni(1)-O(7)	86.24(15)		
O(8)-Ni(1)-O(7)	88.65(15)		
O(5)-Ni(1)-O(11)	90.91(14)		
O(10)-Ni(1)-O(11)	84.84(16)		
O(8)-Ni(1)-O(11)	91.30(16)		
O(7)-Ni(1)-O(11)	94.72(14)		
O(5)-Ni(1)-O(9)	87.12(13)		
O(10)-Ni(1)-O(9)	90.13(15)		
O(8)-Ni(1)-O(9)	93.92(15)		
O(7)-Ni(1)-O(9)	87.19(14)		
O(11)-Ni(1)-O(9)	174.49(14)		
C(2)-C(1)-C(14)	120.1(5)		
C(2)-C(1)-H(1)	120.0		
C(14)-C(1)-H(1)	120.0		
C(1)-C(2)-C(3)	120.1(4)		
C(1)-C(2)-C(15)	117.2(4)		
C(3)-C(2)-C(15)	122.5(4)		
C(4)-C(3)-C(2)	119.4(4)		
C(4)-C(3)-C(16)	120.0(4)		
C(2)-C(3)-C(16)	120.5(4)		
C(3)-C(4)-C(5)	121.3(5)		
C(3)-C(4)-H(4)	119.3		
C(5)-C(4)-H(4)	119.3		
C(4)-C(5)-C(14)	118.7(4)		
C(4)-C(5)-C(6)	120.5(5)		
C(14)-C(5)-C(6)	120.8(4)		
C(12)-C(7)-C(8)	119.9(5)		
C(12)-C(7)-C(6)	120.6(4)		
C(8)-C(7)-C(6)	119.4(5)		
C(9)-C(8)-C(7)	119.6(5)		
C(9)-C(8)-H(8)	120.2		
C(7)-C(8)-H(8)	120.2		
C(8)-C(9)-C(10)	120.8(5)		
C(8)-C(9)-H(9)	119.6		
C(10)-C(9)-H(9)	119.6		
C(9)-C(10)-C(11)	119.8(5)		
C(9)-C(10)-H(10)	120.1		
C(11)-C(10)-H(10)	120.1		
C(10)-C(11)-C(12)	119.7(5)		
C(10)-C(11)-H(11)	120.2		
C(12)-C(11)-H(11)	120.2		
C(7)-C(12)-C(11)	120.2(4)		
C(7)-C(12)-C(13)	121.8(4)		
C(11)-C(12)-C(13)	118.0(5)		
O(2)-C(13)-C(12)	121.9(5)		
O(2)-C(13)-C(14)	121.1(4)		
C(12)-C(13)-C(14)	117.0(5)		
C(1)-C(14)-C(5)	120.4(4)		
C(1)-C(14)-C(13)	118.5(5)		
C(5)-C(14)-C(13)	121.1(4)		
O(3)-C(15)-O(4)	125.0(5)		
O(3)-C(15)-C(2)	118.3(4)		
O(4)-C(15)-C(2)	116.5(5)		
O(6)-C(16)-O(5)	125.9(4)		
O(6)-C(16)-C(3)	118.0(4)		
O(5)-C(16)-C(3)	116.0(5)		
C(16)-O(5)-Ni(1)	126.1(3)		

Table 8.29: Continued: Bond Angles [°] for NiAQDC.

	Angle	Symm. op. atom 1	Symm. op. atom 3
Ni(1)-O(7)-H(7A)	132(3)		
Ni(1)-O(7)-H(7B)	127(3)		
H(7A)-O(7)-H(7B)	89(2)		
Ni(1)-O(8)-H(8A)	104(4)		
Ni(1)-O(8)-H(8B)	114(4)		
H(8A)-O(8)-H(8B)	88(2)		
Ni(1)-O(9)-H(9A)	107(3)		
Ni(1)-O(9)-H(9B)	119(4)		
H(9A)-O(9)-H(9B)	93(2)		
Ni(1)-O(10)-H(10A)	127(4)		
Ni(1)-O(10)-H(10B)	120(4)		
H(10A)-O(10)-H(10B)	90(2)		
Ni(1)-O(11)-H(11A)	119(3)		
Ni(1)-O(11)-H(11B)	123(4)		
H(11A)-O(11)-H(11B)	90(2)		
H(12A)-O(12)-H(12B)	87(2)		
H(13A)-O(13)-H(13B)	84(2)		

8.5 ZnAQDC structure details

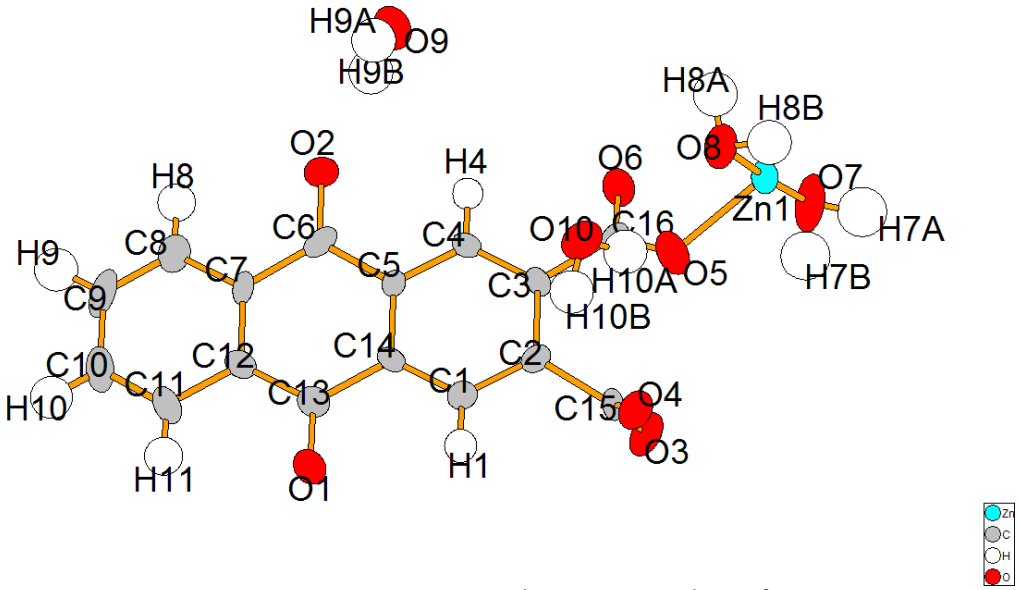

Figure 8.5: Asymmetric unit with atom numbers for ZnAQDC.

Table 8.30: Crystal data and structure refinement for ZnAQDC.

Parameter	Value
Empirical formula	$C_{16}H_{14}O_{10}Zn$
Formula weight	431.64 g·mol^{-1}
Collection Temperature	298(2) K
Wavelength	0.71073Å
Crystal system	Triclinic
Space Group	$P\bar{1}$
Unit cell dimensions	
a	7.629(2)Å
b	7.843(2)Å
c	15.045(5)Å
α	91.409(6)°
β	95.784(5)°
γ	115.160(5)°
Volume	808.4(4)Å^3
Z	2
Calculated density	1.773 g/m^3
Absorption coefficient	1.578 mm^{-1}
F(000)	440
Crystal size	0.5×0.3×0.2 mm
Theta range for data collection	2.73° to 26.02°
Limiting indices	$-9 \leq h \leq 9$, $-9 \leq k \leq 9$, $-18 \leq l \leq 17$
Reflections collected / unique	6709 / 3124 [R(int) = 0.0977]
Data Completeness	97.8 %
Absorption correction	Semi-empirical from equivalents
Max. and min. transmission	0.969 and 0.572
Refinement method	Full-matrix least-squares on F^2
Data / restraints / parameters	3124 / 12 / 269
Goodness-of-fit on F^2	0.947
Final R indices [I>2sigma(I)]	R1 = 0.0663, wR2 = 0.1036
R indices (all data)	R1 = 0.1681, wR2 = 0.1345
Largest diff. peak and hole	0.532 and -0.490 e·Å^{-3}

Table 8.31: Crystal coordinates [Å] and equivalent isotropic displacement parameters [Å^2] for ZnAQDC. U_{eq} is defined as one third of the trace of the orthogonalized U_{ij} tensor.

	x	y	z	U_{eq}
Zn(1)	1.00224(13)	0.71567(12)	0.43583(6)	0.0321(3)
C(1)	0.9008(9)	0.8656(9)	0.8297(4)	0.0265(16)
H(1)	0.9023	0.9774	0.8528	0.032
C(2)	0.9614(9)	0.8605(8)	0.7463(4)	0.0231(15)
C(3)	0.9515(9)	0.6901(9)	0.7100(4)	0.0213(15)
C(4)	0.8839(9)	0.5326(8)	0.7589(4)	0.0237(16)
H(4)	0.8754	0.4186	0.7348	0.028
C(5)	0.8286(9)	0.5414(8)	0.8433(4)	0.0215(15)
C(6)	0.7657(9)	0.3700(9)	0.8928(5)	0.0278(17)
C(7)	0.7333(9)	0.3876(9)	0.9880(4)	0.0247(16)
C(8)	0.6905(9)	0.2335(10)	1.0390(5)	0.0341(18)
H(8)	0.6864	0.1217	1.0144	0.041
C(9)	0.6546(10)	0.2457(11)	1.1248(5)	0.046(2)
H(9)	0.6227	0.1414	1.1588	0.055
C(10)	0.6657(10)	0.4132(11)	1.1617(5)	0.043(2)
H(10)	0.6451	0.4215	1.2212	0.051
C(11)	0.7061(10)	0.5670(10)	1.1129(4)	0.0349(18)
H(11)	0.7094	0.6777	1.1385	0.042
C(12)	0.7425(9)	0.5566(9)	1.0243(4)	0.0257(16)
C(13)	0.7850(9)	0.7212(9)	0.9703(4)	0.0270(17)
C(14)	0.8382(9)	0.7101(9)	0.8794(4)	0.0227(15)
C(15)	1.0529(11)	1.0406(9)	0.6994(4)	0.0250(16)
C(16)	1.0076(9)	0.6701(9)	0.6195(4)	0.0277(17)
O(1)	0.7815(7)	0.8645(6)	1.0010(3)	0.0408(13)
O(2)	0.7409(7)	0.2174(6)	0.8583(3)	0.0422(13)
O(3)	1.2329(7)	1.1150(6)	0.7064(3)	0.0396(13)
O(4)	0.9402(6)	1.1011(6)	0.6594(3)	0.0331(12)
O(5)	0.9934(8)	0.7791(7)	0.5631(3)	0.0486(14)
O(6)	1.0715(7)	0.5510(6)	0.6052(3)	0.0426(13)
O(7)	1.2913(8)	0.7768(8)	0.4467(4)	0.0586(16)
H(7A)	1.368(9)	0.845(8)	0.408(3)	0.070
H(7B)	1.331(11)	0.884(6)	0.480(4)	0.070
O(8)	0.7033(8)	0.6485(7)	0.4203(3)	0.0468(14)
H(8A)	0.628(9)	0.538(4)	0.392(4)	0.056
H(8B)	0.706(10)	0.698(7)	0.368(2)	0.056
O(9)	0.5294(8)	0.0157(7)	0.6885(3)	0.0468(14)
H(9A)	0.429(6)	0.040(9)	0.697(4)	0.056
H(9B)	0.587(8)	0.079(9)	0.739(3)	0.056
O(10)	0.5388(7)	0.7237(6)	0.5788(4)	0.0462(14)
H(10A)	0.649(6)	0.782(8)	0.556(4)	0.055
H(10B)	0.579(9)	0.822(6)	0.618(3)	0.055

Table 8.32: Anisotropic displacement parameters [Å^2] for ZnAQDC. The anisotropic displacement factor exponent takes the form $-2\pi^2[h^2a^{*2}U^{11} + ... + 2hka^*b^*U^{12}]$.

	U^{11}	U^{22}	U^{33}	U^{23}	U^{13}	U^{12}
Zn(1)	0.0492(6)	0.0271(5)	0.0274(5)	0.0090(4)	0.0155(4)	0.0207(4)
C(1)	0.031(4)	0.022(4)	0.027(4)	0.002(3)	0.002(3)	0.011(3)
C(2)	0.020(4)	0.019(4)	0.026(4)	0.004(3)	-0.002(3)	0.006(3)
C(3)	0.035(4)	0.025(4)	0.013(4)	0.006(3)	0.002(3)	0.022(3)
C(4)	0.028(4)	0.022(4)	0.022(4)	-0.004(3)	0.003(3)	0.011(3)
C(5)	0.019(4)	0.021(4)	0.019(4)	0.003(3)	0.003(3)	0.002(3)
C(6)	0.020(4)	0.018(4)	0.043(5)	0.006(4)	0.005(3)	0.006(3)
C(7)	0.022(4)	0.027(4)	0.025(4)	0.011(3)	0.012(3)	0.008(3)
C(8)	0.032(4)	0.036(5)	0.033(5)	0.010(4)	0.001(4)	0.014(4)
C(9)	0.046(5)	0.045(6)	0.045(5)	0.034(4)	0.010(4)	0.015(4)
C(10)	0.036(5)	0.060(6)	0.024(4)	0.015(4)	0.003(4)	0.012(4)
C(11)	0.045(5)	0.045(5)	0.020(4)	0.004(4)	0.008(4)	0.022(4)
C(12)	0.022(4)	0.030(4)	0.024(4)	-0.005(3)	0.003(3)	0.010(3)
C(13)	0.030(4)	0.029(4)	0.026(4)	0.001(3)	0.001(3)	0.017(4)
C(14)	0.027(4)	0.023(4)	0.018(4)	-0.004(3)	0.003(3)	0.011(3)
C(15)	0.037(5)	0.026(4)	0.019(4)	0.009(3)	0.013(4)	0.018(4)
C(16)	0.026(4)	0.019(4)	0.032(4)	0.004(3)	0.009(3)	0.003(3)
O(1)	0.062(4)	0.035(3)	0.033(3)	0.003(2)	0.017(3)	0.025(3)
O(2)	0.067(4)	0.023(3)	0.036(3)	0.002(2)	0.012(3)	0.018(3)
O(3)	0.025(3)	0.038(3)	0.055(4)	0.019(3)	0.013(3)	0.010(3)
O(4)	0.034(3)	0.031(3)	0.046(3)	0.014(2)	0.011(2)	0.023(3)
O(5)	0.091(4)	0.052(3)	0.032(3)	0.015(2)	0.023(3)	0.054(3)
O(6)	0.059(4)	0.038(3)	0.042(3)	0.006(2)	0.028(3)	0.027(3)
O(7)	0.046(4)	0.077(4)	0.052(4)	0.039(3)	0.018(3)	0.022(3)
O(8)	0.050(4)	0.047(3)	0.049(4)	0.017(3)	0.022(3)	0.021(3)
O(9)	0.044(3)	0.059(4)	0.043(3)	0.003(3)	0.014(3)	0.026(3)
O(10)	0.037(3)	0.037(3)	0.057(4)	0.004(3)	0.007(3)	0.009(3)

Table 8.33: Symmetry operations used in the following tables for ZnAQDC.

	Operation
#1	'x,y,z'
#2	'-x,-y,-z'

Table 8.34: Bond Lengths [Å] for ZnAQDC.

	Angle	Symm. op. atom 1	Symm. op. atom 3
Zn(1)-O(6)	1.984(5)	2	
Zn(1)-O(4)	2.000(4)	2	
Zn(1)-O(7)	2.036(6)		
Zn(1)-O(8)	2.097(5)		
C(1)-C(14)	1.377(8)		
C(1)-C(2)	1.385(8)		
C(1)-H(1)	0.9300		
C(2)-C(3)	1.400(8)		
C(2)-C(15)	1.514(8)		
C(3)-C(4)	1.383(8)		
C(3)-C(16)	1.492(8)		
C(4)-C(5)	1.387(8)		
C(4)-H(4)	0.9300		
C(5)-C(14)	1.387(8)		
C(5)-C(6)	1.471(8)		
C(6)-O(2)	1.222(7)		
C(6)-C(7)	1.491(8)		
C(7)-C(8)	1.384(8)		
C(7)-C(12)	1.392(8)		
C(8)-C(9)	1.357(9)		
C(8)-H(8)	0.9300		
C(9)-C(10)	1.378(10)		
C(9)-H(9)	0.9300		
C(10)-C(11)	1.364(9)		
C(10)-H(10)	0.9300		
C(11)-C(12)	1.396(8)		
C(11)-H(11)	0.9300		
C(12)-C(13)	1.476(8)		
C(13)-O(1)	1.217(7)		
C(13)-C(14)	1.477(8)		
C(15)-O(3)	1.234(7)		
C(15)-O(4)	1.258(7)		
C(16)-O(6)	1.247(7)		
C(16)-O(5)	1.248(7)		
O(4)-Zn(1)	2.000(4)	2	
O(6)-Zn(1)	1.984(5)	2	
O(7)-H(7A)	0.89(2)		
O(7)-H(7B)	0.88(2)		
O(8)-H(8A)	0.88(2)		
O(8)-H(8B)	0.89(2)		
O(9)-H(9A)	0.88(2)		
O(9)-H(9B)	0.87(2)		
O(10)-H(10A)	0.88(2)		
O(10)-H(10B)	0.88(2)		

Table 8.35: Bond Angles [°] for ZnAQDC.

	Angle	Symm. op. atom 1	Symm. op. atom 3
O(6)-Zn(1)-O(7)	91.5(2)	2	
O(4)-Zn(1)-O(7)	85.67(19)	2	
O(5)-Zn(1)-O(8)	84.8(2)		
O(6)-Zn(1)-O(8)	87.24(19)	2	
O(4)-Zn(1)-O(8)	93.55(18)	2	
O(7)-Zn(1)-O(8)	178.1(2)		
C(14)-C(1)-C(2)	122.0(6)		
C(14)-C(1)-H(1)	119.0		
C(2)-C(1)-H(1)	119.0		
C(1)-C(2)-C(3)	119.0(6)		
C(1)-C(2)-C(15)	120.1(5)		
C(3)-C(2)-C(15)	120.7(6)		
C(4)-C(3)-C(2)	119.1(6)		
C(4)-C(3)-C(16)	118.3(5)		
C(2)-C(3)-C(16)	122.6(6)		
C(3)-C(4)-C(5)	121.2(6)		
C(3)-C(4)-H(4)	119.4		
C(5)-C(4)-H(4)	119.4		
C(4)-C(5)-C(14)	119.8(6)		
C(4)-C(5)-C(6)	118.1(6)		
C(14)-C(5)-C(6)	122.1(6)		
O(2)-C(6)-C(5)	122.1(6)		
O(2)-C(6)-C(7)	120.3(6)		
C(5)-C(6)-C(7)	117.6(5)		
C(8)-C(7)-C(12)	120.7(6)		
C(8)-C(7)-C(6)	119.3(6)		
C(12)-C(7)-C(6)	120.0(6)		
C(9)-C(8)-C(7)	120.0(7)		
C(9)-C(8)-H(8)	120.0		
C(7)-C(8)-H(8)	120.0		
C(8)-C(9)-C(10)	119.8(7)		
C(8)-C(9)-H(9)	120.1		
C(10)-C(9)-H(9)	120.1		
C(11)-C(10)-C(9)	121.6(7)		
C(11)-C(10)-H(10)	119.2		
C(9)-C(10)-H(10)	119.2		
C(10)-C(11)-C(12)	119.4(7)		
C(10)-C(11)-H(11)	120.3		
C(12)-C(11)-H(11)	120.3		
C(7)-C(12)-C(11)	118.6(6)		
C(7)-C(12)-C(13)	121.2(6)		
C(11)-C(12)-C(13)	120.1(6)		
O(1)-C(13)-C(12)	120.7(6)		
O(1)-C(13)-C(14)	120.8(6)		
C(12)-C(13)-C(14)	118.5(5)		
C(1)-C(14)-C(5)	118.9(6)		
C(1)-C(14)-C(13)	121.2(5)		
C(5)-C(14)-C(13)	119.8(6)		
O(3)-C(15)-O(4)	126.8(6)		
O(3)-C(15)-C(2)	115.6(6)		
O(4)-C(15)-C(2)	117.5(6)		
O(6)-C(16)-O(5)	123.8(6)		
O(6)-C(16)-C(3)	118.7(6)		
O(5)-C(16)-C(3)	117.5(6)		
C(15)-O(4)-Zn(1)	127.8(4)		2
C(16)-O(5)-Zn(1)	117.9(4)		
C(16)-O(6)-Zn(1)	144.5(5)		2
Zn(1)-O(7)-H(7A)	122(5)		
Zn(1)-O(7)-H(7B)	96(5)		
H(7A)-O(7)-H(7B)	86(2)		

Table 8.36: Continued: Bond Angles [°] for for ZnAQDC.

	Angle	Symm. op. atom 1	Symm. op. atom 3
Zn(1)-O(8)-H(8A)	115(5)		
Zn(1)-O(8)-H(8B)	94(5)		
H(8A)-O(8)-H(8B)	88(2)		
H(9A)-O(9)-H(9B)	88(2)		
H(10A)-O(10)-H(10B)	87(2)		

8.6 CaFDC structure details

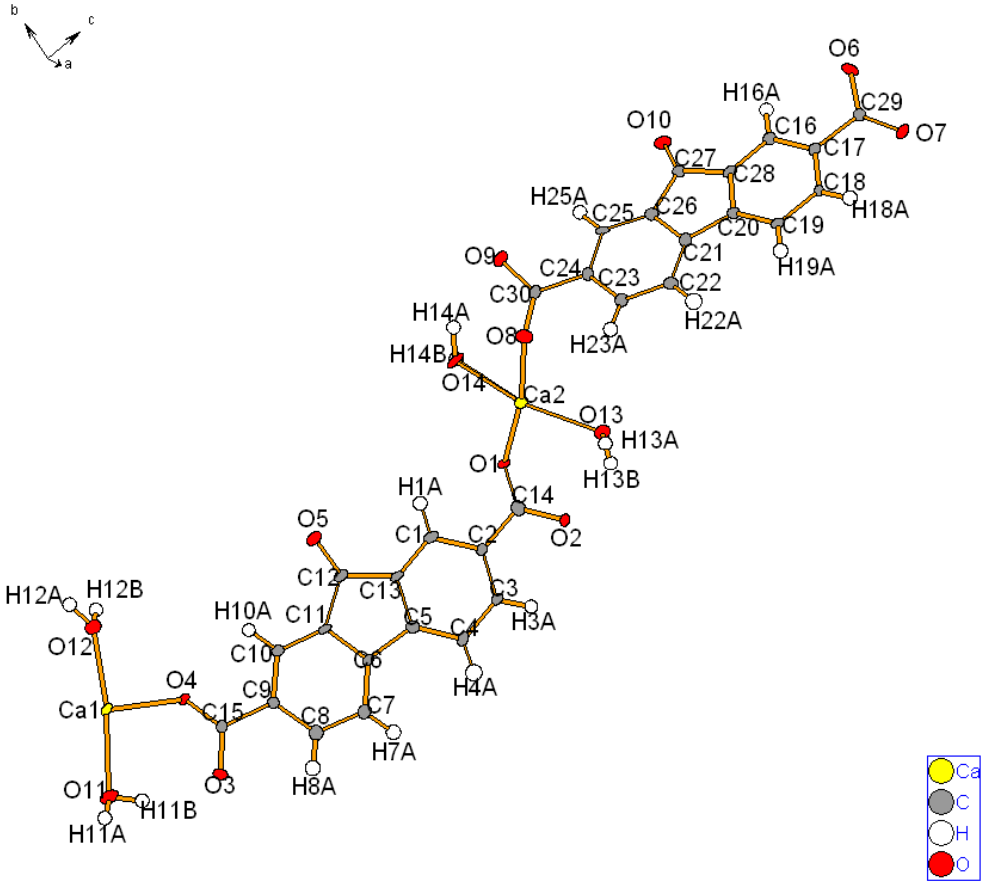

Figure 8.6: Asymmetric unit with atom numbers for CaFDC.

Table 8.37: Crystal data and structure refinement for CaFDC.

Parameter	Value
Empirical formula	$C_{30}H_{20}Ca_2O_{14}$
Formula weight	684.64 g·mol^{-1}
Collection Temperature	100(2) K
Wavelength	0.77490Å
Crystal system	Monoclinic
Space Group	$P2(1)$
Unit cell dimensions	
a	7.5411(16)Å
b	6.6118(14)Å
c	27.999(6)Å
α	90°
β	97.053(3)°
γ	90°
Volume	1385.4(5)Å^3
Z	2
Calculated density	1.641 g/m^3
Absorption coefficient	0.613 mm^{-1}
F(000)	704
Crystal size	0.16×0.06×0.01 mm
Theta range for data collection	2.97° to 29.36°
Limiting indices	$-9 \leq h \leq 9$, $-8 \leq k \leq 8$, $-35 \leq l \leq 35$
Reflections collected / unique	15211 / 5824 [R(int) = 0.0414]
Data Completeness	99.1%
Absorption correction	Semi-empirical with SADABS
Max. and min. transmission	0.99 and 0.91
Refinement method	Full-matrix least-squares on F^2
Data / restraints / parameters	5824 / 142 / 440
Goodness-of-fit on F^2	1.046
Final R indices [I>2sigma(I)]	R1 = 0.0818, wR2 = 0.2182
R indices (all data)	R1 = 0.0856, wR2 = 0.2220
Absolute structure parameter	0.09(8)
Extinction coefficient	0
Largest diff. peak and hole	1.770 and -0.923 e·Å^{-3}

Table 8.38: Crystal coordinates [Å] and equivalent isotropic displacement parameters [Å^2] for CaFDC. U_{eq} is defined as one third of the trace of the orthogonalized U_{ij} tensor.

	x	y	z	U_{eq}
Ca(1)	0.2290(2)	0.3608(3)	0.99531(6)	0.0125(4)
Ca(2)	-0.2537(2)	0.2541(3)	0.50212(6)	0.0117(3)
C(1)	0.4551(15)	0.5012(14)	1.4238(3)	0.0183(19)
C(2)	0.0423(11)	0.0077(13)	0.5755(3)	0.0104(14)
C(3)	0.0462(12)	0.6166(14)	1.0753(3)	0.0118(14)
C(4)	0.4567(14)	0.1064(16)	0.9242(3)	0.0180(17)
C(5)	0.3242(10)	0.7477(12)	1.2488(3)	0.0099(14)
C(6)	0.1248(10)	-0.0172(12)	0.6277(3)	0.0090(13)
C(7)	0.3768(11)	0.4753(13)	1.3712(3)	0.0115(14)
C(8)	0.4531(9)	-0.1419(13)	0.8563(3)	0.0112(14)
H(22A)	0.5152	-0.2343	0.8784	0.013
C(9)	0.3214(12)	-0.0590(14)	0.7762(3)	0.0150(15)
C(10)	0.3149(11)	0.1900(12)	0.8410(3)	0.0124(15)
H(24A)	0.2829	0.3192	0.8520	0.015
C(11)	0.0566(10)	0.3594(13)	1.1420(3)	0.0123(13)
H(25A)	-0.0018	0.2664	1.1194	0.015
C(12)	0.1818(11)	0.4397(14)	1.2227(3)	0.0137(15)
C(13)	0.0977(10)	0.5551(13)	1.1267(3)	0.0108(13)
C(14)	0.1725(10)	0.2452(12)	0.7517(3)	0.0109(14)
C(15)	0.1012(13)	0.3000(12)	1.1903(3)	0.0167(17)
H(29A)	0.0764	0.1669	1.2004	0.020
C(16)	0.1837(11)	0.6988(12)	1.1592(3)	0.0119(15)
H(30A)	0.2107	0.8312	1.1491	0.014
C(17)	0.3864(10)	0.6368(12)	1.3392(3)	0.0113(13)
H(33A)	0.4356	0.7631	1.3502	0.014
C(18)	0.1055(10)	0.1379(12)	0.6608(3)	0.0099(12)
H(34A)	0.0461	0.2600	0.6506	0.012
C(19)	0.2281(10)	0.2646(13)	1.3065(3)	0.0133(15)
H(35A)	0.1721	0.1410	1.2960	0.016
C(20)	0.2607(11)	-0.0736(13)	0.7241(3)	0.0110(14)
C(21)	0.2407(11)	0.4240(13)	1.2749(3)	0.0111(14)
C(22)	0.3020(11)	0.2929(12)	1.3551(3)	0.0133(16)
H(38A)	0.3001	0.1839	1.3771	0.016
C(23)	0.4077(12)	-0.2000(11)	0.8078(3)	0.0166(17)
H(39A)	0.4353	-0.3313	0.7971	0.020
C(24)	0.1739(11)	0.1112(13)	0.7087(3)	0.0140(16)
C(25)	0.2762(10)	-0.2315(13)	0.6918(3)	0.0134(15)
H(41A)	0.3319	-0.3556	0.7022	0.016
C(26)	0.2712(11)	0.1333(13)	0.7931(3)	0.0118(15)
C(27)	0.2064(10)	-0.2005(12)	0.6432(3)	0.0145(17)
H(43A)	0.2147	-0.3060	0.6206	0.017
C(28)	0.2269(11)	0.6367(13)	1.2069(3)	0.0128(16)
C(29)	0.3227(10)	0.6085(12)	1.2911(3)	0.0114(15)
C(30)	0.4081(10)	0.0493(13)	0.8724(3)	0.0110(15)
H(1A)	-0.342(10)	-0.143(10)	0.445(3)	0.013
H(3A)	-0.302(8)	0.687(7)	0.531(3)	0.013
H(7A)	0.219(6)	0.796(3)	0.9798(12)	0.013
H(9A)	0.191(7)	-0.022(10)	1.044(3)	0.013
H(1B)	-0.240(11)	-0.143(10)	0.481(2)	0.013
H(3B)	-0.143(8)	0.664(10)	0.543(3)	0.013
H(7B)	0.347(4)	0.737(5)	0.959(2)	0.013
H(9B)	0.333(7)	-0.046(8)	1.031(2)	0.013
O(1)	-0.2619(10)	-0.0495(10)	0.4567(2)	0.0215(14)
O(2)	0.0449(9)	-0.1465(11)	0.54797(18)	0.0190(12)
O(3)	-0.2323(9)	0.5764(10)	0.5352(2)	0.0182(13)
O(4)	-0.0197(8)	0.1760(9)	0.5621(2)	0.0135(13)
O(5)	0.4979(9)	0.3461(11)	1.4486(2)	0.0188(13)
O(6)	0.5252(7)	-0.0320(9)	0.9534(2)	0.0092(11)
O(7)	0.2398(8)	0.6886(9)	0.9618(2)	0.0164(13)
O(8)	0.4244(7)	0.2815(9)	0.93834(19)	0.0109(11)

Table 8.39: Continued: Crystal coordinates [Å] and equivalent isotropic displacement parameters [Å^2] for CaFDC. U_{eq} is defined as one third of the trace of the orthogonalized U_{ij} tensor.

	x	y	z	U_{eq}
O(9)	0.2850(8)	0.0640(9)	1.0438(2)	0.0150(13)
O(10)	0.4564(9)	0.6791(10)	1.4408(2)	0.0180(14)
O(11)	0.0130(8)	0.8079(9)	1.0661(2)	0.0158(13)
O(12)	0.0180(9)	0.4852(9)	1.0431(2)	0.0162(13)
O(13)	0.1032(8)	0.4144(8)	0.7525(2)	0.0153(12)
O(14)	0.3917(8)	0.9164(9)	1.2483(2)	0.0151(12)

Table 8.40: Anisotropic displacement parameters [Å^2] for CaFDC. The anisotropic displacement factor exponent takes the form $-2\pi^2[h^2a^{*2}U^{11} + ... + 2hka^*b^*U^{12}]$.

	U^{11}	U^{22}	U^{33}	U^{23}	U^{13}	U^{12}
Ca(1)	0.0131(7)	0.0082(8)	0.0154(7)	-0.0020(6)	-0.0021(6)	-0.0017(7)
Ca(2)	0.0104(6)	0.0073(7)	0.0160(7)	0.0011(6)	-0.0036(6)	0.0024(6)
C(1)	0.036(6)	0.010(4)	0.010(3)	0.002(3)	0.005(4)	0.003(4)
C(2)	0.008(2)	0.011(2)	0.0118(16)	0.0000(16)	-0.0025(16)	0.0006(17)
C(3)	0.011(2)	0.012(2)	0.0129(18)	0.0022(16)	0.0024(17)	0.0037(18)
C(4)	0.025(4)	0.017(4)	0.013(4)	0.002(3)	0.006(4)	0.001(4)
C(5)	0.008(2)	0.011(2)	0.012(2)	-0.0002(17)	0.0035(16)	-0.0005(17)
C(6)	0.007(2)	0.009(2)	0.0105(17)	-0.0007(15)	0.0009(16)	-0.0020(16)
C(7)	0.011(2)	0.010(2)	0.013(2)	0.0007(16)	0.0005(17)	0.0016(17)
C(8)	0.008(3)	0.011(3)	0.015(3)	0.000(3)	0.002(3)	0.004(3)
C(9)	0.017(2)	0.013(2)	0.0141(19)	-0.0022(18)	0.0007(17)	0.0013(18)
C(10)	0.013(4)	0.006(3)	0.019(4)	0.000(3)	0.005(3)	-0.002(3)
C(11)	0.012(2)	0.0115(18)	0.0134(19)	0.0019(15)	0.0024(16)	-0.0010(17)
C(12)	0.016(2)	0.012(2)	0.0133(19)	0.0022(17)	0.0003(17)	0.0005(18)
C(13)	0.011(2)	0.0100(18)	0.0112(18)	0.0006(16)	0.0001(16)	-0.0015(16)
C(14)	0.007(3)	0.008(4)	0.018(4)	0.000(3)	0.003(3)	0.001(3)
C(15)	0.024(4)	0.011(4)	0.015(4)	-0.003(3)	-0.001(3)	-0.001(3)
C(16)	0.016(4)	0.006(3)	0.014(4)	-0.004(3)	0.005(3)	0.001(3)
C(17)	0.011(2)	0.011(2)	0.013(2)	0.0004(16)	0.0024(17)	-0.0005(17)
C(18)	0.009(2)	0.010(2)	0.0113(17)	-0.0004(15)	0.0027(16)	0.0005(17)
C(19)	0.014(3)	0.009(4)	0.016(4)	-0.003(3)	0.000(3)	0.003(3)
C(20)	0.012(2)	0.009(2)	0.0121(18)	0.0012(17)	0.0021(16)	0.0037(17)
C(21)	0.012(2)	0.009(2)	0.0119(18)	-0.0009(17)	0.0020(16)	-0.0017(17)
C(22)	0.022(4)	0.009(4)	0.008(3)	0.001(3)	0.001(3)	0.005(3)
C(23)	0.023(4)	0.010(4)	0.016(4)	0.003(3)	-0.003(3)	0.003(3)
C(24)	0.019(4)	0.007(4)	0.016(4)	-0.001(3)	0.004(3)	0.006(3)
C(25)	0.015(3)	0.009(4)	0.016(4)	0.002(3)	0.000(3)	-0.005(3)
C(26)	0.013(4)	0.007(4)	0.016(4)	-0.002(3)	0.001(3)	0.004(3)
C(27)	0.014(4)	0.012(4)	0.017(4)	0.001(3)	-0.002(3)	-0.006(3)
C(28)	0.014(2)	0.011(2)	0.013(2)	-0.0011(17)	0.0012(17)	-0.0013(17)
C(29)	0.012(4)	0.006(3)	0.017(4)	0.001(3)	0.004(3)	-0.001(3)
C(30)	0.011(2)	0.010(2)	0.011(2)	-0.0001(17)	-0.0013(17)	0.0021(17)
O(1)	0.024(3)	0.011(3)	0.029(3)	-0.004(3)	0.002(3)	0.000(3)
O(2)	0.032(3)	0.014(3)	0.011(2)	-0.003(3)	0.004(2)	0.004(3)
O(3)	0.0178(19)	0.015(2)	0.0211(19)	-0.0013(16)	0.0019(16)	0.0031(17)
O(4)	0.018(3)	0.007(3)	0.014(3)	0.000(2)	-0.005(2)	0.004(2)
O(5)	0.030(3)	0.008(3)	0.018(3)	0.004(3)	0.001(3)	0.003(3)
O(6)	0.0045(17)	0.0107(18)	0.0115(18)	0.0004(15)	-0.0034(14)	0.0022(14)
O(7)	0.011(3)	0.005(3)	0.032(3)	0.002(2)	0.000(3)	0.002(2)
O(8)	0.0098(18)	0.0084(18)	0.0140(17)	-0.0027(15)	0.0002(14)	0.0046(15)
O(9)	0.0116(19)	0.0134(19)	0.0201(19)	-0.0009(15)	0.0018(15)	-0.0021(16)
O(10)	0.023(3)	0.016(3)	0.013(3)	-0.007(2)	-0.002(3)	-0.005(3)
O(11)	0.016(3)	0.010(3)	0.021(3)	0.005(2)	0.003(2)	0.000(2)
O(12)	0.020(3)	0.013(3)	0.017(3)	-0.002(2)	0.007(3)	-0.007(3)
O(13)	0.016(3)	0.008(3)	0.021(3)	0.002(2)	0.003(2)	-0.001(2)
O(14)	0.013(3)	0.011(3)	0.022(3)	-0.004(2)	0.003(2)	-0.003(2)

Table 8.41: Symmetry operations used in the following tables for CaFDC.

	Operation
#1	'x,y,z'
#2	'-x,y+1/2,-z'

Table 8.42: Bond Lengths [Å] for CaFDC.

	Angle	Symm. op. atom 1	Symm. op. atom 3
Ca(1)-O(12)	2.349(7)		
Ca(1)-O(8)	2.360(6)		
Ca(1)-O(7)	2.367(7)		
Ca(1)-O(11)	2.374(6)	2	
Ca(1)-O(9)	2.394(6)		
Ca(1)-C(3)	3.133(8)	2	
Ca(2)-O(3)	2.321(7)		
Ca(2)-O(2)	2.328(7)	2	
Ca(2)-O(5)	2.332(6)	1	
Ca(2)-O(4)	2.338(6)		
Ca(2)-O(1)	2.372(7)		
Ca(2)-O(10)	2.395(7)	2	
Ca(2)-C(1)	3.191(10)	2	
Ca(2)-H(1B)	2.70(8)		
C(1)-O(5)	1.258(11)		
C(1)-O(10)	1.269(11)		
C(1)-C(7)	1.528(11)		
C(1)-Ca(2)	3.191(10)	2	
C(2)-O(4)	1.247(10)		
C(2)-O(2)	1.280(11)		
C(2)-C(6)	1.525(10)		
C(3)-O(12)	1.253(11)		
C(3)-O(11)	1.308(11)		
C(3)-C(13)	1.499(10)		
C(3)-Ca(1)	3.133(8)	2	
C(4)-O(8)	1.257(12)		
C(4)-O(6)	1.291(11)		
C(4)-C(30)	1.499(11)		
C(5)-O(14)	1.227(10)		
C(5)-C(28)	1.497(11)		
C(5)-C(29)	1.501(10)		
C(6)-C(18)	1.402(11)		
C(6)-C(27)	1.404(11)		
C(7)-C(22)	1.383(12)		
C(7)-C(17)	1.401(11)		
C(8)-C(30)	1.398(11)		
C(8)-C(23)	1.412(10)		
C(8)-H(22A)	0.9500		
C(9)-C(23)	1.391(11)		
C(9)-C(26)	1.423(12)		
C(9)-C(20)	1.479(11)		
C(10)-C(26)	1.390(11)		
C(10)-C(30)	1.409(11)		
C(10)-H(24A)	0.9500		
C(11)-C(15)	1.409(10)		
C(11)-C(13)	1.409(12)		
C(11)-H(25A)	0.9500		
C(12)-C(15)	1.382(11)		
C(12)-C(28)	1.431(12)		
C(12)-C(21)	1.478(11)		
C(13)-C(16)	1.417(11)		
C(14)-O(13)	1.236(10)		
C(14)-C(24)	1.495(11)		
C(14)-C(26)	1.496(11)		
C(15)-H(29A)	0.9500		
C(16)-C(28)	1.396(11)		
C(16)-H(30A)	0.9500		
C(17)-C(29)	1.385(11)		
C(17)-H(33A)	0.9500		

Table 8.43: Continued: Bond Lengths [Å].

	Angle	Symm. op. atom 1	Symm. op. atom 3
C(18)-C(24)	1.387(11)		
C(18)-H(34A)	0.9500		
C(19)-C(21)	1.387(12)		
C(19)-C(22)	1.417(10)		
C(19)-H(35A)	0.9500		
C(20)-C(25)	1.395(12)		
C(20)-C(24)	1.428(11)		
C(21)-C(29)	1.417(11)		
C(22)-H(38A)	0.9500		
C(23)-H(39A)	0.9500		
C(25)-C(27)	1.412(11)		
C(25)-H(41A)	0.9500		
C(27)-H(43A)	0.9500		
O(1)-H(1A)	0.90(2)		
O(1)-H(1B)	0.92(2)		
O(2)-Ca(2)	2.328(7)	2	
O(3)-H(3A)	0.90(2)		
O(3)-H(3B)	0.90(2)		
O(5)-Ca(2)	2.332(6)	1	
O(6)-Ca(1)	2.313(5)	2	
O(7)-H(7A)	0.894(19)		
O(7)-H(7B)	0.886(19)		
O(9)-H(9A)	0.91(2)		
O(9)-H(9B)	0.91(2)		
O(10)-Ca(2)	2.395(7)	2	
O(11)-Ca(1)	2.374(6)	2	

Table 8.44: Bond Angles [°] for CaFDC.

	Angle	Symm. op. atom 1	Symm. op. atom 3
O(12)-Ca(1)-O(7)	87.9(2)		
O(8)-Ca(1)-O(7)	83.2(2)		
O(6)-Ca(1)-O(11)	168.9(2)	2	2
O(12)-Ca(1)-O(11)	87.1(2)		2
O(8)-Ca(1)-O(11)	88.1(2)		2
O(7)-Ca(1)-O(11)	84.8(2)		2
O(6)-Ca(1)-O(9)	80.0(2)	2	
O(12)-Ca(1)-O(9)	92.8(2)		
O(8)-Ca(1)-O(9)	96.9(2)		
O(7)-Ca(1)-O(9)	164.4(2)		
O(11)-Ca(1)-O(9)	110.8(2)	2	
O(6)-Ca(1)-C(3)	165.5(2)	2	2
O(12)-Ca(1)-C(3)	95.6(2)		2
O(8)-Ca(1)-C(3)	83.0(2)		2
O(7)-Ca(1)-C(3)	105.9(2)		2
O(11)-Ca(1)-C(3)	22.5(2)	2	2
O(9)-Ca(1)-C(3)	89.6(2)		2
O(3)-Ca(2)-O(2)	87.8(3)		2
O(3)-Ca(2)-O(5)	91.6(2)		1
O(2)-Ca(2)-O(5)	95.1(2)	2	1
O(3)-Ca(2)-O(4)	84.7(2)		
O(2)-Ca(2)-O(4)	89.3(2)	2	
O(5)-Ca(2)-O(4)	174.1(2)	1	
O(3)-Ca(2)-O(1)	170.5(3)		
O(2)-Ca(2)-O(1)	83.8(3)	2	
O(5)-Ca(2)-O(1)	84.8(2)	1	
O(4)-Ca(2)-O(1)	99.5(2)		
O(3)-Ca(2)-O(10)	86.7(2)		2
O(2)-Ca(2)-O(10)	174.1(2)	2	2
O(5)-Ca(2)-O(10)	87.4(2)	1	2
O(4)-Ca(2)-O(10)	87.9(2)		2
O(1)-Ca(2)-O(10)	101.8(3)		2
O(3)-Ca(2)-C(1)	103.7(2)		2
O(2)-Ca(2)-C(1)	162.0(3)	2	2
O(5)-Ca(2)-C(1)	98.4(3)	1	2
O(4)-Ca(2)-C(1)	78.2(2)		2
O(1)-Ca(2)-C(1)	85.5(2)		2
O(10)-Ca(2)-C(1)	20.6(2)	2	2
O(3)-Ca(2)-H(1B)	168.3(10)		
O(2)-Ca(2)-H(1B)	95.4(16)	2	
O(5)-Ca(2)-H(1B)	99.3(13)	1	
O(4)-Ca(2)-H(1B)	84.1(12)		
O(1)-Ca(2)-H(1B)	19.5(10)		
O(10)-Ca(2)-H(1B)	89.5(16)	2	
C(1)-Ca(2)-H(1B)	70.6(15)	2	
O(5)-C(1)-O(10)	123.9(8)		
O(5)-C(1)-C(7)	118.9(8)		
O(5)-C(1)-Ca(2)	100.3(5)		2
C(7)-C(1)-Ca(2)	121.8(6)		2
O(4)-C(2)-O(2)	124.1(7)		
O(4)-C(2)-C(6)	118.7(7)		
O(2)-C(2)-C(6)	117.2(7)		
O(12)-C(3)-O(11)	121.1(7)		
O(12)-C(3)-C(13)	120.3(8)		
O(11)-C(3)-C(13)	118.2(7)		
O(12)-C(3)-Ca(1)	82.1(5)		2
C(13)-C(3)-Ca(1)	145.0(6)		2
O(8)-C(4)-O(6)	122.1(8)		
O(8)-C(4)-C(30)	120.2(8)		

Table 8.45: Continued: Bond Angles [°] for CaFDC.

	Angle	Symm. op. atom 1	Symm. op. atom 3
O(6)-C(4)-C(30)	117.7(8)		
O(14)-C(5)-C(28)	127.0(8)		
O(14)-C(5)-C(29)	127.5(7)		
C(28)-C(5)-C(29)	105.5(7)		
C(18)-C(6)-C(27)	120.3(7)		
C(18)-C(6)-C(2)	119.4(7)		
C(27)-C(6)-C(2)	120.1(7)		
C(22)-C(7)-C(17)	120.5(7)		
C(22)-C(7)-C(1)	120.4(7)		
C(17)-C(7)-C(1)	119.1(7)		
C(30)-C(8)-C(23)	121.1(7)		
C(30)-C(8)-H(22A)	119.5		
C(23)-C(8)-H(22A)	119.5		
C(23)-C(9)-C(26)	120.7(7)		
C(23)-C(9)-C(20)	130.4(8)		
C(26)-C(9)-C(20)	108.9(7)		
C(26)-C(10)-C(30)	117.7(8)		
C(26)-C(10)-H(24A)	121.1		
C(30)-C(10)-H(24A)	121.1		
C(15)-C(11)-C(13)	120.8(7)		
C(15)-C(11)-H(25A)	119.6		
C(13)-C(11)-H(25A)	119.6		
C(15)-C(12)-C(28)	120.4(7)		
C(15)-C(12)-C(21)	131.1(8)		
C(28)-C(12)-C(21)	108.5(7)		
C(11)-C(13)-C(16)	121.4(7)		
C(11)-C(13)-C(3)	120.0(7)		
C(16)-C(13)-C(3)	118.6(8)		
O(13)-C(14)-C(24)	126.6(7)		
O(13)-C(14)-C(26)	127.1(8)		
C(24)-C(14)-C(26)	106.2(7)		
C(12)-C(15)-C(11)	118.6(8)		
C(12)-C(15)-H(29A)	120.7		
C(11)-C(15)-H(29A)	120.7		
C(28)-C(16)-C(13)	116.8(8)		
C(28)-C(16)-H(30A)	121.6		
C(13)-C(16)-H(30A)	121.6		
C(29)-C(17)-C(7)	118.6(7)		
C(29)-C(17)-H(33A)	120.7		
C(7)-C(17)-H(33A)	120.7		
C(24)-C(18)-C(6)	119.3(7)		
C(24)-C(18)-H(34A)	120.4		
C(6)-C(18)-H(34A)	120.4		
C(21)-C(19)-C(22)	117.5(8)		
C(21)-C(19)-H(35A)	121.2		
C(22)-C(19)-H(35A)	121.2		
C(25)-C(20)-C(24)	121.2(7)		
C(25)-C(20)-C(9)	130.4(8)		
C(24)-C(20)-C(9)	108.4(7)		
C(19)-C(21)-C(29)	120.8(7)		
C(19)-C(21)-C(12)	130.4(8)		
C(29)-C(21)-C(12)	108.8(7)		
C(7)-C(22)-C(19)	121.6(8)		
C(7)-C(22)-H(38A)	119.2		
C(19)-C(22)-H(38A)	119.2		
C(9)-C(23)-C(8)	117.9(8)		
C(9)-C(23)-H(39A)	121.0		
C(8)-C(23)-H(39A)	121.0		
C(18)-C(24)-C(20)	120.2(7)		
C(18)-C(24)-C(14)	131.6(7)		

Table 8.46: Continued: Bond Angles [°] for CaFDC.

	Angle	Symm. op. atom 1	Symm. op. atom 3
C(20)-C(24)-C(14)	108.2(7)		
C(20)-C(25)-C(27)	117.7(8)		
C(20)-C(25)-H(41A)	121.2		
C(27)-C(25)-H(41A)	121.2		
C(10)-C(26)-C(9)	121.3(7)		
C(10)-C(26)-C(14)	130.6(8)		
C(9)-C(26)-C(14)	108.1(7)		
C(6)-C(27)-C(25)	121.4(8)		
C(6)-C(27)-H(43A)	119.3		
C(25)-C(27)-H(43A)	119.3		
C(16)-C(28)-C(12)	121.9(7)		
C(16)-C(28)-C(5)	129.7(8)		
C(12)-C(28)-C(5)	108.4(7)		
C(17)-C(29)-C(21)	120.8(7)		
C(17)-C(29)-C(5)	130.5(7)		
C(21)-C(29)-C(5)	108.7(7)		
C(8)-C(30)-C(10)	121.2(7)		
C(8)-C(30)-C(4)	120.0(7)		
C(10)-C(30)-C(4)	118.8(8)		
Ca(2)-O(1)-H(1A)	139(6)		
Ca(2)-O(1)-H(1B)	101(6)		
H(1A)-O(1)-H(1B)	82(4)		
C(2)-O(2)-Ca(2)	130.5(6)		2
Ca(2)-O(3)-H(3A)	133(6)		
Ca(2)-O(3)-H(3B)	135(6)		
H(3A)-O(3)-H(3B)	85(4)		
C(2)-O(4)-Ca(2)	129.5(5)		
C(1)-O(5)-Ca(2)	134.3(7)		1
C(4)-O(6)-Ca(1)	147.0(6)		2
Ca(1)-O(7)-H(7A)	119(2)		
Ca(1)-O(7)-H(7B)	117(2)		
H(7A)-O(7)-H(7B)	90(3)		
C(4)-O(8)-Ca(1)	125.4(6)		
Ca(1)-O(9)-H(9A)	116(6)		
Ca(1)-O(9)-H(9B)	119(5)		
H(9A)-O(9)-H(9B)	81(3)		
C(1)-O(10)-Ca(2)	117.9(6)		2
C(3)-O(11)-Ca(1)	113.4(5)		2
C(3)-O(12)-Ca(1)	125.9(6)		

8.7 SrFDC structure details

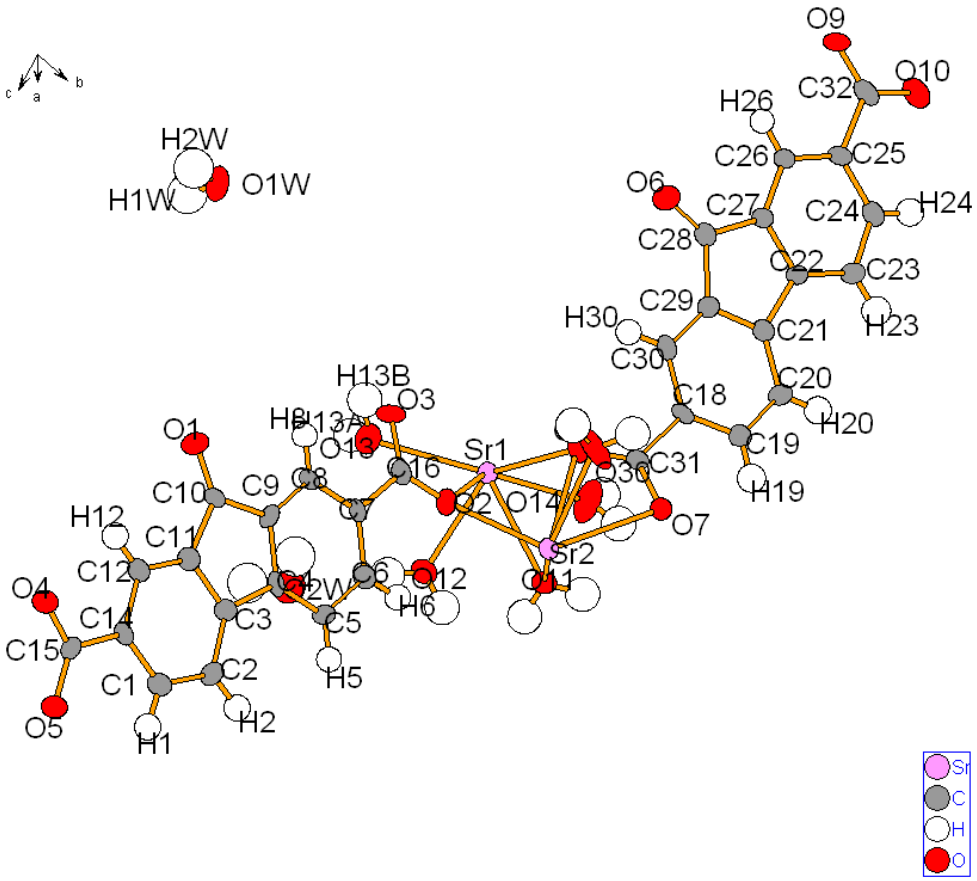

Figure 8.7: Asymmetric unit with atom numbers for SrFDC.

Table 8.47: Crystal data and structure refinement for SrFDC.

Parameter	Value
Empirical formula	$C_{30}H_{26}O_{17}Sr_2$
Formula weight	833.75 g·mol^{-1}
Collection Temperature	298(2) K
Wavelength	0.71073Å
Crystal system	Triclinic
Space Group	$P\bar{1}$
Unit cell dimensions	
a	8.578(2)Å
b	11.836(3)Å
c	15.626(4)Å
α	72.437(4)°
β	78.722(5)°
γ	85.437(4)°
Volume	1483.1(7)Å^3
Z	2
Calculated density	1.867 g/m^3
Absorption coefficient	3.683 mm^{-1}
F(000)	836
Crystal size	3×.1×.05 mm
Theta range for data collection	2.84° to 26.02°
Limiting indices	$-10 \leq h \leq 10$, $-14 \leq k \leq 14$, $-19 \leq l \leq 18$
Reflections collected / unique	12487 / 5769 [R(int) = 0.0618]
Data Completeness	98.4%
Absorption correction	Semi-empirical from equivalents
Max. and min. transmission	.832 and .588
Refinement method	Full-matrix least-squares on F^2
Data / restraints / parameters	5769 / 21 / 487
Goodness-of-fit on F^2	1.029
Final R indices [I>2sigma(I)]	R1 = 0.0523, wR2 = 0.1145
R indices (all data)	R1 = 0.0932, wR2 = 0.1345
Largest diff. peak and hole	1.510 and -0.526 e·Å^{-3}

Table 8.48: Crystal coordinates [Å] and equivalent isotropic displacement parameters [Å^2] for SrFDC. U_{eq} is defined as one third of the trace of the orthogonalized U_{ij} tensor.

	x	y	z	U_{eq}
Sr(1)	0.75784(6)	0.59240(4)	-0.01243(4)	0.02178(16)
Sr(2)	0.48891(6)	0.83117(4)	0.08721(3)	0.02028(16)
C(1)	0.1211(6)	0.3919(5)	0.6996(4)	0.0255(13)
H(1)	0.1436	0.4058	0.7514	0.031
C(2)	0.2095(7)	0.4485(5)	0.6150(4)	0.0261(14)
H(2)	0.2861	0.5032	0.6087	0.031
C(3)	0.1789(6)	0.4200(4)	0.5403(4)	0.0208(12)
C(4)	0.2536(6)	0.4628(4)	0.4439(4)	0.0215(13)
C(5)	0.3745(6)	0.5416(5)	0.4007(4)	0.0235(13)
H(5)	0.4203	0.5799	0.4333	0.028
C(6)	0.4265(7)	0.5626(5)	0.3074(4)	0.0248(13)
H(6)	0.5066	0.6167	0.2774	0.030
C(7)	0.3619(6)	0.5049(4)	0.2580(4)	0.0197(12)
C(8)	0.2383(7)	0.4257(4)	0.3017(4)	0.0235(13)
H(8)	0.1922	0.3877	0.2690	0.028
C(9)	0.1865(6)	0.4054(4)	0.3936(4)	0.0229(13)
C(10)	0.0600(7)	0.3275(5)	0.4581(4)	0.0224(13)
C(11)	0.0603(7)	0.3403(5)	0.5499(4)	0.0230(13)
C(12)	-0.0306(7)	0.2890(5)	0.6336(4)	0.0255(13)
H(12)	-0.1111	0.2376	0.6394	0.031
C(14)	-0.0003(6)	0.3151(4)	0.7094(4)	0.0209(12)
C(15)	-0.1008(7)	0.2645(4)	0.8017(4)	0.0221(13)
C(16)	0.4250(6)	0.5275(4)	0.1579(4)	0.0210(12)
C(18)	0.6212(7)	0.8983(4)	-0.2241(4)	0.0216(12)
C(19)	0.7188(7)	0.9908(5)	-0.2790(4)	0.0301(14)
H(19)	0.7583	1.0403	-0.2524	0.036
C(20)	0.7584(7)	1.0109(5)	-0.3729(4)	0.0287(14)
H(20)	0.8270	1.0710	-0.4091	0.034
C(21)	0.6930(7)	0.9390(4)	-0.4106(4)	0.0216(13)
C(22)	0.7095(7)	0.9399(4)	-0.5078(4)	0.0219(13)
C(23)	0.7996(7)	1.0100(5)	-0.5859(4)	0.0314(15)
H(23)	0.8635	1.0683	-0.5833	0.038
C(24)	0.7927(7)	0.9912(5)	-0.6688(4)	0.0286(14)
H(24)	0.8563	1.0357	-0.7217	0.034
C(25)	0.6918(7)	0.9066(5)	-0.6747(4)	0.0244(13)
C(26)	0.6001(7)	0.8386(4)	-0.5949(4)	0.0217(13)
H(26)	0.5314	0.7830	-0.5972	0.026
C(27)	0.6115(6)	0.8540(4)	-0.5125(4)	0.0219(13)
C(28)	0.5269(7)	0.7940(5)	-0.4177(4)	0.0237(13)
C(29)	0.5874(6)	0.8510(5)	-0.3569(4)	0.0217(12)
C(30)	0.5541(7)	0.8267(5)	-0.2640(4)	0.0242(13)
H(30)	0.4887	0.7644	-0.2281	0.029
C(31)	0.5912(6)	0.8732(4)	-0.1213(4)	0.0198(12)
C(32)	0.6782(7)	0.8955(5)	-0.7654(4)	0.0284(14)
O(1)	-0.0293(5)	0.2656(4)	0.4400(3)	0.0362(11)
O(2)	0.5306(5)	0.6046(3)	0.1200(3)	0.0266(9)
O(3)	0.3705(5)	0.4685(4)	0.1163(3)	0.0324(10)
O(4)	-0.2202(5)	0.2075(3)	0.8066(3)	0.0298(10)
O(5)	-0.0573(5)	0.2799(3)	0.8704(3)	0.0321(10)
O(6)	0.4268(5)	0.7191(4)	-0.3952(3)	0.0358(11)
O(7)	0.5885(5)	0.9586(3)	-0.0884(2)	0.0249(9)
O(8)	0.5714(5)	0.7677(3)	-0.0724(3)	0.0301(10)
O(9)	0.5839(5)	0.8223(3)	-0.7682(3)	0.0318(10)
O(10)	0.7677(5)	0.9579(4)	-0.8357(3)	0.0426(12)
O(11)	0.7957(5)	0.7800(3)	0.0457(3)	0.0277(10)
H(11A)	0.860(6)	0.763(5)	0.084(3)	0.053(11)
H(11B)	0.850(7)	0.842(4)	0.008(3)	0.053(11)
O(12)	0.9834(5)	0.5210(3)	0.0950(3)	0.0291(10)
H(12A)	0.933(7)	0.475(4)	0.146(3)	0.053(11)
H(12B)	0.984(8)	0.584(4)	0.118(4)	0.053(11)

Table 8.49: Continued: Crystal coordinates [Å] and equivalent isotropic displacement parameters [Å^2] for SrFDC. U_{eq} is defined as one third of the trace of the orthogonalized U_{ij} tensor.

	x	y	z	U_{eq}
O(13)	0.7147(6)	0.3694(4)	0.0725(3)	0.0442(12)
H(13A)	0.790(5)	0.319(5)	0.064(5)	0.054(9)
H(13B)	0.644(5)	0.345(6)	0.051(5)	0.054(9)
O(14)	0.9617(6)	0.7378(4)	-0.1303(3)	0.0541(15)
H(14A)	0.958(7)	0.811(3)	-0.133(4)	0.054(9)
H(14B)	1.043(6)	0.737(5)	-0.173(4)	0.054(9)
O(30)	0.2626(6)	0.8699(6)	-0.0063(4)	0.0698(19)
H(30A)	0.252(7)	0.923(4)	-0.055(3)	0.054(9)
H(30B)	0.178(5)	0.833(5)	0.011(4)	0.054(9)
O(1W)	0.0604(5)	0.0409(3)	0.1069(3)	0.0382(11)
H(1W)	-0.029(4)	0.009(6)	0.136(5)	0.070(13)
H(2W)	0.126(6)	-0.016(5)	0.128(5)	0.070(13)
O(2W)	0.8637(6)	0.3363(4)	0.2697(3)	0.0489(13)
H(3W)	0.857(8)	0.266(3)	0.306(4)	0.070(13)
H(4W)	0.770(5)	0.343(6)	0.256(5)	0.070(13)

Table 8.50: Anisotropic displacement parameters [Å^2] for SrFDC. The anisotropic displacement factor exponent takes the form $-2\pi^2[h^2a^{*2}U^{11} + ... + 2hka^*b^*U^{12}]$.

	U^{11}	U^{22}	U^{33}	U^{23}	U^{13}	U^{12}
Sr(1)	0.0246(3)	0.0217(3)	0.0187(3)	-0.0055(2)	-0.0031(2)	-0.0022(2)
Sr(2)	0.0243(3)	0.0200(3)	0.0151(3)	-0.0032(2)	-0.0024(2)	-0.0025(2)
C(1)	0.025(3)	0.031(3)	0.020(3)	-0.007(2)	-0.003(3)	-0.004(2)
C(2)	0.025(3)	0.026(3)	0.026(4)	-0.006(3)	0.000(3)	-0.011(2)
C(3)	0.020(3)	0.023(3)	0.019(3)	-0.008(2)	-0.001(2)	0.000(2)
C(4)	0.023(3)	0.020(3)	0.015(3)	0.004(2)	-0.001(2)	-0.002(2)
C(5)	0.023(3)	0.027(3)	0.021(3)	-0.006(2)	-0.004(3)	-0.010(2)
C(6)	0.024(3)	0.029(3)	0.018(3)	-0.004(2)	0.000(3)	-0.007(2)
C(7)	0.023(3)	0.017(2)	0.015(3)	0.001(2)	-0.004(2)	0.001(2)
C(8)	0.027(3)	0.024(3)	0.018(3)	-0.001(2)	-0.010(3)	-0.004(2)
C(9)	0.023(3)	0.017(3)	0.026(4)	-0.004(2)	-0.001(3)	-0.007(2)
C(10)	0.029(3)	0.024(3)	0.015(3)	-0.004(2)	-0.008(3)	-0.002(2)
C(11)	0.022(3)	0.024(3)	0.022(3)	-0.006(2)	-0.003(3)	0.000(2)
C(12)	0.031(3)	0.025(3)	0.020(3)	-0.004(2)	-0.007(3)	-0.001(2)
C(14)	0.024(3)	0.023(3)	0.012(3)	-0.001(2)	-0.001(2)	-0.002(2)
C(15)	0.025(3)	0.018(3)	0.022(3)	-0.005(2)	0.000(3)	-0.006(2)
C(16)	0.019(3)	0.022(3)	0.018(3)	-0.001(2)	-0.001(2)	0.002(2)
C(18)	0.029(3)	0.026(3)	0.011(3)	-0.007(2)	-0.006(2)	0.002(2)
C(19)	0.039(4)	0.027(3)	0.025(4)	-0.003(3)	-0.011(3)	-0.007(3)
C(20)	0.038(4)	0.029(3)	0.020(3)	-0.009(3)	-0.002(3)	-0.013(3)
C(21)	0.026(3)	0.022(3)	0.017(3)	-0.007(2)	-0.003(3)	0.001(2)
C(22)	0.029(3)	0.020(3)	0.019(3)	-0.008(2)	-0.006(3)	-0.002(2)
C(23)	0.039(4)	0.033(3)	0.025(4)	-0.006(3)	-0.008(3)	-0.016(3)
C(24)	0.032(4)	0.032(3)	0.018(3)	0.000(3)	-0.005(3)	-0.007(3)
C(25)	0.027(3)	0.029(3)	0.021(3)	-0.009(2)	-0.010(3)	-0.002(2)
C(26)	0.027(3)	0.022(3)	0.018(3)	-0.006(2)	-0.006(3)	-0.004(2)
C(27)	0.027(3)	0.024(3)	0.015(3)	-0.006(2)	-0.003(3)	-0.005(2)
C(28)	0.022(3)	0.024(3)	0.023(3)	-0.003(2)	-0.007(3)	0.000(2)
C(29)	0.019(3)	0.024(3)	0.020(3)	-0.006(2)	-0.001(2)	-0.005(2)
C(30)	0.030(3)	0.022(3)	0.018(3)	-0.001(2)	-0.005(3)	0.001(2)
C(31)	0.021(3)	0.021(3)	0.019(3)	-0.009(2)	-0.006(2)	0.004(2)
C(32)	0.032(4)	0.038(3)	0.013(3)	-0.006(3)	-0.002(3)	0.002(3)
O(1)	0.039(3)	0.042(2)	0.029(3)	-0.008(2)	-0.003(2)	-0.022(2)
O(2)	0.034(2)	0.0227(19)	0.019(2)	-0.0029(16)	0.0022(19)	-0.0046(17)
O(3)	0.040(3)	0.043(2)	0.020(2)	-0.0166(19)	-0.005(2)	-0.012(2)
O(4)	0.029(2)	0.040(2)	0.018(2)	-0.0062(18)	0.0016(18)	-0.0152(19)
O(5)	0.039(3)	0.039(2)	0.019(2)	-0.0071(19)	-0.002(2)	-0.0162(19)
O(6)	0.043(3)	0.040(2)	0.025(2)	-0.0088(19)	0.000(2)	-0.018(2)
O(7)	0.034(2)	0.0224(19)	0.019(2)	-0.0061(16)	-0.0047(18)	-0.0031(17)
O(8)	0.050(3)	0.023(2)	0.015(2)	-0.0020(16)	-0.0053(19)	0.0019(18)
O(9)	0.039(3)	0.038(2)	0.023(2)	-0.0108(19)	-0.010(2)	-0.013(2)
O(10)	0.045(3)	0.057(3)	0.017(2)	0.002(2)	0.001(2)	-0.019(2)
O(11)	0.028(2)	0.031(2)	0.026(3)	-0.0077(19)	-0.0082(19)	-0.0052(18)
O(12)	0.034(3)	0.033(2)	0.021(2)	-0.0095(18)	-0.004(2)	0.0003(19)
O(13)	0.050(3)	0.032(2)	0.049(3)	-0.003(2)	-0.014(3)	-0.007(2)
O(14)	0.066(4)	0.031(2)	0.051(3)	-0.011(2)	0.027(3)	-0.011(2)
O(30)	0.034(3)	0.113(5)	0.034(3)	0.031(3)	-0.014(3)	-0.022(3)
O(1W)	0.034(3)	0.026(2)	0.045(3)	0.001(2)	-0.001(2)	-0.0018(19)
O(2W)	0.047(3)	0.056(3)	0.040(3)	-0.014(2)	0.005(3)	-0.012(3)

Table 8.51: Symmetry operations used in the following tables for SrFDC.

	Operation
#1	‘x,y,z’
#2	‘-x,-y,-z’

Table 8.52: Bond Lengths [Å] for SrFDC.

	Angle	Symm. op. atom 1	Symm. op. atom 3
Sr(1)-O(8)	2.574(4)		
Sr(1)-O(2)	2.580(4)		
Sr(1)-O(13)	2.591(4)		
Sr(1)-O(14)	2.592(4)		
Sr(1)-O(11)	2.704(4)		
Sr(1)-O(12)	2.726(4)		
Sr(1)-O(12)	2.801(4)	2	
Sr(2)-O(9)	2.518(4)	1	
Sr(2)-O(7)	2.528(3)	2	
Sr(2)-O(4)	2.547(4)	2	
Sr(2)-O(2)	2.584(4)		
Sr(2)-O(30)	2.584(5)		
Sr(2)-O(11)	2.651(4)		
Sr(2)-O(7)	2.706(4)		
Sr(2)-O(8)	2.764(4)		
Sr(2)-C(31)	3.100(5)		
Sr(2)-C(32)	3.353(6)	1	
C(1)-C(2)	1.388(7)		
C(1)-C(14)	1.392(7)		
C(1)-H(1)	0.9300		
C(2)-C(3)	1.385(8)		
C(2)-H(2)	0.9300		
C(3)-C(11)	1.398(7)		
C(3)-C(4)	1.465(7)		
C(4)-C(5)	1.379(7)		
C(4)-C(9)	1.405(8)		
C(5)-C(6)	1.390(7)		
C(5)-H(5)	0.9300		
C(6)-C(7)	1.384(8)		
C(6)-H(6)	0.9300		
C(7)-C(8)	1.399(7)		
C(7)-C(16)	1.500(7)		
C(8)-C(9)	1.370(7)		
C(8)-H(8)	0.9300		
C(9)-C(10)	1.488(7)		
C(10)-O(1)	1.225(6)		
C(10)-C(11)	1.488(8)		
C(11)-C(12)	1.373(8)		
C(12)-C(14)	1.386(8)		
C(12)-H(12)	0.9300		
C(14)-C(15)	1.502(7)		
C(15)-O(4)	1.248(6)		
C(15)-O(5)	1.270(7)		
C(16)-O(3)	1.255(6)		
C(16)-O(2)	1.265(6)		
C(18)-C(19)	1.390(7)		
C(18)-C(30)	1.405(8)		
C(18)-C(31)	1.515(7)		
C(19)-C(20)	1.390(8)		
C(19)-H(19)	0.9300		
C(20)-C(21)	1.377(7)		
C(20)-H(20)	0.9300		
C(21)-C(29)	1.390(7)		
C(21)-C(22)	1.494(8)		
C(22)-C(23)	1.378(8)		
C(22)-C(27)	1.397(7)		
C(23)-C(24)	1.392(8)		
C(23)-H(23)	0.9300		
C(24)-C(25)	1.408(7)		
C(24)-H(24)	0.9300		

Table 8.53: Continued: Bond Lengths [Å] for SrFDC.

	Angle	Symm. op. atom 1	Symm. op. atom 3
C(25)-C(26)	1.390(8)		
C(25)-C(32)	1.490(8)		
C(26)-C(27)	1.377(7)		
C(26)-H(26)	0.9300		
C(27)-C(28)	1.500(8)		
C(28)-O(6)	1.209(6)		
C(28)-C(29)	1.505(8)		
C(29)-C(30)	1.368(7)		
C(30)-H(30)	0.9300		
C(31)-O(8)	1.257(6)		
C(31)-O(7)	1.263(6)		
C(32)-O(9)	1.248(7)		
C(32)-O(10)	1.269(7)		
C(32)-Sr(2)	3.353(6)	1	
O(3)-Sr(1)	2.428(4)	2	
O(4)-Sr(2)	2.547(4)	2	
O(7)-Sr(2)	2.528(3)	2	
O(9)-Sr(2)	2.518(4)	1	
O(11)-H(11A)	0.86(3)		
O(11)-H(11B)	0.89(3)		
O(12)-Sr(1)	2.801(4)	2	
O(12)-H(12A)	0.87(3)		
O(12)-H(12B)	0.92(3)		
O(13)-H(13A)	0.86(3)		
O(13)-H(13B)	0.85(3)		
O(14)-H(14A)	0.86(3)		
O(14)-H(14B)	0.87(3)		
O(30)-H(30A)	0.84(3)		
O(30)-H(30B)	0.83(3)		
O(1W)-H(1W)	0.86(3)		
O(1W)-H(2W)	0.87(3)		
O(2W)-H(3W)	0.86(3)		
O(2W)-H(4W)	0.86(3)		

Table 8.54: Bond Angles [°] for SrFDC.

	Angle	Symm. op. atom 1	Symm. op. atom 3
O(8)-Sr(1)-O(13)	133.88(15)		
O(2)-Sr(1)-O(13)	79.26(14)		
O(3)-Sr(1)-O(14)	99.41(16)	2	
O(8)-Sr(1)-O(14)	79.78(15)		
O(2)-Sr(1)-O(14)	136.04(13)		
O(13)-Sr(1)-O(14)	142.21(16)		
O(3)-Sr(1)-O(11)	142.79(14)	2	
O(8)-Sr(1)-O(11)	68.01(12)		
O(2)-Sr(1)-O(11)	69.56(12)		
O(13)-Sr(1)-O(11)	132.42(14)		
O(14)-Sr(1)-O(11)	69.08(14)		
O(3)-Sr(1)-O(12)	141.92(13)	2	
O(8)-Sr(1)-O(12)	142.72(12)		
O(2)-Sr(1)-O(12)	94.71(12)		
O(13)-Sr(1)-O(12)	73.00(14)		
O(14)-Sr(1)-O(12)	88.34(16)		
O(11)-Sr(1)-O(12)	74.72(12)		
O(3)-Sr(1)-O(12)	80.52(13)	2	2
O(8)-Sr(1)-O(12)	134.14(12)		2
O(2)-Sr(1)-O(12)	153.36(12)		2
O(13)-Sr(1)-O(12)	76.10(14)		2
O(14)-Sr(1)-O(12)	66.45(13)		2
O(11)-Sr(1)-O(12)	121.85(12)		2
O(12)-Sr(1)-O(12)	68.53(13)		2
O(9)-Sr(2)-O(7)	82.70(12)	1	2
O(9)-Sr(2)-O(4)	82.92(13)	1	2
O(7)-Sr(2)-O(4)	80.97(12)	2	2
O(9)-Sr(2)-O(2)	90.45(12)	1	
O(7)-Sr(2)-O(2)	167.83(12)	2	
O(4)-Sr(2)-O(2)	88.24(12)	2	
O(9)-Sr(2)-O(30)	149.67(17)	1	
O(7)-Sr(2)-O(30)	80.46(19)	2	
O(4)-Sr(2)-O(30)	69.67(15)	2	
O(2)-Sr(2)-O(30)	101.12(18)		
O(9)-Sr(2)-O(11)	78.34(13)	1	
O(7)-Sr(2)-O(11)	117.64(12)	2	
O(4)-Sr(2)-O(11)	151.18(13)	2	
O(2)-Sr(2)-O(11)	70.34(12)		
O(30)-Sr(2)-O(11)	131.93(16)		
O(9)-Sr(2)-O(7)	131.48(12)	1	
O(7)-Sr(2)-O(7)	77.05(12)	2	
O(4)-Sr(2)-O(7)	134.97(12)	2	
O(2)-Sr(2)-O(7)	114.85(11)		
O(30)-Sr(2)-O(7)	68.25(13)		
O(11)-Sr(2)-O(7)	73.19(12)		
O(9)-Sr(2)-O(8)	142.89(13)	1	
O(7)-Sr(2)-O(8)	122.49(11)	2	
O(4)-Sr(2)-O(8)	124.54(12)	2	
O(2)-Sr(2)-O(8)	68.50(11)		
O(30)-Sr(2)-O(8)	66.93(17)		
O(11)-Sr(2)-O(8)	66.08(12)		
O(7)-Sr(2)-O(8)	47.66(10)		
C(2)-C(1)-C(14)	122.1(5)		
C(2)-C(1)-H(1)	119.0		
C(14)-C(1)-H(1)	119.0		
C(3)-C(2)-C(1)	117.2(5)		
C(3)-C(2)-H(2)	121.4		
C(1)-C(2)-H(2)	121.4		
C(2)-C(3)-C(11)	121.0(5)		
C(2)-C(3)-C(4)	129.7(5)		

Table 8.55: Continued: Bond Angles [°] for SrFDC.

	Angle	Symm. op. atom 1	Symm. op. atom 3
C(11)-C(3)-C(4)	109.3(5)		
C(5)-C(4)-C(9)	119.8(5)		
C(5)-C(4)-C(3)	131.0(5)		
C(9)-C(4)-C(3)	109.1(5)		
C(4)-C(5)-C(6)	118.6(5)		
C(4)-C(5)-H(5)	120.7		
C(6)-C(5)-H(5)	120.7		
C(7)-C(6)-C(5)	121.6(5)		
C(7)-C(6)-H(6)	119.2		
C(5)-C(6)-H(6)	119.2		
C(6)-C(7)-C(8)	119.8(5)		
C(6)-C(7)-C(16)	119.7(5)		
C(8)-C(7)-C(16)	120.4(5)		
C(9)-C(8)-C(7)	118.6(5)		
C(9)-C(8)-H(8)	120.7		
C(7)-C(8)-H(8)	120.7		
C(8)-C(9)-C(4)	121.6(5)		
C(8)-C(9)-C(10)	131.1(5)		
C(4)-C(9)-C(10)	107.4(5)		
O(1)-C(10)-C(11)	126.0(5)		
O(1)-C(10)-C(9)	127.4(5)		
C(11)-C(10)-C(9)	106.6(4)		
C(12)-C(11)-C(3)	121.0(5)		
C(12)-C(11)-C(10)	131.4(5)		
C(3)-C(11)-C(10)	107.6(5)		
C(11)-C(12)-C(14)	118.8(5)		
C(11)-C(12)-H(12)	120.6		
C(14)-C(12)-H(12)	120.6		
C(12)-C(14)-C(1)	119.8(5)		
C(12)-C(14)-C(15)	120.5(5)		
C(1)-C(14)-C(15)	119.6(5)		
O(4)-C(15)-O(5)	123.8(5)		
O(4)-C(15)-C(14)	118.2(5)		
O(5)-C(15)-C(14)	118.0(5)		
O(3)-C(16)-O(2)	123.4(5)		
O(3)-C(16)-C(7)	118.2(5)		
O(2)-C(16)-C(7)	118.4(5)		
C(19)-C(18)-C(30)	119.9(5)		
C(19)-C(18)-C(31)	119.8(5)		
C(30)-C(18)-C(31)	120.3(5)		
C(20)-C(19)-C(18)	121.4(5)		
C(20)-C(19)-H(19)	119.3		
C(18)-C(19)-H(19)	119.3		
C(21)-C(20)-C(19)	117.8(5)		
C(21)-C(20)-H(20)	121.1		
C(19)-C(20)-H(20)	121.1		
C(20)-C(21)-C(29)	121.2(5)		
C(20)-C(21)-C(22)	130.4(5)		
C(29)-C(21)-C(22)	108.4(5)		
C(23)-C(22)-C(27)	120.4(5)		
C(23)-C(22)-C(21)	130.5(5)		
C(27)-C(22)-C(21)	109.1(5)		
C(22)-C(23)-C(24)	118.3(5)		
C(22)-C(23)-H(23)	120.8		
C(24)-C(23)-H(23)	120.8		
C(23)-C(24)-C(25)	121.7(5)		
C(23)-C(24)-H(24)	119.2		
C(25)-C(24)-H(24)	119.2		
C(26)-C(25)-C(24)	118.7(5)		

Table 8.56: Continued: Bond Angles [°] for SrFDC.

	Angle	Symm. op. atom 1	Symm. op. atom 3
C(26)-C(25)-C(32)	121.1(5)		
O(7)-C(31)-Sr(2)	60.3(3)		
C(18)-C(31)-Sr(2)	173.3(4)		
O(9)-C(32)-O(10)	123.2(6)		
O(9)-C(32)-C(25)	118.4(5)		
O(10)-C(32)-C(25)	118.3(6)		
O(10)-C(32)-Sr(2)	85.7(4)		1
C(25)-C(32)-Sr(2)	154.2(4)		1
C(16)-O(2)-Sr(1)	124.7(3)		
C(16)-O(2)-Sr(2)	126.1(3)		
Sr(1)-O(2)-Sr(2)	101.30(12)		
C(16)-O(3)-Sr(1)	164.3(4)		2
C(15)-O(4)-Sr(2)	134.9(3)		2
C(31)-O(7)-Sr(2)	151.6(4)		2
C(31)-O(7)-Sr(2)	95.8(3)		
Sr(2)-O(7)-Sr(2)	102.95(12)	2	
C(31)-O(8)-Sr(1)	134.8(4)		
C(31)-O(8)-Sr(2)	93.2(3)		
Sr(1)-O(8)-Sr(2)	96.78(12)		
C(32)-O(9)-Sr(2)	122.1(4)		1
Sr(2)-O(11)-Sr(1)	96.43(12)		
Sr(2)-O(11)-H(11A)	124(5)		
Sr(1)-O(11)-H(11A)	112(4)		
Sr(2)-O(11)-H(11B)	112(4)		
Sr(1)-O(11)-H(11B)	120(4)		
H(11A)-O(11)-H(11B)	95(3)		
Sr(1)-O(12)-Sr(1)	111.47(13)		2
Sr(1)-O(12)-H(12A)	104(4)		
Sr(1)-O(12)-H(12A)	113(4)	2	
Sr(1)-O(12)-H(12B)	102(4)		
Sr(1)-O(12)-H(12B)	129(4)	2	
H(12A)-O(12)-H(12B)	95(3)		
Sr(1)-O(13)-H(13A)	119(5)		
Sr(1)-O(13)-H(13B)	108(5)		
H(13A)-O(13)-H(13B)	99(4)		
Sr(1)-O(14)-H(14A)	121(4)		
Sr(1)-O(14)-H(14B)	139(4)		
H(14A)-O(14)-H(14B)	100(4)		
Sr(2)-O(30)-H(30A)	130(4)		
Sr(2)-O(30)-H(30B)	123(4)		
H(30A)-O(30)-H(30B)	106(4)		
H(1W)-O(1W)-H(2W)	100(4)		
H(3W)-O(2W)-H(4W)	99(4)		
C(24)-C(25)-C(32)	120.1(5)		
C(27)-C(26)-C(25)	119.6(5)		
C(27)-C(26)-H(26)	120.2		
C(25)-C(26)-H(26)	120.2		
C(26)-C(27)-C(22)	121.2(5)		
C(26)-C(27)-C(28)	130.5(5)		
C(22)-C(27)-C(28)	108.3(5)		
O(6)-C(28)-C(27)	127.5(5)		
O(6)-C(28)-C(29)	127.2(5)		
C(27)-C(28)-C(29)	105.3(4)		
C(30)-C(29)-C(21)	121.3(5)		
C(30)-C(29)-C(28)	129.8(5)		
C(21)-C(29)-C(28)	108.9(5)		
C(29)-C(30)-C(18)	118.2(5)		
C(29)-C(30)-H(30)	120.9		
C(18)-C(30)-H(30)	120.9		

Table 8.57: Continued: Bond Angles [°] for SrFDC.

	Angle	Symm. op. atom 1	Symm. op. atom 3
O(8)-C(31)-O(7)	122.7(5)		
O(8)-C(31)-C(18)	118.4(4)		
O(7)-C(31)-C(18)	118.9(5)		
O(8)-C(31)-Sr(2)	62.9(3)		

8.8 BaFDC structure details

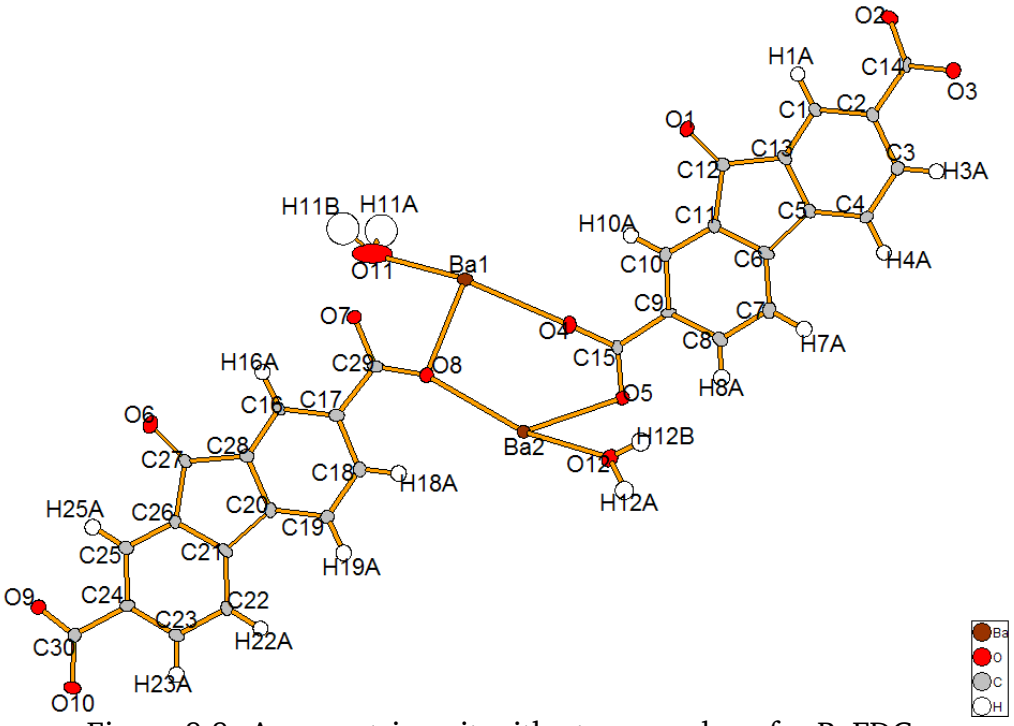

Figure 8.8: Asymmetric unit with atom numbers for BaFDC.

Table 8.58: Crystal data and structure refinement for BaFDC.

Parameter	Value
Empirical formula	$C_{15}H_8BaO_6$
Formula weight	421.55 g·mol^{-1}
Collection Temperature	100(2) K
Wavelength	0.77490Å
Crystal system	Triclinic
Space Group	P1
Unit cell dimensions	
a	6.7676(6) Å
b	7.2311(7) Å
c	14.1591(13) Å
α	82.763(2)°
β	84.102(2)°
γ	66.047(2)°
Volume	627.17(10)Å^3
Z	2
Calculated density	2.232 g/m^3
Absorption coefficient	3.994 mm^{-1}
F(000)	404
Crystal size	0.12×0.08×0.02 mm
Theta range for data collection	3.17° to 33.59°
Limiting indices	$-9 \leq h \leq 9$, $-10 \leq k \leq 10$,$0 \leq l \leq 20$
Reflections collected / unique	3737 / 3737 [R(int) = 0.0000]
Data Completeness	99.1%
Absorption correction	Semi-empirical from equivalents
Max. and min. transmission	0.9244 and 0.6457
Refinement method	Full-matrix least-squares on F^2
Data / restraints / parameters	3737 / 9 / 410
Goodness-of-fit on F^2	1.038
Final R indices [I>2sigma(I)]	R1 = 0.0258, wR2 = 0.0672
R indices (all data)	R1 = 0.0265, wR2 = 0.0676
Absolute Structure Parameter	0.143(19)
Largest diff. peak and hole	1.908 and -1.173 e·Å^{-3}

Table 8.59: Crystal coordinates [Å] and equivalent isotropic displacement parameters [Å^2] for BaFDC. U_{eq} is defined as one third of the trace of the orthogonalized U_{ij} tensor.

	x	y	z	U_{eq}
Ba(1)	-0.44487(4)	0.07349(4)	0.48041(2)	0.01216(10)
Ba(2)	-0.10026(3)	0.43896(3)	0.39963(2)	0.01129(10)
O(1)	-0.5169(8)	0.1401(7)	0.9451(4)	0.0159(8)
O(2)	-0.6843(8)	0.3213(9)	1.3228(4)	0.0164(9)
O(3)	-0.5113(8)	0.5070(8)	1.3557(4)	0.0143(8)
O(4)	-0.3654(9)	0.3670(9)	0.5651(4)	0.0142(11)
O(5)	-0.3644(12)	0.6748(11)	0.5374(5)	0.0152(13)
O(6)	-0.0202(8)	-0.3636(7)	-0.0542(4)	0.0169(9)
O(7)	-0.1613(13)	-0.1851(11)	0.3246(5)	0.0183(14)
O(8)	-0.1378(10)	0.1079(9)	0.3438(4)	0.0144(11)
O(9)	-0.0554(7)	-0.0692(7)	-0.4314(4)	0.0126(8)
O(10)	0.1329(8)	0.1247(8)	-0.4699(4)	0.0139(8)
C(1)	-0.5581(9)	0.3632(9)	1.1263(4)	0.0104(10)
H(1A)	-0.5864	0.2454	1.1463	0.012
C(2)	-0.5518(12)	0.4882(12)	1.1929(6)	0.0112(13)
C(3)	-0.5089(10)	0.6625(9)	1.1615(4)	0.0118(10)
H(3A)	-0.4985	0.7428	1.2074	0.014
C(4)	-0.4810(9)	0.7204(9)	1.0634(4)	0.0109(10)
H(4A)	-0.4572	0.8402	1.0427	0.013
C(5)	-0.4899(11)	0.5947(10)	0.9985(5)	0.0115(11)
C(6)	-0.4653(10)	0.6111(10)	0.8928(5)	0.0118(10)
C(7)	-0.4283(10)	0.7556(9)	0.8283(4)	0.0123(10)
H(7A)	-0.4183	0.8711	0.8491	0.015
C(8)	-0.4062(10)	0.7262(10)	0.7319(4)	0.0132(11)
H(8A)	-0.3778	0.8228	0.6869	0.016
C(9)	-0.4242(11)	0.5602(9)	0.6985(4)	0.0105(10)
C(10)	-0.4623(10)	0.4142(9)	0.7643(4)	0.0120(10)
H(10A)	-0.4739	0.2993	0.7436	0.014
C(11)	-0.4825(11)	0.4424(9)	0.8603(5)	0.0108(10)
C(12)	-0.5115(10)	0.3060(9)	0.9450(4)	0.0115(10)
C(13)	-0.5223(10)	0.4155(9)	1.0309(5)	0.0110(10)
C(14)	-0.5848(13)	0.4368(12)	1.2959(6)	0.0079(15)
C(15)	-0.3867(16)	0.5346(15)	0.5940(7)	0.0115(17)
C(16)	-0.0592(10)	-0.1337(9)	0.1242(4)	0.0113(10)
H(16A)	-0.0886	-0.2502	0.1461	0.014
C(17)	-0.0563(11)	-0.0013(10)	0.1884(5)	0.0123(11)
C(18)	-0.0085(10)	0.1685(9)	0.1542(4)	0.0127(10)
H(18A)	-0.0034	0.2545	0.1985	0.015
C(19)	0.0313(10)	0.2140(9)	0.0575(4)	0.0125(10)
H(19A)	0.0643	0.3286	0.0359	0.015
C(20)	0.0217(10)	0.0876(9)	-0.0066(5)	0.0107(10)
C(21)	0.0442(11)	0.0977(9)	-0.1123(5)	0.0116(10)
C(22)	0.0797(9)	0.2399(9)	-0.1800(4)	0.0109(10)
H(22A)	0.0975	0.3535	-0.1613	0.013
C(23)	0.0884(10)	0.2104(9)	-0.2767(4)	0.0126(10)
H(23A)	0.1181	0.3029	-0.3238	0.015
C(24)	0.0543(13)	0.0485(12)	-0.3049(6)	0.0110(14)
C(25)	0.0199(10)	-0.0948(10)	-0.2369(4)	0.0122(10)
H(25A)	-0.0021	-0.2066	-0.2554	0.015
C(26)	0.0187(12)	-0.0685(9)	-0.1420(5)	0.0110(11)
C(27)	-0.0113(10)	-0.1995(10)	-0.0556(4)	0.0121(10)
C(28)	-0.0177(10)	-0.0883(9)	0.0278(5)	0.0101(10)
C(29)	-0.1224(17)	-0.0266(16)	0.2925(7)	0.0126(18)
C(30)	0.0461(17)	0.0287(13)	-0.4104(7)	0.0144(18)
O(11)	-0.6402(14)	-0.0838(15)	0.3743(8)	0.052(3)
H(11A)	-0.777(10)	-0.06(2)	0.399(10)	0.063
H(11B)	-0.65(2)	-0.205(11)	0.368(11)	0.063
O(12)	0.1560(10)	0.5540(10)	0.5035(5)	0.0167(12)
H(12A)	0.228(14)	0.635(12)	0.489(6)	0.020
H(12B)	0.172(16)	0.563(15)	0.565(2)	0.020

Table 8.60: Anisotropic displacement parameters [Å^2] for BaFDC. The anisotropic displacement factor exponent takes the form $-2\pi^2[h^2a^{*2}U^{11} + ... + 2hka^*b^*U^{12}]$.

	U^{11}	U^{22}	U^{33}	U^{23}	U^{13}	U^{12}
Ba(1)	0.0116(2)	0.0126(2)	0.0121(2)	0.00142(17)	-0.00002(17)	-0.00554(18)
Ba(2)	0.0129(2)	0.0134(2)	0.0099(2)	-0.00139(16)	0.00025(16)	-0.00773(18)
O(1)	0.020(2)	0.011(2)	0.016(2)	-0.0034(16)	0.0010(17)	-0.0065(17)
O(2)	0.018(2)	0.026(3)	0.011(2)	-0.0007(19)	0.0007(17)	-0.015(2)
O(3)	0.015(2)	0.016(2)	0.014(2)	-0.0027(17)	-0.0017(16)	-0.0077(18)
O(4)	0.016(2)	0.013(3)	0.013(2)	-0.0034(19)	-0.0023(18)	-0.004(2)
O(5)	0.021(2)	0.012(2)	0.014(3)	-0.003(2)	0.004(2)	-0.008(2)
O(6)	0.020(2)	0.012(2)	0.019(2)	-0.0036(17)	-0.0012(17)	-0.0057(17)
O(7)	0.031(3)	0.018(3)	0.012(3)	-0.001(2)	0.000(2)	-0.017(3)
O(8)	0.016(2)	0.014(3)	0.015(3)	-0.005(2)	0.004(2)	-0.008(2)
O(9)	0.0139(19)	0.0095(19)	0.013(2)	0.0003(16)	-0.0021(16)	-0.0032(16)
O(10)	0.0143(19)	0.019(2)	0.011(2)	0.0025(18)	-0.0017(17)	-0.0105(18)
C(1)	0.010(2)	0.013(3)	0.009(2)	-0.0024(19)	0.0013(19)	-0.005(2)
C(2)	0.010(3)	0.013(3)	0.010(3)	-0.003(2)	0.001(2)	-0.005(2)
C(3)	0.012(2)	0.013(3)	0.013(3)	-0.003(2)	0.002(2)	-0.007(2)
C(4)	0.012(2)	0.009(2)	0.013(3)	-0.0012(19)	0.0013(19)	-0.006(2)
C(5)	0.011(3)	0.014(3)	0.010(3)	-0.003(2)	0.001(2)	-0.006(2)
C(6)	0.007(2)	0.019(3)	0.010(3)	0.000(2)	0.000(2)	-0.007(2)
C(7)	0.012(2)	0.011(2)	0.012(2)	-0.0018(19)	-0.005(2)	-0.002(2)
C(8)	0.015(2)	0.014(3)	0.010(2)	0.000(2)	0.000(2)	-0.005(2)
C(9)	0.012(3)	0.006(2)	0.011(3)	0.0043(19)	-0.001(2)	-0.003(2)
C(10)	0.014(2)	0.011(2)	0.012(2)	-0.004(2)	0.001(2)	-0.006(2)
C(11)	0.011(2)	0.010(3)	0.011(3)	-0.0025(19)	0.000(2)	-0.003(2)
C(12)	0.012(2)	0.013(2)	0.011(2)	0.000(2)	-0.0011(19)	-0.006(2)
C(13)	0.011(2)	0.014(3)	0.008(2)	-0.0007(19)	-0.001(2)	-0.004(2)
C(14)	0.007(3)	0.008(3)	0.009(3)	-0.004(2)	-0.003(2)	-0.002(2)
C(15)	0.014(3)	0.013(4)	0.010(3)	-0.005(3)	0.002(3)	-0.007(3)
C(16)	0.014(2)	0.014(3)	0.006(2)	-0.0014(19)	0.0001(19)	-0.006(2)
C(17)	0.011(3)	0.011(3)	0.013(3)	0.000(2)	0.002(2)	-0.004(2)
C(18)	0.015(2)	0.011(3)	0.012(3)	-0.003(2)	0.001(2)	-0.004(2)
C(19)	0.016(3)	0.013(3)	0.011(2)	-0.0011(19)	-0.001(2)	-0.008(2)
C(20)	0.008(2)	0.012(3)	0.013(3)	-0.006(2)	0.003(2)	-0.004(2)
C(21)	0.012(2)	0.015(3)	0.008(3)	-0.002(2)	0.003(2)	-0.005(2)
C(22)	0.011(2)	0.011(2)	0.010(2)	-0.0034(19)	0.0002(19)	-0.003(2)
C(23)	0.012(2)	0.013(3)	0.011(3)	0.001(2)	0.001(2)	-0.005(2)
C(24)	0.012(3)	0.011(3)	0.012(3)	0.001(2)	-0.001(2)	-0.006(2)
C(25)	0.013(2)	0.015(3)	0.011(3)	0.000(2)	-0.001(2)	-0.008(2)
C(26)	0.015(3)	0.010(3)	0.008(3)	-0.001(2)	-0.002(2)	-0.005(2)
C(27)	0.015(2)	0.017(3)	0.008(2)	-0.003(2)	0.0010(19)	-0.009(2)
C(28)	0.007(2)	0.010(3)	0.011(3)	-0.0004(19)	0.000(2)	-0.0014(19)
C(29)	0.015(4)	0.013(4)	0.010(3)	0.003(3)	-0.003(2)	-0.006(3)
C(30)	0.019(3)	0.009(4)	0.014(3)	-0.003(3)	0.003(3)	-0.005(3)
O(11)	0.026(4)	0.037(5)	0.072(7)	0.021(4)	0.017(4)	-0.003(3)
O(12)	0.012(3)	0.022(3)	0.021(3)	-0.005(2)	-0.001(2)	-0.012(2)

Table 8.61: Symmetry operations used in the following tables for BaFDC.

	Operation
#1	'x,y,z'

Table 8.62: Bond Lengths [Å] for BaFDC.

	Angle	Symm. op. atom 1	Symm. op. atom 3
Ba(1)-O(5)	2.737(7)	1	
Ba(1)-O(10)	2.755(5)	1	
Ba(1)-O(8)	2.756(6)		
Ba(1)-O(9)	2.778(5)	1	
Ba(1)-O(4)	2.817(6)		
Ba(1)-O(2)	2.863(5)	1	
Ba(1)-O(7)	3.050(7)		
Ba(1)-C(29)	3.221(11)		
Ba(1)-O(3)	3.282(5)	1	
Ba(1)-C(14)	3.374(9)	1	
Ba(1)-Ba(2)	4.1745(4)		
Ba(2)-O(7)	2.672(7)	1	
Ba(2)-O(8)	2.726(6)		
Ba(2)-O(2)	2.737(5)	1	
Ba(2)-O(3)	2.745(5)	1	
Ba(2)-O(5)	2.749(7)		
Ba(2)-O(10)	2.774(5)	1	
Ba(2)-O(12)	2.805(6)		
Ba(2)-O(4)	2.927(6)		
Ba(2)-C(15)	3.178(10)		
Ba(2)-Ba(1)	4.3277(5)	1	
Ba(2)-Ba(1)	4.4593(5)	1	
O(1)-C(12)	1.215(8)		
O(2)-C(14)	1.273(10)		
O(2)-Ba(2)	2.737(5)	1	
O(2)-Ba(1)	2.863(5)	1	
O(3)-C(14)	1.274(9)		
O(3)-Ba(2)	2.745(5)	1	
O(3)-Ba(1)	3.282(5)	1	
O(4)-C(15)	1.275(11)		
O(5)-C(15)	1.259(12)		
O(5)-Ba(1)	2.737(7)	1	
O(6)-C(27)	1.210(8)		
O(7)-C(29)	1.296(12)		
O(7)-Ba(2)	2.672(7)	1	
O(8)-C(29)	1.251(12)		
O(9)-C(30)	1.245(11)		
O(9)-Ba(1)	2.778(5)	1	
O(10)-C(30)	1.272(11)		
O(10)-Ba(1)	2.755(5)	1	
O(10)-Ba(2)	2.774(5)	1	
C(1)-C(13)	1.381(8)		
C(1)-C(2)	1.401(10)		
C(1)-H(1A)	0.9500		
C(2)-C(3)	1.414(10)		
C(2)-C(14)	1.476(12)		
C(3)-C(4)	1.415(8)		
C(3)-H(3A)	0.9500		
C(4)-C(5)	1.393(8)		
C(4)-H(4A)	0.9500		
C(5)-C(13)	1.413(9)		
C(5)-C(6)	1.484(9)		
C(6)-C(7)	1.383(8)		
C(6)-C(11)	1.408(9)		
C(7)-C(8)	1.391(8)		
C(7)-H(7A)	0.9500		
C(8)-C(9)	1.397(9)		
C(8)-H(8A)	0.9500		
C(9)-C(10)	1.405(9)		
C(9)-C(15)	1.498(12)		

Table 8.63: Continued: Bond Lengths [Å] for BaFDC.

	Angle	Symm. op. atom 1	Symm. op. atom 3
C(10)-C(11)	1.383(8)		
C(10)-H(10A)	0.9500		
C(11)-C(12)	1.504(9)		
C(12)-C(13)	1.513(9)		
C(14)-Ba(1)	3.374(9)	1	
C(16)-C(28)	1.391(8)		
C(16)-C(17)	1.407(9)		
C(16)-H(16A)	0.9500		
C(17)-C(18)	1.409(9)		
C(17)-C(29)	1.507(12)		
C(18)-C(19)	1.392(8)		
C(18)-H(18A)	0.9500		
C(19)-C(20)	1.392(8)		
C(19)-H(19A)	0.9500		
C(20)-C(28)	1.421(9)		
C(20)-C(21)	1.483(9)		
C(21)-C(22)	1.393(8)		
C(21)-C(26)	1.400(9)		
C(22)-C(23)	1.403(8)		
C(22)-H(22A)	0.9500		
C(23)-C(24)	1.393(10)		
C(23)-H(23A)	0.9500		
C(24)-C(25)	1.398(10)		
C(24)-C(30)	1.527(13)		
C(25)-C(26)	1.379(9)		
C(25)-H(25A)	0.9500		
C(26)-C(27)	1.499(10)		
C(27)-C(28)	1.498(9)		
O(11)-H(11A)	0.90(2)		
O(11)-H(11B)	0.91(2)		
O(12)-H(12A)	0.89(2)		
O(12)-H(12B)	0.90(2)		

Table 8.64: Bond Angles [°] for BaFDC.

	Angle	Symm. op. atom 1	Symm. op. atom 3
O(5)-Ba(1)-O(8)	111.2(2)	1	
O(10)-Ba(1)-O(8)	149.37(16)	1	
O(11)-Ba(1)-O(9)	135.9(2)		1
O(5)-Ba(1)-O(9)	76.03(19)	1	1
O(10)-Ba(1)-O(9)	137.60(14)	1	1
O(8)-Ba(1)-O(9)	73.03(16)		1
O(11)-Ba(1)-O(4)	159.0(2)		
O(5)-Ba(1)-O(4)	131.69(19)	1	
O(10)-Ba(1)-O(4)	107.69(17)	1	
O(8)-Ba(1)-O(4)	83.77(18)		
O(9)-Ba(1)-O(4)	64.70(15)	1	
O(11)-Ba(1)-O(2)	60.9(2)		1
O(5)-Ba(1)-O(2)	128.0(2)	1	1
O(10)-Ba(1)-O(2)	75.35(14)	1	1
O(8)-Ba(1)-O(2)	74.70(16)		1
O(9)-Ba(1)-O(2)	145.48(14)	1	1
O(4)-Ba(1)-O(2)	100.00(16)		1
O(11)-Ba(1)-O(7)	63.5(2)		
O(5)-Ba(1)-O(7)	71.55(18)	1	
O(10)-Ba(1)-O(7)	124.44(19)	1	
O(8)-Ba(1)-O(7)	45.03(19)		
O(9)-Ba(1)-O(7)	82.76(18)	1	
O(4)-Ba(1)-O(7)	126.38(19)		
O(2)-Ba(1)-O(7)	83.13(19)	1	
O(11)-Ba(1)-C(29)	77.7(3)		
O(5)-Ba(1)-C(29)	94.3(2)	1	
O(10)-Ba(1)-C(29)	136.7(2)	1	
O(8)-Ba(1)-C(29)	22.5(2)		
O(9)-Ba(1)-C(29)	81.8(2)	1	
O(4)-Ba(1)-C(29)	106.2(2)		
O(2)-Ba(1)-C(29)	72.9(2)	1	
O(7)-Ba(1)-C(29)	23.6(2)		
O(11)-Ba(1)-O(3)	101.8(2)		1
O(5)-Ba(1)-O(3)	164.73(16)	1	1
O(10)-Ba(1)-O(3)	101.62(13)	1	1
O(8)-Ba(1)-O(3)	58.28(16)		1
O(9)-Ba(1)-O(3)	108.51(13)	1	1
O(4)-Ba(1)-O(3)	61.30(14)		1
O(2)-Ba(1)-O(3)	41.71(13)	1	1
O(7)-Ba(1)-O(3)	94.27(16)		1
C(29)-Ba(1)-O(3)	72.4(2)		1
O(11)-Ba(1)-C(14)	80.0(2)		1
O(5)-Ba(1)-C(14)	144.5(2)	1	1
O(10)-Ba(1)-C(14)	93.32(17)	1	1
O(8)-Ba(1)-C(14)	59.2(2)		1
O(9)-Ba(1)-C(14)	124.72(18)	1	1
O(4)-Ba(1)-C(14)	83.18(18)		1
O(2)-Ba(1)-C(14)	21.62(16)	1	1
O(7)-Ba(1)-C(14)	82.3(2)		1
C(29)-Ba(1)-C(14)	64.8(2)		1
O(3)-Ba(1)-C(14)	22.01(15)	1	1
O(11)-Ba(1)-Ba(2)	130.8(2)		
O(5)-Ba(1)-Ba(2)	138.87(16)	1	
O(10)-Ba(1)-Ba(2)	137.80(11)	1	
O(8)-Ba(1)-Ba(2)	40.14(12)		
O(9)-Ba(1)-Ba(2)	67.71(10)	1	
O(4)-Ba(1)-Ba(2)	44.43(12)		
O(2)-Ba(1)-Ba(2)	79.78(10)	1	
O(7)-Ba(1)-Ba(2)	84.92(14)		
C(29)-Ba(1)-Ba(2)	62.54(18)		

Table 8.65: Continued: Bond Angles [°] for BaFDC.

	Angle	Symm. op. atom 1	Symm. op. atom 3
O(3)-Ba(1)-Ba(2)	41.05(8)	1	
C(14)-Ba(1)-Ba(2)	58.16(14)	1	
O(7)-Ba(2)-O(8)	137.0(2)	1	
O(7)-Ba(2)-O(2)	86.8(2)	1	1
O(8)-Ba(2)-O(2)	91.94(17)		1
O(7)-Ba(2)-O(3)	89.6(2)	1	1
O(8)-Ba(2)-O(3)	65.91(17)		1
O(2)-Ba(2)-O(3)	141.97(15)	1	1
O(7)-Ba(2)-O(5)	77.5(2)	1	
O(8)-Ba(2)-O(5)	124.76(19)		
O(2)-Ba(2)-O(5)	139.5(2)	1	
O(3)-Ba(2)-O(5)	75.75(19)	1	
O(7)-Ba(2)-O(10)	143.8(2)	1	1
O(8)-Ba(2)-O(10)	76.44(17)		1
O(2)-Ba(2)-O(10)	77.10(15)	1	1
O(3)-Ba(2)-O(10)	122.68(15)	1	1
O(5)-Ba(2)-O(10)	94.02(19)		1
O(7)-Ba(2)-O(12)	75.3(2)	1	
O(8)-Ba(2)-O(12)	142.56(19)		
O(2)-Ba(2)-O(12)	67.94(18)	1	
O(3)-Ba(2)-O(12)	146.61(16)	1	
O(5)-Ba(2)-O(12)	72.0(2)		
O(10)-Ba(2)-O(12)	68.62(18)	1	
O(7)-Ba(2)-O(4)	121.51(19)	1	
O(8)-Ba(2)-O(4)	82.24(16)		
O(2)-Ba(2)-O(4)	143.43(16)	1	
O(3)-Ba(2)-O(4)	67.02(16)	1	
O(5)-Ba(2)-O(4)	45.8(2)		
O(10)-Ba(2)-O(4)	66.41(15)	1	
O(12)-Ba(2)-O(4)	95.41(17)		
O(7)-Ba(2)-C(15)	100.5(2)	1	
O(8)-Ba(2)-C(15)	105.6(2)		
O(2)-Ba(2)-C(15)	143.1(2)	1	
O(3)-Ba(2)-C(15)	74.7(2)	1	
O(5)-Ba(2)-C(15)	23.1(2)		
O(10)-Ba(2)-C(15)	76.0(2)	1	
O(12)-Ba(2)-C(15)	79.0(2)		
O(4)-Ba(2)-C(15)	23.7(2)		
O(7)-Ba(2)-Ba(1)	140.57(17)	1	
O(8)-Ba(2)-Ba(1)	40.67(12)		
O(2)-Ba(2)-Ba(1)	127.43(12)	1	
O(3)-Ba(2)-Ba(1)	51.75(11)	1	
O(5)-Ba(2)-Ba(1)	84.42(15)		
O(10)-Ba(2)-Ba(1)	71.38(10)	1	
O(12)-Ba(2)-Ba(1)	131.29(13)		
O(4)-Ba(2)-Ba(1)	42.35(12)		
C(15)-Ba(2)-Ba(1)	65.21(17)		
O(7)-Ba(2)-Ba(1)	113.87(17)	1	1
O(8)-Ba(2)-Ba(1)	91.04(13)		1
O(2)-Ba(2)-Ba(1)	40.46(11)	1	1
O(3)-Ba(2)-Ba(1)	155.53(11)	1	1
O(5)-Ba(2)-Ba(1)	114.53(16)		1
O(10)-Ba(2)-Ba(1)	38.34(10)	1	1
O(12)-Ba(2)-Ba(1)	52.93(13)		1
O(4)-Ba(2)-Ba(1)	103.30(11)		1
C(15)-Ba(2)-Ba(1)	105.79(19)		1
Ba(1)-Ba(2)-Ba(1)	105.483(11)		1
O(7)-Ba(2)-Ba(1)	41.96(15)	1	1
O(8)-Ba(2)-Ba(1)	146.56(13)		1
O(2)-Ba(2)-Ba(1)	118.51(12)	1	1

Table 8.66: Continued: Bond Angles [°] for BaFDC.

	Angle	Symm. op. atom 1	Symm. op. atom 3
O(3)-Ba(2)-Ba(1)	80.98(10)	1	1
O(5)-Ba(2)-Ba(1)	35.53(15)		1
O(10)-Ba(2)-Ba(1)	121.26(12)	1	1
O(12)-Ba(2)-Ba(1)	67.83(13)		1
O(4)-Ba(2)-Ba(1)	80.59(12)		1
C(15)-Ba(2)-Ba(1)	58.63(18)		1
Ba(1)-Ba(2)-Ba(1)	113.720(10)		1
Ba(1)-Ba(2)-Ba(1)	120.758(9)	1	1
C(14)-O(2)-Ba(2)	126.3(5)		1
C(14)-O(2)-Ba(1)	102.4(5)		1
Ba(2)-O(2)-Ba(1)	101.19(16)	1	1
C(14)-O(3)-Ba(2)	133.3(5)		1
C(14)-O(3)-Ba(1)	83.1(5)		1
Ba(2)-O(3)-Ba(1)	87.20(13)	1	1
C(15)-O(4)-Ba(1)	162.3(6)		
C(15)-O(4)-Ba(2)	89.3(5)		
Ba(1)-O(4)-Ba(2)	93.22(17)		
C(15)-O(5)-Ba(1)	153.3(6)		1
C(15)-O(5)-Ba(2)	98.0(6)		
Ba(1)-O(5)-Ba(2)	108.8(2)	1	
C(29)-O(7)-Ba(2)	160.8(7)		1
C(29)-O(7)-Ba(1)	85.6(6)		
Ba(2)-O(7)-Ba(1)	102.2(2)	1	
C(29)-O(8)-Ba(2)	159.9(6)		
C(29)-O(8)-Ba(1)	100.1(6)		
Ba(2)-O(8)-Ba(1)	99.20(18)		
C(30)-O(9)-Ba(1)	128.7(5)		1
C(30)-O(10)-Ba(1)	133.7(6)		1
C(30)-O(10)-Ba(2)	123.1(6)		1
Ba(1)-O(10)-Ba(2)	103.01(15)	1	1
C(13)-C(1)-C(2)	118.3(6)		
C(13)-C(1)-H(1A)	120.9		
C(2)-C(1)-H(1A)	120.9		
C(1)-C(2)-C(3)	119.8(7)		
C(1)-C(2)-C(14)	120.4(7)		
C(3)-C(2)-C(14)	119.7(7)		
C(2)-C(3)-C(4)	121.7(6)		
C(2)-C(3)-H(3A)	119.1		
C(4)-C(3)-H(3A)	119.1		
C(5)-C(4)-C(3)	117.4(6)		
C(5)-C(4)-H(4A)	121.3		
C(3)-C(4)-H(4A)	121.3		
C(4)-C(5)-C(13)	120.4(6)		
C(4)-C(5)-C(6)	130.6(6)		
C(13)-C(5)-C(6)	109.0(5)		
C(7)-C(6)-C(11)	120.1(6)		
C(7)-C(6)-C(5)	131.2(6)		
C(11)-C(6)-C(5)	108.7(6)		
C(6)-C(7)-C(8)	117.9(6)		
C(6)-C(7)-H(7A)	121.1		
C(8)-C(7)-H(7A)	121.1		
C(7)-C(8)-C(9)	122.6(6)		
C(7)-C(8)-H(8A)	118.7		
C(9)-C(8)-H(8A)	118.7		
C(8)-C(9)-C(10)	119.2(6)		
C(8)-C(9)-C(15)	119.1(6)		
C(10)-C(9)-C(15)	121.5(7)		
C(11)-C(10)-C(9)	118.2(6)		
C(11)-C(10)-H(10A)	120.9		
C(9)-C(10)-H(10A)	120.9		

Table 8.67: Continued: Bond Angles [°] for BaFDC.

	Angle	Symm. op. atom 1	Symm. op. atom 3
C(10)-C(11)-C(6)	121.9(6)		
C(10)-C(11)-C(12)	129.1(6)		
C(6)-C(11)-C(12)	108.9(5)		
O(1)-C(12)-C(11)	127.7(6)		
O(1)-C(12)-C(13)	127.1(6)		
C(11)-C(12)-C(13)	105.1(5)		
C(1)-C(13)-C(5)	122.3(6)		
C(1)-C(13)-C(12)	129.6(6)		
C(5)-C(13)-C(12)	108.2(5)		
O(2)-C(14)-O(3)	121.6(8)		
O(2)-C(14)-C(2)	119.1(7)		
O(3)-C(14)-C(2)	119.4(7)		
O(2)-C(14)-Ba(1)	56.0(4)		1
O(3)-C(14)-Ba(1)	74.9(5)		1
C(2)-C(14)-Ba(1)	146.4(5)		1
O(5)-C(15)-O(4)	121.7(9)		
O(5)-C(15)-C(9)	119.0(8)		
O(4)-C(15)-C(9)	119.2(8)		
O(5)-C(15)-Ba(2)	58.9(5)		
O(4)-C(15)-Ba(2)	67.1(5)		
C(9)-C(15)-Ba(2)	154.7(6)		
C(28)-C(16)-C(17)	117.8(6)		
C(28)-C(16)-H(16A)	121.1		
C(17)-C(16)-H(16A)	121.1		
C(16)-C(17)-C(18)	119.9(6)		
C(16)-C(17)-C(29)	121.2(7)		
C(18)-C(17)-C(29)	118.7(7)		
C(19)-C(18)-C(17)	122.1(6)		
C(19)-C(18)-H(18A)	119.0		
C(17)-C(18)-H(18A)	119.0		
C(18)-C(19)-C(20)	118.4(6)		
C(18)-C(19)-H(19A)	120.8		
C(20)-C(19)-H(19A)	120.8		
C(19)-C(20)-C(28)	119.7(6)		
C(19)-C(20)-C(21)	132.1(6)		
C(28)-C(20)-C(21)	108.2(5)		
C(22)-C(21)-C(26)	119.6(6)		
C(22)-C(21)-C(20)	131.3(6)		
C(26)-C(21)-C(20)	109.1(5)		
C(21)-C(22)-C(23)	118.1(6)		
C(21)-C(22)-H(22A)	121.0		
C(23)-C(22)-H(22A)	121.0		
C(24)-C(23)-C(22)	121.4(6)		
C(24)-C(23)-H(23A)	119.3		
C(22)-C(23)-H(23A)	119.3		
C(23)-C(24)-C(25)	120.4(7)		
C(23)-C(24)-C(30)	120.6(7)		
C(25)-C(24)-C(30)	118.9(7)		
C(26)-C(25)-C(24)	117.8(6)		
C(26)-C(25)-H(25A)	121.1		
C(24)-C(25)-H(25A)	121.1		
C(25)-C(26)-C(21)	122.6(6)		
C(25)-C(26)-C(27)	128.6(6)		
C(21)-C(26)-C(27)	108.8(5)		
O(6)-C(27)-C(28)	127.6(6)		
O(6)-C(27)-C(26)	126.9(6)		
C(28)-C(27)-C(26)	105.4(5)		
C(16)-C(28)-C(20)	122.1(6)		
C(16)-C(28)-C(27)	129.5(6)		

Table 8.68: Continued: Bond Angles [°] for BaFDC.

	Angle	Symm. op. atom 1	Symm. op. atom 3
C(20)-C(28)-C(27)	108.4(5)		
O(8)-C(29)-O(7)	123.2(9)		
O(8)-C(29)-C(17)	118.0(8)		
O(7)-C(29)-C(17)	118.8(9)		
O(8)-C(29)-Ba(1)	57.4(5)		
O(7)-C(29)-Ba(1)	70.8(5)		
C(17)-C(29)-Ba(1)	155.5(6)		
O(9)-C(30)-O(10)	125.4(9)		
O(9)-C(30)-C(24)	117.7(8)		
O(10)-C(30)-C(24)	116.8(8)		
Ba(1)-O(11)-H(11A)	109(9)		
Ba(1)-O(11)-H(11B)	139(10)		
H(11A)-O(11)-H(11B)	82(4)		
Ba(2)-O(12)-H(12A)	134(6)		
Ba(2)-O(12)-H(12B)	138(5)		
H(12A)-O(12)-H(12B)	86(4)		
C(10)-C(11)-C(6)	121.9(6)		
C(10)-C(11)-C(12)	129.1(6)		
C(6)-C(11)-C(12)	108.9(5)		
O(1)-C(12)-C(11)	127.7(6)		
O(1)-C(12)-C(13)	127.1(6)		
C(11)-C(12)-C(13)	105.1(5)		
C(1)-C(13)-C(5)	122.3(6)		
C(1)-C(13)-C(12)	129.6(6)		
C(5)-C(13)-C(12)	108.2(5)		
O(2)-C(14)-O(3)	121.6(8)		

8.9 CdFDC structure details

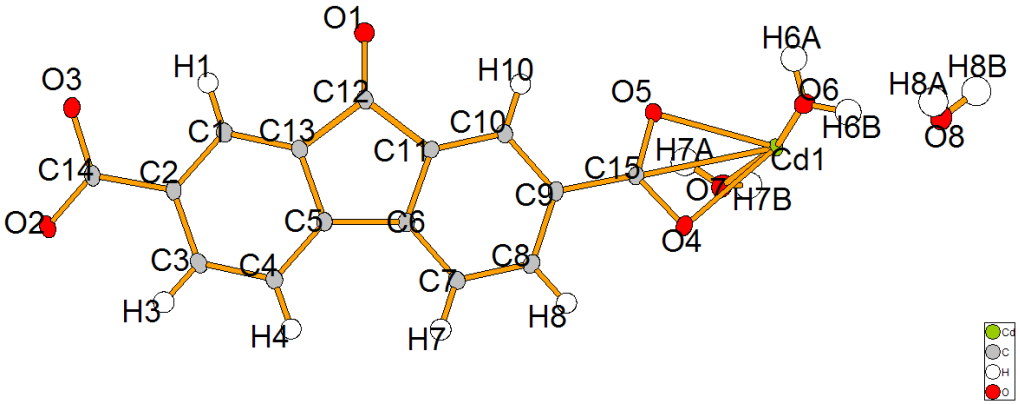

Figure 8.9: Asymmetric unit with atom numbers for CdFDC.

Table 8.69: Crystal data and structure refinement for CdFDC.

Parameter	Value
Empirical formula	$C_{15}H_12O_8Cd$
Formula weight	432.65 g·mol^{-1}
Collection Temperature	100(2) K
Wavelength	0.77490Å
Crystal system	Monoclinic
Space Group	$P2(1)/c$
Unit cell dimensions	
a	7.7123(2) Å
b	28.5057(8)Å
c	6.6459(2) Å
α	90°
β	105.050(2)°
γ	90°
Volume	1410.95(7)Å^3
Z	4
Calculated density	2.037 g/m^3
Absorption coefficient	1.982 mm^{-1}
F(000)	856
Crystal size	0.18×0.08×0.03 mm
Theta range for data collection	3.08° to 33.61°
Limiting indices	$-11 \leq h \leq 10$, $-39 \leq k \leq 40$,$-9 \leq l \leq 9$
Reflections collected / unique	20326 / 4304 [R(int) = 0.0523]
Data Completeness	99.7%
Absorption correction	Semi-empirical from equivalents
Max. and min. transmission	0.90 and 0.68
Refinement method	Full-matrix least-squares on F^2
Data / restraints / parameters	4304 / 15 / 235
Goodness-of-fit on F^2	1.045
Final R indices [I>2sigma(I)]	R1 = 0.0257, wR2 = 0.0676
R indices (all data)	R1 = 0.0288, wR2 = 0.0695
Extinction coefficient	0
Largest diff. peak and hole	0.594 and -0.486 e·Å^{-3}

Table 8.70: Crystal coordinates [Å] and equivalent isotropic displacement parameters [Å^2] for CdFDC. U_{eq} is defined as one third of the trace of the orthogonalized U_{ij} tensor.

	x	y	z	U_{eq}
Cd(1)	0.783610(16)	0.523252(4)	0.330768(19)	0.01055(5)
C(1)	0.4144(2)	0.18545(6)	0.3702(3)	0.0117(3)
H(1)	0.2871	0.1837	0.3295	0.014
C(2)	0.5192(2)	0.14461(6)	0.3966(3)	0.0116(3)
C(3)	0.7070(2)	0.14768(6)	0.4595(3)	0.0122(3)
H(3)	0.7765	0.1197	0.4770	0.015
C(4)	0.7940(2)	0.19101(6)	0.4970(3)	0.0119(3)
H(4)	0.9212	0.1928	0.5421	0.014
C(5)	0.6901(2)	0.23129(6)	0.4669(3)	0.0104(3)
C(6)	0.7429(2)	0.28140(6)	0.4818(3)	0.0107(3)
C(7)	0.9104(2)	0.30256(6)	0.5306(3)	0.0126(3)
H(7)	1.0169	0.2843	0.5681	0.015
C(8)	0.9189(2)	0.35164(6)	0.5234(3)	0.0119(3)
H(8)	1.0327	0.3667	0.5566	0.014
C(9)	0.7631(2)	0.37889(6)	0.4683(3)	0.0111(3)
C(10)	0.5935(2)	0.35724(6)	0.4205(3)	0.0117(3)
H(10)	0.4868	0.3755	0.3837	0.014
C(11)	0.5853(2)	0.30889(6)	0.4282(3)	0.0106(3)
C(12)	0.4259(2)	0.27692(6)	0.3771(3)	0.0119(3)
O(1)	0.26768(18)	0.28792(5)	0.3192(2)	0.0171(3)
C(13)	0.5016(2)	0.22843(6)	0.4049(3)	0.0108(3)
C(14)	0.4301(3)	0.09775(6)	0.3430(3)	0.0123(3)
O(2)	0.51881(19)	0.06241(5)	0.3188(2)	0.0163(3)
O(3)	0.25901(18)	0.09631(5)	0.3130(2)	0.0149(3)
C(15)	0.7735(2)	0.43118(6)	0.4434(3)	0.0106(3)
O(4)	0.92334(18)	0.45208(5)	0.4995(2)	0.0150(3)
O(5)	0.63122(18)	0.45317(4)	0.3552(2)	0.0135(2)
O(6)	0.72896(18)	0.54311(5)	0.6454(2)	0.0154(3)
H(6A)	0.6174(19)	0.5440(10)	0.633(4)	0.023
H(6B)	0.780(4)	0.5679(7)	0.700(4)	0.023
O(7)	0.8136(2)	0.48861(5)	0.0282(2)	0.0171(3)
H(7A)	0.729(3)	0.4705(8)	-0.029(4)	0.026
H(7B)	0.819(4)	0.5063(9)	-0.071(4)	0.026
O(8)	0.8619(2)	0.62203(5)	0.8435(2)	0.0195(3)
H(8A)	0.831(4)	0.6181(10)	0.956(3)	0.029
H(8B)	0.819(4)	0.6485(6)	0.798(4)	0.029

Table 8.71: Anisotropic displacement parameters [Å^2] for CdFDC. The anisotropic displacement factor exponent takes the form $-2\pi^2[h^2a^{*2}U^{11} + ... + 2hka^*b^*U^{12}]$.

	U^{11}	U^{22}	U^{33}	U^{23}	U^{13}	U^{12}
Cd(1)	0.01018(8)	0.00669(8)	0.01377(8)	0.00134(4)	0.00129(5)	0.00008(4)
C(1)	0.0122(8)	0.0089(7)	0.0130(8)	-0.0004(6)	0.0012(6)	-0.0002(6)
C(2)	0.0141(8)	0.0079(7)	0.0124(7)	-0.0006(6)	0.0025(6)	-0.0013(6)
C(3)	0.0138(8)	0.0090(7)	0.0128(7)	-0.0004(6)	0.0018(6)	0.0014(6)
C(4)	0.0121(8)	0.0095(7)	0.0134(8)	0.0000(6)	0.0020(6)	0.0000(6)
C(5)	0.0113(8)	0.0086(7)	0.0108(7)	0.0001(5)	0.0019(6)	-0.0008(6)
C(6)	0.0123(8)	0.0090(7)	0.0106(7)	0.0002(6)	0.0023(6)	-0.0003(6)
C(7)	0.0117(8)	0.0093(7)	0.0158(8)	-0.0001(6)	0.0015(6)	0.0007(6)
C(8)	0.0106(8)	0.0110(8)	0.0136(8)	-0.0009(6)	0.0024(6)	-0.0023(6)
C(9)	0.0125(8)	0.0086(7)	0.0116(7)	0.0000(6)	0.0024(6)	-0.0019(6)
C(10)	0.0121(8)	0.0090(7)	0.0141(8)	0.0001(6)	0.0036(6)	0.0001(6)
C(11)	0.0093(7)	0.0094(7)	0.0129(7)	-0.0008(6)	0.0025(6)	-0.0011(6)
C(12)	0.0125(8)	0.0089(7)	0.0140(8)	0.0001(6)	0.0030(6)	0.0000(6)
O(1)	0.0134(7)	0.0133(7)	0.0240(7)	0.0011(5)	0.0036(5)	0.0000(5)
C(13)	0.0113(8)	0.0086(7)	0.0119(7)	0.0000(5)	0.0021(6)	0.0004(6)
C(14)	0.0159(8)	0.0085(7)	0.0109(7)	0.0001(6)	0.0005(6)	-0.0008(6)
O(2)	0.0175(7)	0.0085(6)	0.0214(7)	-0.0029(5)	0.0022(5)	0.0004(5)
O(3)	0.0133(6)	0.0099(6)	0.0195(7)	-0.0020(5)	0.0007(5)	-0.0017(5)
C(15)	0.0119(8)	0.0089(7)	0.0108(7)	0.0009(6)	0.0027(6)	-0.0012(6)
O(4)	0.0121(6)	0.0101(6)	0.0212(7)	0.0012(5)	0.0011(5)	-0.0024(5)
O(5)	0.0118(6)	0.0088(6)	0.0193(6)	0.0030(5)	0.0029(5)	0.0004(4)
O(6)	0.0125(6)	0.0152(7)	0.0188(7)	-0.0020(5)	0.0042(5)	-0.0016(5)
O(7)	0.0176(7)	0.0162(6)	0.0175(7)	-0.0015(5)	0.0045(5)	-0.0034(5)
O(8)	0.0203(7)	0.0160(7)	0.0221(7)	-0.0003(5)	0.0054(6)	-0.0015(5)

Table 8.72: Symmetry operations used in the following tables for CdFDC.

	Operation
#1	'x,y,z'
#2	'-x,y+1/2,-z+1/2'
#3	'-x,-y,-z'
#4	'x,-y-1/2,z-1/2'

Table 8.73: Bond Lengths [Å] for CdFDC.

	Angle	Symm. op. atom 1	Symm. op. atom 3
Cd(1)-O(7)	2.3050(15)		
Cd(1)-O(6)	2.3080(14)		
Cd(1)-O(5)	2.3447(13)		
Cd(1)-O(4)	2.3561(14)	3	
Cd(1)-O(4)	2.4305(13)		
Cd(1)-O(2)	2.5437(14)	2	
Cd(1)-C(15)	2.7357(17)		
Cd(1)-C(14)	2.7516(18)	2	
C(1)-C(13)	1.388(2)		
C(1)-C(2)	1.402(2)		
C(1)-H(1)	0.9500		
C(2)-C(3)	1.402(2)		
C(2)-C(14)	1.502(2)		
C(3)-C(4)	1.397(2)		
C(3)-H(3)	0.9500		
C(4)-C(5)	1.385(2)		
C(4)-H(4)	0.9500		
C(5)-C(13)	1.407(2)		
C(5)-C(6)	1.481(2)		
C(6)-C(7)	1.386(2)		
C(6)-C(11)	1.412(2)		
C(7)-C(8)	1.402(2)		
C(7)-H(7)	0.9500		
C(8)-C(9)	1.397(2)		
C(8)-H(8)	0.9500		
C(9)-C(10)	1.406(2)		
C(9)-C(15)	1.504(2)		
C(10)-C(11)	1.381(2)		
C(10)-H(10)	0.9500		
C(11)-C(12)	1.496(2)		
C(12)-O(1)	1.221(2)		
C(12)-C(13)	1.493(2)		
C(14)-O(2)	1.251(2)		
C(14)-O(3)	1.283(2)		
C(14)-Cd(1)	2.7515(18)	2	
O(2)-Cd(1)	2.5436(14)	2	
O(3)-Cd(1)	2.2792(14)	2	
C(15)-O(4)	1.267(2)		
C(15)-O(5)	1.267(2)		
O(4)-Cd(1)	2.3561(13)	3	
O(6)-H(6A)	0.844(13)		
O(6)-H(6B)	0.845(13)		
O(7)-H(7A)	0.843(13)		
O(7)-H(7B)	0.839(13)		
O(8)-H(8A)	0.845(13)		
O(8)-H(8B)	0.848(13)		

Table 8.74: Bond Angles [°] for CdFDC.

	Angle	Symm. op. atom 1	Symm. op. atom 3
O(7)-Cd(1)-O(5)	82.02(5)		
O(6)-Cd(1)-O(5)	86.19(5)		
O(3)-Cd(1)-O(4)	86.79(5)	2	3
O(7)-Cd(1)-O(4)	104.15(5)		3
O(6)-Cd(1)-O(4)	82.59(5)		3
O(5)-Cd(1)-O(4)	131.06(5)		3
O(3)-Cd(1)-O(4)	162.65(5)	2	
O(7)-Cd(1)-O(4)	84.94(5)		
O(6)-Cd(1)-O(4)	87.15(5)		
O(5)-Cd(1)-O(4)	55.04(4)		
O(4)-Cd(1)-O(4)	76.88(5)	3	
O(3)-Cd(1)-O(2)	54.37(5)	2	2
O(7)-Cd(1)-O(2)	97.87(5)		2
O(6)-Cd(1)-O(2)	83.20(5)		2
O(5)-Cd(1)-O(2)	88.61(4)		2
O(4)-Cd(1)-O(2)	136.41(4)	3	2
O(4)-Cd(1)-O(2)	142.97(5)		2
O(3)-Cd(1)-C(15)	168.51(5)	2	
O(7)-Cd(1)-C(15)	81.03(5)		
O(6)-Cd(1)-C(15)	87.86(5)		
O(5)-Cd(1)-C(15)	27.54(5)		
O(4)-Cd(1)-C(15)	104.32(5)	3	
O(4)-Cd(1)-C(15)	27.59(5)		
O(2)-Cd(1)-C(15)	116.07(5)	2	
O(3)-Cd(1)-C(14)	27.56(5)	2	2
O(7)-Cd(1)-C(14)	98.60(5)		2
O(6)-Cd(1)-C(14)	87.74(5)		2
O(5)-Cd(1)-C(14)	115.48(5)		2
O(4)-Cd(1)-C(14)	111.48(5)	3	2
O(4)-Cd(1)-C(14)	169.53(5)		2
O(2)-Cd(1)-C(14)	26.97(5)	2	2
C(15)-Cd(1)-C(14)	143.00(5)		2
C(13)-C(1)-C(2)	118.30(16)		
C(13)-C(1)-H(1)	120.9		
C(2)-C(1)-H(1)	120.9		
C(1)-C(2)-C(3)	120.17(16)		
C(1)-C(2)-C(14)	119.71(16)		
C(3)-C(2)-C(14)	119.99(16)		
C(4)-C(3)-C(2)	121.31(16)		
C(4)-C(3)-H(3)	119.3		
C(2)-C(3)-H(3)	119.3		
C(5)-C(4)-C(3)	118.32(17)		
C(5)-C(4)-H(4)	120.8		
C(3)-C(4)-H(4)	120.8		
C(4)-C(5)-C(13)	120.62(16)		
C(4)-C(5)-C(6)	130.65(16)		
C(13)-C(5)-C(6)	108.69(15)		
C(7)-C(6)-C(11)	120.45(16)		
C(7)-C(6)-C(5)	131.17(16)		
C(11)-C(6)-C(5)	108.34(15)		
C(6)-C(7)-C(8)	118.36(16)		
C(6)-C(7)-H(7)	120.8		
C(8)-C(7)-H(7)	120.8		
C(9)-C(8)-C(7)	121.28(16)		
C(9)-C(8)-H(8)	119.4		
C(7)-C(8)-H(8)	119.4		
C(8)-C(9)-C(10)	120.09(16)		
C(8)-C(9)-C(15)	120.85(15)		
C(10)-C(9)-C(15)	118.90(16)		
C(11)-C(10)-C(9)	118.58(16)		

Table 8.75: Continued: Bond Angles [°] for CdFDC.

	Angle	Symm. op. atom 1	Symm. op. atom 3
C(11)-C(10)-H(10)	120.7		
C(9)-C(10)-H(10)	120.7		
C(10)-C(11)-C(6)	121.22(16)		
C(10)-C(11)-C(12)	129.94(16)		
C(6)-C(11)-C(12)	108.78(15)		
O(1)-C(12)-C(13)	127.09(17)		
O(1)-C(12)-C(11)	127.57(16)		
C(13)-C(12)-C(11)	105.31(15)		
C(1)-C(13)-C(5)	121.26(16)		
C(1)-C(13)-C(12)	129.80(16)		
C(5)-C(13)-C(12)	108.87(15)		
O(2)-C(14)-O(3)	121.94(17)		
O(2)-C(14)-C(2)	120.97(17)		
O(3)-C(14)-C(2)	116.99(16)		
O(2)-C(14)-Cd(1)	67.22(10)		2
O(3)-C(14)-Cd(1)	55.27(9)		2
C(2)-C(14)-Cd(1)	166.68(12)		2
C(14)-O(2)-Cd(1)	85.81(11)		2
C(14)-O(3)-Cd(1)	97.17(11)		2
O(4)-C(15)-O(5)	121.17(16)		
O(4)-C(15)-C(9)	120.28(16)		
O(5)-C(15)-C(9)	118.44(15)		
O(4)-C(15)-Cd(1)	62.67(9)		
O(5)-C(15)-Cd(1)	58.79(9)		
C(9)-C(15)-Cd(1)	170.71(12)		
C(15)-O(4)-Cd(1)	165.79(12)		3
C(15)-O(4)-Cd(1)	89.74(10)		
Cd(1)-O(4)-Cd(1)	103.12(5)	3	
C(15)-O(5)-Cd(1)	93.67(11)		
Cd(1)-O(6)-H(6A)	110.1(19)		
Cd(1)-O(6)-H(6B)	114.8(19)		
H(6A)-O(6)-H(6B)	112(3)		
Cd(1)-O(7)-H(7A)	114(2)		
Cd(1)-O(7)-H(7B)	118(2)		
H(7A)-O(7)-H(7B)	102(3)		
H(8A)-O(8)-H(8B)	105(3)		

8.10 MnFDC structure details

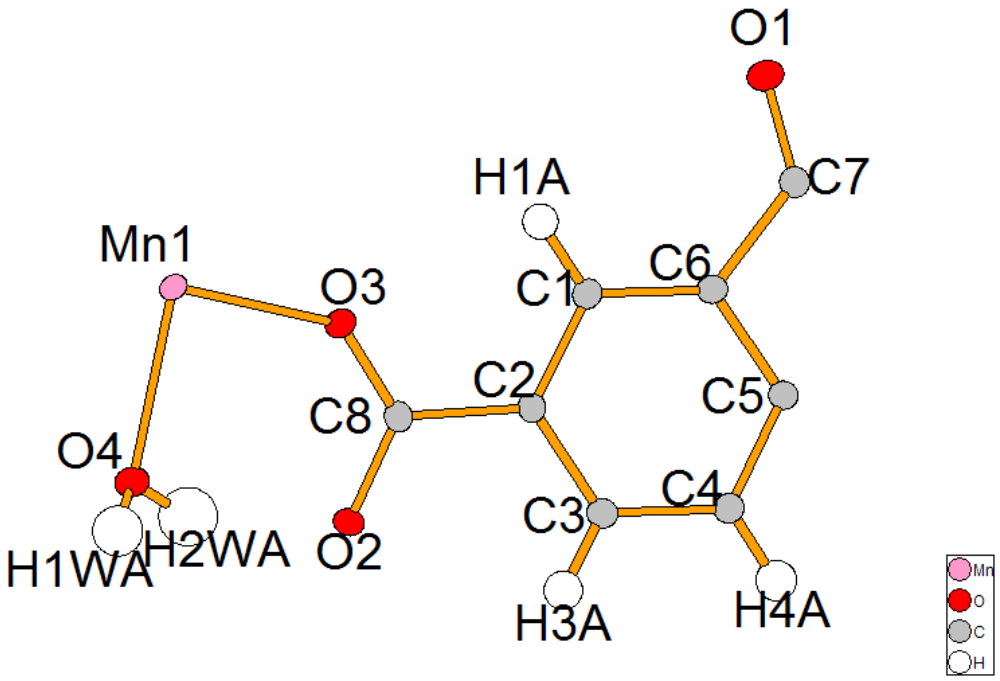

Figure 8.10: Asymmetric unit with atom numbers for MnFDC.

Table 8.76: Crystal data and structure refinement for MnFDC.

Parameter	Value
Empirical formula	$C_{15}H_{10}O_7Mn$
Formula weight	357.17 g·mol^{-1}
Collection Temperature	100(2) K
Wavelength	0.77490Å
Crystal system	Monoclinic
Space Group	$C2/c$
Unit cell dimensions	
a	26.943(2)Å
b	7.2476(6)Å
c	6.9261(5)Å
α	90°
β	97.703(2)°
γ	90°
Volume	1340.27Å^3
Z	4
Calculated density	1.770 g/m^3
Absorption coefficient	1.287 mm^{-1}
F(000)	724
Crystal size	0.11×0.03×0.01 mm
Theta range for data collection	3.95° to 33.60°
Limiting indices	$-38 \leq h \leq 38$, $0 \leq k \leq 10$,$0 \leq l \leq 9$
Reflections collected / unique	14469 / 2016 [R(int) = 0.0351]
Data Completeness	99.2%
Absorption correction	Semi-empirical from equivalents
Max. and min. transmission	0.93 and 0.84
Refinement method	Full-matrix least-squares on F^2
Data / restraints / parameters	2016 / 0 / 116
Goodness-of-fit on F^2	1.045
Final R indices [I>2sigma(I)]	R1 = 0.0258, wR2 = 0.0631
R indices (all data)	R1 = 0.0312, wR2 = 0.0660
Extinction coefficient	0
Largest diff. peak and hole	0.502 and -0.290e·Å^{-3}

Table 8.77: Crystal coordinates [Å] and equivalent isotropic displacement parameters [Å^2] for MnFDC. U_{eq} is defined as one third of the trace of the orthogonalized U_{ij} tensor.

	x	y	z	U_{eq}
Mn(1)	0.2500	0.7500	0.0000	0.01056(8)
O(1)	0.0000	0.8255(2)	0.2500	0.0243(4)
O(2)	0.21209(4)	0.33697(13)	0.21582(17)	0.01266(19)
O(3)	0.19208(4)	0.63223(14)	0.14824(16)	0.0142(2)
C(1)	0.09294(5)	0.57709(19)	0.2192(2)	0.0132(3)
H(1A)	0.1034	0.7017	0.2112	0.016
C(2)	0.12705(5)	0.43129(18)	0.2148(2)	0.0121(2)
C(3)	0.11108(5)	0.24814(19)	0.2289(2)	0.0158(3)
H(3A)	0.1348	0.1512	0.2301	0.019
C(4)	0.06095(5)	0.2049(2)	0.2411(3)	0.0171(3)
H(4A)	0.0503	0.0804	0.2476	0.021
C(5)	0.02732(5)	0.34959(19)	0.2433(2)	0.0137(3)
C(6)	0.04362(5)	0.53403(18)	0.2356(2)	0.0131(3)
C(7)	0.0000	0.6581(3)	0.2500	0.0145(4)
C(8)	0.18054(5)	0.47134(18)	0.1920(2)	0.0111(2)
O(4)	0.28846(4)	0.48028(14)	0.03761(19)	0.0150(2)
H(1WA)	0.2971(8)	0.413(3)	-0.048(4)	0.032(6)
H(2WA)	0.2719(9)	0.408(4)	0.104(4)	0.044(7)

Table 8.78: Anisotropic displacement parameters [Å^2] for MnFDC. The anisotropic displacement factor exponent takes the form $-2\pi^2[h^2a^{*2}U^{11} + ... + 2hka^*b^*U^{12}]$.

	U^{11}	U^{22}	U^{33}	U^{23}	U^{13}	U^{12}
Mn(1)	0.01050(12)	0.00762(12)	0.01372(13)	-0.00029(10)	0.00218(12)	-0.00109(10)
O(1)	0.0183(7)	0.0113(7)	0.0441(11)	0.000	0.0069(7)	0.000
O(2)	0.0116(4)	0.0101(4)	0.0162(5)	0.0012(4)	0.0020(4)	0.0017(3)
O(3)	0.0132(4)	0.0102(4)	0.0197(5)	0.0012(4)	0.0046(4)	-0.0009(4)
C(1)	0.0117(6)	0.0111(5)	0.0169(7)	0.0011(5)	0.0022(5)	-0.0008(5)
C(2)	0.0096(5)	0.0120(5)	0.0149(7)	0.0010(5)	0.0017(5)	-0.0002(5)
C(3)	0.0123(6)	0.0113(6)	0.0241(8)	0.0012(5)	0.0036(5)	0.0008(5)
C(4)	0.0121(6)	0.0112(5)	0.0284(8)	0.0018(5)	0.0039(5)	-0.0001(5)
C(5)	0.0116(6)	0.0114(6)	0.0185(7)	-0.0001(5)	0.0032(5)	0.0003(5)
C(6)	0.0121(6)	0.0101(6)	0.0172(7)	0.0006(5)	0.0022(5)	0.0005(5)
C(7)	0.0115(8)	0.0122(8)	0.0195(10)	0.000	0.0013(7)	0.000
C(8)	0.0101(5)	0.0122(6)	0.0110(6)	-0.0007(5)	0.0018(5)	-0.0002(4)
O(4)	0.0163(4)	0.0111(4)	0.0184(6)	0.0000(4)	0.0053(5)	0.0001(4)

Table 8.79: Symmetry operations used in the following tables for MnFDC.

	Operation
#1	'x,y,z'
#2	'-x,y,-z+1/2'
#3	'x+1/2,y+1/2,z'
#4	'-x+1/2,y+1/2,-z+1/2'
#5	'-x,-y,-z'
#6	'x,-y,z-1/2'
#7	'-x+1/2,-y+1/2,-z'
#8	'x+1/2,-y+1/2,z-1/2'

Table 8.80: Bond Lengths [Å] for MnFDC.

	Angle	Symm. op. atom 1	Symm. op. atom 3
Mn(1)-O(2)	2.1853(11)	4	
Mn(1)-O(3)	2.1557(10)		
Mn(1)-O(3)	2.1557(10)	7	
Mn(1)-O(4)	2.2114(10)		
Mn(1)-O(4)	2.2114(10)	7	
O(1)-C(7)	1.213(3)		
O(2)-Mn(1)	2.1853(11)	4	
O(2)-C(8)	1.2888(15)		
O(3)-C(8)	1.2544(16)		
C(1)-H(1A)	0.9500		
C(1)-C(2)	1.4034(18)		
C(1)-C(6)	1.3845(18)		
C(2)-C(3)	1.4028(18)		
C(2)-C(8)	1.4990(18)		
C(3)-H(3A)	0.9500		
C(3)-C(4)	1.3999(19)		
C(4)-H(4A)	0.9500		
C(4)-C(5)	1.387(2)		
C(5)-C(5)	1.487(3)	2	
C(5)-C(6)	1.4103(19)		
C(6)-C(7)	1.4938(18)		
C(7)-C(6)	1.4937(18)	2	
O(4)-H(1WA)	0.82(3)		
O(4)-H(2WA)	0.86(3)		

Table 8.81: Bond Angles [°] for MnFDC.

	Angle	Symm. op. atom 1	Symm. op. atom 3
O(2)-Mn(1)-O(3)	91.95(4)	4	7
O(2)-Mn(1)-O(4)	89.65(4)	6	7
O(2)-Mn(1)-O(4)	90.35(4)	4	7
O(2)-Mn(1)-O(4)	90.35(4)	6	
O(2)-Mn(1)-O(4)	89.65(4)	4	
O(3)-Mn(1)-O(3)	180.0		7
O(3)-Mn(1)-O(4)	87.22(4)		
O(3)-Mn(1)-O(4)	92.78(4)		7
O(3)-Mn(1)-O(4)	87.22(4)	7	7
O(3)-Mn(1)-O(4)	92.78(4)	7	
O(4)-Mn(1)-O(4)	180.00(5)		7
Mn(1)-O(2)-C(8)	123.64(9)	4	
Mn(1)-O(3)-C(8)	134.58(9)		
H(1A)-C(1)-C(2)	121.0		
H(1A)-C(1)-C(6)	121.0		
C(2)-C(1)-C(6)	118.07(12)		
C(1)-C(2)-C(3)	120.20(12)		
C(1)-C(2)-C(8)	119.87(12)		
C(3)-C(2)-C(8)	119.92(12)		
C(2)-C(3)-H(3A)	119.2		
C(2)-C(3)-C(4)	121.56(13)		
H(3A)-C(3)-C(4)	119.2		
C(3)-C(4)-H(4A)	121.0		
C(3)-C(4)-C(5)	117.93(13)		
H(4A)-C(4)-C(5)	121.0		
C(4)-C(5)-C(5)	130.85(8)		2
C(4)-C(5)-C(6)	120.59(13)		
C(5)-C(5)-C(6)	108.55(8)	2	
C(1)-C(6)-C(5)	121.60(13)		
C(1)-C(6)-C(7)	129.95(12)		
C(5)-C(6)-C(7)	108.45(12)		
O(1)-C(7)-C(6)	127.02(8)		
O(1)-C(7)-C(6)	127.02(8)		2
C(6)-C(7)-C(6)	105.96(16)		2
O(2)-C(8)-O(3)	123.55(12)		
O(2)-C(8)-C(2)	117.85(12)		
O(3)-C(8)-C(2)	118.59(12)		
Mn(1)-O(4)-H(1WA)	127.6(17)		
Mn(1)-O(4)-H(2WA)	109.5(17)		
H(1WA)-O(4)-H(2WA)	104(2)		

8.11 Additional Experimental Conditions

As with any work, there are far more experiments than those that are ultimately reported. The follow is a list of some of the additional experiments and experimental conditions used throughout this thesis.

Chapter 3 outlines experiments using nanoparticles of yttrium aluminum garnet. The experimental conditions listed in that chapter are those that were optimized through the conditions listed in Table 8.82. All of these were in the same reverse emulsion process described in the chapter. The columns list the sample number, solvent, surfactanct, the ratio of the solvent to the surfactant, reflux time and temperature, hydrolyzing base, calcination conditions, and results.

In addition to the nanoparticles above, some addition inorganic phosphors were prepared of a vanadate with the formula MVO_4. In these compounds the vanadate group as a sensitizer and transfers energy to the emitter ion, usually a small concentration of europium or terbium. In Table 8.83, these reactions are listed. Some are solvent/surfact emulsion reactions, while the others are classic ceramics bulk oxide preparations. The same emulsion technique was applied in hopes of making nanoparticles, but it was ultimate found that small particles of these were not accessible through this route.

The cerium oxalate formate compounds described in Chapter 4 were discovered in the course of looking for anhydrous, rare earth framework compounds. Quite a few others were identified along the way, and the experimental procedures followed are contained in Tables 8.84 through 8.91. The tables give a sample number, whether the heating was by microwave or convention methods, the metal source and amount, the ligand source and amount, solvent used, if there were any extra additions, the heating time and temperature, and the results.

Tables 8.92 and 8.93 list the experimental conditions used for the anthraquinone frameworks in Chapter 5, along with some additional metals of which single crystal samples were never attained.

Many experiments were carried out using the fluorenone dicarboxylic acid ligand. They are summarized in Tables 8.94 to 8.95. These were all carried out hydrothermally with conventional heating and the column heading are equivalent to those in the preceeding tables.

Table 8.82: Addition $Y_3Al_5O_12$ nanoparticle experiments

Sample	Compound	Solvent	Surfactant	Surf/Solv (mL)	Reflux T(C)	Reflux (h)	Base	Calcined (C)	Notes	Results
JF005	YAG	Cyclohex	Span80	1/40	90	0	none	1200 / 1h		
JF005a	YAG	Cyclohex	Span80	1/40	90	0	acetone	N/A	no precipitate	nothing
JF005b	YAG	Cyclohex	Span80	1/40	90	0	TEA-OH	1200 / 1		
JF008	YAG	Cyclohex	Span80	1/40	90	40	TEA-OH	1200 / 1	Center layer formed in centrifuge indicates JF010	
JF010	YAG	Cyclohex	Span80	1/40	90	2	TEA-OH	1300 / 1	Center Layer from JF008	Good spheres
JF012	YAG	Cyclohex	Span80	1/40	90	15	TEA-OH	1300 / 1		Not bad, some rods also formed
JF013	YAG	Cyclohex	Span80	1/40	90	72	TEA-OH	1300 / 1		looks like ripening/fusing
JF014	YAG		N/A		0	N/A		1600 / 6	Solid State Route	bulk processing
JF015	YAG	Cyclohex	Span80	2/40	90	48	TEA-OH	1300 / 4		fused on calcination
JF016	YAG	Cyclohex	Span80	2/40	90	48	TEA	1300 / 4		fused on calcination
JF017	YAG		0	90	48	TEA-OH		1300 / 4	Precipiation Route (no emulsion)	No morphology control
JF018	YAG	Cyclohex	Span80	2/40	90	48	TEA-OH	1300 / 4	Center Layer from JF015	Very good spheres 200
JF019	YAG	none	none	2/40					surfactant only, no emulsion	surfactant does not disperse
JF020	YAG	Cyclohex	Span80	3/40	90	48	TEA-OH	1350 / 2		spheres fused in calcine
JF024	YAG	Cyclohex	Span80	2/40	60	48	TEA-OH	1300 / 2	3 layers formed (Prec, disk, supernant)	from precipitate, poor morphology
JF025	YAG	Cyclohex	Span80	2/40	90	48	NH4OH	1300 / 2	precipitate only	larger spheres 300nm
JF029	YAG	Cyclohex	Span80	2/40	60	48	TEA-OH	1300 / 2	Center Disk from JF024. Ecru color	Good spheres
JF030	YAG	Cyclohex	Span80	2/40	60	48	TEA-OH	1300 / 2	Supernant from JF024	Good spheres
JF042	YAG	n-hexane	Span80	2/40	90	48	TEA-OH	1300/2		
JF043	YAG	n-hexane	Span80	2/40	90	48	TEA	1300/2		

Table 8.83: Vanadate phosphor experiments

Sample	Compound	Solvent	Surfactant	Surf/Solv (mL)	Reflux T(C)	Reflux (h)	Base	Calcined (C)	Results
JF044a	Y0.95Eu0.05VO4	Cyclohex	Span80	2/40	90	48	TEA-OH	600/2	
JF044b	Y0.95Eu0.05VO4	Cyclohex	Span80	2/40	90	48	TEA		
JF045	Y0.95Eu0.05VO4	Bulk Oxide						600/10, 850/10	
JF047	Y0.65Bi0.30Eu0.05VO4	Bulk Oxide						850/40	
JF048	Y0.70Bi0.25Eu0.05VO4	Bulk Oxide						650/4, 850/10	
JF049	Y0.95Eu0.05VO4	n-hexane	Span80	2/40	90	48	TEA-OH	1um spheres in SEM	
JF050	Y0.6Bi0.35Eu0.05VO4	Bulk Oxide							
JF051	Gd0.55Bi0.40Eu0.05VO4	Bulk Oxide							
JF052	Gd0.50Bi0.45Eu0.05VO4	Bulk Oxide							
JF053	Y0.65Bi0.30Eu0.05VO4	Cyclohex	Span80	1/20	90	48	TEA-OH		
JF054	Gd0.45Bi0.50Eu0.05VO4	Bulk Oxide							
JF055	Gd0.6Bi0.35Eu0.05VO4	Bulk Oxide							
JF057	Tb0.65Bi0.3VO4								

Table 8.84: Oxalate framework experiments

Sample Bomb	MW or Oven	Metal	amt	Ligand	amt	Solvent	amt	Extras	temp	time	results
117 - 25	Oven	$La(NO_3)_3$	0.5 mmol	Oxalic	0.5 mmol	H_2O	10 mL		4 days	150	powdery spheres, not crystalline
117 - 27	Oven	$La(NO_3)_3$	0.5 mmol	Oxalic	0.5 mmol	H_2O	10 mL		4 days	150	Final pH 4, small dendritic crystals
117 - 40	Oven	$La(NO_3)_3$	0.5 mmol	Oxalic	0.5 mmol	H_2O	10 mL		4 days	150	small dendritic crystals
119 - 38	Oven	$La(NO_3)_3$	5 mmol	Oxalic	10 mmol	H_2O	10 mL		3 days	150	little white balls
119 - 58	Oven	$La(NO_3)_3$	2.5 mmol	Oxalic	5 mmol	H_2O	10 mL		3 days	150	little white balls
119 - 71	Oven	$La(NO_3)_3$	0.5 mmol	Oxalic	1 mmol	H_2O	10 mL		3 days	150	tiny crystallites
120 - 25	Oven	$La(NO_3)_3$	2.5 mmol	Oxalic	5 mmol	H_2O	10 mL		5 days	180	tiny crystallites
120 - 27	Oven	$La(NO_3)_3$	2.5 mmol	Oxalic	5 mmol	H_2O	10 mL		5 days	200	tiny crystallites
120 - 38	Oven	$La(NO_3)_3$	2.5 mmol	Oxalic	5 mmol	H_2O	10 mL		5 days	180	tiny crystallites
120 - 40	Oven	$La(NO_3)_3$	2.5 mmol	Oxalic	5 mmol	H_2O	10 mL		5 days	180	tiny crystallites
120 - 58	Oven	$La(NO_3)_3$	2.5 mmol	Oxalic	5 mmol	H_2O	10 mL		5 days	180	biggest crystallites so far, still too small
120 - 71	Oven	$La(NO_3)_3$	2.5 mmol	Oxalic	5 mmol	H_2O	10 mL		5 days	150	tiny crystallites
121 - 1	MW	$La(NO_3)_3$	1.25 mmol	Oxalic	2.5 mmol	H_2O	5 mL	30 sec pre stir	30 min	180	tiny crystallites
121 - 2	MW	$La(NO_3)_3$	1.25 mmol	Oxalic	2.5 mmol	H_2O	5 mL	30 sec pre stir	1h	180	tiny crystallites
121 - 3	MW	$La(NO_3)_3$	1.25 mmol	Oxalic	2.5 mmol	H_2O	5 mL	30 sec pre stir	2h	180	tiny crystallites
122 - 1	MW	$La(NO_3)_3$	0.3 mmol	Oxalic	0.6 mmol	H_2O	5 mL	$EuNO_3$	30 min	180	
122 - 2	MW	$La(NO_3)_3$	0.3 mmol	Oxalic	0.6 mmol	H_2O	5 mL	$Ce(NO_3)_3$	30 min	180	
123 - 1	MW	$La(NO_3)_3$	0.25 mmol	Oxalic	0.5 mmol	H_2O	5 mL	1mL TEA	5 min	200	TEA floated on top
123 - 2	MW	$La(NO_3)_3$	0.25 mmol	Oxalic	0.5 mmol	H_2O	5 mL	1mL TEA	30 min	180	TEA floated on top
123 - 3	MW	$La(NO_3)_3$	0.25 mmol	Oxalic	0.5 mmol	H_2O	5 mL	no stir	200C, 1 min then 60C, 10 h		still small crystals
124 - 25	Oven	$La(NO_3)_3$	2.5 mmol	Oxalic	5 mmol	H_2O	10 mL		3 days	180	
124 - 27	Oven	$La(NO_3)_3$	2.5 mmol	Oxalic	5 mmol	H_2O	10 mL		3 days	200	biggest so far
124 - 38	Oven	$La(NO_3)_3$	0.5 mmol	Oxalic	1 mmol	H_2O	10 mL		3 days	180	
124 - 40	Oven	$La(NO_3)_3$	0.5 mmol	Oxalic	1 mmol	H_2O	10 mL		3 days	200	
126 - 58	Oven	$Y(NO_3)_3$	0.5 mmol	Oxalic	1 mmol	H_2O	10 mL			180	

Table 8.85: Oxalate framework experiments, continued

Sample Bomb	MW or Oven	Metal	amt	Ligand	amt	Solvent	amt	Extras	temp	time	results
126 - 71	Oven	$Y(NO_3)_3$	0.5 mmol	Oxalic	1 mmol	H_2O	10 mL	50mg $Ce(NO_3)_3$		180	
127 - 25	Oven	$La(NO_3)_3$	0.25 mmol	Oxalic	0.5 mmol	H_2O	10 mL			180	
128 - 27	Oven	$La(NO_3)_3$	2.5 mmol	Oxalic	5 mmol	H_2O	10 mL			200	
129 - 1	MW	$Y(NO_3)_3$	1 mmol	Oxalic	2.5 mmol	H_2O	5 mL		1 h	180	
129 - 2	MW	$Y(NO_3)_3$	0.5 mmol	Oxalic	1 mmol	H_2O	5 mL		1 h	180	
129 - 3	MW	$Y(NO_3)_3$	1 mmol	Oxalic	2.5 mmol	H_2O	5 mL	0.1 mmol $Ce(NO_3)_3$	1 h	180	
129 - 4	MW	$Y(NO_3)_3$	0.5 mmol	Oxalic	1 mmol	H_2O	5 mL	0.05 mmol $Ce(NO_3)_3$	1 h	180	
129 - 5	MW	$Y(NO_3)_3$	1 mmol	Ammonium Oxalate	2.5 mmol	H_2O	5 mL	0.1 mmol $Ce(NO_3)_3$	1 h	180	
129 - 6	MW	$Y(NO_3)_3$	0.5 mmol	Ammonium Oxalate	1 mmol	H_2O	5 mL	0.05 mmol $Ce(NO_3)_3$	1 h	180	
129 - 7	MW	$Y(NO_3)_3$	1 mmol	Oxamic	2.5 mmol	H_2O	5 mL	0.1 mmol $Ce(NO_3)_3$	1 h	180	
129 - 8	MW	$Y(NO_3)_3$	0.5 mmol	Oxamic	1 mmol	H_2O	5 mL	0.05 mmol $Ce(NO_3)_3$	1 h	180	
130 - 38	Oven	$La(NO_3)_3$	2.5 mmol	Oxalic	5 mmol	H_2O	10mL	2 mL 2M HNO_3	7 days	180	single crystals mixed with powder. Degraded in air.
136 - 25	Oven	$La(NO_3)_3$	0.5 mmol	Oxalic	1 mmol	H_2O	10mL	2 mL 2M HNO_3	3 days	180	No solid product
136 - 38	Oven	$La(NO_3)_3$	0.1 mmol	Oxalic	0.2 mmol	H_2O	10mL	2 mL 2M HNO_3	3 days	180	No solid product
136 - 58	Oven	$La(NO_3)_3$	0.5 mmol	Oxalic	1 mmol	H_2O	10mL	0.1 mmol $EuNO_3$, 2 mL 2M HNO_3	3 days	180	No solid product
136 - 71	Oven	$La(NO_3)_3$	0.5 mmol	Oxalic	1 mmol	H_2O	10mL	2 mL 2M HNO_3	3 days	200	No solid product
139 - 3	MW	$La(NO_3)_3$	0.5 mmol	Oxalic	1 mmol	H_2O	4 mL	1 mL 2M HNO_3	30 min	180	
139 - 4	MW	$La(NO_3)_3$	0.1 mmol	Oxalic	0.2 mmol	H_2O	4 mL	1 mL 2M HNO_3	30 min	180	
140 - 36	Oven	$La(NO_3)_3$	2.5 mmol	Oxalic	5 mmol	H_2O	10mL	2 mL 2M HNO_3	3 days	180	No solid product
140 - 38	Oven	$La(NO_3)_3$	0.25 mmol	Oxalic	0.5 mmol	H_2O	10mL	0.2 mL 2M HNO_3	3 days	180	No solid product
140 - 40	Oven	$La(NO_3)_3$	0.5 mmol	Oxalic	1 mmol	H_2O	10mL	0.2 mL 2M HNO_3	3 days	180	small crystallites
144 - 1	MW	$La(NO_3)_3$	0.25 mmol	Oxalic	0.5 mmol	H_2O	5 mL		1 h	100	
144 - 2	MW	$La(NO_3)_3$	0.25 mmol	Oxalic	0.5 mmol	H_2O	5 mL		1 h	125	
144 - 3	MW	$La(NO_3)_3$	0.25 mmol	Oxalic	0.5 mmol	H_2O	5 mL		1 h	150	

Table 8.86: Oxalate framework experiments, continued

Sample Bomb	MW or Oven	Metal	amt	Ligand	amt	Solvent	amt	Extras	temp	time	results
144 - 4	MW	$La(NO_3)_3$	0.25 mmol	Oxalic	0.5 mmol	H_2O	5 mL		1 h	180	
144 - 5	MW	$La(NO_3)_3$	0.25 mmol	Oxalic	0.5 mmol	H_2O	5 mL		1 h	200	
146 - 25	Oven	$La(NO_3)_3$	0.5 mmol	Oxalic	1 mmol	H_2O	10 mL	0.1 mL 3M Hcl	4 days	180	
146 - 38	Oven	$Y(NO_3)_3$	0.5 mmol	Oxalic	1 mmol	H_2O	10 mL	0.1 mL 3M Hcl	4 days	180	
146 - 40	Oven	$Ce(NO_3)_3$	0.5 mmol	Oxalic	1 mmol	H_2O	10 mL	0.1 mL 3M Hcl	4 days	180	
147 - 27	Oven	$La(NO_3)_3$	0.5 mmol	Oxalic	1 mmol	H_2O	10 mL		3 days	100	
147 - 58	Oven	$La(NO_3)_3$	0.5 mmol	Oxalic	1 mmol	H_2O	10 mL		3 days	125	
148 - 25	Oven	La-OX-5%Eu prec.	0.1g	Oxalic	0.1g	H_2O	10 mL		3 days	180	
148 - 38	Oven	La-OX-5%Eu prec.	0.1g	Oxalic	0.1g	H_2O	10 mL		3 days	150	
148 - 40	Oven	La-OX-5%Eu prec.	0.1g	Oxalic	0.1g	H_2O	10 mL		3 days	200	
155 - 27	Oven	Y-Ox-Prec.	0.15g	Oxalic	1 mmol	H_2O	10 mL	0.01g $Ce(NO_3)$	4 days	180	
155 - 58	Oven	$Y(NO_3)_3$	0.5 mmol	Oxalic	1 mmol	H_2O	10 mL	0.01g $Ce(NO_3)$	4 days	180	
157 - 25	Oven	$La(NO_3)_3$	0.5 mmol	Oxalic	1 mmol	H_2O	10 mL	100uL 3M HCl	4 days	180	
157 - 71	Oven	$La(NO_3)_3$	0.5 mmol	Oxalic	1 mmol	H_2O	10 mL	150uL 3M HCl	4 days	180	crystals of Lanthanum Nitrate Chloride
158 - 1	MW	La-ox-prec	0.1 g	Oxalic	0.1 g	H_2O	5 mL	0.02g $Ce(NO_3)_3$	1 h	200	
158 - 2	MW	La-ox-prec	0.1 g	Oxalic	0.1 g	H_2O	5 mL	0.02g $YbNO_3$	1 h	200	
158 - 3	MW	La-ox-prec	0.1 g	Oxalic	0.1 g	H_2O	5 mL	0.02g $ErNO_3$	1 h	200	
158 - 4	MW	La-ox-prec	0.1 g	Oxalic	0.1 g	H_2O	5 mL	0.01g $LuNO_3$	1 h	200	
158 - 5	MW	Y-Ox-prec	0.1 g	Oxalic	0.1 g	H_2O	5 mL	0.02g $Ce(NO_3)_3$	1 h	200	
158 - 6	MW	Y-Ox-prec	0.1 g	Oxalic	0.1 g	H_2O	5 mL	0.02g $YbNO_3$	1 h	200	
158 - 7	MW	Y-Ox-prec	0.1 g	Oxalic	0.1 g	H_2O	5 mL	0.02g $ErNO_3$	1 h	200	
158 - 8	MW	Y-Ox-prec	0.1 g	Oxalic	0.1 g	H_2O	5 mL	0.01g $LuNO_3$	1 h	200	
160 - 25	Oven	$La(NO_3)_3$	0.5 mmol	Oxalic	1 mmol	H_2O	10 mL	150uL 3M HCl	4 days	180	
160 - 27	Oven	$La(NO_3)_3$	0.5 mmol	Oxalic	1 mmol	H_2O	11 mL	150uL 3M HCl	4 days	200	
160 - 38	Oven	$Ce(NO_3)_3$	0.5 mmol	Oxalic	1 mmol	H_2O	10 mL	150uL 3M HCl	4 days	180	
160 - 40	Oven	$Y(NO_3)_3$	0.5 mmol	Oxalic	1 mmol	H_2O	10 mL	150uL 3M HCl	4 days	180	
160 - 58	Oven	$La(NO_3)_3$	0.5 mmol	Oxalic	1 mmol	H_2O	12 mL	0.025mmol $Ce(NO_3)_3$, 150uL 3M HCl	4 days	180	

Table 8.87: Oxalate framework experiments, continued

Sample Bomb	MW or Oven	Metal	amt	Ligand	amt	Solvent	amt	Extras	temp	time	results
160 - 71	Oven	$La(NO_3)_3$	0.5 mmol	Oxalic	1 mmol	H_2O	13 mL	0.025mmol $EuNO_3$	4 days	180	
163 - 25	Oven	$Ce(NO_3)_3$	0.5 mmol	Oxalic	1 mmol	H_2O	10 mL	200uL 3M HCl	4 days	200	pXRD→ CeO2
163 - 58	Oven	$Ce(NO_3)_3$	0.5 mmol	Oxalic	1 mmol	H_2O	10 mL	300uL 3M HCl	4 days	200	pXRD→ CeO2
163 - 71	Oven	$Ce(NO_3)_3$	0.5 mmol	Oxalic	1 mmol	H_2O	10 mL	400uL 3M HCl	4 days	200	pXRD→ CeO2
166 - 1	MW	La-OX Precursor	1mmol			H_2O	5mL		1h	19bar	crud
166 - 25	Oven	La-OX Precursor	1mmol			H_2O	5mL		2 days	200	crud
166 - 58	Oven	Y-Ox-prec	1mmol						2 days	200	crap
168 - 58	Oven	$La(NO_3)_3$	0.25mmol	Oxalic	0.5 mmol	H_2O	5mL		9 days	225	spherical particles and little triangles
171 - 25	Oven	$La(C_2O_4)_3$	0.5mmol	Oxalic	1 mmol	H_2O	10mL		2 days	180	microcrystalline
171 - 27	Oven	$La(C_2O_4)_3$	0.5mmol	Oxalic	1 mmol	H_2O	10mL		2 days	200	some rod shaped crystals, mostly junk
171 - 40	Oven	$La(OH)_3$	0.5mmol	Oxalic	2 mmol	H_2O	10mL		2 days	180	tiny crystals
171 - 58	Oven	$La(OH)_3$	0.5mmol	Oxalic	2 mmol	H_2O	10mL		2 days	200	larger crystals. Might run on xrd
171 - 71	Oven	$La(C_2O_4)_3$	0.5mmol	Oxalic	1 mmol	H_2O	10mL		2 days	225	poorly defined powders
172 - 1	MW	$La(C_2O_4)_3$	0.1mmol	Oxalic	0.5 mmol	H_2O	5mL		20min, 20min	180, 200	
172 - 2	MW	$LaCl_3$	0.1mmol	Oxalic	0.5 mmol	H_2O	5mL		20min, 20min	180, 200	
172 - 3	MW	$La(Ac)_3$	0.1mmol	Oxalic	0.5 mmol	H_2O	5mL		20min, 20min	180, 200	
172 - 4	MW	$La(OH)_3$	0.1mmol	Oxalic	0.5 mmol	H_2O	5mL		20min, 20min	180, 200	
172 - 5	MW	YCl_3	0.1mmol	Oxalic	0.5 mmol	H_2O	5mL		20min, 20min	180, 200	big crystals. Cooled to RT between steps.
173 - 40	Oven	$La(OH)_3$	0.1	Oxalic	0.4	H_2O	10mL		2 days	200	no
173 - 58	Oven	$La(OH)_3$	0.05	Oxalic	0.4	H_2O	10mL		2 days	200	big crystals
173 - 71	Oven	$La(OH)_3$	0.1	Oxalic	0.4	H_2O	10mL		2 days	225	no
174 - 3	MW	YCl_3	0.1mmol	Oxalic	0.5mmol	H_2O	5mL		20min, 20min	180, 200	same morphology as 172.5 but smaller
174 - 4	MW	YCl_3	0.1mmol	Oxalic	0.5mmol	H_2O	5mL		20 min	200	no product. Needs 2 step heat

Table 8.88: Oxalate framework experiments, continued

Sample Bomb	MW or Oven	Metal	amt	Ligand	amt	Solvent	amt	Extras	temp	time	results
174 - 5	MW	YCl_3	0.05mmol	Oxalic	0.25mmol	H_2O	5mL		1 h	200	no product
174 - 8	MW	YCl_3	0.09mmol	Oxalic	0.5mmol	H_2O	5mL	0.01mmol $CeCl_{33}$	1 h	200	
174 - 10	MW	YCl_3	0.1mmol	Oxalic	0.5mmol	H_2O	5mL		20min, 20min	180, 200	very small crystals
174 - 11	MW	YCl_3	0.1mmol	Oxalic	0.5mmol	H_2O	5mL		20min, 40min	180, 200	
174 - 12	MW	YCl_3	0.1mmol	Oxalic	0.5mmol	H_2O	5mL		20min, 20min	150, 200	big-ish crystals
174 - 13	MW	YCl_3	0.1mmol	Oxalic	0.5mmol	H_2O	5mL		20min, 20min	125, 200	not well formed
174 - 14	MW	YCl_3	0.1mmol	Oxalic	0.5mmol	H_2O	5mL		40min, 20min	180, 200	very small crystals
174 - 15	MW	YCl_3	0.1mmol	Oxalic	0.5mmol	H_2O	5mL		10, 10, 10	150, 180, 200	
174 - 16	MW	YCl_3	0.1mmol	Oxalic	0.5mmol	H_2O	5mL		20min, 1 min	180, 225	different morpholoy
174 - 17	MW	YCl_3	0.1mmol	Oxalic	0.5mmol	H_2O	5mL		20min, 20min	200, 180	very small crystals
174 - 18	MW	YCl_3	0.1mmol	Oxalic	0.5mmol	H_2O	5mL		20min, 40min	180, 200	eh
174 - K1	Oven	YCl_3	0.2mmol	Oxalic	1mmol	H_2O	10mL		2 days	200	brownish, dissolved in acetone
176 - 1	MW	YCl_3	0.09mmol	Oxalic	0.5mmol	H_2O	5mL	0.01mmol $CeCl_{33}$	20min, 20min	180, 200	cooled to RT between, no stir bar
176 - 2	MW	YCl_3	0.095mmol	Oxalic	0.5mmol	H_2O	5mL	0.005 mmol $CeCl_{33}$	20min, 20min	180, 200	cooled to RT between, no stir bar
176 - 3	MW	YCl_3	0.085mmol	Oxalic	0.5mmol	H_2O	5mL	0.015mmol $CeCl_{33}$	20min, 20min	180, 200	cooled to RT between, no stir bar
176 - 4	MW	YCl_3	0.09mmol	Oxalic	0.5mmol	H_2O	5mL	0.01mmol $EuNO_3$	20min, 20min	180, 200	cooled to RT between, no stir bar
176 - 5	MW	$GdCl_3$	0.1mmol	Oxalic	0.5mmol	H_2O	5mL		20min, 20min	180, 200	cooled to RT between, no stir bar
176 - 13	MW	$GdCl_3$	0.05mmol	Oxalic	0.25mmol	H_2O	5mL		2h	200	microcrystalline

Table 8.89: Oxalate framework experiments, continued

Sample Bomb	MW or Oven	Metal	amt	Ligand	amt	Solvent	amt	Extras	temp	time	results
176 - 17	MW	$GdCl_3$	0.1	Oxalic	0.5mmol	H_2O	5mL		2h	200	microcrystalline
176 - 25	Oven	$GdCl_3$	0.2	Oxalic	1mmol	H_2O	10mL		2 days	225	no solid product
176 - 40	Oven	$GdCl_3$	0.4	Oxalic	2mmol	H_2O	10mL		2 days	225	no solid product
176 - K1	Oven	$GdCl_3$	0.1	Oxalic	0.5mmol	H_2O	5mL		2 days	250	no solid product
177 - 25	Oven	$EuNO_3$	0.1	Oxalic	0.5	H_2O	10		200	2 days	microcrystalline, faint red from vuv lamp
177 - 27	Oven	$EuNO_3$	0.1	NH_3-Ox	0.5	H_2O	10		225	2 days	no product
177 - 38	Oven	$EuNO_3$	0.1	Oxalic	0.5	H_2O	10		225	2 days	no product
177 - 40	Oven	$GdCl_3$	0.2	Oxalic	1	H_2O	10mL		2 days	200	microcrystalline
177 - 58	Oven	$GdCl_3$	0.1	Oxalic	1	H_2O	10mL		2 days	200	tiny crystals, low yield
177 - 71	Oven	Eu_2O_3	0.1	Oxalic	0.2	H_2O	10		200	2 days	microcrystalline
177 - 73	Oven	Eu_2O_3	0.1	NH_3-Ox	0.2	H_2O	10		200	2 days	tan powder, red emission under both lamps
178 - 6	Oven	$LaCl_3$	0.2	Oxalic	1	H_2O	10mL	1mmol HBO3	2 days	200	no product
180 - 1	MW	$CeCl_{33}$	0.1	Oxalic	0.5	H_2O	10		1 h	200	big crystals, poor quality
180 - 58	Oven	$CeCl_{33}$	0.2	Oxalic	1	H_2O	10		2 days	180	large needle crystals
180 - 71	Oven	$CeCl_{33}$	0.2	Oxalic	1	H_2O	10		2 days	200	same morphology, lower yield
180 - 73	Oven	$CeCl_{33}$	0.2	Oxalic	1	H_2O	10		2 days	225	no product
182 - 25	Oven	$LaCl_3$	0.2	Oxalic	0.5	H_2O	10mL	0.5 mmol formic acid	2 days	200	no solid product
182 - 40	Oven	$GdCl_3$	0.2	Oxalic	0.5	H_2O	10mL	0.5 mmol formic acid	2 days	200	no solid product
182 - 58	Oven	$CeCl_{33}$	0.2	Oxalic	0.5	H_2O	10mL	0.5 mmol formic acid	2 days	200	Needle Crystals
182 - 71	Oven	YCl_3	0.2	Oxalic	0.5	H_2O	10mL	0.5 mmol formic acid	2 days	200	no solid product
188 - 58	Oven	YCl_3:10%$CeCl_3$	0.05	Oxalic	0.2	H_2O	10mL		2 days	200	no solid product
188 - 71	Oven	YCl_3:10%$CeCl_3$	1	Oxalic	4	H_2O	10mL		2 days	200	no solid product
188 - 73	Oven	YCl_3:10%$CeCl_3$	0.2	Oxalic	1	H_2O	10mL		2 days	225	no solid product
188 - 71a	Oven	YCl_3:10%$CeCl_3$	0.2	Oxalic	1	H_2O	10mL		2 days	200	crystals + powder
189 - 25	Oven	$EuCl_3$	0.05	Oxalic	0.4	H_2O	10		200	2 days	
189 - 27	Oven	$EuCl_3$	0.2	Oxalic	1	H_2O	10		200	2 days	big crystals, red emission under uv

Table 8.90: Oxalate framework experiments, continued

Sample Bomb	MW or Oven	Metal	amt	Ligand	amt	Solvent	amt	Extras	temp	time	results
189 - 27.1	Oven	$EuCl_3$	0.2	Oxalic	1	H_2O	10		200	2 days	same morphology as 27
189 - 40	Oven	EuF3	0.05	Oxalic	0.4	H_2O	10		200	2 days	
191 - 25	Oven	$GdCl_3$	1	Oxalic	5	H_2O	10mL		2 days	200	No products
191 - 40	Oven	$GdCl_3$	1	Oxalic	5	H_2O	10mL		2 days	225	No products
191 - 58	Oven	$GdCl_3$	1	Oxalic	5	H_2O	10mL		2 days	250	No products
192 - 6	both	YCl_3:10%$CeCl_3$	0.2	Oxalic	1	H_2O	5mL		30 min, 1 day	150(MW), 250(Oven)	No Products
192 - K1	both	YCl_3:10%$CeCl_3$	0.2	Oxalic	1	H_2O	5mL		30 min, 1 day	150(MW), 225(Oven)	No Products
193 - 1	MW	YCl_3	0.18	Oxalic	1	H_2O	10mL	0.02 $HoCl_3$	30, 30	180, 200	same as 172
193 - 6	Oven	$EuCl_3$	0.2	Oxalic	1	H_2O	10		250	2 days	no products
193 - 25	Oven	YCl_3	0.18	Oxalic	1	H_2O	10mL	0.02 $HoCl_3$	2 days	200	no products
193 - 27	Oven	YCl_3	0.1	Oxalic	1	H_2O	10mL	0.1 $HoCl_3$	2 days	200	microcrystalline
193 - 40	Oven	YCl_3	0.196	Oxalic	1	H_2O	10mL	0.004 $CeCl_{33}$	2 days	200	
193 - 58	Oven	YCl_3	0.19	Oxalic	1	H_2O	10mL	0.01 $CeCl_{32}$	2 days	200	
193 - 73	Oven	$La(OH)_3$	0.1	Oxalic	1	H_2O	10mL		2 days	200	
193 - K1	Oven	$EuCl_3$	0.2	Oxalic	1	H_2O	10		225	2 days	no products
195 - 1	MW	YCl_3	0.2	Oxalic	1	H_2O	10mL		30, 30	150, 200	
195 - 2	MW	YCl_3:10%$CeCl_3$	0.2	Oxalic	1	H_2O	10mL				
196 - 27	Oven	$La(OH)_3$	0.15	Oxalic	1	H_2O	10mL		3 days	200	nice crystals.
196 - 40	Oil Bath	$La(OH)_3$	0.15	Oxalic	1	H_2O	10mL	Stirred in bath	3 days	200	small crystals
197 - 6	Oven	$La(OH)_3$	0.1	$f_4$terephthalic	0.1	DMF	5mL		3 days	125	powders
197 - 25	Oven	$CeCl_{33}$	0.1	Oxalic (anhyd)	0.5	D2O	5mL		3 days	180	
197 - 58	Oven	$EuCl_3$	0.1	Oxalic (anhyd)	0.5	D2O	5		200	3 days	No Products
197 - 71	Oven	$EuCl_3$	1	Oxalic	5	H_2O	5		225	3 days	no producs
197 - 73	Oven	$GdCl_3$	1	Oxalic	5	H_2O	5mL		3 days	225	
197 - A	Oven	$EuCl_3$	1	Oxalic	5	H_2O	50		200	3 days	two morphologies, needles and blocks
197 - K1	Oven	172.3 + oxalic				H_2O	10mL		3 days	250	
199 - 25	Oven	$GdCl_3$	0.1	Oxalic	0.5	H_2O	5mL	0.5mL 5M KOH	2 days	225	whitish but not solid
199 - 27	Oven	$GdCl_3$	0.1	Oxalic	0.5	H_2O	5mL	10 drops 5M KOH	2 days	225	plate-like crystals

Table 8.91: Oxalate framework experiments, continued

Sample Bomb	MW or Oven	Metal	amt	Ligand	amt	Solvent	amt	Extras	temp	time	results
199 - 40	Oven	$GdCl_3$	0.1	Oxalic	0.5	H_2O	5mL	12 drops 5M KOH	2 days	225	powder
199 - A	Oven	$GdCl_3$	1	Oxalic	5	H_2O	50mL	1.6mL 5M KOH	2 days	225	plate-like crystals, too thin to run
200 - 58	Oven	$La(OH)_3/Ce(OH)_3$	0.147/0.003	Oxalic	1	H_2O	10mL		3 days	200	crystals, no luminescence
200 - 71	Oven	$La(OH)_3/Ce(OH)_3$	0.1425/0.0075	Oxalic	1	H_2O	10mL		3 days	200	crystals, no luminescence
200 - 73	Oven	$La(OH)_3/Ce(OH)_3$	0.0135/0.015	Oxalic	1	H_2O	10mL		3 days	200	crystals, no luminescence
201 - 6	Oven	Eu_2O_3	0.2	Oxalic	1	H_2O	10mL		200	3 days	powder, red emission
203 - 25	Oven	$GdCl_3$	0.1	Oxalic	0.5	H_2O	5mL	200uL 5M KOH	2 days	250	microcrystalline powder
203 - 27	Oven	$GdCl_3$	0.1	Oxalic	0.5	H_2O	5mL	250uL 5M KOH	2 days	250	microcrystalline powder
203 - 40	Oven	$GdCl_3$	0.1	Oxalic	0.5	H_2O	5mL	225uL 5M KOH	2 days	250	microcrystalline powder
204 - 58	Oven	$EuCl_3$	0.1	Oxalic	0.5	H_2O	5mL	100uL 5M KOH	225	3 days	twinned crystals
204 - 71	Oven	$EuCl_3$	0.1	Oxalic	0.5	H_2O	5mL	150uL 5M KOH	225	3 days	bad crystals
204 - 73	Oven	$EuCl_3$	0.1	Oxalic	0.5	H_2O	5mL	200uL 5M KOH	225	3 days	powder
205 - 25	Oven	$GdCl_3$	0.1	Oxalic	0.5	H_2O	5mL	100uL 5M KOH	2 days	250	powder
205 - 27	Oven	$GdCl_3$	0.1	Oxalic	0.5	H_2O	5mL	150uL 5M KOH	2 days	250	powder
205 - 40	Oven	$GdCl_3$	0.1	Oxalic	0.5	H_2O	5mL	175uL 5M KOH	2 days	250	powder

Table 8.92: Anthraquinone framework experiments

Sample Bomb	MW or Oven	Metal	amt	Ligand	amt	Solvent	amt	Extras	temp	time	results
T1 - 37	$Zn(Ac)_2$	0.02	AQDC	0.02	Water	5mL		90	1 day	small crystals	
T1 - 39	$Zn(Ac)_2$	0.02	AQDC	0.02	Water	5mL		100	1 day	polyxtalline	
T1 - 50	$Zn(Ac)_2$	0.02	AQDC	0.02	Water	5mL		125	1 day	polyxtalline	
T1 - 52	$Zn(Ac)_2$	0.02	AQDC	0.02	Water	5mL		150	1 day	polyxtalline	
T1 - 53	$Zn(Ac)_2$	0.02	AQDC	0.02	Water	5mL		180	1 day	polyxtalline	
T1 - 54	$Sr(Ac)_2$	0.02	AQDC	0.02	Water	5mL		100	1 day	polyxtalline	
T1 - 59	$Sr(Ac)_2$	0.02	AQDC	0.02	Water	5mL		125	1 day	polyxtalline	
T1 - 60	$Sr(Ac)_2$	0.02	AQDC	0.02	Water	5mL		150	1 day	polyxtalline	
T4 - 37	$Zn(Ac)_2$	0.02	AQDC	0.02	Water	5mL		90	1 day	small crystals	
T4 - 39	$Mn(Ac)_2$	0.02	AQDC	0.02	Water	5mL		90	1 day	small crystals	
T4 - 50	$Co(Ac)_2$	0.02	AQDC	0.02	Water	5mL		90	1 day	tiny crystals	
T4 - 52	$Cu(Ac)_2$	0.02	AQDC	0.02	Water	5mL		90	1 day	polyxtalline	
T4 - 53	$Ni(Ac)_2$	0.02	AQDC	0.02	Water	5mL		90	1 day	small crystals	
T4 - 54	$Zn(Ac)_2$	0.02	AQDC	0.02	Water	5mL	0.1 4-4' bipy	90	1 day	polyxtalline	
T4 - 59	$Zn(Ac)_2$	0.02	AQDC	0.02	Water	5mL	0.1 mmol bipyridal ethane	90	1 day	polyxtalline	
T5 - 37	YCl_3	0.02	AQDC	0.02	Water	5mL		90	1 day	polyxtalline	
T5 - 39	$La(Ac)_3$	0.02	AQDC	0.02	Water	5mL		90	1 day	polyxtalline	
T5 - 50	CuS_2	0.02	AQDC	0.02	Water	5mL		90	1 day	polyxtalline	
T5 - 52	$CuCl_2$	0.02	AQDC	0.02	Water	5mL		90	1 day	polyxtalline	
T5 - 53	$ZnCl_2$	0.02	AQDC	0.02	Water	5mL		90	1 day	multiphase	

Table 8.93: Anthraquinone framework experiments, continued

Sample Bomb	MW or Oven	Metal	amt	Ligand	amt	Solvent	amt	Extras	temp	time	results
T5 - 54	$Zn(NO_3)_2$	0.02	AQDC	0.02	Water	5mL		90	1 day	multiphase	
T5 - 59	$Ca(Ac)_2$	0.02	AQDC	0.02	Water	5mL		90	1 day	crystals	
T5 - 60	$Ba(Ac)_2$	0.02	AQDC	0.02	Water	5mL		90	1 day	crystals	
T19 - 1	$Ba(Ac)_2$	0.02	AQDC	0.02	Water	5mL		60	1 day	polyxtalline	
T19 - 2	$Ba(Ac)_2$	0.02	AQDC	0.02	Water	5mL	1 drop KOH	60	1 day	no xtal	
T19 - 3	$Ba(Ac)_2$	0.02	AQDC	0.02	Water	5mL	1 drop KOH	90	1 day	polyxtalline	
T19 - 4	$Ba(Ac)_2$	0.02	AQDC	0.02	Water	5mL	3 drop KOH	60	1 day	polyxtalline	
T19 - 5	$Ba(Ac)_2$	0.02	AQDC	0.02	Water	5mL	2 drop KOH	90	1 day	polyxtalline	
T19 - 6	$Ba(Ac)_2$	0.02	AQDC	0.02	Water	5mL	4 drop KOH	90	1 day	polyxtalline	
T22 - 1	$Ba(Ac)_2$	0.02	AQDC	0.02	Water	4mL	1 mL DMF	90	1 day	polyxtalline	
T22 - 2	$Ba(Ac)_2$	0.02	AQDC	0.02	Water	4mL	1 mL MeOH	90	1 day	polyxtalline	
T22 - 3	$Ba(Ac)_2$	0.02	AQDC	0.02	Water	4mL	1 mL EtOH	90 1 day	polyxtalline		
T22 - 4	$Ba(Ac)_2$	0.02	AQDC	0.02	Water	4mL	1 mL Ethylene Glycol	90 1 day	polyxtalline		
T22 - 5	$Ba(Ac)_2$	0.02	AQDC	0.02	DMF	5mL		90 1 day	polyxtalline		
T22 - 6	$Ba(Ac)_2$	0.02	AQDC	0.02	Water	5mL		100 1 day	polyxtalline		
393 - 35	$Fe(NO_3)_3$	0.02	AQDC	0.02	Water	5mL		100	1 day	polyxtalline	
393 - 37	$FeCl_2$	0.02	AQDC	0.02	Water	5mL	0.01 K acetate	100	1 day	polyxtalline	
393 - 39	$Al(NO_3)_3$	0.01	AQDC	0.02	Water	5mL		100	1 day	polyxtalline	
393 - 52	$Al(NO_3)_3$	0.02	AQDC	0.02	Water	5mL		100	1 day	polyxtalline	

Table 8.94: Fluorenone framework experiments. All values in mmol unless otherwise noted. 1 drop is approximately 0.08 mL.

Sample Bomb	Metal	amt	Ligand	amt	Solvent	amt	Extras	temp	time	results
263 - 22	$Y(Ac)_3$	0.2	FDC	0.2	H_2O	5 mL		100	2 days	polyxtalline
263 - 24	$Y(Ac)_3$	0.2	FDC	0.2	H_2O	5 mL		125	2 days	polyxtalline
263 - 28	$Y(Ac)_3$	0.2	FDC	0.2	H_2O	5 mL		180	2 days	polyxtalline
263 - 34	$Y(Ac)_3$	0.2	FDC	0.2	H_2O	5 mL		200	2 days	polyxtalline
263 - 35	$Mn(Ac)_2$	0.2	FDC	0.2	H_2O	5 mL		180	2 days	polyxtalline
263 - 39	$Tb(Ac)_3$	0.2	FDC	0.2	H_2O	5 mL		180	2 days	polyxtalline
263 - 53	$Ce(Ac)_3$	0.2	FDC	0.2	H_2O	5 mL		180	2 days	polyxtalline
263 - 54	$Eu(Ac)_3$	0.2	FDC	0.2	H_2O	5 mL		180	2 days	polyxtalline
264 - 22	$LaCl_3$	0.3	FDC	0.2	H_2O	10 mL		180	2 days	polyxtalline
264 - 24	$LaCl_3$	0.3	FDC	0.2	H_2O	5 mL	5 mL IPA	180	2 days	polyxtalline
264 - 28	$CeCl_{33}$	0.3	FDC	0.2	IPA	10 mL		180	2 days	polyxtalline
264 - 34	$LaCl_3$	1	FDC	0.2	H_2O	10 mL		180	2 days	polyxtalline
264 - 35	$TbCl_3$	0.1	FDC	0.2	MeOH	5 mL		180	2 days	polyxtalline
264 - 39	$TbCl_3$	0.1	FDC	0.2	THF	5 mL		180	2 days	polyxtalline
264 - 53	$SnCl_2$	0.2	FDC	0.2	H_2O	5 mL		180	2 days	polyxtalline
264 - 54	$CuCl_2$	0.2	FDC	0.2	H_2O	5 mL		180	2 days	polyxtalline
265 - 22	$Sr(Ac)_2$	0.2	FDC	0.1	H_2O	5 mL	pH 7	180	2 days	polyxtalline
265 - 24	$Sr(Ac)_2$	0.2	FDC	0.1	H_2O	5 mL	pH 12	180	2 days	polyxtalline
265 - 28	$Sr(Ac)_2$	0.2	FDC	0.1	H_2O	5 mL	pH 13	180	2 days	polyxtalline
265 - 34	$Sr(Ac)_2$	0.2	FDC	0.1	H_2O	5 mL	pH 4	180	2 days	polyxtalline
265 - 35	$Sr(Ac)_2$	0.2	FDC	0.1	H_2O	5 mL	pH 6	180	2 days	polyxtalline
265 - 39	$Sr(Ac)_2$	0.2	FDC	0.1	H_2O	5 mL	pH 5	180	2 days	polyxtalline
265 - 53	$Sr(Ac)_2$	0.5	FDC	0.2	DMF	10 mL		180	2 days	polyxtalline
265 - 54	$Sr(Ac)_2$	0.5	FDC	0.2	H_2O	5 mL	5 mL DMF	180	2 days	polyxtalline
266 - 22	$Sr(Ac)_2$	0.2	FDC	0.1	H_2O	5 mL	4 drop 1M HCl	180	2 days	polyxtalline

Table 8.95: Fluorenone framework experiments, continued

Sample Bomb	Metal	amt	Ligand	amt	Solvent	amt	Extras	temp	time	results
266 - 24	$Sr(Ac)_2$	0.2	FDC	0.1	H_2O	5 mL	6 drop 1M HCl	180	2 days	polyxtalline
266 - 28	$Sr(Ac)_2$	0.2	FDC	0.1	H_2O	5 mL	12 drop 1M HCl	180	2 days	polyxtalline
266 - 34	$Sr(Ac)_2$	0.2	FDC	0.1	H_2O	5 mL	6 drop 1M +HNO3	180	2 days	polyxtalline
266 - 35	$Sr(Ac)_2$	0.2	FDC	0.1	H_2O	5 mL	10 drops 1M HNO3	180	2 days	polyxtalline
266 - 39	$Sr(Ac)_2$	0.2	FDC	0.1	H_2O	5 mL	10 drops 1M Acetic	180	2 days	polyxtalline
266 - 53	$Sr(Ac)_2$	0.2	FDC	0.1	H_2O	5 mL	HCl to pH 1	180	2 days	polyxtalline
266 - 54	$Sr(Ac)_2$	0.2	FDC	0.1	H_2O	5 mL	KF to pH 5	180	2 days	polyxtalline
267 - 22	$ZnCl_2$	0.2	FDC	0.1	H_2O	5 mL	0.05 mmol 1,2,4 triazole	150	4 days	polyxtalline
267 - 24	$ZnCl_2$	0.2	FDC	0.1	H_2O	5 mL	0.05 mmol pyrazine	150	4 days	polyxtalline
267 - 28	$ZnCl_2$	0.2	FDC	0.1	H_2O	5 mL	0.05 mmol imidazole	150	4 days	polyxtalline
267 - 34	$ZnCl_2$	0.2	FDC	0.1	H_2O	5 mL	0.05 mmol 44’ bpy	150	4 days	polyxtalline
267 - 35	$ZnCl_2$	0.2	FDC	0.1	H_2O	5 mL	0.05 mmol oxamide	150	4 days	polyxtalline
267 - 39	$ZnCl_2$	0.2	FDC	0.1	H_2O	5 mL	0.05 mmol azodicarboximid	150	4 days	polyxtalline
267 - 53	$ZnCl_2$	0.2	FDC	0.1	H_2O	5 mL	0.05 mmol 124 triazole	100	4 days	polyxtalline
267 - 54	$ZnCl_2$	0.2	FDC	0.1	H_2O	5 mL		180	3 days	polyxtalline
273 - 22	Zn Propionate	0.2	FDC	0.1	H_2O	5 mL	0.05 mmol 44’ bpy	180	3 days	polyxtalline
273 - 24	Zn Propionate	0.2	FDC	0.1	H_2O	5 mL	0.05 mmol 44’ bpy	180	3 days	polyxtalline
273 - 28	$Zn(NO_3)_2$	0.2	FDC	0.1	H_2O	5 mL	0.05 mmol 44’ bpy	180	3 days	polyxtalline
273 - 34	$Zn(NO_3)_2$	0.2	FDC	0.1	H_2O	5 mL	0.05 mmol 44’ bpy	200	3 days	polyxtalline
273 - 39	$Zn(Ac)_2$	0.5	FDC	0.1	H_2O	5 mL	0.05 mmol 44’ bpy	180	3 days	polyxtalline
273 - 54	$Sn(Ac)_2$	0.2	FDC	0.1	H_2O	5 mL	0.05 mmol 44’ bpy	180	3 days	polyxtalline
286 - 22	$FeCl_2$	0.2	FDC	0.1	H_2O	5 mL	0.05 imidizole	180	3 days	organic crystals
286 - 24	$Cu(Ac)_2$	0.2	FDC	0.1	H_2O	5 mL	0.05 imidizole	180	3 days	copper oxalate
289 - 5	$Ca(Ac)_2$	0.2	FDC	0.1	H_2O	40 mL	0.05 imidizole	180	4 days	small crystals, poor diffractions
290 - 22	$Zn(Ac)_2$	0.1	FDC	0.05	H_2O	10 mL	0.025 imidizole	125	3 days	polyxtalline

Table 8.96: Fluorenone framework experiments, continued

Sample Bomb	Metal	amt	Ligand	amt	Solvent	amt	Extras	temp	time	results
290 - 24	$Zn(Ac)_2$	0.1	FDC	0.05	H_2O	10 mL	0.025 imidizole	150	3 days	polyxtalline
290 - 28	$Zn(Ac)_2$	0.1	FDC	0.05	H_2O	10 mL	0.025 imidizole	180	3 days	polyxtalline, bright luminescence
290 - 34	$ZnCl_2$	0.1	FDC	0.05	H_2O	10 mL	0.025 imidizole	125	3 days	polyxtalline
290 - 35	$ZnCl_2$	0.1	FDC	0.05	H_2O	10 mL	0.025 imidizole	150	3 days	polyxtalline
290 - 39	$ZnCl_2$	0.1	FDC	0.05	H_2O	10 mL	0.025 imidizole	180	3 days	polyxtalline
290 - 50	Zn Propionate	0.1	FDC	0.1	H_2O	10 mL	0.05 Imidizole	180	3 days	polyxtalline
290 - 51	$Zn(Ac)_2$	0.1	FDC	0.05	H_2O	10 mL		180	3 days	polyxtalline
290 - 52	$Zn(Ac)_2$	0.1	FDC	0.05	H_2O	5 mL	5mL DMF	125	3 days	polyxtalline
290 - 59	$Zn(Ac)_2$	0.1	FDC	0.05	H_2O	5 mL	5mL DCM	125	3 days	polyxtalline
292 - 22	$Zn(Ac)_2$	0.1	FDC	0.05	H_2O	10 mL	0.025 imidizole	200	3 days	polyxtalline
292 - 24	$Zn(Ac)_2$	0.1	FDC	0.05	H_2O	10 mL	0.025 imidizole, 2 drops 1M KOH	200	3 days	polyxtalline
292 - 28	$Zn(Ac)_2$	0.1	FDC	0.05	H_2O	10 mL	0.025 imidizole,4 drops 1M KOH	200	3 days	no solids
292 - 34	$Zn(Ac)_2$	0.1	FDC	0.05	H_2O	10 mL	0.025 imidizole, 6 drops 1M KOH	200	3 days	no solids
292 - 35	$Zn(Ac)_2$	0.1	FDC	0.05	H_2O	10 mL	0.025 imidizole, 8 drops 1M KOH	200	3 days	no solids
292 - 39	$Zn(Ac)_2$	0.1	FDC	0.05	H_2O	10 mL	0.025 imidizole, 1mL PEG	200	3 days	decomposed
292 - 50	$Zn(Ac)_2$	0.1	FDC	0.05	H_2O	10 mL	0.025 imidizole, 2 drops 1M HCl	200	3 days	polyxtalline
292 - 51	$Zn(Ac)_2$	0.1	FDC	0.05	H_2O	10 mL	0.025 imidizole, 0.05 NaCl	200	3 days	polyxtalline
304 - 22	$Mg(CO_3)_2$	0.1	FDC	0.05	H_2O	10 mL	0.025 imidizole	180	7 days	polyxtalline
304 - 24	$Ca(CO_3)_2$	0.05	FDC	0.05	H_2O	10 mL	0.025 imidizole	180	7 days	polyxtalline
304 - 28	$Ba(Ac)_2$	0.05	FDC	0.05	H_2O	10 mL	0.025 imidizole	180	7 days	polyxtalline
304 - 34	$Zn(Ac)_2$	0.05	FDC	0.05	H_2O	10 mL	0.025 imidizole	180	7 days	polyxtalline
304 - 35	$Mg(CO_3)_2$	0.1	FDC	0.05	H_2O	10 mL	0.025 pyrazine	180	7 days	polyxtalline
304 - 39	$Ca(CO_3)_2$	0.05	FDC	0.05	H_2O	10 mL	0.025 pyrazine	180	7 days	polyxtalline
304 - 50	$Ba(Ac)_2$	0.05	FDC	0.05	H_2O	10 mL	0.025 pyrazine	180	7 days	polyxtalline
304 - 51	$Zn(Ac)_2$	0.05	FDC	0.05	H_2O	10 mL	0.025 pyrazine	180	7 days	polyxtalline

Table 8.97: Fluorenone framework experiments, continued

Sample Bomb	Metal	amt	Ligand	amt	Solvent	amt	Extras	temp	time	results
304 - 52	AgCl	0.1	FDC	0.05	H_2O	10 mL		180	7 days	polyxtalline
310 - 4	$Ca(Ac)_2$	1	FDC	0.5	H_2O	50 mL	0.25 imidizole	180	2 days	polyxtalline
310 - 5	$Mg(Ac)_2$	1	FDC	0.5	H_2O	50 mL	0.25 imidizole	180	2 days	polyxtalline
310 - 6	$Ba(Ac)_2$	1	FDC	0.5	H_2O	50 mL	0.25 imidizole	180	2 days	polyxtalline
310 - 7	$Zn(Ac)_2$	1	FDC	0.5	H_2O	50 mL	0.25 imidizole	180	2 days	polyxtalline
323 - 22	$Ca(Ac)_2$	0.1	FDC	0.05		2.5 mL	2.5 mL ethylene glycol	180	2 days	polyxtalline
323 - 24	$Ca(Ac)_2$	0.05	FDC	0.05		3 mL	2 mL ethylene glycol, 1 drop KOH	180	2 days	polyxtalline
323 - 28	$Ca(Ac)_2$	0.05	FDC	0.05		3 mL	2 mL ethylene glycol, 2 drop KOH	180	2 days	polyxtalline
323 - 54	$Ca(Ac)_2$	0.05	FDC	0.05		3 mL	2 mL ethylene glycol, 4 drop KOH	180	2 days	polyxtalline
334 - 1	$Ca(Ac)_2$	0.025	FDC	0.025	H_2O	3 mL	3 mL DMF	60	1 day	no solids
334 - 2	$Ca(Ac)_2$	0.025	FDC	0.025	DMF	6 mL		60	1 day	no solids
334 - 3	$Zn(Ac)_2$	0.025	FDC	0.025	H_2O	3 mL	3 mL DMF	60	1 day	no solids
334 - 4	$Zn(Ac)_2$	0.025	FDC	0.025	DMF	6 mL		60	1 day	no solids
349 - 6	$CaCl_2$	0.05	FDC	0.05	H_2O	5 mL	0.025 imidizole	180	2 days	polyxtalline
349 - 10	$CaCl_2$	0.05	FDC	0.05	H_2O	5 mL		180	2 days	polyxtalline
349 - 12	$CaCl_2$	0.1	FDC	0.05	H_2O	5 mL	0.025 imidizole	180	2 days	polyxtalline
349 - 21	$Ca(Ac)_2$	0.05	FDC	0.05	H_2O	5 mL	0.05 Imidizole	180	2 days	small xtals, bright luminescence
349 - 22	$Ca(Ac)_2$	0.05	FDC	0.05	H_2O	5 mL		180	2 days	small xtals
349 - 23	$Ca(Ac)_2$	0.15	FDC	0.05	H_2O	5 mL		180	2 days	small xtals
349 - 24	$Ca(Ac)_2$	0.1	FDC	0.05	H_2O	5 mL		180	2 days	polyxtalline
349 - 28	$Ca(Ac)_2$	0.2	FDC	0.05	H_2O	5 mL		180	2 days	polyxtalline
349 - 34	$Ca(Ac)_2$	0.05	FDC	0.05	H_2O	5 mL	0.025 imidizole	180	2 days	polyxtalline
349 - 35	$Ca(Ac)_2$	0.1	FDC	0.05	H_2O	5 mL	0.025 imidizole	180	2 days	polyxtalline
349 - 37	$Ca(Ac)_2$	0.15	FDC	0.05	H_2O	5 mL	0.025 imidizole	180	2 days	polyxtalline
349 - 39	$Ca(Ac)_2$	0.2	FDC	0.05	H_2O	5 mL	0.025 imidizole	180	2 days	polyxtalline

Table 8.98: Fluorenone framework experiments, continued

Sample Bomb	Metal	amt	Ligand	amt	Solvent	amt	Extras	temp	time	results
349 - 53	$Ca(NO_3)_2$	0.1	FDC	0.05	H_2O	5 mL		180	2 days	polyxtalline
349 - 54	$Ca(NO_3)_2$	0.05	FDC	0.05	H_2O	5 mL	0.025 imidizole	180	2 days	polyxtalline
350 - 28	$Ca(Ac)_2$	0.05	FDC	0.05	H_2O	5 mL	0.2 mL NH4OH	170	2 days	small xtals
350 - 34	$Ca(Ac)_2$	0.05	FDC	0.05	H_2O	5 mL	0.2 mL TEA(OH)	170	2 days	polyxtalline
350 - 35	$Ca(Ac)_2$	0.05	FDC	0.05	H_2O	5 mL	0.2 mL pyrazine	170	2 days	small xtals
350 - 37	$Ca(Ac)_2$	0.05	FDC	0.05	H_2O	5 mL	0.2 mL tributylamine	170	2 days	polyxtalline
350 - 39	$Ca(Ac)_2$	0.05	FDC	0.05	H_2O	5 mL	0.2 mL triethanolamine	170	2 days	polyxtalline
350 - 23	$Mn(Ac)_2$	0.05	FDC	0.05	H_2O	5 mL		170	2 days	polyxtalline
350 - 24	$Mn(Ac)_2$	0.05	FDC	0.05	H_2O	5 mL	0.05 imidizole	170	2 days	sludge
350 - 53	$Mn(Ac)_2$	0.05	FDC	0.05	H_2O	5 mL	0.05 bipyradalethane	170	2 days	polyxtalline
350 - 54	$Mn(Ac)_2$	0.05	FDC	0.05	H_2O	5 mL	0.2 mL TEA(OH)	170	2 days	polyxtalline
352 - 6	$Zn(Ac)_2$	0.05	FDC	0.05	H_2O	5 mL	1 drop 1M NH4OH	175	2 days	polyxtalline
352 - 10	$Zn(Ac)_2$	0.05	FDC	0.05	H_2O	5 mL	2 drop 1M NH4OH	175	2 days	polyxtalline
352 - 12	$Zn(Ac)_2$	0.05	FDC	0.05	H_2O	5 mL	3 drop 1M NH4OH	175	2 days	polyxtalline
352 - 21	$Zn(Ac)_2$	0.05	FDC	0.05	H_2O	5 mL	4 drop 1M NH4OH	175	2 days	polyxtalline
352 - 22	$Zn(Ac)_2$	0.05	FDC	0.05	H_2O	5 mL	5 drop 1M NH4OH	175	2 days	polyxtalline
352 - 23	$Zn(Ac)_2$	0.05	FDC	0.05	H_2O	5 mL	0.025 imidizole	175	2 days	polyxtalline
352 - 24	$Zn(Ac)_2$	0.05	FDC	0.05	H_2O	5 mL	0.05 Imidizole	175	2 days	polyxtalline
352 - 28	$Zn(Ac)_2$	0.05	FDC	0.05	H_2O	5 mL	0.1 imidizole	175	2 days	polyxtalline
352 - 34	$Zn(Ac)_2$	0.05	FDC	0.05	H_2O	5 mL	0.025 piperazine	175	2 days	polyxtalline
352 - 35	$Zn(Ac)_2$	0.05	FDC	0.05	H_2O	5 mL	0.05 piperazine	175	2 days	polyxtalline
352 - 37	$Zn(Ac)_2$	0.05	FDC	0.05	H_2O	5 mL	0.1 piperazine	175	2 days	no solids
352 - 39	$Zn(Ac)_2$	0.05	FDC	0.05	H_2O	5 mL		175	2 days	polyxtalline
352 - 50	$Zn(Ac)_2$	0.1	FDC	0.05	H_2O	5 mL		175	2 days	polyxtalline
352 - 52	$Zn(Ac)_2$	0.15	FDC	0.05	H_2O	5 mL		175	2 days	polyxtalline

Table 8.99: Fluorenone framework experiments, continued

Sample Bomb	Metal	amt	Ligand	amt	Solvent	amt	Extras	temp	time	results
352 - 53	$Zn(Ac)_2$	0.05	FDC	0.05	H_2O	5 mL		175	2 days	no solids
352 - 54	$Zn(Ac)_2$	0.2	FDC	0.05	H_2O	5 mL		175	2 days	polyxtalline
352 - 59	$Zn(Ac)_2$	0.1	FDC	0.05	H_2O	5 mL	0.05 imidizole	175	2 days	polyxtalline
352 - 60	$Zn(Ac)_2$	0.1	FDC	0.05	H_2O	5 mL	2 drop 1M NH4OH	175	2 days	polyxtalline
369 - 6	$Ca(Ac)_2$	0.02	NaFDC	0.02	H_2O	5 mL		180	2 days	no solids
369 - 10	$Ca(NO_3)_2$	0.02	NaFDC	0.02	H_2O	5 mL		180	2 days	no solids
369 - 12	$CaCl_2$	0.02	NaFDC	0.02	H_2O	5 mL		180	2 days	no solids
369 - 21	$Ca(Ac)_2$	0.02	NaFDC	0.02	H_2O	5 mL		150	2 days	no solids
369 - 22	$Ca(NO_3)_2$	0.02	NaFDC	0.02	H_2O	5 mL		150	2 days	small crystals, poor diffractions
369 - 23	$CaCl_2$	0.02	NaFDC	0.02	H_2O	5 mL		150	2 days	no solids
370 - 6	$Ca(NO_3)_2$	0.025	NaFDC	0.05	H_2O	7 mL		150	2 days	polyxtalline
370 - 10	$Ca(NO_3)_2$	0.05	NaFDC	0.05	H_2O	7 mL		150	2 days	good xtals
370 - 12	$Ca(NO_3)_2$	0.75	NaFDC	0.05	H_2O	7 mL		150	2 days	polyxtalline
370 - 21	$Ca(NO_3)_2$	0.1	NaFDC	0.05	H_2O	7 mL		150	2 days	polyxtalline
370 - 22	$CaCl_2$	0.1	NaFDC	0.05	H_2O	7 mL		150	2 days	polyxtalline
370 - 23	$CaCl_2$	0.075	NaFDC	0.05	H_2O	7 mL	0.02 LiF	150	2 days	polyxtalline
395 - 21	$Ba(Ac)_2$	0.1	FDC	0.1	H_2O	5mL	2 drop 1M NaOH	150	2 days	polyxtalline
395 - 22	$Ba(Ac)_2$	0.1	FDC	0.1	H_2O	5mL	3 drop 1M NaOH	150	2 days	polyxtalline
395 - 23	$Ba(Ac)_2$	0.1	FDC	0.1	H_2O	5mL	4 drop 1M NaOH	150	2 days	synchrotron size xtals
395 - 24	$Ba(Ac)_2$	0.1	FDC	0.1	H_2O	5mL	5 drop 1M NaOH	150	2 days	synchrotron size xtals
395 - 28	$Ba(Ac)_2$	0.1	FDC	0.1	H_2O	5mL	6 drop 1M NaOH	150	2 days	powder
395 - 34	$Ba(Ac)_2$	0.1	FDC	0.1	H_2O	5mL	7 drop 1M NaOH	150	2 days	powder
395 - 35	$Ba(Ac)_2$	0.1	NaFDC	0.1	H_2O	5mL		150	2 days	no solids
395 - 37	$Ba(Ac)_2$	0.1	NaFDC	0.1	H_2O	5mL	4 drop 1M HCl	150	2 days	no solids
397 - 21	$Cd(Ac)_2$	0.05	FDC	0.05	H_2O	5 mL	1 drop 1M NaOH	180	2 days	small xtals

Table 8.100: Fluorenone framework experiments, continued

Sample Bomb	Metal	amt	Ligand	amt	Solvent	amt	Extras	temp	time	results
397 - 22	$Cd(Ac)_2$	0.05	FDC	0.05	H_2O	5 mL	2 drop 1M NaOH	180	2 days	polyxtalline
397 - 23	$Ca(Ac)_2$	0.05	FDC	0.05	H_2O	5 mL	3 drop 1M NaOH	180	2 days	powder
397 - 24	$Ca(Ac)_2$	0.05	FDC	0.05	H_2O	5 mL	4 drop 1M NaOH	180	2 days	powder
397 - 28	$Mg(Ac)_2$	0.05	FDC	0.05	H_2O	5 mL	1 drop 1M NaOH	180	2 days	good xtals
397 - 34	$Mg(Ac)_2$	0.05	FDC	0.05	H_2O	5 mL	2 drop 1M NaOH	180	2 days	polyxtalline
397 - 35	$Mg(Ac)_2$	0.05	FDC	0.05	H_2O	5 mL	3 drop 1M NaOH	180	2 days	powder
397 - 37	$Mg(Ac)_2$	0.05	FDC	0.05	H_2O	5 mL	4 drop 1M NaOH	180	2 days	powder
399 - 6	$Zn(Ac)_2$	0.05	FDC	0.05	H_2O	5 mL		150	2 days	polyxtalline
399 - 10	$Zn(Ac)_2$	0.05	FDC	0.05	H_2O	5 mL		180	2 days	polyxtalline
399 - 12	$Zn(Ac)_2$	0.05	FDC	0.05	H_2O	5 mL		200	2 days	polyxtalline
399 - 21	$Zn(Ac)_2$	0.05	FDC	0.05	H_2O	5 mL		180	2 days	polyxtalline
399 - 23	$Zn(Ac)_2$	0.05	FDC	0.05	H_2O	5 mL	1 drop 1M NaOH	180	2 days	polyxtalline
399 - 24	$Zn(Ac)_2$	0.05	FDC	0.05	H_2O	5 mL		180	2 days	polyxtalline
399 - 28	$Zn(Ac)_2$	0.05	FDC	0.05	H_2O	5 mL		180	2 days	polyxtalline
399 - 34	$Mn(Ac)_2$	0.05	FDC	0.05	H_2O	5 mL		150	2 days	polyxtalline
399 - 35	$Mn(Ac)_2$	0.05	FDC	0.05	H_2O	5 mL		180	2 days	small xtals
399 - 37	$Mn(Ac)_2$	0.05	FDC	0.05	H_2O	5 mL		200	2 days	small xtals
399 - 39	$Mn(Ac)_2$	0.05	FDC	0.05	H_2O	5 mL		180	2 days	polyxtalline
399 - 50	$Mn(Ac)_2$	0.05	FDC	0.05	H_2O	5 mL	1 drop 1M NaOH	180	2 days	polyxtalline
399 - 52	$Mn(Ac)_2$	0.05	FDC	0.05	H_2O	5 mL		180	2 days	polyxtalline
399 - 53	$Mn(Ac)_2$	0.05	FDC	0.05	H_2O	5 mL		180	2 days	small xtals
400 - 6	$Zn(Ac)_2$	0.05	FDC	0.05	H_2O	5 mL		190	2 days	polyxtalline
400 - 10	$Zn(Ac)_2$	0.05	FDC	0.05	H_2O	5 mL	1 drop 0.5M KOH	190	2 days	polyxtalline
400 - 12	$Zn(Ac)_2$	0.05	FDC	0.05	H_2O	5 mL	2 drop 0.5M KOH	180	2 days	polyxtalline
400 - 21	$Zn(Ac)_2$	0.05	FDC	0.05	H_2O	5 mL	1 drop 0.5M KOH	180	2 days	polyxtalline

Table 8.101: Fluorenone framework experiments, continued

Sample Bomb	Metal	amt	Ligand	amt	Solvent	amt	Extras	temp	time	results
400 - 23	$Zn(Ac)_2$	0.05	FDC	0.05	H_2O	5 mL	2 drop 0.5M KOH	180	2 days	polyxtalline
400 - 24	$Zn(Ac)_2$	0.05	FDC	0.05	H_2O	5 mL	3 drop 0.5M KOH	180	2 days	no solids
400 - 28	$Zn(Ac)_2$	0.05	FDC	0.05	H_2O	5 mL	4 drop 0.5M KOH	180	2 days	no solids
400 - 34	$Zn(Ac)_2$	0.05	FDC	0.05	H_2O	5 mL	1 drop 1M Acetic	180	2 days	polyxtalline
400 - 35	$Zn(Ac)_2$	0.05	FDC	0.05	H_2O	5 mL	2 drop 1M Acetic	180	2 days	polyxtalline
400 - 37	$Zn(Ac)_2$	0.05	FDC	0.05	H_2O	5 mL	3 drop 1M Acetic	190	2 days	no solids
400 - 39	$Zn(Ac)_2$	0.05	FDC	0.05	H_2O	5 mL	4 drop 1M Acetic	180	2 days	no solids
400 - 50	$Zn(Ac)_2$	0.05	FDC	0.05	H_2O	5 mL	2 drop 0.5M KOH	150	2 days	polyxtalline

Bibliography

[1] S. Nakamura and G. Fasol. *The blue laser diode: GaN based blue light emitters*. Springer, Berlin, 1997.

[2] M. S. Shur and Artūras Žukauskas. Solid-state lighting: Toward superior illumination. *P IEEE*, 93:1691, 2005.

[3] G. Blasse and A. Bril. Investigation of some Ce^{3+} activated phosphors. *J. Chem. Phys.*, 47(12):5139–5145, 1967.

[4] G. Blasse and A. Bril. A new phosphor for flying-spot cathod-ray tubes for color television: Yellow-emitting $Y_3Al_5O_{12}$-Ce^{3+}. *Appl. Phys. Lett*, 11(2):53–54, 1967.

[5] P. Schlotter, R. Schmidt, and J. Schneider. Luminescence conversion of blue light emitting diodes. *Appl. Phys. A*, 64:417, 1997.

[6] M. Zachau, D. Becker, D. Berben, T. Fiedler, F. Jermann, and F. Zwaschka. Phosphors for solid state lighting. *Proc. SPIE*, 6910:691010, 2008.

[7] S. Neeraj, N. Kijima, and A.K. Cheetham. Novel red phosphors for solid state lighting. *Solid State Commun.*, 131:65–69, 2004.

[8] K. S. Sohn, D. H. Park, S. H. Cho, J. S. Kwak, and J. S. Kim. Computational evolutionary optimization of red phosphor for use in tricolor white leds. *Chem. Mater.*, 18:1768–1722, 2006.

[9] H. S. Yoo, W. B. Im, J. H. Kang, and D. Y. Jeon. Preparation and photoluminescence properties of $YAl_3(BO_3)_4$:Tb^{3+}, Bi^{3+} phosphor under VUV/UV excitation. *Optical Materials*, 31:131–135, 2008.

[10] W. B. Im, N. N. Fellows, S. P. DenBaars, R. Seshadri, and Y. I. Kim. $LaSr_2AlO_5$, a Versatile Host Compound for Ce^{3+}-Based Yellow Phosphors: Structural Tuning of Optical Properties and Use in Solid-State White Lighting. *Chem. Mater.*, 21:2957–2966, 2009.

[11] S. Neeraj, N. Kijima, and A. K. Cheetham. Novel red phosphors for solid state lighting: the system $Bi_xLn_{1-x}VO_4$:Eu^{3+}/Sm^{3+} (Ln=Y,Gd). *Solid State Commun.*, 131:65–69, 2004.

[12] R. Mueller-Mach, G. Mueller, M.R. Krames, H.A. Hoppe, F. Stadler, W. Schnick, T. Juestel, and P. Schmidt. Highly efficient all-nitride phosphor-converted white light emitting diode. *Phys. Stat. Sol. A*, 202:1727, 2005.

[13] R. Le Toquin and A.K. Cheetham. Red-emitting cerium-based phosphor materials for solid-state lighting applications. *Chem. Phys. Lett.*, 423:352, 2006.

[14] Energy Efficiency US Department of Energy and Renewable Energy. Energy efficient lighting and light emitting diodes. http://www.netl.doe.gov/ssl/usingLeds/, May 2006.

[15] Matteo Meneghini, Lorenzo-Roberto Trevisanello, Francesco de Zuani, Nicola Trivellin, Gaudenzio Meneghesso, and Enrico Zanoni. Extensive analysis of the degradation of phosphor-converted leds. *SPIE Ninth International Conference on Solid State Lighting*, 7422(1):74220H, 2009.

[16] Commision International de l'Eclairage. *International Lighting Vocabulary*. Publ. CIE, 1987.

[17] Navigant Consulting Inc. Energy savings potential of solid state lighting in general illumination applications. Technical report, U. S. Department of Energy, Lighting and Research Development, 2006.

[18] Energy Efficiency and Renewable Energy. Color quality of white LEDs. Technical report, U. S. Department of Energy, 2006. www1.eere.energy.gov/buildings/ssl/color_quality.html.

[19] J. Schanda. The concept of color rendering revisted. In *First European Conference on Color in Graphics Imaging and Vision*, volume 4, pages 2–5, University Poitiers, France, 2002.

[20] Kevin Dowling. Standards required for further penetration of solid-state lighting. *LEDs Magazine*, pages 28–31, 2007.

[21] Wikimedia commons spectra posted by Deglr6328, collected on a Ocean Optics HR2000 spectrometer. http://en.wikipedia.org/wiki/User:Deglr6328.

[22] John Beckman. *A history of inventions, discoveries, and origins*, volume 2. Henry G. Bohn, London, 4th edition, 1846.

[23] Shigeo Shionoya and William M. Yen, editors. *Phosphor Handbook*. CRC Press, 1999.

[24] Gary Wulfsberg. *Inorganic Chemistry*. University Science Books, Sausalito, California, 2000.

[25] David Knight. *Humphry Davy: Science and Power*. Cambridge University Press, Cambridge, UK, 1992.

[26] C. Ronda. *Luminescence: From theory to applications*. Wiley, Weinheim, Germany, 2008.

[27] P. Yang, P. Deng, and Z. Yin. Concentration quenching in Yb:YAG. *J. Lumines.*, 97:51–54, 2002.

[28] M. J. Dejneka, A. Streltsov, S. Pal, A. G. Frutos, C. L. Powell, K. Yost, P. K. Yuen, U. Müller, and J. Lahiri. Rare earth-doped glass microbarcodes. *P. Natl. Acad. Sci. USA*, 100:389–393, 2003.

[29] J.L. Wu, G. Gundiah, and A.K. Cheetham. Structure-property correlations in ce-doped garnet phosphors for use in solid state lighting. *Chem. Phys. Lett.*, 441:250–254, 2007.

[30] V. Bachmann, C. Ronda, O. Oeckler, W. Schnick, and A. Meijerink. Color point tuning for (Sr,Ca,Ba)$Si_2O_2N_2$:Eu^{2+} for White Light LEDs. *Chem. Mater.*, 21:316–325, 2009.

[31] H. N. Russell and F. A. Saunders. New regularities in the spectra of the alkaline earths. *Astrophys. J.*, 61:38–69, 1925.

[32] W.-C. Ke, C. C. Lin, R.-S. Liu, and M.-C. Kuo. Energy transfer and significant improvement moist stability of $BaMgAl_{10}O_{17}$:Eu^{2+},Mn^{2+} as a phosphor for white light-emitting diodes. *J. Electrochem. Soc*, 157:J307, 2010.

[33] G. Gundiah, Y. Shimomura, N. Kijima, and A. K. Cheetham. Novel red phosphors based upon vanadate garnets for solid state lighting applications. *Chem. Phys. Lett.*, 455:279–283, 2008.

[34] N. Sabbatini and M. Guardigli. Luminescent lanthanide complexes as photochemical supramolecular devices. *Coord. Chem. Rev.*, 123:201–228, 1993.

[35] A. K. Cheetham, C. N. R. Rao, and R. K. Feller. Structural diversity and chemical trends in hybrid inorganic-organic framework materials. *Chem. Commun.*, 46:4780–4795, 2006.

[36] S. Kitagawa, R. Kitaura, and S. Noro. Functional porous coordination polymers. *Angew. Chem. Int. Ed.*, 43:2334–2375, 2004.

[37] C. N. R. Rao, A. K. Cheetham, and A. Thirumurugan. Hybrid inorganic-organic materials: a new family in condensed matter physics. *J. Phys.-Condens. Mat.*, 20:083202, 2008.

[38] O. M. Yaghi, M. O'Keefe, N. W. Ockwig, H. K. Chae, M. Eddaoudi, and J. Kim. Reticular synthesis and the design of new materials. *Nature*, 423:705–714, 2003.

[39] G. Férey. Building units design and scale chemistry. *J. Solid State Chem.*, 152:37–48, 2000.

[40] L. Tosheva and V. P. Valtchev. Nanozeolites: Synthesis, crystallization mechanism, and applications. *Chem. Mater.*, 17:2494–2513, 2005.

[41] M. E. Davies. Ordered porous materials for emerging applications. *Nature*, 417:813–821, 2002.

[42] M. G. Valdés, A. I. Pérez-Cordoves, and M. E. Diíz-García. Zeolites and zeolite-based materials in analytical chemistry. *TRAC-Trend. Anal. Chem.*, 25:24–30, 2006.

[43] M. Eddaoudi, H. L. Li, and O. M. Yaghi. Highly porous and stable metal-organic frameworks: Structre design and sorption properties. *J. Am. Chem. Soc.*, 122:1391–1397, 2000.

[44] S. Kitagawa, R. Kitaura, and S. Noro. Functional porous coordination polymers. *Angew. Chem. Int. Ed.*, 43:2334–2375, 2004.

[45] P. M. Forster, A. R. Burbank, C. Livage, G. Férey, and A. K. Cheetham. The role of temperature in the synthesis of hybrid inorganic-organic materials: the example of cobalt succinates. *Chem. Commun.*, 368:368–369, 2004.

[46] C. Livage, C. Egger, M. Nogues, and G. Férey. Hybrid open frameworks (MIL-n) Part 5: Synthesis and crystal structure of MIL-9. *J. Mater. Chem.*, 8:2743–2747, 1998.

[47] K. C. Kam, K. L. M. Young, and A. K. Cheetham. Chemical and structural diversity in chiral magnesium tartrates and their racemic and *meso* analogues. *Crys. Growth and Design*, 7:1522–1532, 2007.

[48] S. Petoud, S. M. Cohen, J.-C. G. Bünzli, and K. N. Raymond. Stable Lanthanide Luminescence Agents Highly Emissive in Aqueous Solution: Multidentate 2-Hydroxyisophthalamide Complexes of Sm^{3+}, Eu^{3+}, Tb^{3+}, Dy^{3+}. *J. Am. Chem. Soc.*, 125:13324–13325, 2003.

[49] M. D. Allendorf, C. A. Bauer, R. K. Bhakta, and R. J. T. Houk. Luminescent metal-organic frameworks. *Chem. Soc. Rev.*, 38:1330–1352, 2009.

[50] C. A. Bauer, T. V. Timofeeva, T. B. Settersten, B. D. Patterson, V. H. Liu, B. A. Simmons, and M. D. Allendorf. Influence of connectivity and porosity on ligand-based luminescence in zinc metal-organic frameworks. *J. Amer. Chem. Soc.*, 129:7316–7144, 2007.

[51] S. F. A. Kettle. *Coordination Compounds*. Nelson, 1977.

[52] M. Du, X. J. Jiang, and X. J. Zhao. Molecular tectonics of mixed-ligand metal-organic frameworks: Positional isomeric effect, metal-directed assembly, and structural diversification. *Inorg. Chem.*, 46:3984–3995, 2007.

[53] X. Wang and Y. Li. Synthesis and characterization of lanthanide hydroxide single-crystal nanowires. *Angew. Chem. Int. Ed.*, 41:4790–4793, 2002.

[54] X. Chen, X. Sun, and Y. Li. Self-assembling vanadium oxide nanotubes by organic molecular templates. *Inorg. Chem.*, 41:4523–4530, 2002.

[55] Z. Lu, L. Wen, Z. Ni, Y. Li, H. Zhu, and Q. Meng. Syntheses, structures, and photoluminescent and magnetic studies of metalorganic frameworks assembled with 5-sulfosalicylic acid and 1,4-bis(imidazol-1-ylmethyl)-benzene. *Cryst. Growth Des.*, 7:268–274, 2007.

[56] Y.S. Lin and R.S. Liu. Chemical substitution effects of tb in yag:ce phosphors. *J. Lumines.*, 122-123:580–582, 2007.

[57] M.-X. Li, Z.-X. Miao, M. Shao, S.-W. Liang, and S.-R. Zhu. Metal-organic frameworks constructed from 2,4,6-tris(4-pyridyl)-1,3,5-triazine. *Inorg. Chem.*, 47:4481–4489, 2008.

[58] L. Song, S. W. Du, J. D. Lin, H. Zhou, and T. Li. A 3D metalorganic framework with rare 3-fold interpenetrating dia-g nets based on silver(I) and novel tetradentate imidazolate ligand: Synthesis, structure, and possible ferroelectric property. *Cryst. Growt Des.*, 7:2268–2271, 2007.

[59] M. Ouyang, J.L. Huang, C.L. Cheung, and C.M. Lieber. Energy gaps in "metallic" single-walled carbon nanotubes. *Science*, 292:702–705, 2001.

[60] X. Y. Wu, Y. J. Liang, R. Liu, and Y. Z. Li. The photoluminescence properties of Y_2O_3:Eu^{3+} prepared by surfactant assisted co-precipitation-molten salt synthesis. *Mater. Res. Bull*, 45:594, 2010.

[61] Bruker. SAINT Frame Integration Software, Bruker AXS Inc., 2000.

[62] G. M. Sheldrick. *SADABS User Guide*. University of Göttingen, Göttingen, Germany, 1995.

[63] G.M. Sheldrick. A short history of SHELX. *Acta Cryst*, A64:112–122, 2008.

[64] A. K. Cheetham and P. Day. *Solid State Chemistry Techniques*. Oxford University Press, Oxford, UK, 1988.

[65] V. Pankratov, D. Millers, L. Grigorjeva, W. Lojkowski, and A. Kareiva. Time-resolved luminescence of nanocrystalline inorganic complex oxides. *J. Phys.: Conf. Ser.*, 93:012037, 2007.

[66] Y.C. Kang, H.S. Roh, and B.S. Park. Preparation of Y_2O_3:Eu phosphor particles of filled morphology at high precursor concentrations by spray pyrolysis. *Adv. Mater.*, 12:451, 2000.

[67] R.P. Rao. Preparation and characterization of fine-grain yttrium-based phosphors by sol-gel process. *J. Electrochem. Soc.*, 143:189, 1996.

[68] G.O. Mueller, R.B. Mueller-Mach, D. Bertram, T. Juestel, P.J. Schmidt, and J. Opitz. Light-emitting devices utilizing nanoparticles, 2006. U.S. Patent 7083490 B2.

[69] Dongdong Jin. Nanophosphors for white light LEDS. *Chem. Eng. Comm.*, 194:1666–1687, 2007.

[70] Wei-Ning Wang, W. Widiyastuti, T. Ogi, I.W. Lenggoro, and K. Okuyama. Photoluminescence optimization of luminescent nanocomposites fabricated by spray pyrolysis of a colloid-solution precursor. *Chem. Mater.*, 19:1723, 2007.

[71] W-N Wang, W. Widiyastuti, T. Ogi, I. W. Lenggoro, and K. Okuyama. Correlations between crystallite/particle size and photoluminesce properties of submicrometer phosphors. *Chem. Mater.*, 19:1723–1730, 2007.

[72] Yu Hua Wang and Feng Li. Synthesis of $BaAl_{12}O_{19}$:Mn^{2+} nanophosphors by a reverse microemulsion method and its photouminescence properties under VUV excitation. *J. Lumines.*, 122-123:866–868, 2007.

[73] L. Zhou, J. Shi, and M. Gong. Preparation of SrR_2O_4:Eu^{3+} (R=Y, Lu) phosphor and its photoluminescence properties. *Mat. Lett.*, 59:2079–2084, 2005.

[74] T. S. Copeland, B. I. Lee, J. Qi, and A. K. Elrod. Synthesis and luminescent properties of Mn^{2+}-doped zinc silicate phosphors by sol-gel methods. *J. Lumines.*, 97, 2002.

[75] T.J. Lou, J.H. Zeng, X.D. Lou, H.L. Fu, Y.F. Wang, R.L. Ma, L.J. Tong, and Y.L. Chen. A facile synthesis to Zn_2SiO_4:Mn^{2+} phosphor with controllable size and morphology at low temperature. *J. Colloid Interface Sci.*, 314:510–513, 2007.

[76] J. Wan, X. Chen, Z. Wang, L. Mu, and Y. Qian. One-dimensional rice-like Mn-doped Zn_2SiO_4: Preparation, characterization, luminescent properties and its stability. *J. Crys. Growth*, 280:239–243, 2005.

[77] H. Jio, Q. Ma, L. L. He, Z. Liu, and Q. L. Wu. Low temperature syntehsis of YAG:Ce phosphors by LiF assisted sol-gel combustion method. *Powder Technol.*, 198:229–232, 2010.

[78] W. G. Gao, Y. S. Hu, W. D. Zhuang, S. S. Mang, Y. H. Liu, and H. Q. He. A novel method for the synthesis of YAG:Ce phosphor. *J. Rare Earth*, 27:886–890, 2009.

[79] K. Guo, H. H. Chen, X. X. Guo, X. X. Yang, F. F. Xu, and J. T. Zhao. Morphology investigation of yttrium aluminum garnet nano-powders prepared by a sol-gel combustion method. *J. Alloy Compd.*, 500:34–38, 2010.

[80] M. Nyman, L. E. Shea-Rohwer, J. E. Martin, and P. Provencio. Nano-YAG:Ce mechanisms of growth and epoxy-encapsulation. *Chem. Mater.*, 21:1536–1542, 2009.

[81] H. Yang, D.-K. Lee, and Y.-S. Kim. Spectral variations of nano-sized $Y_3Al_5O_{12}$:Ce phosphors via codoping/substitution and their white LED characteristics. *Mater. Chem. Phys.*, 114:665–669, 2009.

[82] S. Mukherjee, V. Sudarsan, R. K. Vatsa, and A. K. Tyagi. Luminescence studies on lanthanide ions (Eu^{3+}, Dy^{3+} and Tb^{3+}) doped YAG:Ce nanophosphors. *J. Lumines.*, 129:69–72, 2009.

[83] M. Chatterjee and M. K. Naskar. Synthesis of YAG hollow microspheres by reverse-emulsion technique. *J. Am. Ceram. Soc.*, 89:1443–1446, 2006.

[84] E. Caponetti, D.C. Matino, and M.L. Saladino. Preparation of Nd:YAG nanopowder in a confined environment. *Langmuir*, 23:3947–3952, 2007.

[85] B. Vaidhyanathan and J.G.P Binner. Microwave assisted synthesis of nanocrystalline YAG. *J. Mater. Sci.*, 41:5954–5957, 2006.

[86] Y. Letichevsky, L. Sominski, J.C. Moreno, and A. Gedanken. The sonochemical and microwave-assisted synthesis of nanosized yag particles. *New J. Chem.*, 29:1445–1449, 2005.

[87] S. Mathur, H Shen, A. Leleckaite, A. Beganskiene, and A. Kareiva. Low-temperature synthesis and characterization of yttrium-gallium garnet $Y_3Ga_5O_{12}$. *Mat. Res. Bull.*, 40:439–446, 2005.

[88] P. Vaqueiro and M. A. López-Quintela. Synthesis of yttrium aluminium garnet by the citrate gel process. *J. Mater. Chem.*, 8:161–163, 1998.

[89] H. Wang, L. Gao, and K. Niihara. Synthesis of nanoscaled yttrium aluminum garnet powder by the co-precipitation method. *Mat. Sci. Eng. A*, 288:1–4, 2000.

[90] X. Li, H. Liu, J. Wang, H. Cui, and F. Han. Yag:ce nano-sized phosphor particles prepared by a solvothermal method. *Mat. Res. Bull.*, 39:1923–1930, 2004.

[91] L.T. Su, A.I.Y. Tok, and F.Y.C. Boey. Photoluminescence phenomena of Ce^{3+}-doped $Y_3Al_5O_{12}$ nanophosphors. *J. Appl. Phys.*, 102:083541, 2007.

[92] L.G. Jacobsohn, B.L. Bennett, R.E. Muenchausen, J.F. Smith, and D.W. Cooke. Luminescent properties of nanophosphors. *Radiat. Meas.*, 42:675–678, 2007.

[93] D. Jia, Y. Wang, X. Guo, K. Li, Y.K. Zou, and W. Jia. Synthesis and characterization of YAG:Ce^{3+} LED nanophosphors. *J. Electrochem. Soc.*, 154:J1–J4, 2007.

[94] H. Kunieda, Y. Fukui, H. Uchiyama, and C. Solans. Spontaneous formation of highly concentrated water-in-oil emulsions. *Langmuir*, 12:2136–2140, 1996.

[95] M. Boutonnet, J. Kizling, P. Stenius, and G. Maire. The preparation of monodisperse colloidal metal particles from microemulsions. *Colloid Surface*, 5:209–225, 1982.

[96] K. Landfester. Synthesis of colloidal particles in miniemulsions. *Ann. Rev. Mater. Res.*, 36:231–279, 2006.

[97] Markus Antonietti and Katherine Landfester. Polyreactions in miniemulsions. *Prog. Polym. Sci.*, 27:689–757, 2002.

[98] J. Eastoe, M. J. Hollamby, and L. Hudson. Recent advances in nanoparticle synthesis with reversed micelles. *Adv. Colloid Interfac.*, 128-130:5–15, 2006.

[99] V. Uskokovic and M. Drofenik. Synthesis of materials within reverse micelles. *Surf. Rev. Lett.*, 12(2):239–277, 2005.

[100] T. Proffen and K. L. Page. Obtaining structural information from the atomic pair distribution function. *Z. Kristallogr.*, 219:130–135, 2004.

[101] M. F. Thorpe S. J. L. Billinge. *Local structure from Diffraction*. Kluwer, New York, 1998.

[102] P. J. Chupas, X. Qui, J. C. Hanson, P. L. Lee, C. P. Grey, and S. J. L. Billinge. Rapid-acquisition pair distribution function (RA-PDF) analysis. *J. Appl. Cryst.*, 36:1342–1347, 2003.

[103] A. P. Hammersley, S. O. Svensson, M. Hanfland, A. N. Fitch, and D. Hausermann. Two-dimensional detector software: From real detector to idealized image or two-theta scan. *High Pressure Research*, 14:235–248, 1996.

[104] H.M. Rietveld. Line profiles of neutron powder-diffraction peaks for structure refinement. *Acta Cryst.*, 22:151–152, 1967.

[105] J.F. Bérar and P. Garnier. Accuracy in powder diffraction. In *Proc. II, International Conference Gaithersburg*, volume 846, page 212. NIST Spec. Publ., 1992. available from http://www.ccp14.ac.uk.

[106] A. C. Larson and R. B. Von Dreele. General structure analysis system (GSAS). *Los Alamos National Laboratory Report LAUR*, 86-748, 2000.

[107] B. H. Toby. EXPGUI: a graphical user interface for GSAS. *J. Appl. Cryst.*, 34:210–213, 2001.

[108] T. Egami and S. J. L. Billinge. *Underneath the Bragg peaks: structural analysis of complex materials*. Pergamon Press Elsevier, Oxford, England, 2003.

[109] B. D. Cullity and S. R. Stock. *Elements of X-ray Diffraction*. Prentice Hall, Upper Saddle River, NJ, 3rd edition, 2001.

[110] X. Qiu, J. W. Thompson, and S. J L. Billinge. PDFgetX2: A GUI driven program to obtain pair distribution function from X-ray powder diffraction data. *J. Appl. Cryst*, 37:678, 2004.

[111] C. L. Farrow, P. Juhas, J. W. Liu, D. Bryndin, E. F. Božin, J. Bloch, T. Proffen, and S. J. L. Billinge. PDFfit2 and PDFgui: computer programs for studying nanostructure in crystals. *J. Phys.: Condens. Matter*, 19:335219, 2007.

[112] N.C. Greenham, I.D.W. Samuel, G.R. Hayes, R.T. Phillips, Y.A.R.R. Kessener, S.C. Moratti, A.B. Holmes, and R.H. Friend. Measurement of absolute photoluminescence quantum efficiencies in conjugated polymers. *Chem. Phys. Lett.*, 241:89, 1995.

[113] W. Becker. *Advanced Time-Correlated Single Photon Counting Techniques*. Springer-Verlag, New York, 2005.

[114] E. Zych, C. Brecher, and J. Glodo. Kinetics of cerium emission in a YAG:Ce single crystal: the role of traps. *J. Phys.-Condens. Mat.*, 12:1947, 2000.

[115] I. Etchart. Photoluminescent excitation and emission of cerium-lanthanum formate framework. Personal Communication.

[116] S.-H. Huang, G.-D. Zhou, and T. C. W. Mak. Crystal structure of lanthanum(iii) oxalate decahydrate. *J. Cryst. Spectrosc*, 21:127–131, 1991.

[117] S. Roméro, A. Mosset, and J. C. Trombe. Two new families of lanthanide mixed-ligand complexes, oxalate carbonate and oxalate formate. *J. Solid State Chem.*, 127:256–266, 1996.

[118] I. V. Kalinina, A. L. Guschin, D. G. Samsonenko, A. V. Gerasimenko, M. N. Sokolov, and V. P. Fedin. Hexaaquatrioxalatodierbium(III) tetrahydrate: $[Er(H_2O)_{32}(C_2O_4)_3]_4H_2O$. *Acta Cryst. E*, E59:m784–m786, 2003.

[119] S. Natarajan, R. Vaidhyanathan, C. N. R. Rao, S. Ayyappan, and A. K. Cheetham. Layered tin(III) oxalates possessing large apertures. *Chem. Mater.*, 11:1633–1639, 1999.

[120] N. Audebrand, E. Jeanneau, T. Bataille, S. Raite, and D. Louër. A family of microporous mixed oxalates with isotypic-framework structures based on eight-coordinate metals. *Solid State Sci.*, 6:579–591, 2004.

[121] M. Camara, C. Daiguebonne, K. Boubekeur, T. Roisnel, Y. Gérault, C. Baux, F. Le Dret, and O. Guillou. Re-investigation of the Er^{3+}-$C_2O_4^{2-}$-H_2O system. *C. R. Chimie*, 6:405, 2003.

[122] G. Vanhoyland, A. Le Bail, J. Mullens, and L. C. Van Poucke. Characterzation and structure determination of ammonium bismuth oxalate hydrate. *Inorg. Chem*, 43:785, 2004.

[123] U. Heinl, P. Hinse, and R. Mattes. Oxalato- and squarato-bridged threedimensional networks. *Z. Anorg. Allg. Chem*, 627:2173, 2001.

[124] K. P. Mörtl, J. P. Sutter, S. Golhen, L. Ouahab, and O. Kahn. Structure and magnetic characteristics of an oxalate-bridged U(IV)-Mn(II) threedimensional network. *Inorg. Chem*, 39:1626, 2000.

[125] T. Bataille, J.-P. Auffrédic, and D. Louër. Ab initio structure determination and dehydration dynamics of yttrium potassium oxalate tetrahydrate studied by x-ray powder diffraction. *Chem. Mater.*, 11:1559, 1999.

[126] E. Jeanneau, N. Audebrand, J.-P. Auffrédic, and D. Louër. Crystal structure, thermal behaviour, and zeolitic properties of $Cd_2Zr(C_2O_4)_4{\cdot}(4+n)H_2O$. *J. Mater. Chem.*, 11:2545, 2001.

[127] E. Jeanneau, N. Audebrand, and D. Louër. Synthesis, crystal structure, and thermal behaviour of $CdZrK_2(C_2O_4)_4{\cdot}(4+n)H_2O$. *J. Mater. Chem.*, 12:2383, 2002.

[128] D. J. Price, A. K. Powell, and P. T. Wood. Hydrothermal crystallization and x-ray structure of anhydrous strontium oxalate. *Polyhedron*, 18:2499–2503, 1999.

[129] E. Jeanneau, N. Audebrand, and D. Louër. beta-CdC_2O_4. *Acta Cryst. C*, C57:1012–1013, 2001.

[130] C. Trifa, A. Bouhali, C. Boudaren, S. Bouacida, and T. Bataille. Anhydrous barium strontium oxalate. *Acta Cryst. E*, 63:i102–i104, 2007.

[131] A. N. Christensen, R. G. Hazell, and I. C. Madsen. Synthesis and characterization of the barium oxalates. *Acta Cryst. B*, B58:808–814, 2002.

[132] E. C. Spencer, R. J. Angel, N. L. Ross, B. E. Hanson, and J. A. K. Howard. Pressure-induced cooperative bond rearrangement in a zinc imidazolate framework: A high-pressure single-crystal X-ray diffraction study. *J. Am. Chem. Soc.*, 131:4022–4026, 2009.

[133] K. W. Chapman, G. J. Halder, and P. J. Chupas. Guest-dependent high pressure phenomena in a nanoporous metalorganic framework material. *J. Am. Chem. Soc.*, 130:10524–10526, 2008.

[134] M. D. Allendorf, R. J. T. Houk, L. Andruszkiewicz, A. A. Talin, J. Pikarsky, A. Choudhury, K. A. Gall, and P. J. Hekseth. Stress induced chemical detection using flexible metal-organic frameworks. *J. Am. Chem. Soc.*, 130:14404–14405, 2008.

[135] D. F. Bahr, J. A. Reid, W. M. Mook, C. A. Bauer, R. Stumpf, A. J. Skulan, N. R. Moody, B. A. Simmons, M. M. Shindel, and M. D. Allendorf. Mechanical properties of cubic zinc carbxylate IRMOF-1 metal organic framework crystals. *Phys. Rev. B*, 76:184106, 2007.

[136] J. C. Tan, J. D. Furman, and A. K. Cheetham. Relating mechanical properties and chemical bonding in an inorganicorganic framework material: A singlecrystal nanoindentation study. *J. Am. Chem. Soc.*, 40:14252–14254, 2009.

[137] J. C. Tan, C. A. Merrill, J. B. Orton, and A. K. Cheetham. Anisotropic mechanical properties of polymorphic hybrid framework materials with different dimensionalities. *Acta Mater.*, 57:3481–3496, 2009.

[138] W. C. Oliver and G. M. Pharr. Review: Measurement of hardness and elastic modulus by instrumented indentation: Advances in understanding and refinements to methodology. *J. Mater. Res.*, 19:3–20, 2004.

[139] W. C. Olilver and G. M. Pharr. An improved technique for determining hardness and elastic modulus using load and displacement sensing indentation experiments. *J. Mater. Res.*, 7:1564–1583, 1992.

[140] C. Kittel. *Introduction to solid state physics*. John Wiley and Sons, New Jersey, 8th edition, 2005.

[141] J.P. Lu. Elastic properties of carbon nanotubes and nanoropes. *Phys. Rev. Lett.*, 79:1297–1300, 1997.

[142] J. C. Tan, T. D. Bennett, and A. K. Cheetham. Chemical structure, network topology, and porosity effects on the mechanical properties of zeolitic imidazolate frameworks. *P. Natl. Acad. Sci. USA*, 107:9938–9943, 2010.

[143] T. D. Bennett, A. L. Goodwin, M. T. Dove, D. A. Keen, M. G. Tucker, E. R. Barney, A. K. Soper, E. G. Bithell, J. C. Tan, and A. K. Cheetham. Structure and properties of an amorphous metal-organic framework. *Phys. Rev. Lett.*, 104:115503, 2010.

[144] L. E. Lyons and J. W. White. Luminescence from anthracene crystals and its temperaturedependence. *J. Chem. Soc.*, pages 5213–5220, 1960.

[145] B. S. Yamanashi and D. M. Hercules. Solution luminescence of anthraquinone, napthoquinone, and some derivatives at room temperature. *Appl. Spectroscopy*, 25:457–460, 1971.

[146] J. D. Scott and W. H. Watson. Polarization of the absorption and emission spectra of 9,10-anthraquinone and 2-methyl-9,10-anthraquinone. *J. Chem. Phys.*, 49:4246–4247, 1968.

[147] H. R. Drott and H. H. Dearman. Polarizations of the lowenergy $S_n \rightarrow S_0$ Transitions in 9,10-Anthraquinone. *J. Chem. Phys.*, 47:1896, 1967.

[148] K. T. Kamtekar, A. P. Monkman, and M. R. Bryce. Recent advances in white organic light-emitting materials and devices. *Adv. Mater.*, 22:572–582, 2009.

[149] G. M. Sheldrick. *Cell_Now*. Bruker-AXS, Inc., Madison, WI, 2004.

[150] J. C. Lashley, M. F. Hundley, A. Migliori, J. L. Sarrao, P. G. Pagliuso, T. W. Darling, M. Jaime, J. C. Cooley, W. L. Hults, L. Morales, D. J. Thoma, J. L. Smith, J. Boerio-Goates, B. F. Woodfield, G. R. Stewart, R. A. Fisher, and N. E. Phillips. Critical examination of heat capacity measurements made on a quantum design physical property measurement system. *Cryogenics*, 43(6):369–378, 2003.

[151] B. C. Melot, R. Tackett, J. O'Brien, A. L. Hector, G. Lawes, R. Seshadri, and A. P. Ramirez. Large low-temperature specific heat in pyrochlore $Bi_2Ti_2O_7$. *Phys. Rev. B*, 79:224111, 2009.

[152] C. Kittel and H. Kroemer. *Thermal Physics*. W. H. Freeman, New York, 2nd edition, 1980.

[153] D. R. Gaskell. *Introduction to the thermodynamics of materials*. Taylor and Francis, New York, 4th edition, 2003.

[154] A. Tari. *The specific heat of matter at low temperatures*. Imperial College Press, London, 2003.

[155] S. Zhou, Z. Fu, J. Zhang, and S. Zhang. Spectral properties of rare-earth ions in nanocrystalline YAG:Re (Re=Ce^{3+}, Pr^{3+}, Tb^{3+}). *J. Lumines.*, 118:179–185, 2006.

[156] J. D. Furman, G. Gundiah, K. Page, N. Pizarro, and A. K. Cheetham. Local structure and time resolved luminescence of emulsion prepared YAG nanoparticles. *Chem. Phys. Lett.*, 465:67–72, 2008.

[157] X. Liu and H. v. Löhneysen. Specific-heat anomaly of amorphous solids at intermediate temperatures (1 to 30 k). *Europhys. Lett.*, 33:617–622, 1996.

[158] M. A. Ramos, S. Vieira, F. J. Bermejo, J. Dawidowski, H. E. Fischer, H. Schober, M. A. González andn C. K. Loong, and D. L. Price. Quantitative assessment of the effects of orientational and positional disorder on glassy dynamics. *Phys. Rev. Lett.*, 78:82–85, 1997.

[159] S. Hayashi, S. Inagi, and T. Fuchigami. Synthesis of 9-substituted fluorene copolymers via chemical and electrochemical polymer reaction and their optoelectronic properties. *Macromolecules*, 42:3755, 2009.

[160] R. Abbel, C. Grenier, M. J. Pouderoijen, J. W. Stouwdam, P. E. L. G. Leclére, R. P. Sijbesma, E. W. Meijer, and A. P. H. J. Schenning. White-light emitting hydrogen-bonded supramolecular copolymers based on π-conjugated oligomers. *J. Am. Chem. Soc.*, 131:833, 2009.

[161] S. R. Amrutha and M. Jayakannan. Control of π-stacking for highly emissive poly(p-phenylenevinylene)s: Synthesis and photoluminescence of new tricyclodecane substituted bulky poly(p-phenylenevinylene)s and its copolymers. *J. Phys. Chem. B*, 110:4083–4091, 2006.

[162] S. R. Amrutha and M. Jayakannan. Probing the π-stacking induced molecular aggregation in π-conjugated polymers, oligomers, and their blends of p-phenylenevinylenes. *J. Phys. Chem. B*, 112:1119–1129, 2008.

[163] L. Akcelrud. Electroluminescent polymers. *Prog. Polym. Sci*, 28:875–962, 2003.

[164] J. Cornil, D. A. dos Santos, X. Crispin, R. Silbey, and J. L. Brédas. Influence of interchain interactions on the absorption and luminescence of conjugated oligomers and polymers: A quantum-chemical characterization. *J. Amer. Chem. Soc.*, 120:1289–1299, 1998.

[165] Z.-F. Chen, R.-G. Xiong, J. Zhang, X.-T. Chen, Z.-L. Xue, and X.-Z. You. 2d molecular square grid with strong blue fluorescent emission: A complex of norfloxacin with zinc(ii). *Inorg. Chem.*, 40:4075–4077, 2001.

[166] E. H. L. Falcão, Naroso, R. K. Feller, G. Wu, F. Wudl, and A. K. Cheetham. Hybrid organicinorganic framework structures: Influence of cation size on metaloxygenmetal connectivity in the alkaline earth thiazolothiazoledicarboxylates. *Inorg. Chem.*, 18:8336–8342, 2008.